Towards Reversible High-Voltage Oxygen Redox in Secondary Alkali-Ion Batteries

John-Joseph Marie

Lincoln College
University of Oxford

A thesis submitted for the degree of
Doctor of Philosophy

Trinity 2022

Abstract

Alkali-Ion batteries today are restricted in energy density by the physical limitations of current cathode materials. One of the most promising avenues to increasing their energy density is to invoke oxygen redox (O-redox) in next generation cathode materials. The oxidation of the oxide sub-lattice, O^{2-}, to O^{-} occurs at a higher voltage than conventional transition metal (TM) redox. In addition, Alkali-rich cathodes displaying O-redox reach far greater charge capacities than conventional cathodes, increasing the energy density provided. However, in many materials, the O^{2-}/O^{-} redox couple is not stable, leading to the reversible cycling of an O^{2-}/O_2 redox couple instead. The formation of molecular O_2 in Alkali-rich cathodes is accompanied by large hysteresis and structural changes, causing further complications over cycling.

In this thesis, specific design principles derived from a fundamental understanding of O-redox will be implemented in an attempt to harness the full potential of O-redox. First, $Li_{1.2}Mn_{0.54}Ni_{0.13}Co_{0.13}O_2$ will be used to investigate voltage fade, a continuous decrease in the average operational voltage, in Li-rich cathode materials. An investigation into the reversibility of the O^{2-}/O_2 redox couple over cycling attributes this loss of voltage to a gradual loss of O^{2-}/O_2 activity, driven by O_2 loss and large-scale structural changes.

Second, the importance of *in operando* techniques in the study of O-redox will be discussed. $Na_{0.6}Mn_{0.8}Li_{0.2}O_2$ will be studied via *in operando* Mn K-edge XAS, investigating claims of Mn^{4+} oxidation. In addition, the development of an operando Soft X-ray Absorption Spectroscopy (SXAS) cell will be presented.

Third, a pillaring strategy aimed at promoting the activity of the O^{2-}/O^{-} redox couple will be investigated. To prevent the inter-layer migration of TM ions which leads to the formation of O_2 in the bulk of O-redox materials, the cationic pillaring of $Na_{0.67}Mn_{0.72}Mg_{0.28}O_2$ using Ca^{2+} will be studied using a novel, room temperature ion-exchange method.

Finally, the $Na_{0.66}Li_{0.1}Ni_{0.3}Mn_{0.6}O_2$ will be introduced as a highly efficient O-redox cathode, combining both TM and O-redox charge compensation. Spectroscopic characterisation of the material will show that the O^{2-}/O^{-} redox couple is active over the first cycle, with no molecular O_2 formed on charge.

Towards Reversible High-Voltage Oxygen Redox in Secondary Alkali-Ion Batteries



John-Joseph Marie

Lincoln College

University of Oxford

A thesis submitted for the degree of
Doctor of Philosophy

Trinity 2022

Let everything happen to you.

Beauty and terror.

Just keep going.

No feeling is final.

- ***Rainer Maria Rilke***

Acknowledgements

My PhD experience has made me appreciate that science is well and truly a group effort, both through collaborative research and through our responsibility to acknowledge the work of others. I would not have made it through this demanding and enjoyable journey without the support and contribution of my family, friends, and colleagues.

Professional

First and foremost, I would like to thank my supervisor, Professor Sir Peter Bruce, F.R.S. for giving me the opportunity to work and learn in a world-class research environment. The outstanding laboratory space you have established in Oxford has inspired me to work to reach my potential as I worked towards my PhD. I would also like to thank the Faraday Institution for funding my four years of research with the PGB Group in Oxford, as well as providing me with opportunities for extracurricular development.

Dr. Jun Chen, it has been an absolute pleasure to share a desk with you for the past two years. Our conversations have always been a welcome break from the lab, and I have thoroughly enjoyed working with you in our mutual struggle to develop oxygen redox cathodes. Liquan Pi, thank you for being someone I could bounce ideas off. It was always nice to see a friendly face in the lab, despite us both working late into the day. Dr. Gregory Rees, thank you for your willingness to try new experiment ideas, and for the countless hours of NMR data collection and analysis throughout the course of my PhD. Dr. Nadia Abdul-Karim, thank you for your tireless work to keep our labs stocked and safe for us to work in. I must also thank Dr. Paul Adamson for reviewing my thesis, and to other members of the PGB group, past and present, with whom I have worked closely with over these past four years, including Dr. Dominic Spencer-Jolly, Dr. Miguel Perez Ozario, Dr. Sofia De Sousa Coutinho and Dr. Mikkel Juelsholt. I would also like to wish all the best to the newer members of the PGB group as they settle in.

Finally, I would like to thank Dr. Robert House. Your mentorship and endless experience have been invaluable to me and so many others in the PGB group. Whether it was 10 am in the lab, or 10 pm on one of our many beam times, you were always willing to offer advice and answer my numerous questions about science. You have taught me the importance of thinking critically about my work, and how best to approach scientific investigation. I am being honest when I say I do not think I would have completed my PhD without your support.

Personal

To my family, thank you for being a constant source of love and support, always being there to welcome me home during family breaks and holidays, and for listening politely as I explained my latest problem at work.

To my sisters, Faron and Chelsea, thank you for keeping me grounded for the past 26 years. I feel grateful that between the three of us we are always there to celebrate each other's achievements and to give support through our setbacks.

To my parents, Dale and Michel. Mum, thank you for proof-reading my whole thesis. I would not be where I am today without the love and support you have both given me throughout my life. Thank you for always pushing me to go one step further, and to always make the most of any opportunity that has come my way. I dedicate this thesis to you both.

Abstract

Alkali-Ion batteries today are restricted in energy density by the physical limitations of current cathode materials. One of the most promising avenues to increasing their energy density is to invoke oxygen redox (O-redox) in next generation cathode materials. The oxidation of the oxide sub-lattice, O^{2-}, to O^{-} occurs at a higher voltage than conventional transition metal (TM) redox. In addition, Alkali-rich cathodes displaying O-redox reach far greater charge capacities than conventional cathodes, increasing the energy density provided. However, in many materials, the O^{2-}/O^{-} redox couple is not stable, leading to the reversible cycling of an O^{2-}/O_2 redox couple instead. The formation of molecular O_2 in Alkali-rich cathodes is accompanied by large hysteresis and structural changes, causing further complications over cycling.

In this thesis, specific design principles derived from a fundamental understanding of O-redox will be implemented in an attempt to harness the full potential of O-redox. First, $Li_{1.2}Mn_{0.54}Ni_{0.13}Co_{0.13}O_2$ will be used to investigate voltage fade, a continuous decrease in the average operational voltage, in Li-rich cathode materials. An investigation into the reversibility of the O^{2-}/O_2 redox couple over cycling attributes this loss of voltage to a gradual loss of O^{2-}/O_2 activity, driven by O_2 loss and large-scale structural changes.

Second, the importance of *in operando* techniques in the study of O-redox will be discussed. $Na_{0.6}Mn_{0.8}Li_{0.2}O_2$ will be studied via *in operando* Mn K-edge XAS, investigating claims of Mn^{4+} oxidation. In addition, the development of an operando Soft X-ray Absorption Spectroscopy (SXAS) cell will be presented.

Third, a pillaring strategy aimed at promoting the activity of the O^{2-}/O^{-} redox couple will be investigated. To prevent the inter-layer migration of TM ions which leads to the formation of O_2 in the bulk of O-redox materials, the cationic pillaring of $Na_{0.67}Mn_{0.72}Mg_{0.28}O_2$ using Ca^{2+} will be studied using a novel, room temperature ion-exchange method.

Finally, the $Na_{0.66}Li_{0.1}Ni_{0.3}Mn_{0.6}O_2$ will be introduced as a highly efficient O-redox cathode, combining both TM and O-redox charge compensation. Spectroscopic characterisation of the material will show that the O^{2-}/O^{-} redox couple is active over the first cycle, with no molecular O_2 formed on charge.

Contents

Recognising the Impact of COVID-19 on this Thesis ..... **xi**
List of figures ..... **xiv**
List of Tables ..... **xx**
List of Abbreviations ..... **xxii**
Publication List ..... **xxiv**

Chapter 1 - Introduction

1.1 Wider Context **2**
1.2 Background and Fundamentals of Li-ion Batteries **3**
1.2.1 Historical Background 3
1.2.2 The Layout of a Li-ion Battery 4
1.2.3 Energy Storage in Alkali-ion Batteries 6
1.3 An Introduction to Li-ion and Na-ion cathodes **9**
1.3.1 Physical Properties of Li-ion and Na-ion Batteries 9
1.3.2 Structural Properties of Layered Li-ion and Na-ion Cathodes 11
1.3.3 The Problem with Cathode Materials 13
1.4 O-redox in Layered Cathode Materials **15**
1.4.1 Understanding 'Anomalous' Capacities in Li-rich Materials 15
1.4.2 Early O-redox Mechanisms 16
1.4.3 Molecular Oxygen Formation in O-redox Cathodes 21
1.4.4 Voltage Fade in O-redox Cathodes 24
1.5 Strategies Towards Reversible High Voltage O-redox **26**
1.5.1 Structural Pillaring 26
1.5.2 Multi-Valent Cation Doping 28
1.5.3 New Superstructure Ordering 28
1.5.4 Embracing the O^{2-}/O_2 Redox Couple 29
1.6 Thesis Objectives **30**
1.7 References **32**

Chapter 2 - Methods

2.1 Materials Synthesis 40
2.1.1 Solid State Synthesis 40
2.1.2 Sol-Gel Synthesis 41
2.1.3 Co-precipitation Synthesis 41
2.2 Materials Characterisation 42
2.2.1 Inductively Coupled Plasma Optical Emission Spectrometry 42
2.2.2 Scanning Electron Microscopy 43
2.2.3 Energy Dispersive X-ray Spectrometry 44
2.2.4 Thermogravimetric Analysis 44
2.3 Electrochemical Methods 45
2.3.1 Electrode Preparation 45
2.3.2 Coin Cell Assembly 45
2.3.3 Cell Cycling 46
2.3.4 Ex-Situ Sample Preparation 47
2.3.5 Operando Electrochemical Mass Spectrometry 48
2.4 Spectroscopic Techniques 49
2.4.1 X-ray Absorption Spectroscopy 49
2.4.2 Extended X-ray Absorption Fine Structure 53
2.4.3 Operando Cells for XAS Experiments 54
2.4.4 Resonant Inelastic X-ray Scattering 56
2.5 Structural Characterisation 58
2.5.1 Nuclear Magnetic Resonance 58
2.5.2 An Introduction to Powder Diffraction 59
2.5.4 Rietveld Refinement 64
2.5.3 Electrochemical Cells for Operando Diffraction Measurements 66
2.5.5 Annular Dark Field Scanning Transmission Electron Microscopy 66
2.5.6 Electron Energy Loss Spectroscopy 67
2.6 References 68

Chapter 3 - Investigating Voltage Fade in Li-rich Layered Oxides

3.1 Introduction 71
3.2 Experimental 73

3.3 Results and Discussion 76
3.3.1 Structural Characterisation 76
3.3.2 Electrochemical Characterisation 80
3.3.3 Low Temperature Annealing of $Li_{1.2}Ni_{0.13}Co_{0.13}Mn_{0.54}O_2$ 84
3.3.4 The Origin of Voltage Fade in Li-rich Cathode Materials 88
3.4 Conclusion 101
3.5 References 103

Chapter 4 - In-Operando Analysis of $Na_{0.6}Mn_{0.8}Li_{0.2}O_2$

4.1 Introduction 105
4.2 Experimental 107
4.3 Results 109
4.3.1 Characterisation of $Na_{0.6}Mn_{0.8}Li_{0.2}O_2$ 109
4.3.2 *In-Operando* Studies of the Mn K-edge in $Na_{0.6}Mn_{0.8}Li_{0.2}O_2$ 111
4.3.3 Investigation on the stability of oxygen holes in $Na_{0.6}Mn_{0.8}Li_{0.2}O_2$ 114
4.3.4 Electrochemical cell development for *In-Operando* analysis of the O K-edge in $Na_{0.6}Mn_{0.8}Li_{0.2}O_2$ 116
4.4 Conclusion 122
4.5 References 122

Chapter 5 - Pillaring as a Strategy to Prevent Bulk Formation of Molecular O_2

5.1 Introduction 125
5.2 Experimental 128
5.3 Results 130
5.3.1 Synthesis and Characterisation of $NaMn_{0.72}Mg_{0.28}O_2$ 130
5.3.2 Investigation of Ca^{2+} Insertion into $Na_{0.67}Mn_{0.72}Mg_{0.28}O_2$ 131
5.3.3 Confirming the Presence of Ca^{2+} in $Na_{0.47}Ca_{0.1}Mn_{0.72}Mg_{0.28}O_2$ 135
5.3.4 Evaluating Ca^{2+} Insertion Limits in $Na_{0.67-2x}Ca_xMn_{0.72}Mg_{0.28}O_2$ 137
5.3.5 Electrochemical Analysis of $Na_{0.47}Ca_{0.1}Mn_{0.72}Mg_{0.28}O_2$ 140
5.3.6 Discussion 142
5.4 Conclusion 144
5.5 References 145

Chapter 6 - $Na_{0.66}Li_{0.1}Ni_{0.3}Mn_{0.6}O_2$ as a Reversible High Voltage O-redox Cathode

6.1 Introduction 147
6.2 Experimental 149
6.3 Results 151
6.3.1 Structural Characterisation 151
6.3.2 Electrochemical Characterisation 154
6.3.3 Surface and Structural Stability Characterisation over Cycling 157
6.3.4 Spectroscopic Characterisation 161
6.3.5 Discussion 165
6.4 Conclusion 168
6.5 References 169

Chapter 7 - Conclusion

7.1 Conclusion 171
7.2 Future Work 173
7.2.1 Investigating Surface Coatings to Prevent O_2 Loss 174
7.2.2 *In Operando* O K-edge XAS and RIXS of O-redox Cathodes 174
7.2.3 Exploring Room Temperature Ion-Exchange 174
7.2.4 Investigating O-redox Activity in Fully Dense Layered Oxides 175
7.2.5 Further Research into Non-Honeycomb Ordered Cathodes 175

Appendices

Appendices for Chapter 3 177
Investigating Voltage Fade in Li-rich Layered Oxides 177
Appendices for Chapter 4 181
In-Operando Analysis of $Na_{0.6}Mn_{0.8}Li_{0.2}O_2$ 181
Appendices for Chapter 5 183
Pillaring as a Strategy to Prevent Bulk Formation of Molecular O_2 183
Appendices for Chapter 6 185
$Na_{0.66}Li_{0.1}Ni_{0.3}Mn_{0.6}O_2$ as a Reversible High Voltage O-redox Cathode 185

Recognising the Impact of COVID-19 on this Thesis

I feel very fortunate that Covid-19 has not had as great an impact on my studies as some of my colleagues. However, there were indeed some unforeseen consequences of the pandemic which affected my research, most notably on the studies presented in chapter 4, which were unable to be completed due to the global disruption caused by the Covid-19 pandemic.

Chapter 4 in this thesis was intended to focus on an *in-operando* investigation of $Na_{0.6}Mn_{0.8}Li_{0.2}O_2$, comprising *in-operando* studies of the Mn and O K-edges via XAS, and of the O K-edge using RIXS. In early 2020, our proposal for beam time was accepted by the BL27SU beamline at the Spring-8 synchrotron in Sayo, Japan, with the experimental time scheduled for July 2020. By the end of March 2020 the effects of Covid-19 were being felt around the world, leading to the closure of the University of Oxford Materials Department until the beginning of August 2020. The awarded beamtime was subsequently rescheduled for February 2021. However, the beam time was cancelled outright in late 2020 following the second wave of Covid-19.

A second experimental proposal with the same experimental aim was submitted and accepted in April 2021, with the time scheduled for February 2022. Unfortunately, travel restrictions barring entry to Japan of foreign visitors were still in force by December 2021, and we made the difficult decision to once again cancel our beamtime.

It is worth considering the reasons for carrying out these experiments at the Spring-8 synchrotron. First, our research group has had a long and successful research

relationship with BL27SU. Second, the BL27SU beamline had previously carried out *in-operando* battery measurements on their beamline, and so had the experience and willingness to support these experiments with our own cell design. Third, the cell developed in this chapter was designed to mount onto the transfer rod in use specifically at the BL27SU end station. For these reasons, BL27SU was the most suitable beamline for these measurements. When the third round of beam time was cancelled in December 2021, attempts were made to carry out this experiment at the B07 beam line at the Diamond Light Source, a soft X-ray XAS beam line with *in-operando* capabilities. However, attempts to secure beamtime through the rapid access route were unsuccessful.

List of Figures

Figure 1.1: Schematic of a conventional Li-ion battery 5
Figure 1.2: Schematic showing a typical electrochemical load curve 6
Figure 1.3: Illustration of the four most common layered crystal structures 12
Figure 1.4: Structural and electrochemical comparison of conventional and O-redox cathodes 14
Figure 1.5: Representation of the local co-ordination environment around oxygen in conventional and O-redox cathodes 17
Figure 1.6: An overview of the peroxo stabilisation theory of O-redox 19
Figure 1.7: Representation of different superstructures which can arise in layered TMO_2 compounds 21
Figure 1.8: Representation of the O-redox processes in the first and subsequent cycles of Li-rich layered oxides 23
Figure 1.9: Representation of the local co-ordination environment around oxygen in a Li-rich layered and a multi-valent cation doped material 27
Figure 1.10: Depiction of the theoretical effect of pillaring on layered materials 28
Figure 1.11: Representation of different superstructures in layered TMO_2 materials ..29

Figure 2.1: Representation of a typical coin cell assembly 46
Figure 2.2: Representation of the cell used for OEMS experiments in this thesis 48
Figure 2.3: Representation of the electronic structure of an atom 50
Figure 2.4: A normalized XAS spectrum of MnO 52
Figure 2.5: Representation of the cell design used for operando XAS and EXAFS experiments 55
Figure 2.6: Representation of the cell design used for operando SXAS experiments ..55
Figure 2.7: Depiction of the key electronic transitions leading to RIXS emission 57
Figure 2.8: Different representations of RIXS data 58
Figure 2.9: Representation of Braggs Law 60

Figure 2.10: Representation of the operando cell used for diffraction experiments 66

Figure 3.1: The structure of $Li_{1.2}Ni_{0.13}Co_{0.13}Mn_{0.54}O_2$ 77
Figure 3.2: Rietveld refinement of co-precipitation synthesised LNCMO 77
Figure 3.3: Rietveld refinement of sol-gel synthesised LNCMO 78
Figure 3.4: SEM images and EDX analysis of pristine LNCMO, as synthesised by co-precipitation and sol-gel method 79
Figure 3.5: Electrochemical analysis of co-precipitation synthesised LNCMO 81
Figure 3.6: Electrochemical analysis of sol-gel synthesised LNCMO 82
Figure 3.7: OEMS analysis of co-precipitation synthesised LNCMO 83
Figure 3.8: OEMS analysis of the sol-gel synthesised LNCMO 84
Figure 3.9: Post-cycling heat treatment of LNCMO cathodes 85
Figure 3.10: Load curve of the 1st cycle, 20th cycle, and 1st cycle after annealing of sol-gel synthesised LNCMO 86
Figure 3.11: ^{6}Li NMR and PXRD analysis on pristine, 20th cycle and annealed cathode films 88
Figure 3.12: Comparison of galvanostatic cycling data for LNMCO cycled at different rates 89
Figure 3.13: Evolution in bulk O-redox activity over cycling, as measured by high-resolution RIXS 91
Figure 3.14: Evolution in intensity of the molecular O_2 signal over cycling 92
Figure 3.15: Formation of voids within Li-rich particles over cycling, as imaged by ADF-STEM 94
Figure 3.16: Investigation of pore formation using ^{129}Xe NMR 95
Figure 3.17: ^{6}Li and ^{17}O NMR isolating slow and fast relaxing environments 96
Figure 3.18: ^{17}O NMR showing the partial reduction of O_2 trapped in voids to form Li-coordinated O^{2-} on the 100th discharge 97
Figure 3.19: Depiction of the voltage fade mechanism over the 2nd cycle 100
Figure 3.20: Depiction of the voltage fade mechanism over the 100th cycle 101

Figure 4.1: Rietveld refinement of NMLO 109
Figure 4.2: Depiction of the ribbon ordering scheme present in the TM layer of $Na_{0.6}Mn_{0.8}Li_{0.2}O_2$ 110

Figure 4.3: Electrochemical cycling of NMLO 110
Figure 4.4: Plot of Mn K-edge HERFD-XAS absorption spectra for measured the Mn standards 111
Figure 4.5: In-operando Mn K-edge XAS spectra for NMLO 112
Figure 4.6: A comparison of the pristine, full charge and full discharge points collected during in-operando Mn K-edge XAS measurements 113
Figure 4.7: O K-edge SXAS and RIXS spectra of NMLO at the top of charge with different ageing periods 115
Figure 4.8: A representation of the cathode side, or cell top, of the in-operando SXAS cell 117
Figure 4.9: A representation of the anode side of the in-operando SXAS cell 117
Figure 4.10: An exploded view of the in-operando SXAS cell 118
Figure 4.11: A comparison of the electrochemical cycling in the operando SXAS cell under external vacuum 120

Figure 5.1: Demonstrating the effect of pillaring on $Na_{0.67}Mn_{0.72}Mg_{0.28}O_2$ 127
Figure 5.2: PXRD refinement for pristine NMMO 130
Figure 5.3: Electrochemical performance of NMMO 131
Figure 5.4: Description of the Ca^{2+} insertion synthesis process 132
Figure 5.5: In-situ measurement of the reaction mixture of NMMO and CaI_2 being left in an air atmosphere 133
Figure 5.6: Comparing the insertion of Ca into NMMO to form CaNMMO under different conditions 134
Figure 5.7: XRD comparison of NMMO, CaNMMO and annealed CaNMMO 135
Figure 5.8: SEM and EDX analysis of CaNMMO 136
Figure 5.9: STEM image of a CaNMMO particle being analysed by EELS 137
Figure 5.10: Structural and electrochemical characterisation of CaNMMO 140
Figure 5.11: PXRD comparison of a) CaNMMO and b) NMMO in the pristine, charged, and discharged states 141

Figure 6.1: Rietveld refinement of NLNMO 151
Figure 6.2: ^{7}Li and ^{23}Na NMR of pristine NLNMO 152

Figure 6.3: SEM images and EDX analysis of pristine NLNMO 152
Figure 6.4: Electrochemical analysis of NLNMO 154
Figure 6.5: GITT analysis of NLNMO over the 1st and 30th cycles 155
Figure 6.6: Further electrochemical analysis of NLNMO 156
Figure 6.7: Ex-situ ^{23}Na and ^{7}Li NMR of multi-cycled NLNMO 157
Figure 6.8: *In-operando* PXRD of NLNMO over the 1st cycle 158
Figure 6.9: Further analysis of the *in-operando* PXRD data 159
Figure 6.10: OEMS analysis of NLNMO 160
Figure 6.11: a) Electrochemical load curve of NLNMO showing the points which were studied using ex-situ spectroscopy. b) Ex-situ Ni K-edge XANES of NLNMO 161
Figure 6.12: Ex-situ measurements of the O K-edge of NLNMO over the 1st cycle by SXAS (a) and RIXS (b) 162
Figure 6.13: Ex-situ measurements of the Ni K-edge XANES in NLNMO over cycling 163
Figure 6.14: Ex-situ measurements of the O K-edge of NLNMO by SXAS 164
Figure 6.15: Ex-situ RIXS measurements of NLNMO over cycling 164

Figure A3.1: NMR deconvolution of ^{6}Li NMR spectrum of pristine LNCMO 178
Figure A3.2: Plots of the individual high resolution RIXS scans taken at different sample locations for the a) 2nd cycle full charge and b) 100th cycle full charge 179
Figure A3.3: Selection of ADF-STEM images taken on 100th cycle LNCMO in the discharged state 179
Figure A3.4: ^{129}Xe NMR data alongside a plot of void size vs chemical shift 180

Figure A4.1: A comparison between two Mn K-edge XAS spectra taken at different spots on a full charge sample of NMLO 181
Figure A4.2: Electrochemical load curve of $Na_2Mn_3O_7$ 182

Figure A5.1: A Load curve comparison of cycling pristine NMMO and NMMO which has been washed in acetone 183
Figure A5.2: A STEM image of a CaNMMO particle being analysed by EELS 184

Figure A6.1: A comparison of the PXRD spectra of NLNMO and that of the *P*63/*mcm* space group 186
Figure A6.2: A comparison of the PXRD spectra of the *P*63/*mmc* space group with the Na 2*d* site full (black) and the Na 2*d* site empty (red) 186
Figure A6.3: Ex-situ PXRD measurements of NLNMO comparing the pristine, 1st cycle and 30th cycle 187
Figure A6.4: Comparison of ex-situ measurements of the Mn K-edge XANES in NLNMO over cycling 187
Figure A6.5: Comparison of ex-situ measurements of the Ni K-edge XANES in NLNMO over cycling 188

List of Tables

Table 1.1: A comparative list of the physical properties of Li and Na.....10

Table 3.1: Elemental composition of LNCMO synthesised by co-precipitation and sol-gel methods as measured by ICP-OES 80

Table 5.1: ICP-OES results from the various Ca-inserted compounds 138
Table 5.2: Le Bail fit results from the various Ca-inserted compounds.....139

Table 6.1: Elemental composition of NLNMO as measured by ICP-OES 153
Table 6.2: A comparison of performance metrics of NLNMO vs other high-performance Na-ion cathode materials 166

Table A3.1: Table of XRD Rietveld refinement parameters for co-precipitation synthesised LNCMO 177
Table A3.2: Table of XRD Rietveld refinement parameters for co-precipitation synthesised LNCMO 178
Table A3.3: Distribution of pore sizes collected from six different ADF-STEM images. 180

Table A4.1: Table of XRD Rietveld refinement parameters for NMLO 181

Table A5.1: Table of XRD Rietveld refinement parameters for pristine NMMO 183

Table A6.1: Table of XRD Rietveld refinement parameters for NLNMO..... 185

List of Abbreviations

ACN: Acetonitrile

ADF- STEM: Annular Dark Field Scanning Transmission Electron Microscopy

AM: Alkali Metal

CaNMMO: $Na_{0.47}Ca_{0.1}Mn_{0.72}Mg_{0.28}O_2$

DFT: Density Functional Theory

DLS: Diamond Light Source

EDX: Energy Dispersive X-ray Spectrometry

EELS: Electron Energy Loss Spectroscopy

EXAFS: Extended X-ray Absorption Fine Structure

GITT: Galvanostatic Intermittent Titration Technique

HERFD-XAS: High Energy Resolution Fluorescence detected X-ray Absorption Spectroscopy

ICP-OES: Inductively Coupled Plasma-Optical Emission Spectrometry

LNCMO: $Li_{1.2}Ni_{0.13}Co_{0.13}Mn_{054}O_2$

LNO: $LiNiO_2$

MAS-NMR: Magic Angle Spinning-Nuclear Magnetic Resonance

MS: Mass Spectrometry

ND: Neutron Diffraction

NLNMO: $Na_{0.66}Li_{0.1}Ni_{0.3}Mn_{0.6}O_2$

NMLO: $Na_{0.6}Mn_{0.8}Li_{0.2}O_2$

NMMO: $Na_{0.67}Mn_{0.72}Mg_{0.28}O_2$

NMR: Nuclear Magnetic Resonance

OEMS:	Online Electrochemical Mass Spectrometry
O-redox:	Oxygen Redox
PC:	Propylene Carbonate
PDF:	Pair Distribution Function
pDOS:	Projected Density of States
PFY:	Partial Fluorescence Yield
PTFE:	Polytetrafluoroethylene
PVDF:	Polyvinylidene fluoride
PXRD:	Powder X-ray Diffraction
RIXS:	Resonant Inelastic X-ray Spectroscopy
SAXS:	Small Angle X-ray Scattering
SEM:	Scanning Electron Microscopy
SOF:	Site Occupancy Factor
STEM:	Scanning Transmission Electron Microscopy
TFY:	Total Fluorescence Yield
TGA:	Thermogravimetric Analysis
TM:	Transition Metal
TMO_2:	Transition Metal Oxide
TOF:	Time of Flight
XANES:	X-ray Absorption Near Edge Structure
XAS:	X-ray Absorption Spectroscopy
XRD:	X-ray Diffraction

Publication List

1. House, R *et al.*, Delocalised electron-holes on oxygen in a battery cathode, *Nature Energy*, (2023).
2. Song, Weixin *et al.*, Imaging structural defects and associated oxygen positions in Li-rich $Li_{1.2}Ni_{0.13}Mn_{0.54}Co_{0.13}O_2$, *Microscopy and Microanalysis*, 28, 2606-2607, (2022).
3. Boivin, Edouard *et al.*., Controlling Iron versus oxygen redox in the layered cathode $Na_{0.67}Fe_{0.5}Mn_{0.5}O_2$: Mitigating voltage and capacity fade by Mg substitution, *Advanced Energy Materials*, 12, 2200702, (2022).
4. Pu, Shengda D *et al.*, Achieving ultra-high rate planar and dendrite-free zinc electroplating for aqueous zinc battery anodes, *Advanced Materials*, , 2202552, (2022).
5. Song, Weixin *et al.*, Direct imaging of oxygen shifts associated with the oxygen redox of Li-rich layered oxides, *Joule*, 6, 1049-1065, (2022).
6. Xu, Xiaoyu *et al.*, Li_2NiO_2F a new oxyfluoride disordered rocksalt cathode material, *Journal of The Electrochemical Society*, 168, 80521, (2021).
7. Song, Weixin *et al.*, Direct imaging of oxygen sub-lattice deformation in Li-rich cathode material using electron ptychography, *Microscopy and Microanalysis*, 27, 2724-2726, (2021).
8. Boivin, Edouard *et al.*, Bulk O_2 formation and Mg displacement explain O-redox in $Na_{0.67}Mn_{0.72}Mg_{0.28}O_2$, *Joule*, 5, 1267-1280, (2021).
9. House, Robert A *et al.*, Covalency does not suppress O_2 formation in 4d and 5d Li-rich O-redox cathodes, *Nature Communications*, 12, 2975, (2021).
10. House, Robert A *et al.*, The role of O_2 in O-redox cathodes for Li-ion batteries, *Nature Energy*, 6, 781-789, (2021).
11. Sharpe, Ryan *et al.*, Redox chemistry and the role of trapped molecular O_2 in Li-rich disordered rocksalt oxyfluoride cathodes, *Journal of the American Chemical Society*, 142, 21799-21809, (2020).
12. House, Robert A *et al.*, First-cycle voltage hysteresis in Li-rich 3d cathodes associated with molecular O_2 trapped in the bulk, *Nature Energy*, 5, 777-785, (2020).
13. Brandt, León Romano *et al.*, Synchrotron X-ray quantitative evaluation of transient deformation and damage phenomena in a single nickel-rich cathode particle, *Energy & Environmental Science*, 13, 3556-3566, (2020).
14. Pu, Shengda D *et al.*, Current-density-dependent electroplating in Ca electrolytes: From globules to dendrites, *ACS Energy Letters*, 5, 2283-2290, (2020).
15. Marie, J.J. *et al.*, Trapped O_2 and the origin of voltage fade in layered Li-rich cathodes (submitted).
16. Marie, J.J. *et al.*, Room temperature solid-state Ca-ion exchange in $Na_{0.67}Mn_{0.72}Mg_{0.28}O_2$ (submitted).
17. Marie, J.J. *et al.*, A high voltage Na-ion cathode utilising Ni-redox and electron holes on O^{2-} (in preparation).

Chapter 1
Introduction

Table of Contents

1.1 Wider Context 2
1.2 Background and Fundamentals of Li-ion Batteries 3
1.2.1 Historical Background 3
1.2.2 The Layout of a Li-ion Battery 4
1.2.3 Energy Storage in Alkali-ion Batteries 6
1.3 An Introduction to Li-ion and Na-ion cathodes 9
1.3.1 Physical Properties of Li-ion and Na-ion Batteries 9
1.3.2 Structural Properties of Layered Li-ion and Na-ion Cathodes. 11
1.3.3 The Problem with Cathode Materials 13
1.4 O-redox in Layered Cathode Materials 15
1.4.1 Understanding 'Anomalous' Capacities in Li-rich Materials 15
1.4.2 Early O-redox Mechanisms 16
1.4.3 Molecular Oxygen Formation in O-redox Cathodes 21
1.4.4 Voltage Fade in O-redox Cathodes 24
1.5 Strategies Towards Reversible High Voltage O-redox 26
1.5.1 Structural Pillaring 26
1.5.2 Multi-Valent Cation Doping 28
1.5.3 New Superstructure Ordering 28
1.5.4 Embracing the O^{2-}/O_2 Redox Couple 29
1.6 Thesis Objectives 30
1.7 References 32

1.1 Wider Context

Electrochemical energy storage plays an important role in today's society. The technological revolution brought in by the commercialisation of the Li-ion battery in the 1990's led to the development of portable electronics such as smartphones and laptops which have become ubiquitous in everyday life. As climate change pushes humanity towards an electrified society, revolutions in electric transportation and renewable energy have further increased the demand for energy storage solutions. This demand is endlessly driving the development of rechargeable batteries with lower costs, higher energy density and longer cycle life.

Compared to other rechargeable cell chemistries, Li-ion technology provides a high energy density, lower self-discharge rates and good cycling stability, establishing it as a key player in energy storage that looks set to lead the field in the coming years.[1–3] This technology is based on a "rocking-chair" mechanism where Li-ions flow reversibly between host structures known as the cathode and the anode, converting chemical energy into electrical energy in a controlled reaction. Graphite is typically used as the anode material while layered transition metal oxides (TMO_2) are conventionally used as the cathode material. However, the performance of state-of-the-art anodes is significantly ahead of state-of-the-art cathodes. In order to reach higher energy densities, new cathode materials and chemistries must be exploited to produce the next-generation of Li-ion batteries.

One promising class of cathode materials are the so-called 'oxygen redox' (O-redox) materials, where both transition metal (TM) centres and lattice oxide ions are active redox components. O-redox materials have generated widespread interest within the research community and industry alike. These materials have the potential to almost double the energy density stored compared to conventional cathode materials while simultaneously reducing our dependence on scarce elements such as cobalt.[4–6] This thesis will explore some

of the fundamental aspects of O-redox in order to further understand the electrochemical behaviour and the accompanying structural changes through ex-situ and *in operando* studies. Furthermore, a search for new materials which can harness the full potential of the O^{2-}/O^{-} redox couple will be presented, guided by specific design principles derived from a fundamental understanding of O-redox.

1.2 Background and Fundamentals of Li-ion Batteries

1.2.1 Historical Background

The world's first electrochemical battery is considered to be Alessandro Volta's "Voltaic Pile", developed in 1799, which consisted of a series of stacked Cu and Zn disks separated by brine-soaked cloth.[7] His discovery, along with the influential work of Michael Faraday, gave birth to the field of electrochemistry. What followed was the development of several battery chemistries over the next century and a half. In 1866, G.L. Leclanche invented the alkaline battery,[7] a cell chemistry which is still in use today. Ni based cell chemistries such as Ni-Cd (1899) and Ni-Fe (1901) were developed by W. Jungner and T. Edison respectively.[8] Perhaps the most successful cell chemistry from this period is the lead acid battery, invented in 1860 by G. Plante,[8] also the world's first rechargeable battery. While these cell chemistries all found practical applications, their low energy density limited the scope of their use.

In the 1970's, a number of different groups began researching a class of materials known as intercalation compounds.[9–13] In such materials ions are stored within a host structure and can be removed and replaced reversibly. Such materials proved to be well suited to the storage of a number of different alkali metal ions, including Lithium (Li) and Sodium (Na). This research eventually led to the commercialization of Li-ion cells comprised of TiS_2 cathodes (developed by M.S. Whittingham[14]) and Li-Al anodes in 1977.[2]

By the 1980's, a substantial amount of research had been undertaken on intercalation compounds involving both Na^+ and Li^+ intercalation from transition metal oxide hosts.[15–20] A significant milestone was the successful use of $LiCoO_2$ as a cathode for Li-ion batteries in 1981, as demonstrated by Goodenough and co-workers.[17] Using $LiCoO_2$, Li^+ could be reversibly de-intercalated from the host structure at much higher voltages than previously reported increasing the energy density available.

However, progress was hampered by the lack of a suitable anode material as the use of Li metal brought with it various safety issues. While a number of research groups successfully demonstrated the use of carbon-based anode materials,[21–23] Akira Yoshino is considered one of the fathers of the Li-ion battery in its modern form. His patent, filed in 1987 for a secondary battery using a $LiCoO_2$ cathode and a carbonaceous anode material, was the basis for future Li-ion batteries.[24] This ultimately led to the commercialization of the Li-ion battery by Sony in 1991 ushering in the era of portable electronics.[25] The contribution that these three great minds have made to science was finally recognised in 2019 with the award of the Nobel Prize for chemistry going to John B. Goodenough, M. Stanley Whittingham and Akira Yoshino "for the development of lithium-ion batteries".[26]

1.2.2 The Layout of a Li-ion Battery

A battery is an electrochemical cell made up of three main components: a cathode, an electrolyte and an anode. In the context of electrochemical cells, the cathode (positive electrode) is defined as the electrode where reduction occurs and the anode (negative electrode) is where oxidation occurs.[27] Within the battery community, there is a convention of calling the positive and negative electrodes the cathode and anode respectively, despite this only being the case when the cell is discharged. This convention will be followed throughout this thesis.

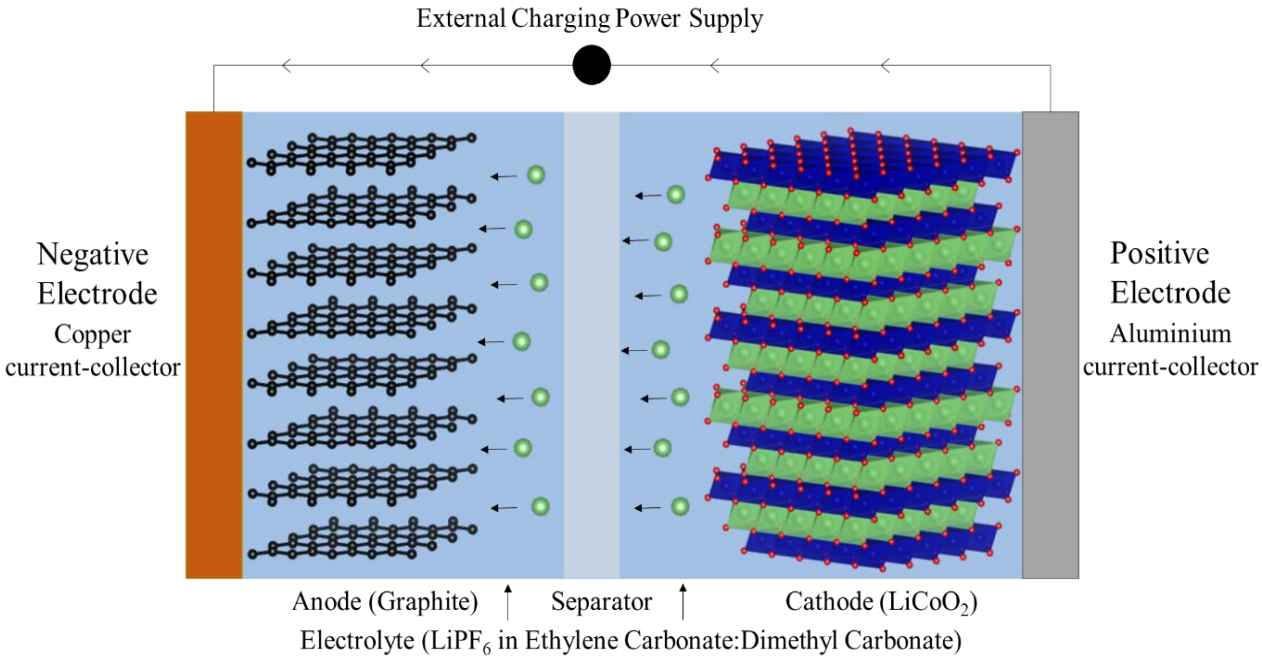

Figure 1.1: Schematic of a conventional Li-ion battery under charging conditions. Li ions move from the cathode to the anode within the cell, passing through a separator, with electrons moving from the positive electrode to the negative electrode through an external circuit.

A schematic of a typical Li-ion battery is shown in Figure 1.1, with the cathode on one side and the anode on the other. Between the two electrodes a liquid electrolyte is present (typically a Li salt e.g. $LiPF_6$) dissolved in a non-aqueous, carbonate-based solvent. The two electrodes are separated using an electronically insulating but permeable membrane which allows the conduction of Li^+ from one electrode to the other. Electrons may flow from one electrode to the other through an external circuit allowing the release or input of electrical energy as needed.

The electrodes are composed of several components. In commercial applications, the active materials in each electrode — typically $LiCoO_2$ for the cathode and graphite for the anode — are the major components (>95% by mass), maximising the energy density available. During the preparation of electrodes the active materials are mixed with a series of conductive additives and binding agents in a solvent to create an electrode slurry which

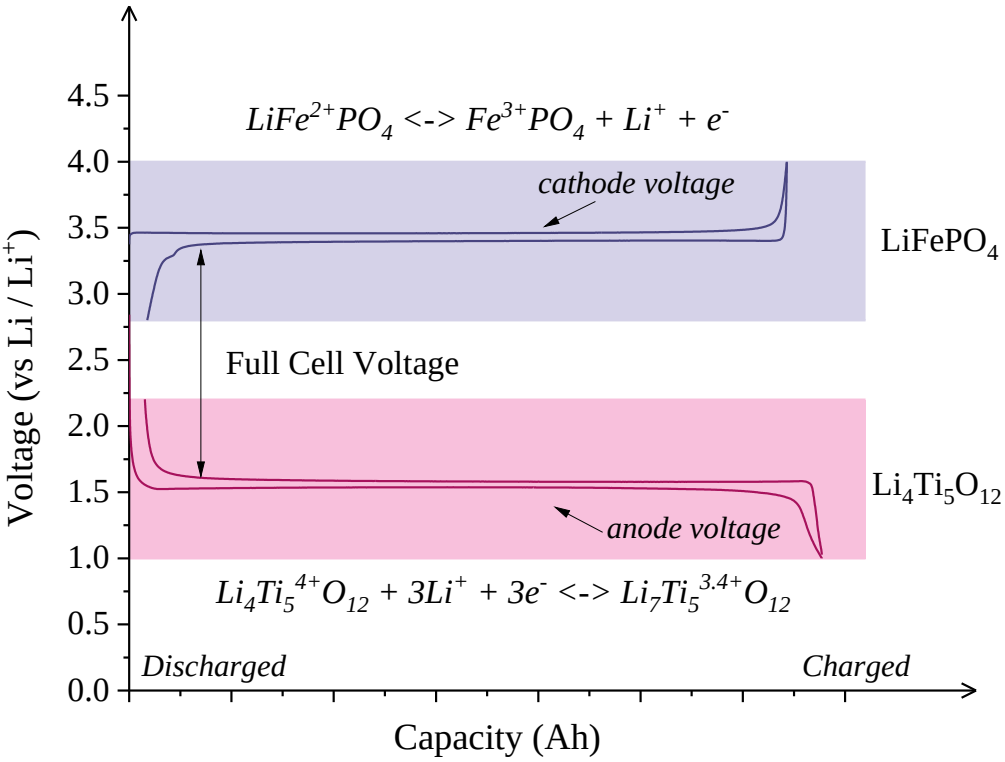

Figure 1.2: Schematic showing the potential variation of each electrode as a function of capacity and how this relates to the full cell voltage. The half reactions relating to each electrode material are also presented.

can be cast onto a metal foil current collector. These cast electrodes can then be cut to the desired specifications before being placed in the cell. The final electrode is porous which allows the liquid electrolyte to permeate the electrode and ensures efficient conduction of Li^+ ions to and from the entire active mass. It should be noted that the layout and operation of a Na-ion battery is analogous to that of a Li-ion battery.

1.2.3 Energy Storage in Alkali-ion Batteries

The process of converting stored chemical energy into electrical energy in a battery is highly efficient. During charge and discharge, each electrode undergoes one half of a reduction-oxidation (redox) reaction, involving the transfer of electrons (through an external circuit) and ions (through the electrochemical cell). These are called half reactions. Taking

a $LiFePO_4$ cathode, as the cell is charged Li^+ de-intercalates from the $FePO_4$ host structure, oxidising Fe from 2+ to 3+ and removing electrons in the process. On discharge, this reaction is reversed, with Li^+ intercalating back into the host structure reducing the Fe from 3+ to 2+. Another half reaction occurs at the anode, where the host structure is reduced on charge and oxidised on discharge. As each half reaction is de-coupled from each other in the cell, the internal chemical state of the battery can be controlled from an external flow of electrons, allowing energy to be stored or released as needed (Figure 1.2).

The total amount of energy which can be stored by a battery is dependent on the voltage and the capacity of the electrode materials, described by the following equation:

$$E = VQ$$

Where *E* is energy in joules, *V* is voltage in volts and *Q* is charge passed in coulombs. Therefore, increases in energy can be made by increasing the operating voltage of a cell or by increasing the amount of extractable charge within a cell.[27]

The operational voltage of a cell is determined by the difference in chemical potential between the cathode and anode materials. The chemical potential is dictated by the electronic structure of each compound.[28] This can be derived through calculation by using density functional theory (DFT) to compute the position of the Fermi level. To raise the chemical potential of the cathode and achieve cells with higher operating voltages, electrons must be extracted from deeper electronic bonding states. The voltages of TM redox couples tend to increase across the period as the 3d states drop in energy due to the stronger effective nuclear charge. This trend also follows as you increase the oxidation state of the TM.[29] However, removing bonding electrons from a material can also induce structural instability and trigger changes in coordination environments of certain elements, so the favoured coordination geometries of the TM ions should also be considered along with the voltage of its redox couples when considering material compositions.

In an electrochemical cell, the composition of the cathode changes during charge and discharge. The voltage of the material under operation can be derived from the rate of change of chemical potential with composition. Homogenous changes in composition, during which Li and electrons will be evenly distributed throughout a single phase, will illicit sloping voltage profiles when plotted versus capacity. In contrast, an inhomogeneous change in composition occurs when phase segregation into two different compositions is energetically favourable over a solid solution. Such changes in composition will lead to a flat voltage plateau as the system shifts from one phase to another.[27] While the change in composition of the cathode determines the operational voltage of that material, it is the difference in chemical potential between the anode and the cathode which determines the equilibrium voltage of the cell. This can be described by the Nernst equation:

$$Q_r = \frac{a_{Red}}{a_{Ox}}$$

$$\Delta G = \Delta G^{\emptyset} + RT \ln Q_r$$

$$-nFE_{cell} = -nFE_{cell}^{\emptyset} + RT \ln Q_r$$

$$E_{cell} = E_{cell}^{\emptyset} - \frac{RT}{zF} \ln Q_r$$

Where Q_r is the reaction quotient determined by the activity of the reaction products (a_{Red}) and reagents (a_{Ox}), G is the Gibbs free energy of the system in joules, R is the ideal gas constant, T is the temperature in kelvin, E is the cell voltage, $E^{\emptyset}$ is the cell voltage at equilibrium, z is the charge of the charge carrier ion and F is the faraday constant.[27]

The capacity of a battery determines how much charge is stored or released by the cell and can be described in two distinct ways. Firstly, and typically for commercial cells, the capacity can be expressed in Ah, which represents the total amount of charge the cell can hold. This can be multiplied by the average operational voltage of the cell to determine the amount of energy stored in Wh. This can then be divided by the mass or volume of the cell

to determine the cell-level gravimetric energy density (Wh kg^{-1}) or volumetric energy density (Wh L^{-1}). Secondly, as is the widely used convention in battery materials research, the capacity can be expressed as the specific capacity of each electrode material, an intrinsic property of the material itself. This is based on the number of carrier ions which can be intercalated into the host structure, determined by the following equation:

$$Specific\ capacity = \frac{zF}{3.6M_w}$$

Where *z* is the number of alkali metal ions transferred per formula unit and M_w is the formula weight of the electrode material in g mol^{-1}. The units for specific capacity are expressed in mAh g^{-1}. The specific capacity is routinely measured in battery research to determine the performance of a new material, presented in a plot of voltage vs capacity.

1.3 An Introduction to Li-ion and Na-ion cathodes

This section will give a brief overview of the material systems which will be studied in this thesis. Many different material classes have been explored as intercalation compounds. For Li-ion materials these include layered $LiTMO_2$ compounds (e.g. $LiNi_{1/3}Mn_{1/3}Co_{1/3}O_2$),[30] spinel type (e.g. $LiMn_2O_4$),[31] disordered rock salt materials (e.g. Li_2MnO_2F),[32] and polyanion chemistries (e.g. $LiFePO_4$).[33] In the Na-ion space these include layered $NaTMO_2$ compounds (e.g. $NaNi_{1/3}Mn_{1/3}Fe_{1/3}O_2$),[34] polyanion chemistries (e.g. $Na_3V_3(PO_4)_3$),[35] and Prussian blue analogues (e.g. $Na_{1.92}Fe[Fe(CN)_6]$).[36] However, the work presented herein will focus on layered Li-ion and Na-ion intercalation compounds. A brief overview of the physical and structural properties of these systems is presented here, before introducing the challenge of discovering new cathode materials.

1.3.1 Physical Properties of Li-ion and Na-ion Batteries

The suitability of Li-ion batteries to energy storage applications stems from the remarkable physical properties of Li (Table 1.1). Li has a small cation radius and is the

	Lithium	***Sodium***
Cation Radius (Å)	0.76	1.06
Molar mass (g mol^{-1})	6.94	22.99
E^o (vs Li / Li$^+$)	0.0 V	0.34 V
Cost (carbonates, $/ton)	17000 (2021 price)[40]	150 (2019 price)[41]
Relative Abundance (ppm)	20	23600
Coordination preference	Octahedral and Tetrahedral	Octahedral and Prismatic

Table 1.1: A comparative list of the physical properties of Li and Na.[38,39]

lightest metal in the periodic table, with one of the lowest reduction potentials of the elements. These properties allow Li to store energy at an energy density high enough to be useful for a wide range of applications.[1] Despite these benefits, Li-ion batteries do have some drawbacks. The cost of Li_2CO_3, a precursor used for cathode material synthesis, was $17000 per ton in 2021. In addition, the mining of Li is of geographical importance, with most operations being carried out in South America and Australia. In addition, there are safety concerns with shipping Li-ion cells, which cannot be transported in a fully discharged state. This will cause oxidation of the Cu current collector on the anode side which leads to dendrite formation in the cell and a number of hazards such as thermal runaway events.[37]

Na-ion intercalation compounds are another important area of research. In terms of performance, Na-ion cathodes cannot compete with Li-ion cathodes. The reduction potential of Na^+/Na is slightly higher than for Li^+/Li, while Na is also significantly heavier and larger than Li, limiting the maximum energy density of Na-ion cathodes. Despite this, Na-ion is still an attractive technology from a cost perspective. Na precursors (such as Na_2CO_3) are far cheaper than the equivalent Li compounds. Na is also over 1000 times more abundant than Li and more evenly distributed worldwide. These properties have helped paint Na-ion technology as a cheaper and more sustainable alternative to Li-ion.[38,39] Moreover, the large

ionic radius of Na allows for a wider variety of elements to be used in the synthesis of Na-ion compounds. Layered structures can form due to large differences in ionic radii of the constituent cations.[40] For example, $NaFeO_2$ can be synthesised as an ideal layered structure, while the synthesis of $LiFeO_2$ forms a disordered rock-salt phase material.[41] This allows for cheaper and more abundant elements such as Fe or Ti to be readily incorporated into Na-ion cathodes, reducing the demand for scarcer elements such as Co. There are also advantages at the cell level. Al, which does not alloy with Na, can be used as the anode current collector, providing cost and weight savings, whereas Cu must be used in Li-ion cells. The compatibility of Na with Al current collectors also allows Na-ion cells to be transported at 0 V, avoiding thermal run-away hazards which have plagued Li-ion batteries.

1.3.2 Structural Properties of Layered Li-ion and Na-ion Cathodes.

Layered cathode materials all share structural similarities, the basis of which can be introduced by looking at $LiCoO_2$. The archetypal cathode material $LiCoO_2$ consists of layers of Li^+ lying between extended sheets of $Co^{3+}O_2^{2-}$, arranged as edge-sharing octahedrons with two faces bordering the Li^+ plane. Many other layered compositions have since been studied, and the current method used for defining layered TMO_2 compounds was proposed in 1980 by Delmas et al.[16] In this system, layered oxide structures are categorised by the coordination of the alkali metal ion layers and the oxygen stacking sequence. Four of the most common layered TMO_2 compounds are illustrated in Figure 1.3. In each case, a letter and a number are assigned to each structure to define it. The letter denotes the coordination environment of the alkali metal ion: *O* for octahedral sites, and *P* for trigonal prismatic sites. The number refers to the minimum number of TMO_2 slabs needed to re-create the oxygen stacking sequence in the unit cell (with the inter-layer position of the oxide anions denoted by *a*, *b*, or *c*). This results in the following four designations and stacking sequences: *P*3 – *ab bc ca*, *O*3 – *ab ca bc*, *P*2 – *ab ba*, and *O*2 – *ab cb*.

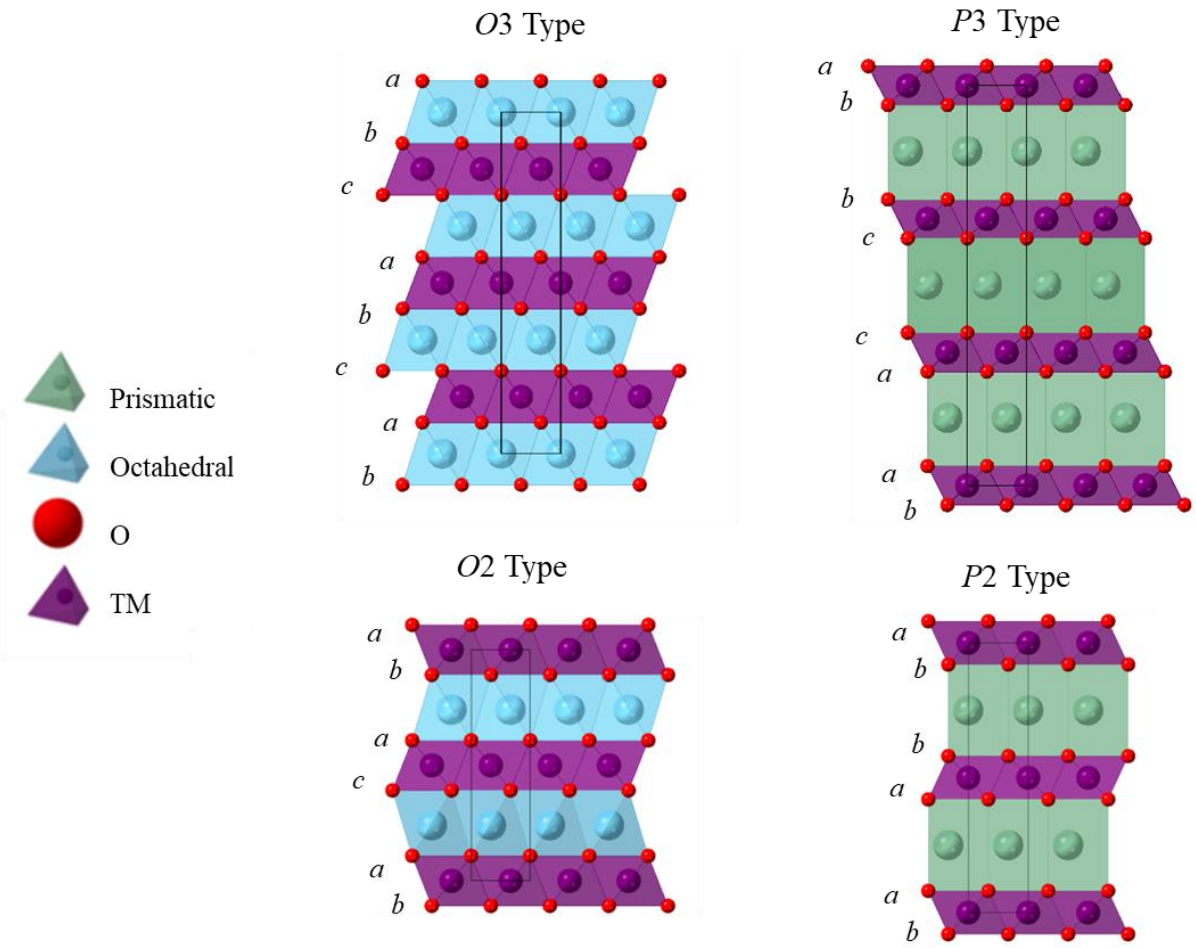

Figure 1.3: Illustration of the four most common layered crystal structures, *O*3, *P*3, *O*2 and *P*2. TM environments are shown in purple, with octahedral alkali metal environments in blue and prismatic alkali metal environments in green. The black lines denote the unit cells for each structure.

As shown in Table 1.1, the coordination environment of the alkali metal ion is primarily dependent on its ionic radius. The use of prime (‘) can be used to indicate a distorted phase.[42] Layered Li-ion compounds are almost exclusively *O*3 type, with both TM and Li^+ occupying octahedral environments. However, *O*2-type Li-ion materials have been prepared through ion exchange methods.[43] The Li^+ diffusion pathway in these materials from octahedron to octahedron goes through an intermediate tetrahedral environment.[44]

Na-ion compounds have a greater diversity of structure types. *O*3 type Na_xTMO_2 structures tend to form at high Na contents (i.e. x > 0.8 mol of Na). Meanwhile, O2 type compounds are generally formed when the material is fully desodiated (i.e. x ~ 0) and can only be prepared through electrochemical methods. *P*2 and *P*3 type Na_xTMO_2 can be

prepared with lower Na content (i.e. $0.5 < x < 0.8$). *P*3 phases are more stable at lower synthesis temperatures, while *P*2-phases tend to form at higher temperatures.

During desodiation the phase changes readily occur due to gliding of the TMO_2 slabs which causes structural transitions between *O*3 and *P*3 and *O*2 and *P*2.[42] It should be noted that phase transitions such as *O*3 to *P*2 cannot occur at room temperature as this would involve breaking the strong TM-O bonds in these materials.[45]

1.3.3 The Problem with Cathode Materials

Current state-of-the-art cathode materials have been optimized from $LiCoO_2$ which has been replaced by binary and ternary transition metal compositions, moving away from the issues of unethical sourcing, high cost, and toxicity associated with Co.[6] The result of this optimization are lithium nickel manganese cobalt oxides (NMC)[30,46,47] and lithium nickel cobalt aluminium oxides (NCA).[48–50] For Na-ion technology, the lack of a suitable cathode material has prevented its commercialization although a number of potential candidates do exist.[51,52]

However, the performance of the cathode currently lags behind that of the anode, limiting the amount of energy that can be stored in a cell. In Li-ion technology, anode materials with specific capacities of 350-500 mAh g^{-1} are commonly available, while state-of-the-art cathode materials are able to store a maximum of ~220 mAh g^{-1}.[53] This gap in performance means more cathode must be used in a cell to be able to balance the capacity provided by the anode. Another point to consider are the voltage limits for each electrode, as graphitic anodes already operate at a voltage close to the fundamental lower limit for Li-ion batteries (~0.25 V vs Li^+/Li). However, the current average operational voltage for cathode materials could be pushed higher. As the voltage and specific capacity of the cathode are properties related to the composition of the cathode itself,[28] new materials must be found which will enhance the available energy density.

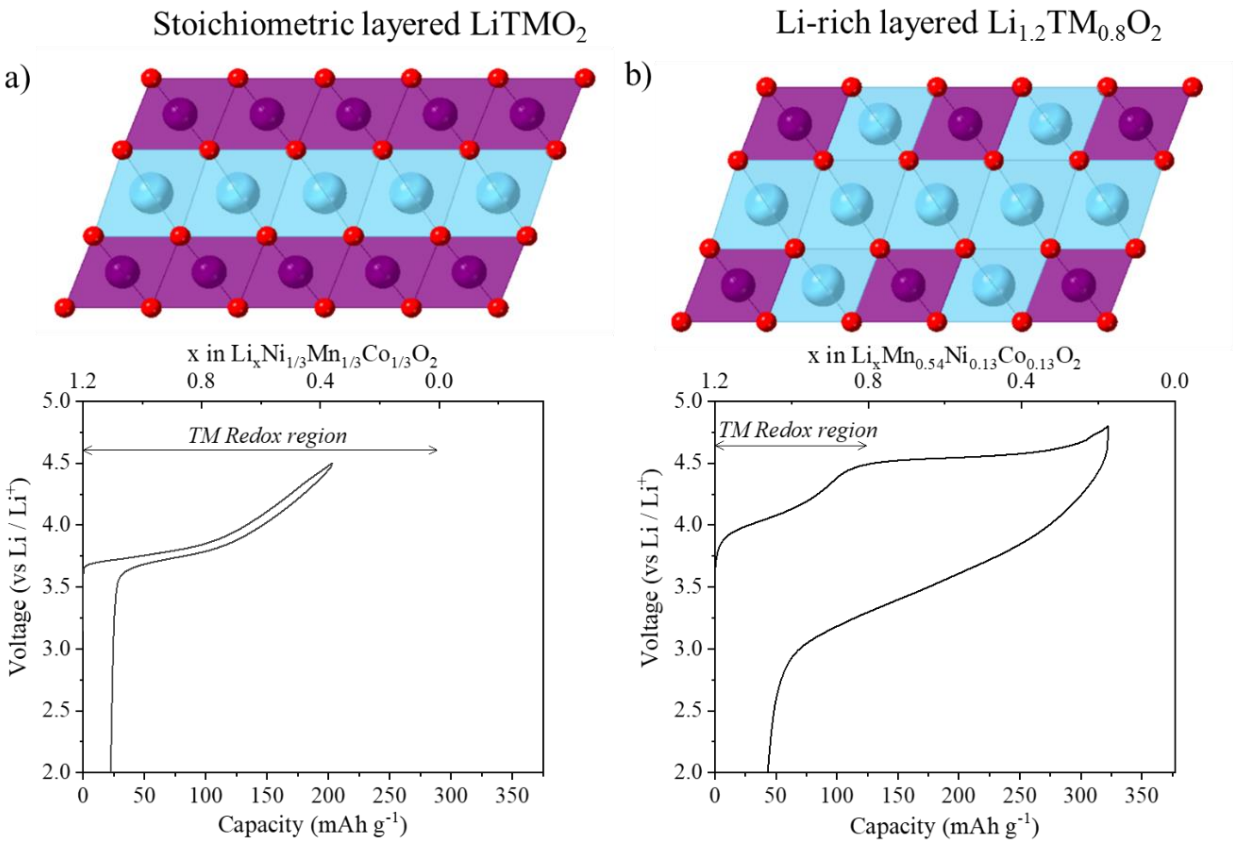

Figure 1.4: A direct comparison between stoichiometric $LiNi_{1/3}Mn_{1/3}Co_{1/3}O_2$ (a) and Li-rich $Li_{1.2}Mn_{0.54}Ni_{0.13}Co_{0.13}O_2$ (b). A structural schematic for each material can be seen at the top of the figure, while a comparison of the cycling activity of each material can be seen below.

In Li-ion systems, one promising class of materials are Li-rich cathode materials, in which a fraction of the TMs in the TM layer are replaced by Li to create a material with a Li:TM ratio greater than 1:1.[54–57] Li-rich materials can reach higher energy densities than conventional cathode materials for two reasons. Firstly, the higher Li content means more Li can be extracted per unit mass, increasing available capacity. Secondly, conventional Li-ion cathode chemistries are based on layered transition metal oxides (TMOs), where the amount of charge stored is limited by the redox processes which occur at the transition metal (TM) centres. In Li-rich materials, more charge can be stored than can be accounted for by the TM centres alone, by invoking the charge storing capabilities of the oxygen sub-lattice.[58–61] This mechanism is known as O-redox and has led to novel cathode systems where both TM centres and lattice oxide ions are active redox components (Figure 1.4). O-

redox is typically characterised by a long, high-voltage plateau being observed on charge and an S-shaped load curve displaying large hysteresis curve are seen on discharge.

O-redox systems have also been explored in Na-ion systems. Na-rich materials have been synthesised, however, due to the larger size of Na ions, this can only be achieved using 4d or 5d transition metals rather than the more conventional 3d transition metals.[62] Other non-Na-rich compounds such as $Na_{0.67}Mn_{0.72}Mg_{0.28}O_2$[63] or $Na_{0.67}Mn_{0.72}Zn_{0.28}O_2$[64] have been shown to be O-redox active, with a similar load curve to the Li-rich materials. A small group of compositions, namely $Na_{0.6}Mn_{0.8}Li_{0.2}O_2$ and $Na_2Mn_3O_7$, are unique in that a high-voltage plateau, which has been attributed to O-redox, is present on both charge and discharge.[65–67]

An ideal cathode material should be able to deliver large amounts of capacity at a high voltage, ensuring high energy density. The load curve should also form a flat, reversible plateau on charge and discharge, ensuring a constant power output which is useful for commercial applications and limits the complexity of the battery management system. Finding a material which could fit these characteristics would represent a huge leap forward in the development of Li-ion and Na-ion batteries. O-redox represents one of the few avenues which will allow both an increase in voltage and capacity. While O-redox materials are theoretically able to provide both these characteristics, several issues currently prevent their commercialisation.

1.4 O-redox in Layered Cathode Materials

1.4.1 Understanding ‘Anomalous’ Capacities in Li-rich Materials

As far back as 1998, Ceder and co-workers proposed the possibility of designing a high voltage cathode material based on the exchange of electrons with lattice oxygen.[68] However the participation of lattice oxygen in redox mechanisms was overlooked as it was believed to be too electronegative to allow oxidation. In the early 2000’s, studies of Li-rich

electrode materials showed ‘anomalous’ capacities exceeding the capacity of TM redox, which began the broader investigation of O-redox materials.[56,69,70] Oxygen evolution was of interest in these early studies, with Delmas et. al. providing evidence of O_2 loss in $Li_{1.12}(Ni_{0.425}Mn_{0.425}Co_{0.15})_{0.88}O_2$ using Rietveld refinements to show changes in the TM/O ratio over cycling. They proposed that surface TM atoms, destabilized by O_2 loss, migrated to vacancies left by Li-ions in the bulk, leading to a structural densification.[71] This mechanism was supported by studies measuring O_2 gas evolution during cycling.[72,73]

However, this model was the subject of debate. Weight loss measurements were used to conclude that O_2 loss from the structure was not sufficient to account for the long plateau seen at 4.5 V.[74] *In situ* X-ray absorption spectroscopy (XAS) was also used to investigate changes to the Mn K-edge,[75] showing limited Mn reduction through discharge, indicating the reversible participation of O-redox was likely. Bringing these findings together, Koga et al. published two papers exploring O-redox in Li-rich NMC.[59,76] The proposed mechanism involved O_2 loss and subsequent densification at the surface with reversible O-redox in the bulk. This was followed by the first direct observation of oxygen participation in the redox process. Oishi and co-workers studied $Li_{1.16}Ni_{0.15}Co_{0.19}Mn_{0.50}O_2$ using Soft X-ray Absorption Spectroscopy (SXAS) to study the O K-edge.[77] An increase in the intensity of the pre-edge feature during charging was observed, showing a change in the electron density around the oxygen, indicating O-redox across the plateau.

1.4.2 Early O-redox Mechanisms

‘Orphaned’ O2p Orbitals as the Origin of O-redox

As the possibility of reversible bulk O-redox became established, several models were proposed to explain the origins of oxygen oxidation. In separate studies led by Bruce and co-workers on $Li_{1.2}Ni_{0.13}Co_{0.13}Mn_{0.54}O_2$,[79] and $Li_{1.2}Ni_{0.2}Mn_{0.6}O_2$,[80] quantitative analysis of

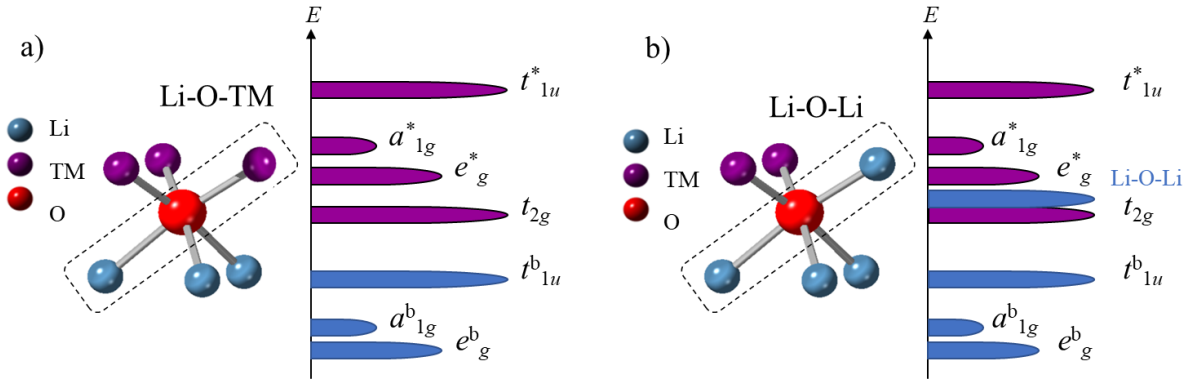

Figure 1.5: Representation of the local co-ordination environment around oxygen in a stoichiometric layered cathode material (a) and a Li-rich layered or disordered cathode material (b). This figure was adapted from [78].

gas evolution during cycling concluded that most of the charge extracted over the plateau region was due the oxidation of lattice oxygen. In addition, Resonant Inelastic X-ray Scattering (RIXS) was used for the first time to study the electronic structure of oxygen. RIXS measurements carried out at 531 eV showed an increase in signal intensity at an emission energy of ~523 eV, attributed to the presence of localized hole states.

Complimentary to this, X-ray Absorption Near Edge Spectroscopy (XANES) was used to investigate changes in the local environment of the TM cations which demonstrated a change in peak energy for Mn, while no variation was observed for Ni or Co over the high voltage plateau. This led Bruce et al. to propose that only oxygens in specific coordination environments could be oxidised, with O^{2-} 2p orbitals having more covalent interactions with Ni^{4+} and Co^{4+}, and more ionic interactions with Mn^{4+} and Li^{+}. As a result of the ionic interactions, unhybridized, localized O2p states are formed near the top of the O^{2-} valence band (Figure 1.5). These are the states that will undergo oxidation over the plateau.

Independently of these experimental reports, Ceder et al. published a substantial theoretical study on the origin of O-redox in Li-rich layered TMOs.[78] Using DFT calculations, the group investigated the projected Density of Sates (pDOS) of the O2p states in cation mixed $LiNiO_2$. A clear increase in the oxygen pDOS was observed once the oxygen

environment was coordinated by an excess of Li atoms (4Li/2Ni). By visualizing the charge density after the extraction of one electron from $LiNiO_2$, Ceder et al. revealed the presence of an isolated O2p orbital along the Li^+-O-Li^+ configuration. These calculations were repeated for other Li-rich TMOs (e.g. Li_2MnO_3), showing the same result. They proposed that while conventional Li layered TMOs have Li^+-O-TM configurations which give rise to hybridised O2p/TM orbitals, the Li^+-O-Li^+ configuration in excess Li layered TMOs cannot hybridise in such a way, since Li 2s orbitals are too low in energy to hybridise with O2p orbitals. Hence, the O2p orbital in a Li^+-O-Li^+ configuration exists as an 'orphaned' orbital, lying higher in energy than the rest of the hybridised O2p band, allowing oxygen to be oxidised within a similar potential window to TM ions.

Building on this work, Chueh and co-workers described how the voltage of O-redox is modulated through the reversible TM migration in and out of the TM plane.[81] They proposed that at high states of charge, the migration of Mn and Ni in $Li_{1.17}Ni_{0.21}Co_{0.08}Mn_{0.54}O_2$ leads to a shift in the DOS of oxygen to higher energies. This pushes the O2p band above the TM band, explaining why oxygen reduction occurs after TM reduction on discharge. This model provides an explanation for why such a large hysteresis is observed on discharge along with a loss of the high voltage plateau and highlights the need to tune the stability of O-redox by mitigating structural rearrangements.

Initial Theory on O-redox Stabilisation

It is now widely accepted that Li^+-O-Li^+ structural arrangements along the O2p orbital present in Li-rich compounds allow O-redox to occur. This theory has been shown to hold true in a wide variety of compounds where similar arrangements to Li^+-O-Li^+ are present along the O2p orbital, such as $NaMn_{2/3}Li_{1/3}O_2$ (Na^+-O-Li^+),[82] $Na_{0.67}Mn_{0.72}Mg_{0.28}O_2$ (Na^+-O-Mg^{2+})[63,83] and $Na_2Mn_3O_7$ (Na^+-O-[_], where [_] are TM vacancies)[67,84]. These materials all

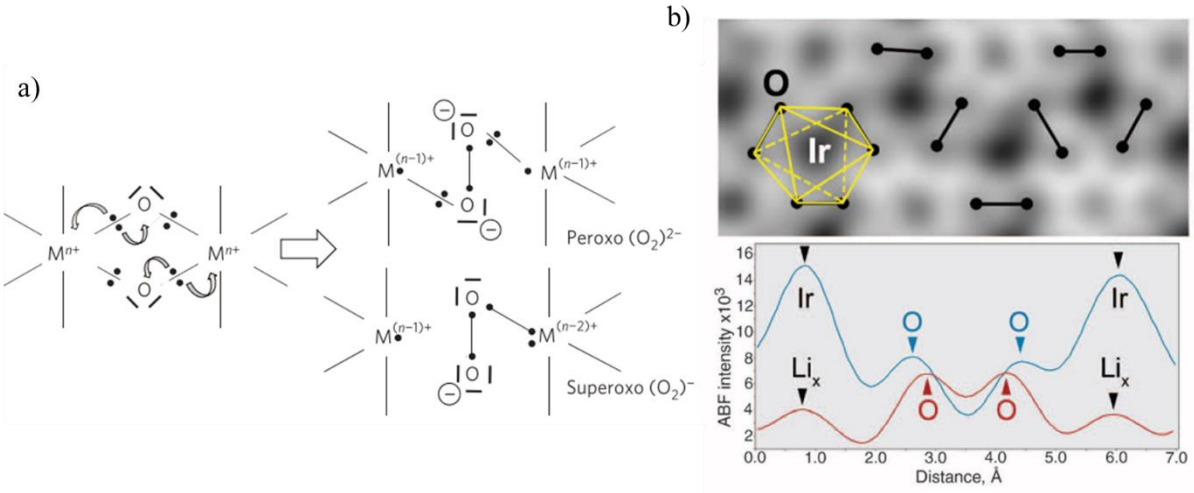

Figure 1.6: An overview of the peroxo stabilisation theory of O-redox. a) Reductive coupling mechanism of two oxo-ligands coordinated to TM centres, leading to single or double reduction of the TM centre. b) ABF-STEM imaging depicting the formation of O-O dimers in Li_2IrO_3, with the ABF intensity profiles along the O-O dimers shown below. Figures adapted from [86] and [87].

display O-redox activity, each with varying degrees of reversibility and hysteresis. However, no clear explanation for how electrons holes were stabilized after formation was successfully proposed. While some thought that the stability of O-redox should be tuned by mitigating structural rearrangements, others proposed that an increase in covalency, present in 4d and 5d Li-rich TM oxides, could provide insight into the stabilisation of oxidised oxygen species.

The first 4d metal system to be studied was $Li_2Ru_{1-y}Mn_yO_3$,[85] a solid solution of the Li_2MnO_3 and Li_2RuO_3, structurally analogous to the 3d Li-rich TM oxides and also exhibiting O-redox capacity. Soon after, Tarascon and co-workers reported on $Li_2Ru_{1-y}Sn_yO_3$, in which they proposed the formation of peroxo-like species at high states of charge due to oxygen oxidation, formed through a reductive coupling mechanism (Figure 1.6).[86] XPS was used to show evidence of O-redox, attributing a new signal in the oxygen K-edge at high voltages to peroxo (O_2^{2-}) species.[86] DFT calculations provided further evidence stating that the driving force for forming peroxo-like species would be a stabilization of the oxygen network, decreasing the O-O bond distances to 2.5Å. In 2015, Tarascon et al. directly visualised the formation of peroxo-like species in charged Li_2IrO_3.[87]

This was of particular importance, as Li_2IrO_3 shows limited hysteresis during charging, suggesting that O-redox could be stabilised by increasing the covalency of the O-TM bond. Using STEM imaging, the authors show how, at high states of charge, the oxygen lattice contracts to form peroxo-like species (Figure 1.6). Complimentary evidence from neutron diffraction and DFT relaxation calculations also support the contraction of the O-O distances. These findings were also supported by DFT models, demonstrating that O-redox in Li_2RuO_3 occurs through the formation of peroxo-like species.[88]

However, a recent study by Chueh et al. challenges these claims.[89] Two structurally analogous compositions were studied: Li_2IrO_3, reportedly showing highly reversible O-redox behaviour, and $Li_2Ir_{1-x}Sn_xO_3$, showing capacity exceeding TM oxidation and voltage hysteresis on discharge. Ir L_3-edge XANES data showed that charge compensation in Li_2IrO_3 comes from the oxidation of Ir^{4+} to $Ir^{5.5+}$, not by O-redox as previously reported.[87] O-redox activity was then studied in $Li_2Ir_{1-x}Sn_xO_3$. RIXS measurements demonstrated that Sn doping into Li_2IrO_3 had 'switched-on' O-redox, while Rietveld refinements showed evidence of Ir and Sn disordering when charged to 4.6V, forming metal-defect pairs. The authors postulate that the cation migration observed is linked to O-redox itself, with DFT results indicating that the formation of metal-defect pairs is accompanied by the formation of two stabilising structural motifs: an O-O dimer or an Ir=O bond.

Further experimental evidence casts doubt on claims of peroxo-like species formation stabilising O-redox. Raman spectroscopy on charged Li-rich layered TMOs showed no evidence of peroxide species.[79,80] In addition, the surface sensitive nature of XPS raises questions about its efficacy to probe oxygen states,[86,87] while RIXS, a photon emission technique with greater bulk sensitivity, provides stronger evidence of O-redox.[4,63,79–81,89,90] Despite these studies, clear experimental evidence of the formation of oxygen dimers remained unaccounted for.

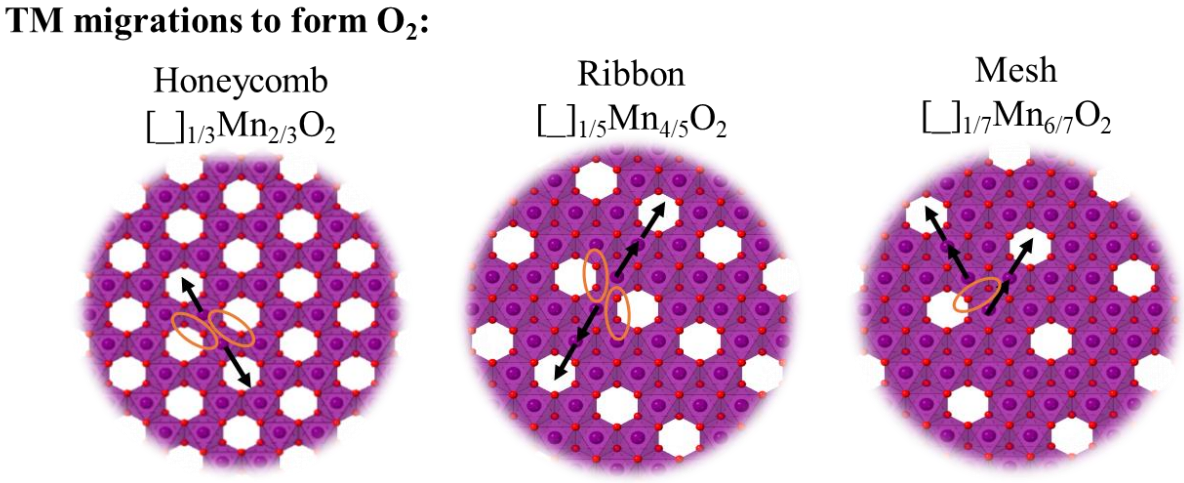

Figure 1.7: Representation of different superstructures which can arise in layered TMO_2 compounds. The arrows depict the in-plane TM migrations required to form O_2 in the charged state, while the circled lattice oxygens depict which O^{2-} anions will disproportionate to form O_2. There are a larger number of in-plane migrations of TM cations going from the honeycomb ordering to the mesh ordering, leading to an increase in superstructure stability. Figure adapted from [66].

1.4.3 Molecular Oxygen Formation in O-redox Cathodes

In a string of very recent publications on O-redox, Bruce and co. workers introduced a new mechanism for the stabilization of oxygen holes involving the formation of molecular O_2. Using a Na-ion analogue of a Li-rich material, $Na_{0.75}Mn_{0.75}Li_{0.25}O_2$, the group proposed that the hysteresis observed in O-redox materials between charge and discharge originates from the oxidation of the oxygen sub-lattice (O^{2-}) to molecular oxygen (O_2).[66] Molecular O_2 was evidenced by a low energy loss RIXS features at 531 eV at the O K-edge. These can be resolved into a progression of peaks arising from the vibrations of an O-O diatomic using high resolution RIXS data, revealing a bond length of 1.2Å. This finding is further supported by DFT calculations, revealing that the formation of molecular O_2 is thermodynamically favourable and requiring cation reorganisation in the TM layer, evidenced by the loss of honeycomb ordering after the first cycle.

To show that such reorganisation can be mitigated, a similar compound, $Na_{0.6}Li_{0.2}Mn_{0.8}O_2$ was also studied, with a ribbon ordering superstructure where the Li-ions are placed further apart in the TM layer. At the top of charge, a previously un-reported

feature can be seen in the O K-edge SXAS data at 528 eV which is subsequently lost on discharge. The authors attribute this to the reversible formation of hole states on the oxygen sub-lattice which is evidenced in the electrochemistry by a high voltage plateau on discharge. The authors proposed that the lack of hysteresis in $Na_{0.6}Li_{0.2}Mn_{0.8}O_2$ arises from the ribbon ordered superstructure, thus allowing the stability of O-redox to be tuned through the TM layer superstructure (Figure 1.7). Comparing honeycomb ordering to ribbon ordering, more Mn cations must migrate to form O_2 in addition to Mn needing to migrate into sites already occupied by Mn cations. The importance of material superstructure is further illustrated by another Na-ion cathode material, $Na_2Mn_3O_7$, which exhibits a mesh superstructure ordering scheme and highly reversible O-redox activity attributed to the formation of hole states on the oxide anions.[67,84]

The formation of molecular O_2 was further explored in a study on $Li_{1.2}Mn_{0.54}Co_{0.13}Ni_{013}O_2$, which aimed to establish the relationship between structural changes and the evolution of the voltage profile over the first and second cycles.[91] High resolution RIXS, ^{17}O NMR and DFT measurements were used to show the formation of molecular O_2 trapped in TM vacancy clusters at the top of charge. *In operando* XRD measurements reveal a loss of the honeycomb superstructure over the first cycle, providing evidence of the irreversible structural changes which occur in conjunction with molecular O_2 formation. High resolution RIXS was applied to investigate the activity of oxygen over the first discharge and subsequent charge. During discharge, the O_2 is gradually reduced as Li is re-intercalated into the structure, forming ionic O^{2-} environments coordinated to 4 Li^+. On charge, these ionic O^{2-} environments are oxidised concurrently with TM redox, leading to an S-shaped load curve on subsequent cycling charge compensated by TM redox and a O^{2-}/O_2 redox couple. The irreversible TM migration which accompanies O_2 formation on charge, and the subsequent change in oxygen environments on discharge, leads to a change

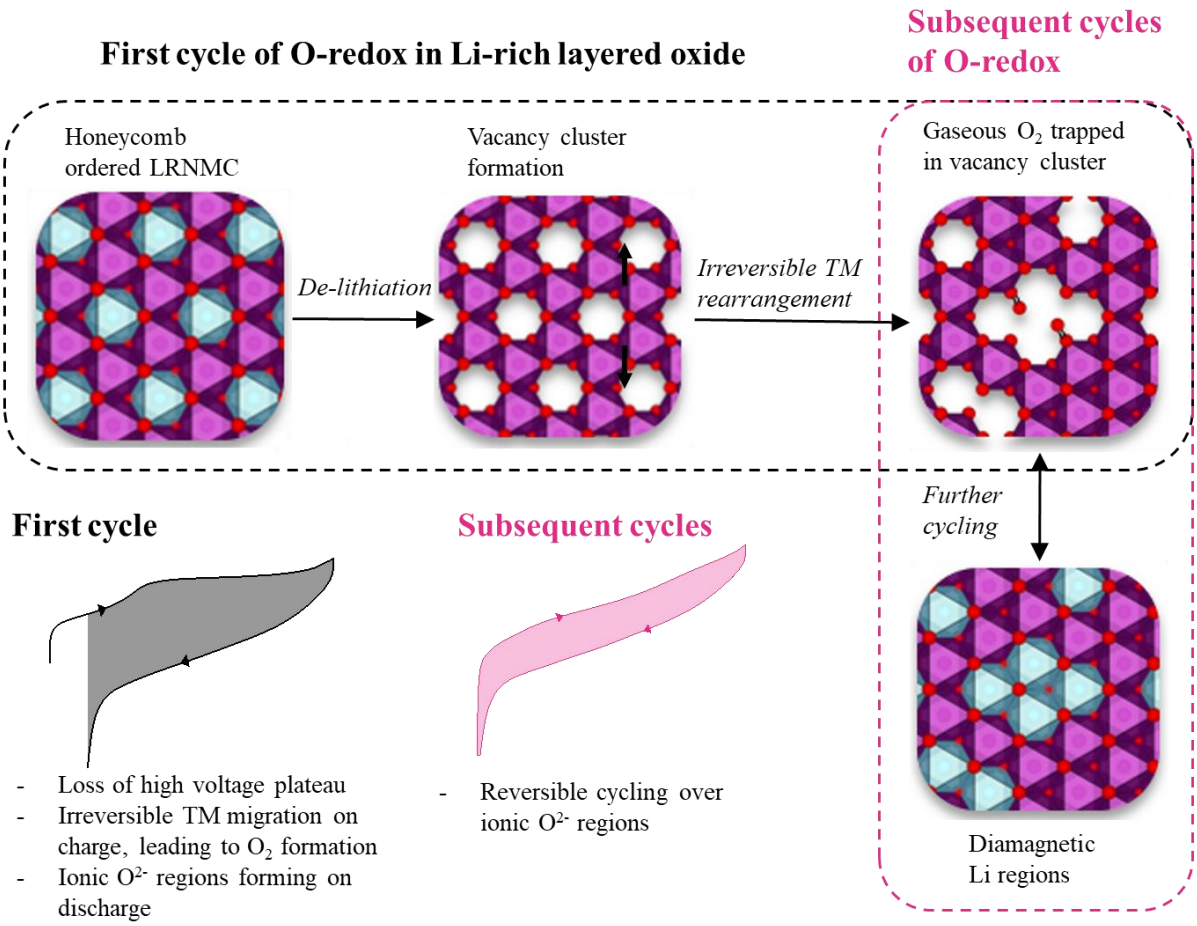

Figure 1.8: Representation of the O-redox processes in the first and subsequent cycles of Li-rich layered oxides. Framed in black are the steps which occur during the first cycle, with de-lithiation of the TM layer leading to vacancies, allowing for the in-plane migration of Mn and the subsequent formation of O_2. Subsequent cycling is framed in pink, with the reversible cycling of O-redox over ionic O^{2-} regions.

in charge compensation mechanism. This explains why the high voltage plateau is lost on the first cycle, replaced by an S shaped load curve on subsequent cycling (Figure 1.8).

Different techniques have provided further evidence for the formation of molecular O_2 in Li-rich NMC. *In operando* small angle X-ray scattering (SAXS) experiments reveal the presence of a feature suggesting the formation of nanopores in the charged structure. This feature, which is partially reversible, provides further evidence of irreversible structural changes, as well as for the formation of TM vacancy clusters during charging.[92] Trapped molecular O_2 has also been detected using Neutron PDF in charged Li-rich NMC.[93] In addition, molecular O_2 formation was investigated in 4d and 5d Li-rich systems. High

resolution RIXS provided evidence of O_2 formation in Li_2RuO_3, $Li_2Ru_{0.5}Sn_{0.5}O_3$ and $Li_2Ir_{0.5}Sn_{0.5}O_3$, while Li_2IrO_3 showed no evidence of O-redox. Direct spectroscopic evidence against the formation of peroxides in 4d and 5d systems was also presented by comparing the RIXS spectra for Li_2O_2 and KO_2 to the charged cathode samples. This revealed that the vibrational progression present in these samples occurs at a different frequency to that of molecular O_2. The formation of molecular O_2 provides an explanation for the irreversible nature of the O-redox plateau, as well as the hysteresis observed in O-redox compounds, with a wide body of evidence backing it. The irreversible high voltage plateau which is observed in most O-redox compounds has been shown to be accompanied by a large, irreversible structural change in the bulk. The formation of a stable O_2 diatomic explains the energy inefficiency of O-redox materials. Finally, this model highlights the effect that the TM layer ordering can have on O-redox, giving a possible route to extracting more of its potential.

1.4.4 Voltage Fade in O-redox Cathodes

A pressing issue which has yet to be fully understood is the voltage fade experienced by Li-rich materials. Over cycling, the average operational voltage of the cathode drops dramatically, impairing the practical use of Li-rich materials. A deeper understanding of voltage fade is required before implementing strategies to avoid it. Initially, voltage fade was believed to have a structural origin. Studies of Li-rich materials have provided extensive evidence of the severe surface and bulk structural re-organisations from layered to spinel-like phases.[59,94–99] Reducing Li^+ diffusivity on cycling through structural disordering (i.e. spinel or rocksalt-like surface layers), could induce a reduction in discharge voltage under galvanostatic cycling conditions. However, GITT measurements demonstrated that voltage fade has a thermodynamic origin, rather than being an overpotential.[100,101]

In 2015, Sathiya et al. contrasted the cycling behaviours of $Li_2Ru_{1-x}Ti_xO_3$ and $Li_2Ru_{1-x}Sn_xO_3$.[102] XPS and STEM imaging were used to demonstrate the progressive trapping of Ti^{4+} in tetrahedral sites, as well as large amounts of cation disorder in $Li_2Ru_{1-x}Ti_xO_3$ over extended cycling, along with extensive voltage fade. By substituting the Ti^{4+} cation for the larger, Sn^{4+}, the voltage fade of the material was shown to decrease significantly, as the large size of the Sn^{4+} cation inhibited its migration through the structure. In 2020, Kang and co-workers also established a correlation between metal migration and voltage fade by contrasting *O*3 and *O*2 type Li-rich materials.[43] They proposed that cation migration in *O*2 type materials was thermodynamically unfavourable due to the large repulsion between face-sharing sites, leading to a reduction in voltage fade in the *O*2 type material.

Spectroscopic measurements of Li-rich NMC cathodes have also revealed changes over cycling. A number of studies have focused on TM oxidation over the first cycle, where $Co^{3+/4+}$ and $Ni^{2+/3+/4+}$ are accepted to be the primary TM redox reactions in Li-rich NMC compositions, with Mn remaining predominantly +4.[58,76,79,103] However, this picture changes over extended cycling. In 2018, Yang et al. used spectroscopy to monitor the charge compensation mechanisms over multiple cycles in $Li_{1.2}Ni_{0.15}Co_{0.1}Mn_{0.55}O_2$.[104] Their findings showed the continuous reduction in valence state of the TM ions, leading to lower voltage redox couples participating in charge compensation, namely $Mn^{3+/4+}$ and $Co^{2+/3+}$.[104] This evidence supports the widely accepted theory that structural reorganisations induced by oxygen extraction from the structure leads to the formation of material defects, promoting further oxygen loss causing further TM reduction in the structure.[43,81,102,105]

Additional structural studies have revealed more severe bulk structural changes than phase changes from layered to spinel. The formation of nano-pores over cycling has been evidenced through STEM imaging, with pores being formed in the bulk of particles.[96,104,106] A reduction in material density has also been measured by He pycnometry.[107] The model

established in these studies claimed that pore formation is due to continuous oxygen loss via the migration of oxygen vacancies from the surface to the bulk. In the most recent work by Csernica et al,[107] an oxygen chemical diffusivity of 10^{-17} cm^2 s^{-1} was calculated using X-ray ptychography. Crucially, it remains unclear what role O-redox processes have on the depletion of bulk oxygen and how this relates to voltage fade.

1.5 Strategies Towards Reversible High Voltage O-redox

Having established a solid understanding of O-redox behaviour across a wide variety of structures, strategies that can mitigate the structural instability following O-redox must be implemented. In order for O-redox cathodes to become viable, compositions must be found in which the reversible formation of oxygen holes (O^{2-}/O^{-}) can be sustained over extended cycling, retaining a high energy density. Such strategies should aim to prevent vacancy cluster formation (and hence molecular O_2) to preserve the coordination environment around oxidised oxide ions for high voltage capacity. Potential ideas following this approach will be introduced below and further explored in this thesis. Another avenue would be to embrace the O^{2-}/O_2 redox mechanism in the bulk of the cathode while inhibiting the surface instability, which will also be discussed.

1.5.1 Structural Pillaring

While in-plane TM migration is primarily responsible for vacancy clustering and O_2 formation, out-of-plane TM migration also has an important role to play and must not be neglected. In Alkali-rich compounds, out of plane migration, especially of redox inactive dopants, can occur leaving behind vacancies in the TM layer and inviting in-plane migration to form vacancy clusters.[63,83,108] One strategy to prevent this is ‘pillaring’, where large, immobile cations are introduced to the structure to force the TM layers further apart making the occupation of AM layer sites by TM ions less favourable. Possible cations include K^+,

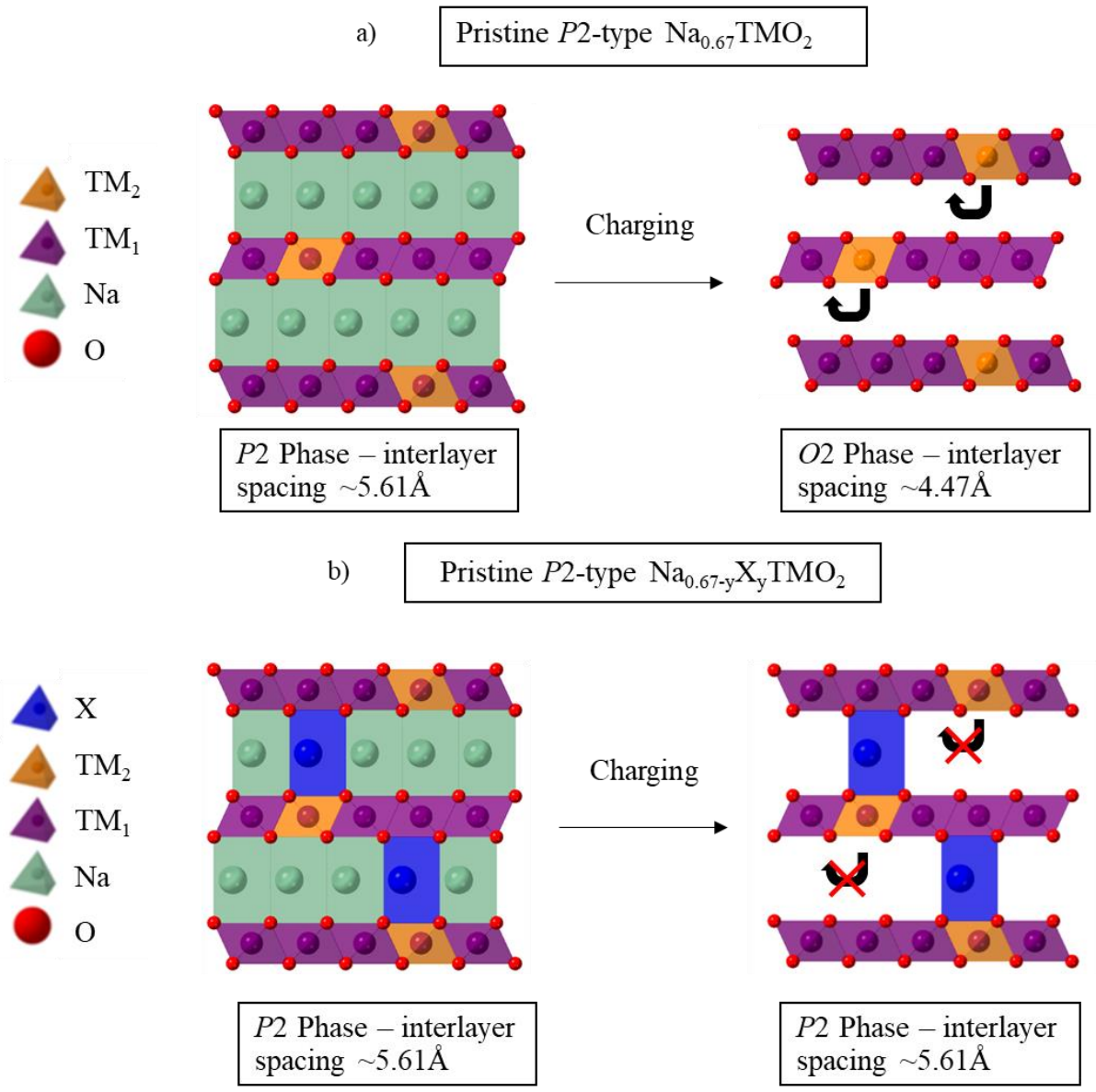

Figure 1.9: Theoretical effect of pillaring on layered structures. a) Structural representation of a pristine, *P*2-type $Na_{0.67}TMO_2$ material. Typically, *P*2-type materials undergo a phase transformation from *P*2 to O2 during charge, which facilitates the migration of cations out of plane. b) Structural representation of pristine *P*2-type $Na_{0.67-y}X_yTMO_2$. It is hoped that by doping large X cations (where X = K^+, Ag^+, Cu^+, Ca^{2+} or Sr^{2+}) into the AM layer, phase changes to O2 will be prevented, inhibiting the out-of-plane migration of cations.

Ag^+, Cu^+, Ca^{2+} and Sr^{2+}. This strategy may also be useful to prevent layer stacking transitions which are commonly observed in Na-ion cathode materials. In such cases, maintaining *P*-type stacking over the entire intercalation range could eliminate out of plane TM migration completely by avoiding the formation of octahedral sites in the Na layer (Figure 1.9).

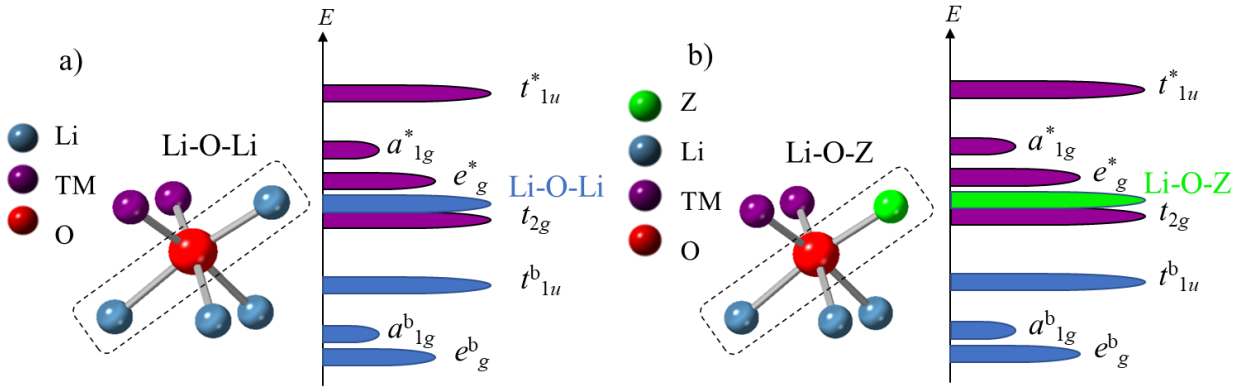

Figure 1.10: Representation of the local co-ordination environment around oxygen in a Li-rich layered (a) and a fully dense layered cathode material doped with a multi-valent cation Z, where Z = Zn^{2+}, Mg^{2+}, Al^{3+}, Ti^{4+} or Sn^{4+} (b).

1.5.2 Multi-Valent Cation Doping

The suppression of TM migration could be achieved by targeting non-Li-rich compositions with fully dense TM layers. For O-redox to be active in these systems, it is crucial to maintain a sufficiently ionic coordination environment around oxygen to trigger oxygen oxidation within a reasonable voltage window (<5 V vs Li^+/Li^0). Dopants which can be considered should be electropositive and redox inactive. This could include cations such as Zn^{2+}, Mg^{2+}, Al^{3+}, Ti^{4+} or Sn^{4+}, all of which have been studied previously in O-redox active materials. It should be noted that this list is non-exhaustive and could feasibly include any stable element from the periodic table. The variety of valence states and ionic radii on offer among these elements should be valuable tools in controlling TM ordering and the ratio of TM:O redox (Figure 1.10). This strategy will be discussed in more detail in chapter 5.

1.5.3 New Superstructure Ordering

O-redox compounds exhibiting a honeycomb ordered arrangement of cations in the TM layer are readily susceptible to extensive in-plane TM migration.[66,83,91] As discussed in section 1.4.3, the rearrangement of TM ions and Li^+ vacancies can be suppressed using different in-plane ordering schemes which allow stabilisation of O^{n-} (n<2) and preservation

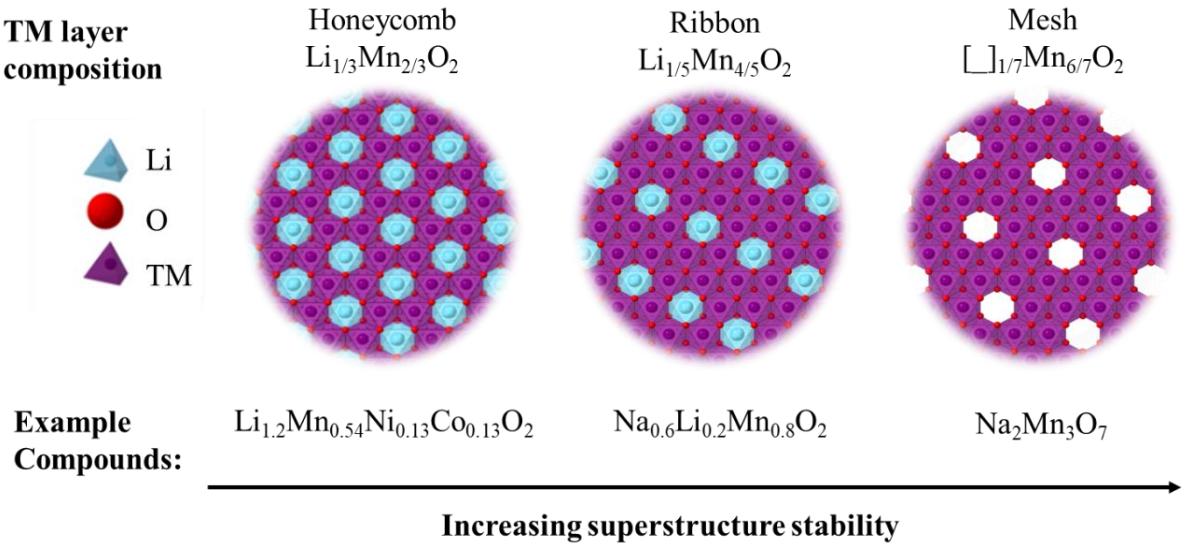

Figure 1.11: Representation of different superstructures which can arise in layered TMO_2 compounds (Honeycomb, Ribbon, Mesh), and example compounds which exhibit these ordering schemes.

of a reversible high voltage plateau. Therefore, research efforts should be focused on targeting compositions and synthesis conditions which favour ordering schemes where Li^+ ions are further spaced. Examples include ribbon or mesh ordering (Figure 1.11). However, out of plane TM migration must also be minimised. A recent study investigating $Na_{0.6}Mn_{0.6}Ti_{0.2}Li_{0.2}O_2$ showed that despite having a ribbon ordered Li^+ arrangement, the load curve displayed a large hysteresis on discharge.[108] This was due to the out of plane migration of Ti^{4+} as well as Li^+, leaving further vacancies in the TM layer causing O_2 formation. Compositions should be targeted which display both high-voltage TM redox and a significant proportion of O-redox capacity. Coulombic charge repulsion between high and low valent metals and minimisation of strain through ionic size ordering will be critical guiding principles for tuning the TM layer configuration.

1.5.4 Embracing the O^{2-}/O_2 Redox Couple

An alternative approach is to accept disorder as an inevitable consequence of O-redox and to adopt the O^{2-}/O_2 redox couple. The consequence of this would be a lower average voltage (i.e. around 3.5 V instead of 4.5 V vs Li/Li^+) and some degree of path-dependent

hysteresis. In this context, there are two possible strategies. The first is the synthesis of disordered rock-salt compounds which is a rapidly growing area of research. Li-rich disordered rocksalt intercalation compounds such as Li_2MnO_2F[32] or $Li_{1.2}Ti_{0.4}Mn_{0.4}O_2$,[109] cycle over a large intercalation range utilising reversible O-redox. These compounds avoid the order-disorder transition in honeycomb layered O-redox compounds due to their already disordered state. In addition, they possess many Li^+-O-Li^+ environments to promote O oxidation and Li-rich sites for O_2 formation with minimal TM rearrangement. The second is to focus on the surface stabilisation of Li-rich cathodes. Oxygen evolution has been extensively reported in Li-rich cathodes, resulting in irreversible damage to the cathode particles leading to densification, voltage fade and poor capacity retention. Oxygen loss has been shown to occur after the formation of under bonded oxygen (i.e. where the ratio of cations and oxygen drops below 1:2) in layered compounds.[110] A possible strategy could be to create a stoichiometric particle surface with a Li-rich bulk, thus allowing O_2 formation in the bulk while supressing O_2 loss at the surface. This has been implemented in a number of different ways, such as doping Ni into Li_2MnO_3 to create Ni-rich surfaces,[111] or through surface treatments forming cathodes with epitaxial, near-stoichiometric surfaces and a Li-rich bulk.[112] Surface modifications such as coatings, fluorination and oxygen vacancy creation at the surface have also proven to be highly effective.[113] Although these strategies will not be explored in this thesis, they represent important areas of wider research.

1.6 Thesis Objectives

The battery industry continues to incrementally improve the energy density of Alkali-ion cells through improved cell design and engineering. However, these improvements are limited by the physical properties of conventional cathode materials. O-redox cathodes raise those limits with respect to conventional cathode materials and have the potential to implement a step change in the available energy density of commercial cells.

The work in this thesis draws heavily on the strong experimental evidence for the formation of molecular O_2 in the bulk of O-redox cathodes to provide new insight into the behaviour of the O-redox process. This work covers both fundamental studies probing the evolution of the O-redox process and materials discovery projects aimed at developing highly efficient O-redox cathodes. Importantly, the objectives of this thesis all tie together with the aim of designing cathode materials which display reversible, high-voltage oxygen redox activity. A more detailed outline of the objectives for each chapter is presented below:

- Investigating voltage fade in Li-rich layered oxides (Chapter 3)
    - To demonstrate the importance of material superstructure on O-redox activity in Li-rich layered oxides
    - To quantify the proportion of charge compensation tied to the O^{2-}/O_2 redox couple and track its evolution during cycling.
- Developing *in operando* methods for the study of O-redox materials (Chapter 4)
    - To study $Na_{0.6}Li_{0.2}Mn_{0.8}O_2$ via *in operando* techniques.
    - To develop an *in operando* electrochemical cell to probe the O K-edge of O-redox cathodes via SXAS and RIXS.
- Pillaring as a strategy to prevent bulk formation of molecular O_2 (Chapter 5)
    - To successfully use large pillaring cations in *P*2-type $Na_{0.67}Mn_{0.72}Mg_{0.28}O_2$ with the aim of preventing cationic inter-layer migration.
    - To establish the mechanism for the solid-state, room-temperature ion exchange of $Na_{0.67}Mn_{0.72}Mg_{0.28}O_2$ with Ca^{2+}.
- $Na_{0.66}Li_{0.1}Ni_{0.3}Mn_{0.6}O_2$ as a Reversible High Voltage O-redox Cathode (Chapter 6)
    - To demonstrate the successful implementation of materials design principles to synthesise a novel O-redox cathode.
    - To produce a cathode material capable of reversible, high-voltage O-redox.

1.7 References

1. Tarascon, J. M. & Armand, M. Issues and challenges facing rechargeable lithium batteries. *Nature* **414**, 359–367 (2001).
2. Whittingham, M. S. Lithium batteries and cathode materials. *Chem. Rev.* **104**, 4271–4301 (2004).
3. Rawles, C. & Moores, S. Lithium Ion Battery Megafactory Assessment. *Benchmark Miner. Intell.* 1–9 (2020).
4. Assat, G. & Tarascon, J. M. Fundamental understanding and practical challenges of anionic redox activity in Li-ion batteries. *Nat. Energy* **3**, 373–386 (2018).
5. Nayak, P. K. *et al.* Review on Challenges and Recent Advances in the Electrochemical Performance of High Capacity Li- and Mn-Rich Cathode Materials for Li-Ion Batteries. *Adv. Energy Mater.* **8**, 1–16 (2018).
6. Larcher, D. & Tarascon, J. M. Towards greener and more sustainable batteries for electrical energy storage. *Nat. Chem.* **7**, 19–29 (2015).
7. Scrosati, B. History of lithium batteries. *J. Solid State Electrochem.* **15**, 1623–1630 (2011).
8. Thackeray, M. M., Wolverton, C. & Isaacs, E. D. Electrical energy storage for transportation - Approaching the limits of, and going beyond, lithium-ion batteries. *Energy Environ. Sci.* **5**, 7854–7863 (2012).
9. Lazzari, M. & Scrosati, B. A Cyclable Lithium Organic Electrolyte Cell Based on Two Intercalation Electrodes. *J. Electrochem. Soc.* **127**, 773 (1980).
10. Gamble, F. R. *et al.* Intercalation complexes of lewis bases and layered sulfides: A large class of new superconductors. *Science (80-.).* **174**, 493–497 (1971).
11. Broadhead, J., Trumbore, F. A. & Basu, S. Metal chalcogenides as reversible cathodes in lithium cells and their future in telecommunications. *J. Electroanal. Chem.* **118**, 241–250 (1981).
12. Murphy, D. W. & Trumbore, F. A. Metal chalcogenides as reversible electrodes in nonaqueous lithium batteries. *J. Cryst. Growth* **39**, 185–199 (1977).
13. Whittingham, M. S. The Electrochemical Characteristics of VSe_2 in Lithium Cells. *Mat. Res. Bull* **13**, 959–965 (1978).
14. Whittingham, M. S. Electrical Energy Storage and Intercalation Chemistry. *Science (80-.).* **192**, (1976).
15. Fouassier, C., Delmas, C. & Hagenmuller, P. Evolution structurale et proprietes physiques des phases A_XMO_2 (A = Na, K; M = Cr, Mn, Co) ($x \leq 1$). *Mater. Res. Bull.* **10**, 443–449 (1975).
16. DELMAS, C., FOUASSIER, C. & HAGENMULLER, P. Structural Classification And Properties of the Layered Oxides. *Physica* 81–85 (1980).
17. Mizushima, K., Jones, P. C., Wiseman, P. J. & Goodenough, J. B. Li_xCoO_2 ($0 < x < 1$): A New Cathode Material for Batteries of High Energy Density. *Solid State Ionics* **3**–**4**, 171–174 (1981).
18. Dickens, P. G., French, S. J., Hight, A. T. & Pye, M. F. Phase relationships in the

ambient temperature $Li_xV_2O_5$ system (0.1<x<1.0). *Mater. Res. Bull.* **14**, 1295–1299 (1979).

19. Murphy, D. W., Christian, P. A., Disalvo, F. J. & Waszczak, J. V. Lithium Incorporation by Vanadium Pentoxide. *Inorg. Chem.* **18**, 2800–2803 (1979).
20. Claude DELMAS, Jean-Jacques BRACONNIER, C. F. and P. H. L. Electrochemical Intercalation of Sodium in Na_xCoO_2 Bronzes. *Solid State Ionics* **3**–**4**, 165–169 (1981).
21. Fong, R., Sacken, U. yon & Dahn, J. R. Studies of Lithium Intercalation into Carbons Using Nonaqueous Electrochemical Cells. *J. Electrochem. Soc.* **137**, 2009 (1990).
22. Basu, S. Ambient Temperature Rechargeable Battery. (1983).
23. Yazami, R. & Touzain, P. A reversible graphite-lithium negative electrode for electrochemical generators. *J. Power Sources* **9**, 365–371 (1983).
24. Akira Yoshino, Kenichi Sanechika, T. N. Secondary battery. (1986).
25. Ozawa, K. Lithium-ion rechargeable batteries with $LiCoO_2$ and carbon electrodes: the $LiCoO_2$/C system. *Solid State Ionics* **69**, 212–221 (1994).
26. The Royal Swedish Academy of Sciences. Press release, Nobel Prize, Chemie 2019. *Nobel Prize Chem. 2019* 1 (2019).
27. Huggins, R. A. *Advanced Batteries. Chemtech* vol. 15 (Springer US: Boston, 2009).
28. Goodenough, J. B. & Kim, Y. Challenges for rechargeable Li batteries. *Chem. Mater.* **22**, 587–603 (2010).
29. Radin, M. D. *et al.* Narrowing the Gap between Theoretical and Practical Capacities in Li-Ion Layered Oxide Cathode Materials. *Adv. Energy Mater.* **7**, 1–33 (2017).
30. Belharouak, I., Sun, Y. K., Liu, J. & Amine, K. $Li(Ni_{1/3}Co_{1/3}Mn_{1/3})O_2$ as a suitable cathode for high power applications. *J. Power Sources* **123**, 247–252 (2003).
31. Przewoz, J. Conduction mechanism in operating a $LiMn_2O_4$ cathode. **146**, 225–237 (2002).
32. House, R. A. *et al.* Lithium manganese oxyfluoride as a new cathode material exhibiting oxygen redox. *Energy Environ. Sci.* **11**, 926–932 (2018).
33. Padhi, A. K., Nanjundaswamy, K. S. & Goodenough, J. B. Phospho-olivines as Positive-Electrode Materials for Rechargeable Lithium Batteries. *J. Electrochem. Soc.* **144**, 1188–1194 (1997).
34. Kim, D. *et al.* Electrochemistry Communications Layered Na $[Ni_{1/3}Fe_{1/3}Mn_{1/3}]O_2$ cathodes for Na-ion battery application. *Electrochem. commun.* **18**, 66–69 (2012).
35. Chen, G., Huang, Q., Wu, T. & Lu, L. Polyanion Sodium Vanadium Phosphate for Next Generation of Sodium-Ion Batteries—A Review. *Adv. Funct. Mater.* **30**, 1–23 (2020).
36. Wang, L. *et al.* Rhombohedral Prussian White as Cathode for Rechargeable Sodium-Ion Batteries. (2015) doi:10.1021/ja510347s.
37. Kalhoff, J., Kim, G.-T., Passerini, S. & Appetecchi, G. B. Safety Assessment of Ionic Liquid-Based Lithium-Ion Battery Prototypes. *J. Power Energy Eng.* **04**, 9–18 (2016).

38. Sawicki, M. & Shaw, L. L. Advances and challenges of sodium ion batteries as post lithium ion batteries. *RSC Adv.* **5**, 53129–53154 (2015).

39. Slater, M. D., Kim, D., Lee, E. & Johnson, C. S. Sodium-ion batteries. *Adv. Funct. Mater.* **23**, 947–958 (2013).

40. YAMADA, A. Systematic Studies on Abundant Battery Materials: Identification and Reaction Mechanisms. *Electrochemistry* **84**, 654–661 (2016).

41. Shannon, R. D. & Prewitt, C. T. Effective ionic radii in oxides and fluorides. *Acta Crystallogr. Sect. B Struct. Crystallogr. Cryst. Chem.* **25**, 925–946 (1969).

42. Han, M. H., Gonzalo, E., Singh, G. & Rojo, T. A comprehensive review of sodium layered oxides: Powerful cathodes for Na-ion batteries. *Energy Environ. Sci.* **8**, 81–102 (2015).

43. Eum, D. *et al.* Voltage decay and redox asymmetry mitigation by reversible cation migration in lithium-rich layered oxide electrodes. *Nat. Mater.* **19**, 419–427 (2020).

44. Katcho, N. A. *et al.* Origins of Bistability and Na Ion Mobility Difference in *P*2- and *O*3- $Na_{2/3}Fe_{2/3}Mn_{1/3}O_2$ Cathode Polymorphs. 1–9 (2017) doi: 10.1002/aenm.201601477.

45. Co, M. & Mn, L. Studies of the layered manganese bronzes, $Na_{2/3}[Mn_{1-2x}M_x]O_2$ with. **126**, 3–24 (1999).

46. Lu, Z., MacNeil, D. D. & Dahn, J. R. Layered $Li[Ni_xCo_{1-2x}Mn_x]O_2$ cathode materials for lithium-ion batteries. *Electrochem. Solid-State Lett.* **4**, 4–8 (2001).

47. Zheng, J. *et al.* Tuning of Thermal Stability in Layered $Li(Ni_xMn_yCo_z)O_2$. *J. Am. Chem. Soc.* **138**, 13326–13334 (2016).

48. Chen, C. H. *et al.* Aluminum-doped lithium nickel cobalt oxide electrodes for high-power lithium-ion batteries. *J. Power Sources* **128**, 278–285 (2004).

49. Li, H. *et al.* Synthesis of Single Crystal $LiNi_{0.88}Co_{0.09}Al_{0.03}O_2$ with a Two-Step Lithiation Method . *J. Electrochem. Soc.* **166**, A1956–A1963 (2019).

50. Ju, S. H., Jang, H. C. & Kang, Y. C. Al-doped Ni-rich cathode powders prepared from the precursor powders with fine size and spherical shape. *Electrochim. Acta* **52**, 7286–7292 (2007).

51. Wang, Q. *et al.* Reaching the Energy Density Limit of Layered *O*3-$NaNi_{0.5}Mn_{0.5}O_2$ Electrodes via Dual Cu and Ti Substitution. *Adv. Energy Mater.* **9**, 1–11 (2019).

52. Clément, R. J., Bruce, P. G. & Grey, C. P. Review—Manganese-Based *P*2-Type Transition Metal Oxides as Sodium-Ion Battery Cathode Materials. *J. Electrochem. Soc.* **162**, A2589–A2604 (2015).

53. Blomgren, G. E. The Development and Future of Lithium Ion Batteries. *J. Electrochem. Soc.* **164**, A5019–A5025 (2017).

54. Lu, Z., MacNeil, D. D. & Dahn, J. R. Layered cathode materials $Li[Ni_xLi_{(1/3-2x/3)}Mn_{(2/3-x/3)}]O_2$ for lithium-ion batteries. *Electrochem. Solid-State Lett.* **4**, 3–7 (2001).

55. Johnson, C. S., Li, N., Lefief, C., Vaughey, J. T. & Thackeray, M. M. Synthesis, characterization and electrochemistry of lithium battery electrodes: X Li_2MnO_3·(1 - X) $LiMn_{0.333}Ni_{0.333}Co_{0.333}O_2$ ($0 \leq x \leq 0.7$). *Chem. Mater.* **20**, 6095–6106 (2008).

56. Lu, Z., Beaulieu, L. Y., Donaberger, R. A., Thomas, C. L. & Dahn, J. R. Synthesis, Structure, and Electrochemical Behavior of $Li[Ni_xLi_{1/3-2x/3}Mn_{2/3-x/3}]O_2$. *J. Electrochem. Soc.* **149**, A778 (2002).

57. Thackeray, M. M., Johnson, C. S., Vaughey, J. T., Li, N. & Hackney, S. A. Advances in manganese-oxide 'composite' electrodes for lithium-ion batteries. *J. Mater. Chem.* **15**, 2257–2267 (2005).

58. Koga, H. *et al.* Operando X-ray Absorption Study of the Redox Processes Involved upon Cycling of the Li-Rich Layered Oxide $Li_{1.20}Mn_{0.54}Co_{0.13}Ni_{0.13}O_2$ in Li Ion Batteries. *J. Phys. Chem. C* **118**, 5700–5709 (2014).

59. Koga, H. *et al.* Different oxygen redox participation for bulk and surface: A possible global explanation for the cycling mechanism of $Li_{1.20}Mn_{0.54}Co_{0.13}Ni_{0.13}O_2$. *J. Power Sources* **236**, 250–258 (2013).

60. Ceder, G. *et al.* Identification of cathode materials for lithium batteries guided by first-principle calculations. *Nature* **392**, 694–696 (1998).

61. Oishi, M. *et al.* Charge compensation mechanisms in $Li_{1.16}Ni_{0.15}Co_{0.19}Mn_{0.50}O_2$ positive electrode material for Li-ion batteries analyzed by a combination of hard and soft X-ray absorption near edge structure. *J. Power Sources* **222**, 45–51 (2013).

62. Tamaru, M., Wang, X., Okubo, M. & Yamada, A. Layered Na_2RuO_3 as a cathode material for Na-ion batteries. *Electrochem. commun.* **33**, 23–26 (2013).

63. Maitra, U. *et al.* Oxygen redox chemistry without excess alkali-metal ions in $Na_{2/3}[Mg_{0.28}Mn_{0.72}]O_2$. *Nat. Chem.* **10**, 288–295 (2018).

64. Zheng, W. *et al.* Stabilizing the oxygen lattice and reversible oxygen redox in Na-deficient cathode oxides. *J. Power Sources* **439**, 227086 (2019).

65. Du, K. *et al.* Exploring reversible oxidation of oxygen in a manganese oxide. *Energy Environ. Sci.* **9**, 2575–2577 (2016).

66. House, R. A. *et al.* Superstructure control of first-cycle voltage hysteresis in oxygen-redox cathodes. *Nature* **577**, 502–508 (2020).

67. Mortemard de Boisse, B. *et al.* Highly Reversible Oxygen-Redox Chemistry at 4.1 V in $Na_{4/7-x}[[_]_{1/7}Mn_{6/7}]O_2$ ([_]: Mn Vacancy). *Adv. Energy Mater.* **2**, 1800409 (2018).

68. Huang, B. *et al.* Identification of cathode materials for lithium batteries guided by first-principles calculations. *Nature* **392**, 694–696 (2002).

69. Lu, Z., MacNeil, D. D. & Dahn, J. R. Layered Cathode Materials $Li[Ni_xLi_{1/3-2x/3}Mn_{2/3-x/3}]O_2$ for Lithium-Ion Batteries. *Electrochem. Solid-State Lett.* **4**, A191 (2002).

70. Lu, Z. & Dahn, J. R. Understanding the Anomalous Capacity of $Li/Li[Ni_xLi_{(1/3-2x/3)}Mn_{(2/3-x/3)}O_2$ Cells Using In Situ X-Ray Diffraction and Electrochemical Studies. *J. Electrochem. Soc.* **149**, A815 (2002).

71. Ni, O. L. Mechanisms Associated with the " Plateau " Observed at High Voltage for the Mechanisms Associated with the " Plateau " Observed at High. **12**, (2008).

72. Armstrong, A. R. *et al.* Demonstrating oxygen loss and associated structural reorganization in the lithium battery cathode $Li[Ni_{0.2}Li_{0.2}Mn_{0.6}]O_2$. *J. Am. Chem. Soc.* **128**, 8694–8698 (2006).

73. Jiang, M., Key, B., Meng, Y. S. & Grey, C. P. Electrochemical and structural study of the layered, 'Li-excess' lithium-ion battery electrode material $Li[Li_{1/9}Ni_{1/3}Mn_{5/9}]O_2$. *Chem. Mater.* (2009) doi:10.1021/cm900279u.

74. Hong, Y.-S., Park, Y. J., Wu, X., Ryu, K. S. & Chang, S. H. Synthesis and Electrochemical Properties of Nanocrystalline $Li[Ni_{0.20}Li_{0.20}Mn_{0.60}O_2$. *Electrochem. Solid-State Lett.* **6**, A166 (2003).

75. Ito, A. *et al.* In situ X-ray absorption spectroscopic study of Li-rich layered cathode material $Li[Ni_{0.17}Li_{0.2}Co_{0.07}Mn_{0.56}]O_2$. *J. Power Sources* **196**, 6828–6834 (2011).

76. Koga, H. *et al.* Reversible Oxygen Participation to the Redox Processes Revealed for $Li_{1.20}Mn_{0.54}Co_{0.13}Ni_{0.13}O_2$. *J. Electrochem. Soc.* **160**, A786–A792 (2013).

77. Oishi, M. *et al.* Charge compensation mechanisms in $Li_{1.16}Ni_{0.15}Co_{0.19}Mn_{0.50}O_2$ positive electrode material for Li-ion batteries analyzed by a combination of hard and soft X-ray absorption near edge structure. *J. Power Sources* **222**, 45–51 (2013).

78. Seo, D. H. *et al.* The structural and chemical origin of the oxygen redox activity in layered and cation-disordered Li-excess cathode materials. *Nat. Chem.* **8**, 692–697 (2016).

79. Luo, K. *et al.* Charge-compensation in 3d-transition-metal-oxide intercalation cathodes through the generation of localized electron holes on oxygen. *Nat. Chem.* **8**, 684–691 (2016).

80. Luo, K. *et al.* Anion Redox Chemistry in the Cobalt Free 3d Transition Metal Oxide Intercalation Electrode $Li[Li_{0.2}Ni_{0.2}Mn_{0.6}]O_2$. *J. Am. Chem. Soc.* **138**, 11211–11218 (2016).

81. Gent, W. E. *et al.* Coupling between oxygen redox and cation migration explains unusual electrochemistry in lithium-rich layered oxides. *Nat. Commun.* **8**, (2017).

82. Wang, Q. *et al.* Unlocking anionic redox activity in *O*3-type sodium 3D layered oxides via Li substitution. *Nat. Mater.* **20**, (2021).

83. Boivin, E. *et al.* Bulk O_2 formation and Mg displacement explain O-redox in $Na_{0.67}Mn_{0.72}Mg_{0.28}O_2$. *Joule* **5**, 1267–1280 (2021).

84. Tsuchimoto, A. *et al.* Nonpolarizing oxygen-redox capacity without O-O dimerization in $Na_2Mn_3O_7$. *Nat. Commun.* 1–7 doi:10.1038/s41467-020-20643-w.

85. Sathiya, M. *et al.* High performance $Li_2Ru_{1-y}Mn_yO_3$ ($0.2 \leq y \leq 0.8$) cathode materials for rechargeable lithium-ion batteries: Their understanding. *Chem. Mater.* **25**, 1121–1131 (2013).

86. Sathiya, M. *et al.* Reversible anionic redox chemistry in high-capacity layered-oxide electrodes. *Nat. Mater.* **12**, 827–835 (2013).

87. McCalla, E. *et al.* Visualization of O-O peroxo-like dimers in high-capacity layered oxides for Li-ion batteries. *Science (80-.).* **350**, 1516–1521 (2015).

88. Saubanère, M., McCalla, E., Tarascon, J. M. & Doublet, M. L. The intriguing question of anionic redox in high-energy density cathodes for Li-ion batteries. *Energy Environ. Sci.* **9**, 984–991 (2016).

89. Csernica, P. M. *et al.* Metal–oxygen decoordination stabilizes anion redox in Li-rich oxides. *Nat. Mater.* **18**, (2019).

90. Dai, K. *et al.* High Reversibility of Lattice Oxygen Redox Quantified by Direct Bulk Probes of Both Anionic and Cationic Redox Reactions. *Joule* **3**, 518–541 (2019).

91. House, R. A. *et al.* First-cycle voltage hysteresis in Li-rich 3*d* cathodes associated with molecular O_2 trapped in the bulk. *Nat. Energy* **5**, 777–785 (2020).

92. Grenier, A. *et al.* Nanostructure Transformation as a Signature of Oxygen Redox in Li-Rich 3d and 4d Cathodes. *J. Am. Chem. Soc.* **143**, 5763–5770 (2021).

93. House, R. A. *et al.* Environmental Science Detection of trapped molecular O_2 in a charged Li-rich cathode by Neutron PDF. 376–383 (2022) doi:10.1039/d1ee02237g.

94. Mohanty, D. *et al.* Investigating phase transformation in the $Li_{1.2}Co_{0.1}Mn_{0.55}Ni_{0.15}O_2$ lithium-ion battery cathode during high-voltage hold (4.5 V) via magnetic, X-ray diffraction and electron microscopy studies. *J. Mater. Chem. A* **1**, 6249–6261 (2013).

95. Xu, B., Fell, C. R., Chi, M. & Meng, Y. S. Identifying surface structural changes in layered Li-excess nickel manganese oxides in high voltage lithium ion batteries: A joint experimental and theoretical study. *Energy Environ. Sci.* **4**, 2223–2233 (2011).

96. Gu, M. *et al.* Formation of the spinel phase in the layered composite cathode used in Li-Ion batteries. *ACS Nano* **7**, 760–767 (2013).

97. Mohanty, D. *et al.* Unraveling the voltage-fade mechanism in high-energy-density lithium-ion batteries: Origin of the tetrahedral cations for spinel conversion. *Chem. Mater.* **26**, 6272–6280 (2014).

98. Wu, Y. *et al.* Probing the initiation of voltage decay in Li-rich layered cathode materials at the atomic scale. *J. Mater. Chem. A* **3**, 5385–5391 (2015).

99. Hua, W. *et al.* Structural insights into the formation and voltage degradation of lithium- and manganese-rich layered oxides. *Nat. Commun.* **10**, 1–11 (2019).

100. Yu, Z. *et al.* Relationship between Voltage Hysteresis and Voltage Decay in Lithium-Rich Layered Oxide Cathodes. *J. Phys. Chem. C* **125**, 16913–16920 (2021).

101. Croy, J. R. *et al.* Examining hysteresis in composite x Li_2MnO_3· (1-x)$LiMO_2$ cathode structures. *J. Phys. Chem. C* **117**, 6525–6536 (2013).

102. Sathiya, M. *et al.* Origin of voltage decay in high-capacity layered oxide electrodes. *Nat. Mater.* **14**, 230–238 (2015).

103. Oishi, M. *et al.* Direct observation of reversible oxygen anion redox reaction in Li-rich manganese oxide, Li_2MnO_3, studied by soft X-ray absorption spectroscopy. *J. Mater. Chem. A* **4**, 9293–9302 (2016).

104. Hu, E. *et al.* Evolution of redox couples in Li- and Mn-rich cathode materials and mitigation of voltage fade by reducing oxygen release. *Nat. Energy* **3**, 690–698 (2018).

105. Dogan, F. *et al.* Re-entrant lithium local environments and defect driven electrochemistry of Li- and Mn-Rich Li-Ion battery cathodes. *J. Am. Chem. Soc.* **137**, 2328–2335 (2015).

106. Yan, P. *et al.* Injection of oxygen vacancies in the bulk lattice of layered cathodes. *Nat. Nanotechnol.* **14**, 602–608 (2019).

107. Csernica, P. M. *et al.* Persistent and partially mobile oxygen vacancies in Li-rich layered oxides. *Nat. Energy* **6**, 642–652 (2021).

108. Eum, D. *et al.* Coupling structural evolution and oxygen-redox electrochemistry in layered transition metal oxides. *Nat. Mater.* (2022) doi:10.1038/s41563-022-01209-1.

109. Yabuuchi, N. *et al.* Origin of stabilization and destabilization in solid-state redox reaction of oxide ions for lithium-ion batteries. *Nat. Commun.* **7**, 1–3 (2016).

110. House, R. A. *et al.* What Triggers Oxygen Loss in Oxygen Redox Cathode Materials? *Chem. Mater.* **31**, 3293–3300 (2019).

111. Boivin, E. *et al.* The Role of Ni and Co in Suppressing O-Loss in Li-Rich Layered Cathodes. *Adv. Funct. Mater.* **31**, (2021).

112. Zhu, Z. *et al.* Gradient Li-rich oxide cathode particles immunized against oxygen release by a molten salt treatment. *Nat. Energy* **4**, 1049–1058 (2019).

113. Qiu, B. *et al.* Gas-solid interfacial modification of oxygen activity in layered oxide cathodes for lithium-ion batteries. *Nat. Commun.* **7**, 1–10 (2016).

Chapter 2
Methods

Table of Contents

2.1 Materials Synthesis 40
2.1.1 Solid State Synthesis 40
2.1.2 Sol-Gel Synthesis 41
2.1.3 Co-precipitation Synthesis 41
2.2 Materials Characterisation 42
2.2.1 Inductively Coupled Plasma Optical Emission Spectrometry 42
2.2.2 Scanning Electron Microscopy 43
2.2.3 Energy Dispersive X-ray Spectrometry 44
2.2.4 Thermogravimetric Analysis 44
2.3 Electrochemical Methods 45
2.3.1 Electrode Preparation 45
2.3.2 Coin Cell Assembly 45
2.3.3 Cell Cycling 46
2.3.4 Ex-Situ Sample Preparation 47
2.3.5 Operando Electrochemical Mass Spectrometry 48
2.4 Spectroscopic Techniques 49
2.4.1 X-ray Absorption Spectroscopy 49
2.4.2 Extended X-ray Absorption Fine Structure 53
2.4.3 Operando Cells for XAS Experiments 54
2.4.4 Resonant Inelastic X-ray Scattering 56
2.5 Structural Characterisation 58
2.5.1 Nuclear Magnetic Resonance 58
2.5.2 An Introduction to Powder Diffraction 59
2.5.4 Rietveld Refinement 64
2.5.3 Electrochemical Cells for Operando Diffraction Measurements 66
2.5.5 Annular Dark Field Scanning Transmission Electron Microscopy 66
2.5.6 Electron Energy Loss Spectroscopy 67
2.6 References 68

2.1 Materials Synthesis

2.1.1 Solid State Synthesis

Solid state synthesis represents the most common route to making mixed metal oxides. To begin with, the precursor materials (commonly used are metal nitrates, carbonates, oxides or hydroxides) are mixed together then heated to high temperatures.[1] A significant amount of energy is required to overcome the lattice energy and promote the diffusion of atoms from their crystallographic sites through the solid. Therefore, solid state reactions require high temperatures (600-1000 ^{o}C) and long reaction times (over 10 hours), to ensure the reaction is not diffusion limited and to promote precursor decomposition. To further reduce the length scales of diffusion, intimate mixing of the precursors is needed. This can be achieved by ball milling the precursors together, forming a homogenous mixture. To ensure good particle-particle contact a dense pellet of the precursor mixture is formed before the heating stage using a hydraulic press and die set.

The choice of reaction atmosphere is another important variable to control, in particular when specific TM oxidation states are being targeted. This can be illustrated using the following reaction as an example:

$$TM^{4+}O_2\ (s) <-> \tfrac{1}{2}\ TM^{3+}{}_2O_3\ (s)\ +\ \tfrac{1}{4}\ O_2\ (g)$$

In the reaction presented above, the oxygen partial pressure is key to achieving a particular oxidation state. At a given temperature, flowing 100% O_2 over the reaction rather than air will increase the partial pressure of O_2 and push the equilibrium to the left-hand side of the equation, favouring higher oxidation states. On the other hand, flowing Ar or H_2 gas over the reaction will favour the right-hand side and TM reduction. Higher temperatures will also tend to favour lower oxidation states, due to the entropy gain from evolving O_2 gas during TM reduction. Synthesis temperature can also be used to favour the formation of

certain ordered phases over others (eg: *P*2 and *P*3 phases of Na-ion compounds). Lastly, the rate of cooling after the annealing step is an important variable to consider. Quenching — the rapid cooling of the sample from the annealing temperature to room temperature — allows the thermodynamic product at the annealing temperature to be captured. Conversely, slow cooling aids the formation of ordered arrangements of atoms within TM oxides.[2]

2.1.2 Sol-Gel Synthesis

Sol-Gel synthesis is a wet-chemical technique used for the synthesis of mixed metal oxides. While there exists many variations of this type of synthesis (Resorcinol Formaldehyde-Gel synthesis method, citric acid assisted sol-gel synthesis),[3,4] the fundamental principles remain the same. The process involves first dissolving the precursors, typically metal nitrates or acetates, to form a concentrated solution. The gelling agents resorcinol and formaldehyde are then added to form a ‘sol’ which is a colloidal suspension. The pH of this solution can be modified to control the rate of gelation, which in turn can influence the mixing of the different precursor components and the final morphology of the product. Once the ‘sol’ is formed it will then be aged or heated to form a ‘gel’. The gel is dried then heated in a low temperature first step to decompose the organic component of the gel. A final high temperature heating step is then applied to form the final product. This method has been successfully used to produce high-performance cathode materials.[3] One of the advantages of the Sol-Gel method is that it facilitates the formation of an intimately mixed precursor mixture.

2.1.3 Co-precipitation Synthesis

Co-precipitation is a synthesis route preferentially used by industry to make high quality cathode material at scale.[5,6] In industry, this reaction is carried out in a Continuously Stirred Tank Reactor (CSTR). This allows the addition of each reagent to be finely

controlled based on the temperature and pH of the reaction solution. The lab scale set-up used in this thesis consisted of a hotplate stirrer, pH meter, a large beaker and two large burettes. First, a basic solution containing the precipitate anion (usually NaOH or Na_2CO_3), and an acidic solution containing the precipitate cation (usually metal sulphates or nitrates) were made up. Each solution is added to one of the large burettes, which are placed above a beaker containing the pH probe and some deionised H_2O. Under continuous stirring, the two solutions are added in concert, making sure to keep the pH as close to a pre-defined point. A third solution can also be used, typically containing ammonia solution, to control particle size and morphology. When making the $Ni_{1/3}Mn_{1/3}Co_{1/3}CO_3$ precursor for $Li_{1.2}Mn_{0.54}Co_{0.13}Ni_{0.13}O_2$, the pH was aimed to be kept at 7.8 to prevent the formation of $Ni(OH)_2$ impurity.

Once all the metal solution has been added, the solution is left to stir overnight to aid the formation of the precipitate precursor. The precipitate can then be washed and dried, before being mixed with further reagents and heated to high temperatures for the annealing step, forming the final product.

2.2 Materials Characterisation

2.2.1 Inductively Coupled Plasma Optical Emission Spectrometry

Inductively Coupled Plasma Optical Emission Spectrometry (ICP-OES) is a technique used to identify the composition of an unknown compound or to confirm the composition of an existing compound. In this technique, Optical Emission Spectrometry is used for elemental identification, by measuring the characteristic emission spectra emitted from atoms as their electrons decay from an excited state.[7] Excitation of the electrons can be induced by a flame or a plasma. In ICP-OES, a plasma is generated from the ionization of argon gas. A spark causes the initial ionization of the Argon. The stripped electrons are then

caught in a magnetic field, accelerating them and causing further collisions with other Argon atoms, stripping more electrons, eventually forming a stable plasma.[8] The sample is then delivered into the plasma, exciting the atoms from the sample causing optical emission. The wavelength and intensity of the emitted light can then be measured, allowing the identification of the elements present as well as their concentration.

While ICP-OES is an extremely powerful tool for deducing elemental concentrations in a sample, sample preparation is key to produce relevant results. The compound must first be fully dissolved using concentrated acid (eg: conc. nitric acid) to ensure no more solid remains in the analyte solution. The analyte concentration may then be diluted to fall within the working range of the instrument. Once the analyte has been prepared, it is fed into the instrument through a nebulizer. This allows the formation of a fine aerosol, which is then pumped into the plasma. To deduce the concentrations of the elements present in the analyte, elemental solutions of known concentrations are measured to form a set of calibration lines. The intensity of the emission from the sample can then be compared to the calibration lines, thus allowing the precise concentration of the analyte to be determined.

2.2.2 Scanning Electron Microscopy

Spatial resolution in microscopy is limited by the wavelength of the incident radiation, as described by the diffraction limit.[10] Over the last century, the advent of electron microscopes has allowed sub-micron resolution to be achieved routinely. This is achieved by using a beam of high energy, short wavelength electrons to image the sample. Scanning Electron Microscopy (SEM) is one example of electron microscopy, which has become a widely used tool for the characterisation of material morphology. In SEM, free electrons are generated from an electron source then accelerated to high energies before being focused onto the sample.[11] The focused beam can then be scanned across the sample to generate a

2D image. The interaction of the electron beam with the sample yields a number of scattering and absorption events. While these events can all be measured using different detectors for further analysis, the emission of low energy secondary electrons is most commonly used for imaging as they allow for high spatial resolution. SEM is used for the characterisation of particle size and shape of cathode materials and can be coupled with other techniques for further characterization.

2.2.3 Energy Dispersive X-ray Spectrometry

Energy Dispersive X-ray Spectrometry (EDX) can be coupled with SEM for the elemental analysis of a sample. The interaction of an electron beam with a sample in an SEM generates different absorption and scattering events: Secondary electrons, auger electrons, back scattered electrons and X-rays.[11] The emitted X-rays are element specific, based on the fundamental principle that the unique atomic structure of an element allows the generation of a unique set of peaks in its emission spectrum. When undertaking EDX analysis, the emission of X-rays from a sample placed in an SEM are measured to study the elemental composition of the sample, as well as a mapping tool to reveal the distribution of elements and check sample homogeneity. EDX can also be used as a quantitative analysis tool.[12]

2.2.4 Thermogravimetric Analysis

Thermogravimetric analysis (TGA) was used to investigate the thermal stability of a compound by placing a known amount of sample on a precision balance within a furnace that can be programmed to follow a specific heating regime.[9] The furnace atmosphere can also be controlled. Changes to the samples mass are recorded throughout the heating regime. This allows the decomposition temperature of compounds to be studied. It can also be used to determine a sample's phase purity and reactivity. TGA can also be combined with Mass Spectrometry (TGA-MS) to investigate the nature of the decomposition products.

2.3 Electrochemical Methods

2.3.1 Electrode Preparation

Before being cycled in a cell, cathode powders must be prepared into electrode films. This is done to aid the handling of the electrode, but also to improve cycling performance. Transition metal oxides are typically poor electrical conductors, as they tend to have the electronic structure of a semiconductor. A conductive additive, typically carbon black, is added to create a conductive network, increasing the conduction of electrons from the active material to the current collector. The addition of a polymer binder (e.g. Polytetrafluoroethylene (PTFE) or Polyvinylidene fluoride (PVDF)) prevents the fine powders from separating, creating a composite film. To prepare the electrode film, active material, carbon black and binding agents are weighed out (a ratio of 80:10:10 in terms of weight was targeted for the work in this thesis). This can be carried out as a wet or dry method. While a wet, casting method is typically used in industry, the electrodes prepared for the work shown in this thesis were all made using a dry mixing method. Using the dry method, the component materials are mixed in a pestle mortar, creating a free-standing electrode film. In a final step, the homogenous mixture is calendared between two rollers to a thickness of ~150µm, increasing inter-particle contact within the electrode. The electrode film can then be cut to size and weighed for the experiment. For the work presented in this thesis, all electrode samples were made via the dry method in an Argon filled glovebox.

2.3.2 Coin Cell Assembly

Coin cells are used daily to power small electronics such as calculators and are the most prevalent method of testing battery materials in a laboratory setting. These small, button-sized cells are easy to assemble, with the parts being stacked in order, before the cell is crimped to ensure it is hermetically sealed (Figure 2.1).[13] The assembly process is usually

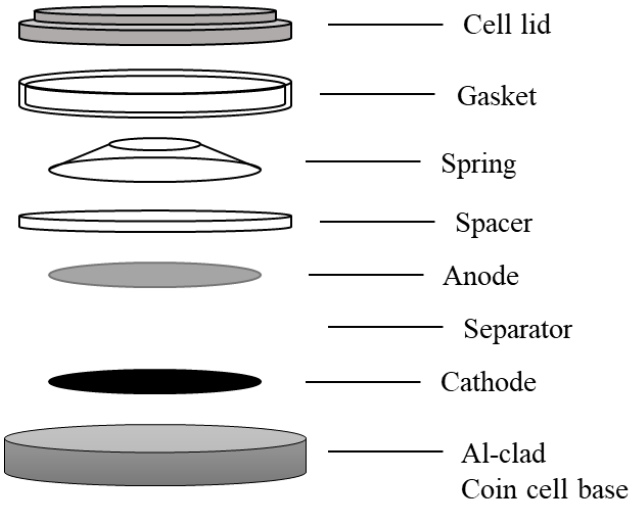

Figure 2.1: Representation of a typical coin cell assembly, with parts labelled to the right.

is first placed in the positive cell casing, followed by a porous glass fibre separator, to carried out in a glove box, with the cells being made in a half cell configuration. The cathode keep the cathode and anode separate. The separator is then soaked in electrolyte, which may consist of a Li or Na based salt (e.g. $NaPF_6$) dissolved in a solvent (e.g. propylene carbonate (PC), acetonitrile(ACN)). A thin, cleaned piece of Li or Na metal foil is then used as the anode, before a stainless-steel spacer and a spring are added. These two components ensure a high internal pressure within the cell, enabling good internal electrical connection. Finally, the cell top is added, being electronically insulated from the cell bottom using a plastic gasket to avoid shorting. The cell is then crimped using a mechanical crimper.

2.3.3 Cell Cycling

Several electrochemical measurement methods are used in the study of battery materials, but by far the most common is galvanostatic cycling. Galvanostatic cycling was used in this thesis to assess a materials electrochemical performance, and in the preparation of samples for ex-situ measurement. In this technique, a constant current is applied to the cell and the variation in cell voltage is measured. When the cell's voltage reaches a pre-defined cut-off limit, the current is reversed, and the cell is discharged until the voltage

reaches the lower cut-off limit. This process can be repeated over any number of cycles. The applied current is set based on the desired charging rate and the mass of active material in the electrode. In industrial applications, the current is set as a function of the amount of time needed to fully charge/discharge a cell of known capacity, also known as a C-rate. However, the current can also be chosen as the current per unit mass of active material (mA/g).[14]

During a galvanostatic measurement, the cell voltage is measured as a function of time. The capacity of the cell (q) can be derived from the following equation:

$$q = \frac{I\Delta t}{m}$$

Where t is the total elapsed time, m is the mass of active material, and I is the applied current. This information can then be plotted as voltage vs capacity, also known as a load curve, to show the cycling performance of a material. It should be noted that low current rates (i.e. 10 mAg^{-1} or C/10) tend to be used to study new materials. Under these conditions, the reaction is kept close to equilibrium conditions throughout cycling, meaning a minimal amount of overpotential will be applied. Alternatively, a cell can be charged under potentiostatic conditions. This involves setting a constant voltage between the two electrodes of the cell, while measuring the current being passed. This method can be useful for reaching the equilibrium state at a specific potential or for fast charging. Due to the small amount of active material which is measured in each cell (5-20 mg), small currents are needed to charge the cells during cycling (0.1-1 mA). To deliver these small currents accurately and precisely, specialised cycling equipment is required. For the work in this thesis, MACCOR cycling equipment or Biologic potentiostats were used.

2.3.4 Ex-Situ Sample Preparation

Most measurements in this thesis were performed on ex-situ samples removed from the cell after charging. As soon as possible after the end of a cell's testing protocol, the coin

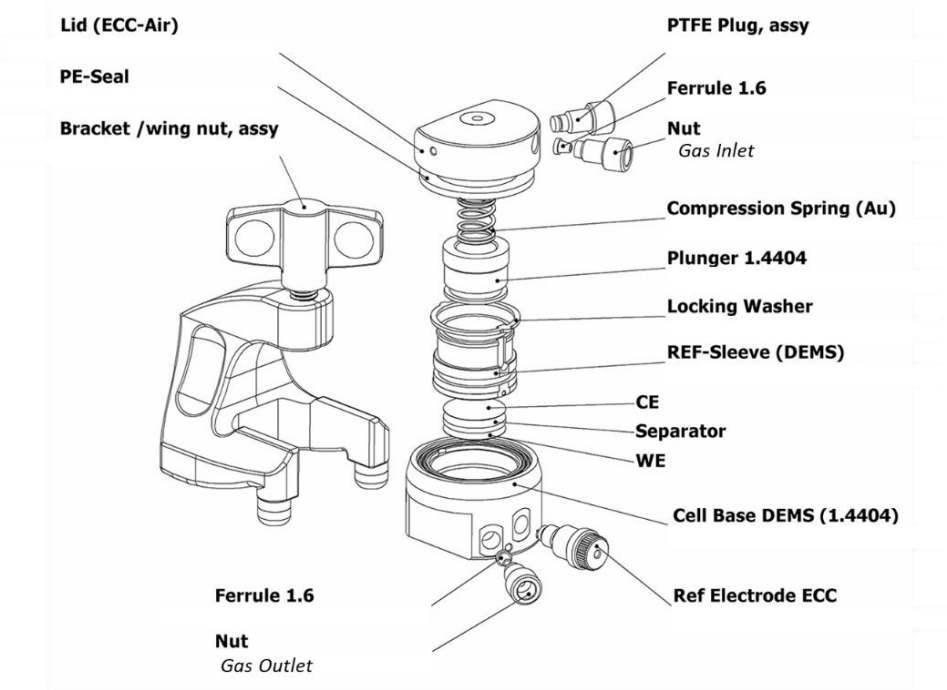

Figure 2.2: Representation of the cell used, designed, and procured from EC-LAB, for OEMS experiments in this thesis. The different parts of the cell are labelled.

cell was moved to an Ar-filled glovebox for disassembly using a de-crimper. The electrode was then removed from the cell casing and washed twice using dry dimethyl carbonate to remove any salt residue from the electrolyte. The electrode was then dried under vacuum and stored in an Ar-filled glovebox before further characterization.

2.3.5 Operando Electrochemical Mass Spectrometry

Operando Electrochemical Mass Spectrometry (OEMS) is a widely used characterization method for the identification and quantification of gases produced during cell cycling. This technique requires a special cell (Figure 2.2), with gas inlets and outlets, to be coupled to a mass spectrometer using sealed tubing. An inert carrier gas (Argon) is then flowed through the cell at a constant rate to collect any evolved gases. The outlet gas is flowed through a mass spectrometer where the gases are ionized by an electron beam. The ionized molecules are then separated based on their mass to charge ratio (m/z), allowing identification and accurate quantification of the evolved gases as a function of time. This allows the release of the gases to be correlated to specific stages of the electrochemical cycle.

2.4 Spectroscopic Techniques

2.4.1 X-ray Absorption Spectroscopy

X-ray Absorption Spectroscopy (XAS) is an element-specific technique used to study transition metal oxidation states and coordination geometries in the bulk crystal structure of materials.[15] In an XAS experiment, a core electron is excited to an unoccupied valence shell state using high energy radiation from a synchrotron source. The basic physical process can be summarized in three steps:

- An incident beam of photons interacts with core electrons.
- Excitation of a core electron to an unoccupied state in one of the outer valence shells, leaving behind a core-hole.
- Decay of a higher-lying electron into the core-hole, and emission of a photon or Auger electron.

This electronic transition is governed by selection rules which state that transitions must be accompanied by a change in orbital angular momentum of delta l = +-1, such that only s – p, p – d, d – f transitions are allowed.[16] These transitions are classified by absorption edges, labelled K, L, M…. depending on the principal quantum number of the lower level in the transition (Figure 2.3). When performing an XAS experiment, a monochromator is used to continuously tune the incident X-rays to a well-defined energy (*E*), depending on the element and the absorption edge being studied.[17] The monochromatic X-ray beam is then scanned through the energy window containing the absorption edge of interest. Signal measurement can be carried out in two modes. The first is transmission mode, where the absorption coefficient (*u*) can be derived using the Beer Lambert law:

$$I_t = I_0\, e^{-ux}$$

$$u(E) \sim \log_{10} \frac{I_0}{I_t}$$

Where I_0 is the incident beam intensity, I_t the transmitted beam intensity and x is the

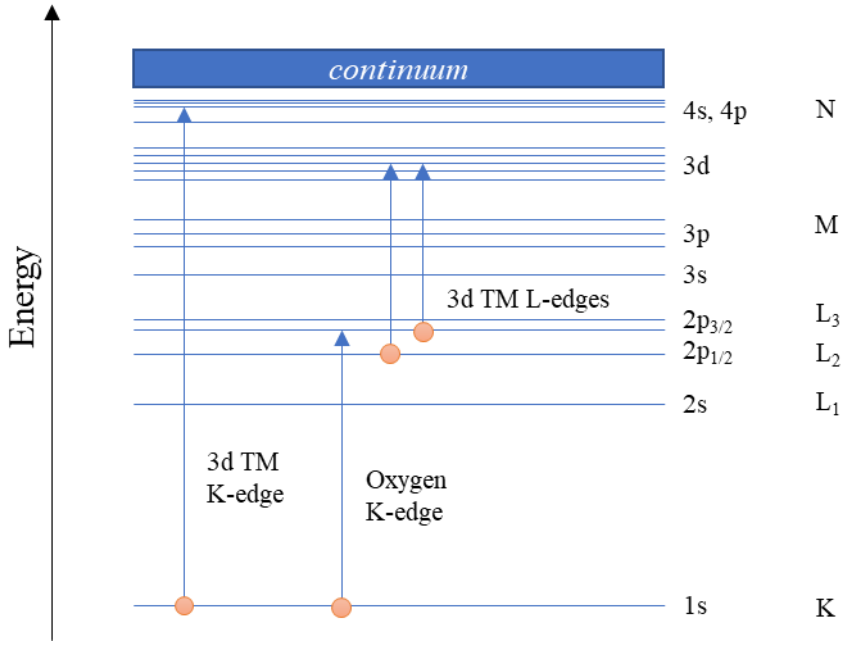

Figure 2.3: Representation of the electronic structure of an atom, showing selected dipole-allowed electronic transitions. Transitions of excited electrons are shown in blue, with labels indicating the orbitals and edges they represent.

sample thickness.[15] The intensities are recorded using a pair of ionization chambers.[16] Transmission mode experiments use hard X-rays (photon energies greater than 3keV) to ensure deeper penetration through the sample, meaning the true bulk of the material is probed. The second experimental mode is fluorescence mode. A detector is placed at an angle (often 90 degrees) to the incident X-ray beam, measuring the intensity of the reflected beam. The absorption coefficient ($u(E)$) at energy E can then be derived based on the following relationship:

$$u(E) \sim \frac{I_f}{I_0}$$

Where I_f is the intensity of the fluoresced beam.[16] Fluorescence mode experiments can be carried out using both hard or soft X-rays (photon energies less than 3keV).[16] The probe depth in fluorescence mode depends on the incident beam energy. While probing depths of ~100nm can be expected in fluorescence experiments using soft X-rays, it is important to note that the attenuation of the incident X-ray beam by the sample follows the Beer-Lambert

Law, showing an exponential decay as the probing depth is increased. Because of this, fluorescence experiments using soft X-rays tend to have significant surface contribution.

In both measurement modes, the absorption coefficient is plotted as a function of energy. As the incident energy is scanned through the binding energy of the core-shell electrons, an abrupt increase in the absorption coefficient is registered as the core-electrons are excited, giving rise to an absorption edge. The position and shape of the absorption edge and pre-edge features can provide important information on the oxidation state of the element being probed and the coordination environment of the atoms.

X-ray Absorption Near Edge Structure

An XAS spectrum of a TM K-edge can be divided into two parts. The absorption edge arises when a core 1s electron is excited to the 4p orbitals or ejected to continuum. The first part of the spectrum is the X-ray Absorption Near Edges Structure (XANES), which is the region around 25 eV from the edge in either direction (Figure 2.4). The position of maximum absorption as a function of energy can be used as a tool for deducing the oxidation state of the element being studied, while the shape of the edge and any pre-edge features can be used to deduce information on the coordination environment of the metal.[16] The pre-edge feature is caused by dipole forbidden 1s to 3d transitions, which can be observed due to distortion of the centro-symmetric coordination environment. For the work shown in this thesis, XANES spectra were analysed using the Athena software package.[18]

Soft X-ray Absorption Spectroscopy

Soft X-ray Absorption Spectroscopy (SXAS) is used to study the transition metal L-edge and the O K-edge of battery materials. The TM L-edge (a 2p to 3d transition) is composed of two features, known as the L_2 and L_3 edges. These arise due to the non-degenerate nature of the 2p orbitals caused by spin orbit coupling.[19] Orbital mixing of O2p

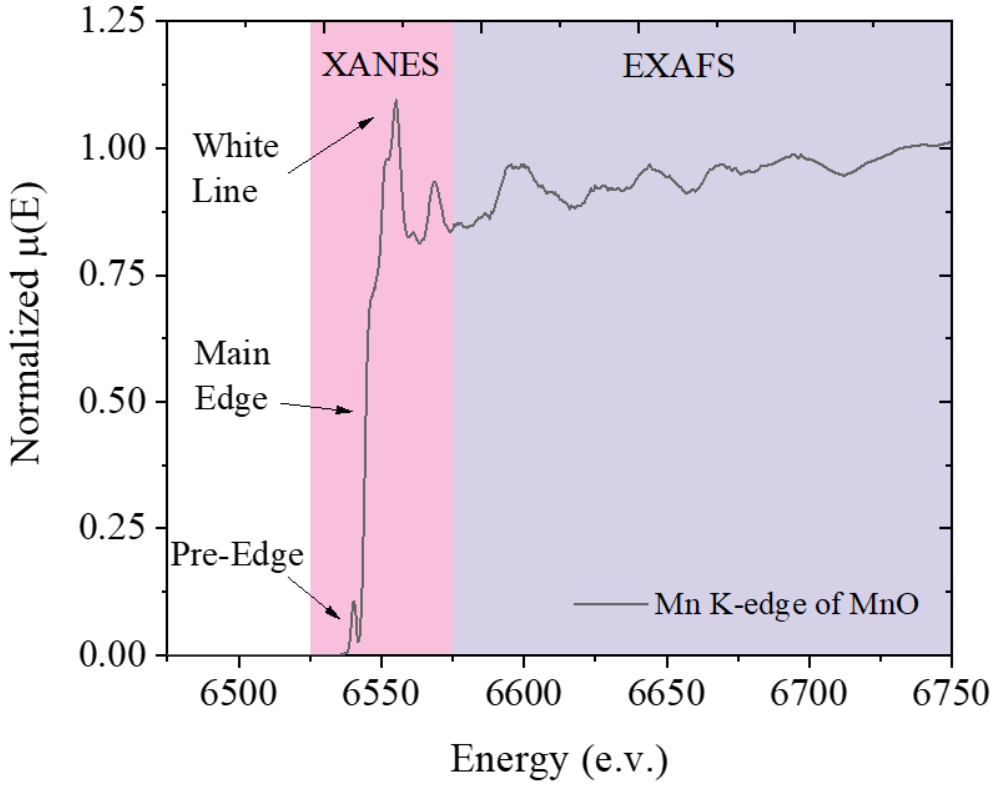

Figure 2.4: A normalized XAS spectrum of MnO, with important characteristics of the spectrum being labelled.

and TM orbitals heavily influences the shape of the O K-edge. The main edge (1s to O2p/TM 4sp transition) is preceded by a pre-edge feature (1s to O2p/TM 3d transition), whose shape is influenced by the valence distribution between the t_{2g} and e_g orbitals of the TM.[20] SXAS allows for the direct probing of unoccupied electronic states, meaning the TM L-edges are very sensitive to the TM oxidation states, while the O K-edge pre-edge feature can indicate the participation of oxygen during charge and discharge.[21]

Soft X-rays are easily attenuated when travelling through air, meaning the measurements must be carried out under ultra-high vacuum (UHV) conditions,[15] and in fluorescence mode due to the low energy of the incident beam. Fluorescence involves the emission of photons with a range of energies. The data gathered from an SXAS experiment can be analysed cumulatively to give Total Fluorescence Yield (TFY) data, or over certain emission energy ranges to give Partial Fluorescence Yield (PFY) data. Fluorescence

measurements can often give rise to self-absorption events, occurring when two element edges are present which are close in energy.

Extracting Oxidation State Information from In Operando Measurements

There are various methods which can be used to track the variations in edge energies across an *in operando* measurement, two of which were actively used in this thesis. The simplest method is known as the half-height method. This method relies on tracking the edge energy at the half height of the edge jump. This method can be employed for the Ni K-edge, as there is no obvious shape change to the edge. The second is known as the integral method.[22] This method is used where there is considerable shape change in the XAS spectra, and follows the following equation:

$$E^{edge} = E_1 + \frac{1}{\mu_2 - \mu_1} \int_{E_1}^{E_2} \mu_2 - \mu(E)\, dE$$

Where E^{edge} is the calculated edge position, μ_1 and μ_2 are the normalized absorption limits chosen for integration, with E_1 and E_2 being the corresponding energy limits. The resulting value of E^{edge} depends on the chosen values of μ_1 and μ_2, and these should be chosen sensibly to include the bulk of the main edge. The integration method has been shown to be insensitive to edge shape, and is well suited to the K-edge XAS data of Mn and Co.

2.4.2 Extended X-ray Absorption Fine Structure

A XANES absorption profile is followed by a series of oscillations which occur beyond the main absorption edge. The incident beam energy above the edge is high enough to eject core electrons to the continuum, allowing them to escape as photoelectrons. This gives them a de Broglie wavelength comparable to interatomic distances within the crystal structure, causing them to be scattered by neighbouring atoms. This generates interference between the outgoing and back-scattered photoelectron waves, giving rise to the oscillation

often seen in the EXAFS region (Figure 2.4). As such, the physical origin of the EXAFS signal is electron scattering, which can reveal structural information in the vicinity of the absorbing atom.[16]

Data reduction must be carried out in order to extract meaningful information from EXAFS, which can be performed using the Athena software package.[18] First, the XAS spectra must be normalized by fitting lines through the post and pre-edge regions. A background function is then used to isolate the fine structure of the EXAFS region, resulting in k-space, where a window function is applied to target the oscillations of interest. The Fourier Transform of this data allows the visualization of the frequencies contributing to the EXAFS signal, resulting in a plot of r-space, showing a series of peaks as a function of *r* (where *r* represents the radial distance from the absorbing atom). The peaks plotted in r-space represent the presence of neighbouring atoms around the absorbing atom, where the intensity of the peak relates to the number of neighbouring atoms and their scattering ability.

2.4.3 Operando Cells for XAS Experiments

In operando XAS measurements allow direct spectroscopic measurements to be taken while the cell is under operation. This gives great insight into the charge compensation mechanisms of battery materials and allows for the measurement of meta-stable samples which may relax over time if prepared for ex-situ measurement. Two cell designs were used to carry out *in operando* XAS and SXAS experiments. Both these cells were designed by Dr. D. Forsterman. For *in operando* hard X-ray XAS and *in operando* EXAFS measurements. The cell was designed to be assembled in a similar way to a coin cell (Figure 2.5). The windows are made of glassy carbon, allowing the passage of X-rays with little attenuation. The cell top is designed with a concave indent, allowing measurements to be carried out in both transmission and fluorescence modes. For soft X-ray *operando* experiments, the following cell design was used. Due to the lower energy and weakly

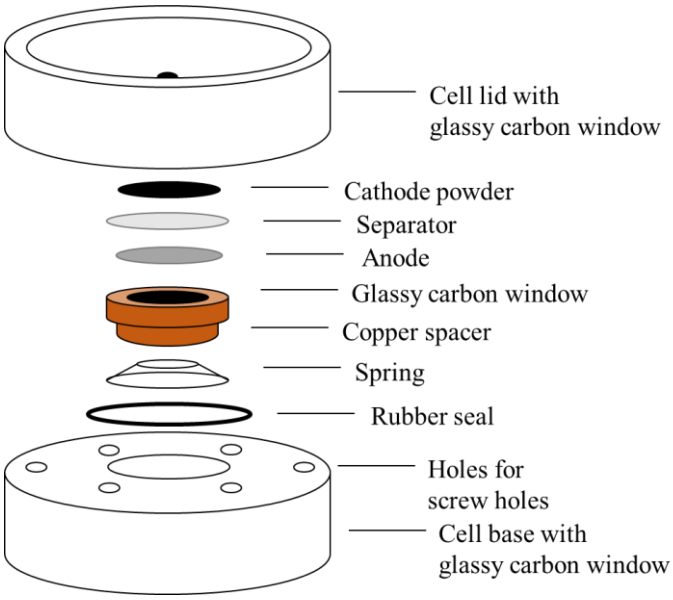

Figure 2.5: Representation of the cell design used for *in operando* XAS and EXAFS experiments. The use of glassy carbon windows allows the synchrotron beam to penetrate the cell with minimal absorption. Cell parts have been labelled on the right.

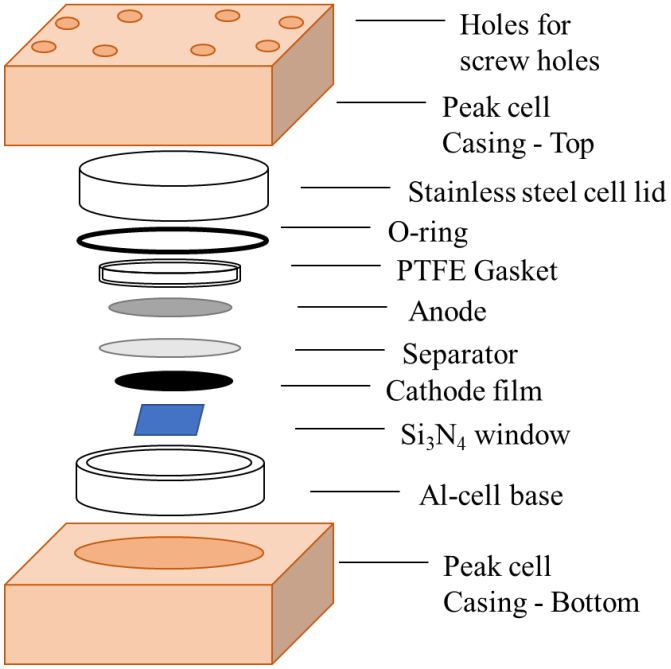

Figure 2.6: Representation of the cell design used for *in operando* SXAS experiments. The use of a Silicon Nitride window allows the synchrotron beam to penetrate the cell with minimal absorption.

penetrating incident beam, this cell can only be used in fluorescence mode. The cell was designed to be assembled in a similar way to a coin cell (Figure 2.6). The window is made of silicon nitride of thickness 150 nm. Choosing the window thickness is trade-off between window stability and attenuation of the X-ray beam.

2.4.4 Resonant Inelastic X-ray Scattering

Resonant Inelastic X-ray Scattering (RIXS) is a spectroscopic technique used to investigate the electronic structure of materials. As discussed previously, an X-ray absorption experiment will excite a core electron to unoccupied states, leaving behind an electron hole. The relaxation event to fill this electron hole will involve either the relaxation of the excited electron or a valence band electron back to the core-hole, resulting in an elastic or inelastic process respectively (Figure 2.7). As such, XAS measurements probe hole states only. The physical process behind RIXS is the inelastic scattering of photons during an X-ray absorption experiment,[23] which allows the valence states to be probed directly. In contrast to XAS experiments, where the photon absorption (transmission mode) or fluorescence (fluorescence mode) is measured as a function of excitation energy, a RIXS experiment will capture the energy-resolved emission of photons at a specific excitation energy.

The data from a single scan at a certain excitation energy can then be plotted as emission intensity as a function of emission energy in a 2D plot (Figure 2.8 a.). Emission spectra taken at different excitation energies can also be plotted together to form a 3D RIXS map (Figure 2.8 b.). RIXS experiments can be carried out on any elemental absorption edge, however for the work in this thesis RIXS experiments were only carried out on the O K-edge. Recent improvements in synchrotron source brightness and grating manufacturing to improve beam focusing, as well as energy resolving detectors, have allowed the development of so-called high-resolution RIXS beamlines to be commissioned, such as the i21 beamline at the Diamond Light Source (DLS).[24] Such beamlines can provide an energy resolution of < 50 meV which allows for a detailed investigation into the electronic structure of materials. Recently, RIXS has become a key spectroscopic technique in the study of O-redox materials.[15,25,26] High-resolution RIXS measurements have offered new insights in

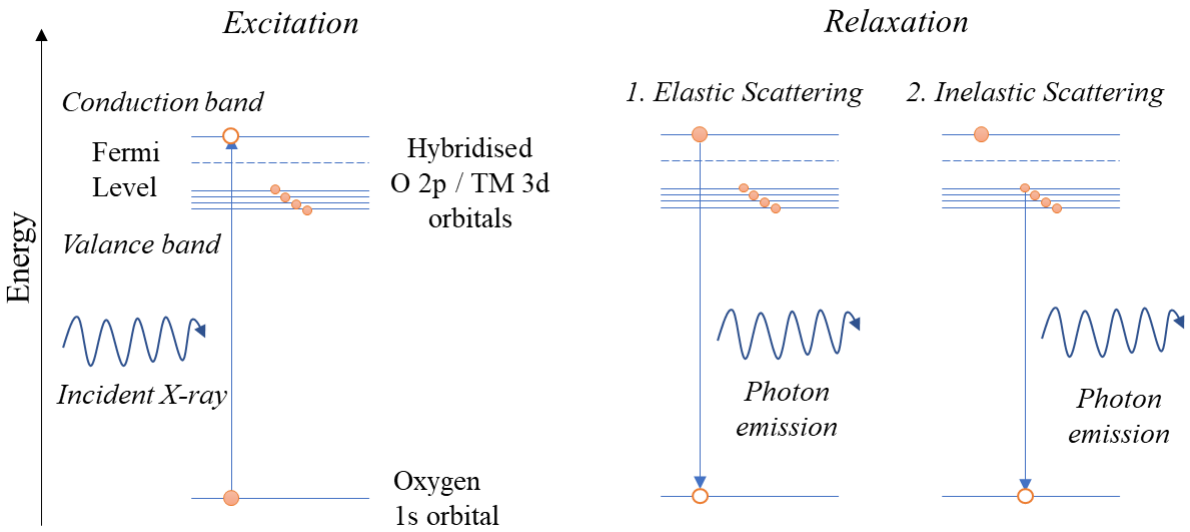

Figure 2.7: Representation of the key electronic transitions leading to RIXS emission via elastic and inelastic scattering at the O K-edge.

determining the nature of the oxidised oxygen at the top of charge. Vibrational progressions measured in an O-K-edge RIXS spectra have been observed, arising from discrete O_2 molecules trapped within the crystal structure of O-redox materials.[27] These results have provided a new theory on the charge compensation mechanism in O-redox materials and have further solidified RIXS as an indispensable technique in the study of O-redox.

Quantitative High Resolution RIXS

RIXS is a spectroscopic technique, and a photon in / photon out technique. This means that different samples can be analysed quantitatively. In this thesis, this technique was used to track the amount of O_2 formed during charging in Li-rich cathode materials. In the high resolution RIXS spectra of O_2, there are two main features associated with O_2: A broad energy loss feature at ~8 eV, and a series of vibrational progression peaks propagating from the elastic RIXS peak at 0 eV. To track the relative amount of O_2, the area under the vibrational progression peaks (from 0.125 eV to 2.2 eV) was integrated. The vibration progression of peaks starting at 0 eV was used as a measure of the quantity of O_2 present, as the peak intensity arises solely from molecular O_2, with no contribution from the oxide ions.

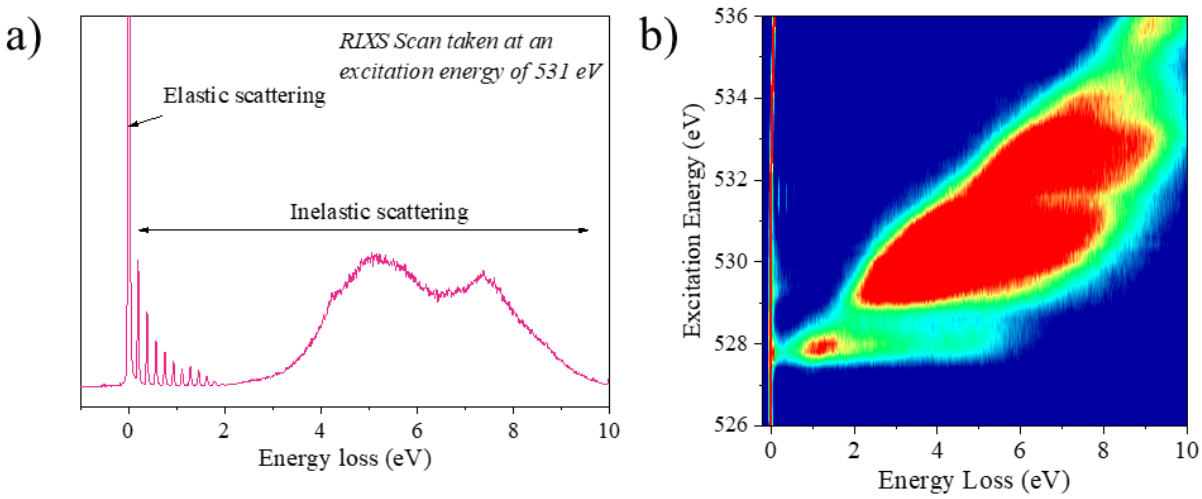

Figure 2.8: a) RIXS emission spectrum at an excitation energy of 531 eV, plotted as energy loss from the elastic peak at 0 eV. b) Map of RIXS emission spectra as a function of different excitation energies (plotted on the y axis).

First, 15 scans were taken for each sample at different locations to average out any sample inhomogeneity. These scans were then z-scored by dividing each scan by its standard deviation to scale the scans in relation to each other. Next, the area under the first vibrational progression peak (from 0.125 eV to 0.3 eV) was integrated and taken as a measure of the relative amount of O_2. For each scan, this results in 15 different areas being given. These were averaged to create a measure of oxygen intensity, with errors coming from the standard deviation of the mean for each data set.

2.5 Structural Characterisation

2.5.1 Nuclear Magnetic Resonance

Nuclear Magnetic Resonance (NMR) spectroscopy is an element-specific technique used to investigate the local environment around the element of interest.[28] All atomic nuclei possess varying degrees of nuclear spin. In an NMR experiment, a sample is exposed to a static magnetic field, causing the spins of the nuclei to align. Next, a second, oscillating magnetic field perpendicular to the first is applied, at a frequency which induces a resonance

in the nuclei being studied. The resonance frequency is heavily dependent on the magnetic field at the resonant nucleus, which in turn is dependent on the chemical environment of the nucleus, thus revealing information about the local environment of the element being studied. This resonance, or perturbation, of the nuclei produces an electromagnetic signal, which can be measured by moving the sample through a coil, inducing a voltage decay. The Fourier transform of this signal can then be plotted as an NMR plot of intensity as a function of frequency.

NMR can be used in the study of solid-state samples. To remove the effects of anisotropic interactions, the sample must be spun at an angle of 54.7^{o} to the external magnetic field (this is Magic Angle Spinning or MAS).[29] This allows for sharper signals and spinning sidebands to be observed in the resulting spectra, easing the process of data analysis. Finally, a general note on Li MAS NMR: ^{6}Li is the least abundant isotope of Li, however it offers improved resolution compared to the ^{7}Li isotope thanks to its lower gyromagnetic ratio and lower quadrupolar and dipolar broadening.[30] Both isotopes were used in this thesis.

2.5.2 An Introduction to Powder Diffraction

Powder diffraction is an important experimental technique used to characterise crystal structures. It is a key technique in the study of battery materials, enabling phase identification and quantification of the compound being studied, as well as monitoring large structural changes which occur during charge and discharge. X-rays, neutrons, and electrons can all be used for diffraction experiments however the concept of diffraction will be explained in the context of X-rays.

Diffraction occurs when waves of the correct wavelength are scattered by an ordered array of atoms, causing constructive and destructive interference in the outgoing wave.[31] X-rays are well-suited for diffraction experiments as their wavelengths (typically 0.2–2 Å) are

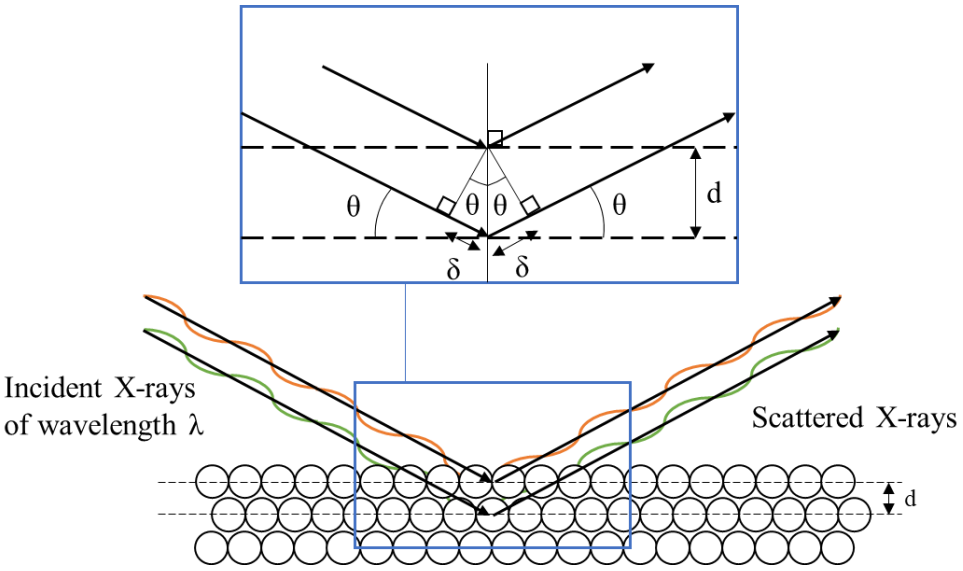

Figure 2.9: Representation of Braggs Law, describing the relationship between the *d* spacing between atomic planes and the diffraction angle and the wavelength of the radiation.

of the same order of magnitude as the inter-atomic distances in the crystal structure (~1–10 Å). In a typical X-ray diffraction experiment, a crystal is subjected to a monochromatic beam of X-rays. The X-ray beam is subsequently scattered by the electron density surrounding the atoms in the crystal structure. This scattering can be considered as the reflection of the incoming beam off of planes of atoms within the crystal structure. These planes are identified by Miller indices, a set of three integer numbers denoted by the letters *hkl*, where each combination of *hkl* values represents a unique plane within the crystal structure. Constructive interference of the reflected beam is observed when X-rays scattered from consecutive planes travel lengths differing by an integer number of wavelengths. This is the basis of Bragg's Law (Figure 2.9), represented by the following equation:

$$n\lambda = 2d_{hkl}\, sin\theta$$

Where *n* is an integer, λ is the wavelength of the incident and scattered radiation, d_{hkl} is the inter-planar spacing of the planes of scattering atoms and θ is the angle between the crystal plane and the incident (or diffracted) beam.[32] The data from an XRD experiment is recorded as a plot of intensity as a function of angle (2θ) where peaks in intensity are observed when the conditions of Bragg's Law are fulfilled. The peak positions are

determined by the arrangement and symmetry of atoms within the crystal structure, which is described by a space group and a set of unit cell parameters, dictating the position and spacing d_{hkl} of the planes. The intensity of the peaks is determined by the identity of the atoms within the diffracting planes. Each atom will scatter radiation to a different extent, where the scattering ability of an atom is quantified by the scattering factor (f_n). This increases with increased electron density and is also strongly dependent on θ and the wavelength of the radiation. As such, the intensity of the diffraction peaks I_{hkl} is proportional to the square of the structure factor (F), described by the following equation:

$$F = \sum_n f_n e^{2\pi n(hx_n + ky_n + lz_n)}$$

Where x, y and z are the unit cell coordinates of the atom n. It should be noted that the intensity of the diffraction peaks can also be influenced by the multiplicity j, describing the number of non-unique reflections at a particular d_{hkl} value.[31] Diffraction peaks will also be broadened to a certain extent due to several factors which can be divided into two groups: instrumental and sample contributions. Instrumental broadening arises from several factors, including misalignment within the diffractometer optics, a non-monochromatic beam or axial divergence of the incident/diffracted beams. Sample contributions to broadening arise from crystallite domain (size) and crystal lattice distortions (strain). These contributions can be separated when doing a Rietveld refinement, extracting a maximum amount of structural information from the diffraction pattern.

Sample Preparation for Powder Diffraction

Powder diffraction experiments rely on the assumption that a statistically large number of crystallites are present and randomly orientated in the beam, ensuring that diffraction is promoted representatively from all reflection planes. This holds true regardless of the radiation source. Therefore, sample preparation is a key step before any powder diffraction

experiment to avoid unwanted artefacts such as preferential orientation. While this is difficult to avoid entirely, it can be particularly difficult for certain sample morphologies with anisotropic shapes. To avoid particle alignment in these cases, care must be taken to not press the powder down, by instead scattering it over an adhesive sample holder if measuring in reflection mode. Another possibility is to measure the sample in transmission mode, where the effects of preferential orientation may be reduced.

X-ray Diffraction

X-ray diffraction (XRD) is the most commonly used method for powder diffraction and can be performed using a laboratory diffractometer or at a synchrotron. Laboratory diffractometers have the advantage of being much easier to access than synchrotron sources, while still being able to give high resolution data. In laboratory experiments, X-rays are generated by irradiating a metal target with electrons, causing the emission of characteristic X-rays. Typically, a Cu source is used, which exhibits radiation at three distinct wavelengths: K_{a1}, K_{a2} and K_b. Good experimental data can be produced using Cu $K_{a1,a2}$ radiation, where a Ni filter is used to remove the Cu K_b radiation. To produce a monochromatic beam of Cu K_{a1} (wavelength of ~1.54 Å) radiation, a Germanium monochromator can be used to filter out the K_{a2} and K_b wavelengths. Absorption of the incident X-rays can be a problem for laboratory diffraction experiments, where the incoming beam is absorbed by the sample, generating fluorescence, increasing the background noise. In the context of battery materials, Co and Fe will fluoresce when using radiation from a Cu source because they strongly absorb the characteristic X-ray emission energies from Cu. To avoid this problem, a different source can be used, such as Mo or Ag, which will generate X-rays of a different wavelength. Lab experiments will usually be carried out using a reflection geometry, where either the source and detector are scanned through θ, or the sample stage by θ and the detector by 2θ.[33] In this case, the sample is laid flat on a sample

holder. These are typically made from a silicon single crystal zero background holder to ensure the sample holder will not contribute to the diffraction pattern.

Synchrotron radiation offers enhanced resolution and shorter collection times compared to laboratory diffractometers, due to the high intensity beam provided by synchrotron sources.[15] A synchrotron produces X-rays by accelerating a high energy beam of electrons through a magnetic field, created by an undulator or a wiggler. The X-rays generated from the accelerating electrons are then directed towards the beamline, where the beam is mono-chromated and collimated before being shone onto the sample. Synchrotron experiments allow for a choice of well-defined wavelength to be used from the continuous X-ray spectrum generated. Experiments will usually be carried out in transmission mode, also known as Debye-Scherrer, where the beam remains stationary and the detector is scanned through 2θ.[33] In transmission mode, the sample is placed in a thin glass capillary, which can be sealed if air sensitive samples are measured. Despite the high intensity of the beam, absorption through the sample must be considered when carrying out refinements.

Neutron Diffraction

Neutron Diffraction (ND) is often used as a complimentary technique to XRD. Neutrons are scattered by the nuclei of the atoms within the crystal structure, which has many implications on the resulting diffraction pattern. In ND, the structure factor F_{hkl} is dependent on the neutron scattering length b, which shows no dependence on atomic number, meaning lighter elements such as Li or Na can be distinguished from heavier elements, and elements adjacent in atomic number can sometimes be very readily differentiated due to different scattering lengths. b also shows no dependence on θ allowing for stronger diffraction at higher angles.[34]

Neutron beams can be generated utilizing the spallation process, where pulses of high-energy protons are fired at a metal target, generating pulses of neutrons. The pulsed neutron

beam is then directed at the sample. The diffraction geometry typically used in ND is based on the principle of time of flight (TOF). In a TOF diffractometer, the diffraction angle is experimentally fixed, and the arrival time of each pulsed neutron is recorded using a series of detector banks placed around the sample at different scattering angles. This experimental setup is based on the relationship between the wavelength of the scattered neutron and its momentum. Incorporating this relationship into Bragg's Law reveals that the inter-planar spacing d_{hkl} is proportional to the time-of-flight through the following relationship:

$$\lambda = \frac{ht}{mL} = 2d_{hkl}\, sin\theta$$

where *h* is planck's constant, *t* is the time of flight, *m* is the neutrons mass and *L* is the path length of the scattered neutron.[34] TOF powder diffraction patterns will usually be displayed in intensity as a function of d-spacing, rather than as a function of 2θ. Due to the low beam intensity provided by neutron sources, more sample is needed to measure diffraction patterns. Around 1g of sample is needed to collect good diffraction patterns. Vanadium cans can be used as the sample holder, due to the weak neutron scattering ability of Vanadium. To aid the comparison of diffraction data from different sources on the same samples, diffraction patterns can be plotted as intensity as a function of the scattering vector *Q*, which represents a wavelength-independent unit of measurement:[34]

$$Q = \frac{4\pi sin\theta}{\lambda} = \frac{2\pi}{d}$$

2.5.4 Rietveld Refinement

The Rietveld method is a structural refinement method developed by Hugo Rietveld as a way of extracting structural information from powder diffraction data.[35] The refinement can be thought of as a "black box" process where the diffraction data is used to guide the refinement of a model structure to match the experimental data through a least-squares minimization process. To begin, a model structure is selected which could conceivably

match the measured data. Peak positions and intensities are then calculated using the unit cell and the structure factor of the model structure. Next, the peaks are fitted using an appropriate peak profile function, which incorporates instrumental and structural dependent broadening. Finally, atomic positions, fractions and thermal displacement parameters are refined until a good fit is achieved between the model and the experimental data. In this thesis, the GSAS-II software package was used for Rietveld refinements.[36]

The goodness of fit (χ^2) of a Rietveld refinement can be calculated in several ways, the most common method being R factors. In any Rietveld method, the quantity being minimized is the squared difference between the observed and calculated peak intensities:

$$\Delta = \sum_i w_i \{ y_i(obs) - y_i(calc) \}^2$$

Where y_i are the peak intensities (observed and calculated), w_i is the weighting given to each intensity difference.[37] When using the R-factors method, two factors in particular are of interest, the weighted profile factor (R_{wp}) and the expected profile factor (R_{exp}). R_{wp} represents the square root of the quantity being minimized weighted by the peak intensities. R_{exp} represents the number of degrees of freedom weighted by the peak intensities. The ratio between R_{wp} and R_{exp} is termed the goodness of fit (χ^2) and can be calculated as per:

$$R_{wp} = \{ \sum_i w_i \{ y_i(obs) - y_i(calc) \}^2 / \sum_i w_i \, y_i(obs)^2 \}^{1/2} \times 100\%$$

$$R_{exp} = \{ (N - P + C) / \sum_i w_i \, y_i(obs)^2 \}^{1/2} \times 100\%$$

$$\chi^2 = (R_{wp}/R_{exp})^2$$

Where N is the total number of observations, P is the number of parameters refined and C is the number of constraints used in the refinement.

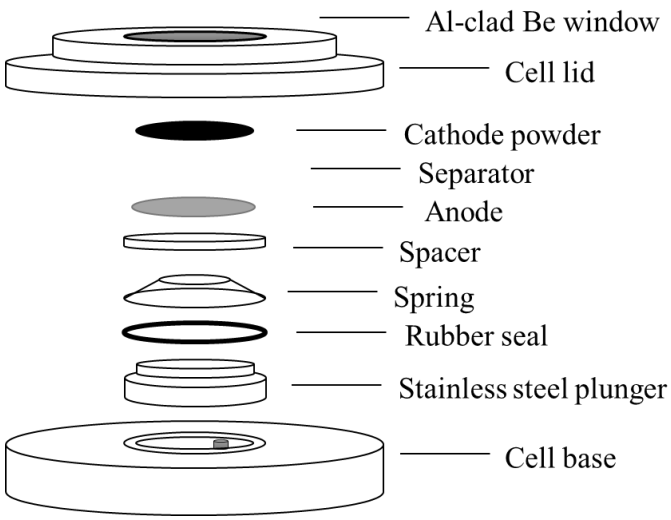

Figure 2.10: Representation of the *in-operando* cell used for diffraction experiments carried out on Rigaku 9kW and 3kW diffractometers. The cell was provided by Rigaku.

2.5.3 Electrochemical Cells for Operando Diffraction Measurements

Operando XRD measurements were carried out using a laboratory X-ray source. These experiments provide an in-depth understanding of the structural changes which occur during charge and discharge in cathode materials. For laboratory-based *in operando* XRD measurements, the cell, provided by Rigaku, is designed to be used in reflection mode, with a Be window facing the cathode material (Figure 2.10). Be metal is one of the few materials that can be used for this purpose as it is mostly transparent to X-rays while also being electrically conductive to be used as a current collector.

2.5.5 Annular Dark Field Scanning Transmission Electron Microscopy

While scanning electron microscopy allows nanoscale resolution, Scanning Transmission Electron Microscopy (STEM) is able to produce angstrom-resolved images using a highly focused beam of electrons which passes through the sample into a detector placed behind the sample grid.[38] Annular Dark Field STEM (ADF-STEM) is an extension of STEM imaging which uses an annular detector to measure the electrons scattered by atoms in the sample as the beam is rastered over them, rather than simply measuring the

intensity variation of the transmitted beam. As a result, atoms in the sample will appear as bright contrast. Scattering in ADF-STEM imaging is typically only well resolved when atomic columns align along the path of the beam, enabling a large number of scatterers to give a clear image. They must also be strong electron scatterers. In contrast to optical microscopes, electron microscopes are not limited in resolution by the wavelength of the electron beam. Instead, aberrations from the optical set-up of the microscope cause blurring and image distortion which limits the resolution of the image. However, sub-angstrom resolution imaging has been made possible by the addition of aberration-correctors to the microscope column.[39] To prepare samples for analysis, first the powder being imaged must be dispersed by sonication in a solvent. The suspension is then drop cast onto a conductive carbon grid, before drying under vacuum to remove the solvent. This leaves individual particles suspended on the mesh. To ensure that high quality images can be taken, it is important that the particle size is small enough to allow for transmission of the electron beam through the sample.

2.5.6 Electron Energy Loss Spectroscopy

Electron Energy Loss Spectroscopy (EELS) allows for the energy-resolved measurement of inelastically scattered electrons from a sample during a STEM experiment.[40] A sample is placed under a beam of electrons, causing scattering events of the incident electron beam with electrons in the structure, which triggers a series of electronic transitions. Each transition is unique to each of the elements in the material, giving rise to characteristic absorption edges which can be seen in the intensity profile of the scattered electrons. The absorption edges seen in EELS are analogous to those seen in XAS and thus can be used to identify the elements present, their relative concentrations and oxidation states from the sample. Due to STEM being a spatially-resolved technique, EELS can be carried out on a local scale, allowing for spatial mapping and line-scan measurements to be done.

2.6 References

1. Smart, L. E. & Moore, E. A. *Solid State Chemistry, 3rd*. *Solid State Chemistry, 3rd* (2005).
2. Du, K. *et al.* Exploring reversible oxidation of oxygen in a manganese oxide. *Energy Environ. Sci.* **9**, 2575–2577 (2016).
3. Luo, K. *et al.* One-Pot Synthesis of Lithium-Rich Cathode Material with Hierarchical Morphology. *Nano Lett.* **16**, 7503–7508 (2016).
4. Li, S. *et al.* Improved electrochemical performance of $Li_{1.2}Mn_{0.54}Ni_{0.13}Co_{0.13}O_2$ cathode material synthesized by citric acid assisted sol-gel method for lithium ion batteries. *AIP Conf. Proc.* **1944**, 1–5 (2018).
5. Liang, L. *et al.* Co-precipitation synthesis of $Ni_{0.6}Co_{0.2}Mn_{0.2}(OH)_2$ precursor and characterization of $LiNi_{0.6}Co_{0.2}Mn_{0.2}O_2$ cathode material for secondary lithium batteries. *Electrochim. Acta* **130**, 82–89 (2014).
6. Li, J. *et al.* Comparison of Single Crystal and Polycrystalline $LiNi_{0.5}Mn_{0.3}Co_{0.2}O_2$ Positive Electrode Materials for High Voltage Li-Ion Cells . *J. Electrochem. Soc.* **164**, A1534–A1544 (2017).
7. Boss, C. B. & Fredeen, K. J. Concepts, Instrumentation and techniques in ICP-OES. *PerkinElmer* 2–11 (2004).
8. Scott, R. H., Fassel, V. A., Kniseley, R. N. & Nixon, D. E. Inductively Coupled Plasma-Optical Emission Analytical Spectrometry: A Compact Facility for Trace Analysis of Solutions. *Anal. Chem.* **46**, 75–80 (1974).
9. Bottom, R. Thermogravimetric Analysis. *Princ. Appl. Therm. Anal.* **1**, 87–118 (1963).
10. Lipson, S. G., Lipson, H. & Tannhauser, D. S. *Optical Physics*. *Optical Physics* (1995). doi:10.1017/cbo9781139170413.
11. Goldstein, J. I. *et al. Microscopy and X-Ray Microanalysis*.
12. Newbury, D. E. & Ritchie, N. W. M. Is scanning electron microscopy/energy dispersive X-ray spectrometry (SEM/EDS) quantitative? *Scanning* **35**, 141–168 (2013).
13. Murray, V., Hall, D. S. & Dahn, J. R. A Guide to Full Coin Cell Making for Academic Researchers. *J. Electrochem. Soc.* **166**, A329–A333 (2019).
14. Lewandowski, C. M., Co-investigator, N. & Lewandowski, C. M. *Lindens Handbook of Batteries 4th Edition*. *The effects of brief mindfulness intervention on acute pain experience: An examination of individual difference* (2015). doi: 10.1017/CBO9781107415324.004.
15. Lin, F. *et al.* Synchrotron X-ray Analytical Techniques for Studying Materials Electrochemistry in Rechargeable Batteries. *Chem. Rev.* **117**, 13123–13186 (2017).
16. McCleverty, J. A. & Meyer, T. J. *Comprehensive Coordination Chemistry II*. *Comprehensive Coordination Chemistry II* (2004). doi:10.1016/C2009-1-28216-5.
17. Zschornack, G. *Handbook of X-ray data*. *Handbook of X-Ray Data* (2007). doi:10.1007/978-3-540-28619-6.

18. Ravel, B. & Newville, M. ATHENA, ARTEMIS, HEPHAESTUS: Data analysis for X-ray absorption spectroscopy using IFEFFIT. *J. Synchrotron Radiat.* **12**, 537–541 (2005).

19. de Groot, F. M. F., Fuggle, J. C., Thole, B. T. & Sawatzky, G. A. 2p x-ray absorption of 3d transition-metal compounds: An atomic multiplet description including the crystal field. *Phys. Rev. B - Condens. Matter Mater. Phys.* **42**, 5459–5468 (1990).

20. Frati, F., Hunault, M. O. J. Y. & De Groot, F. M. F. Oxygen K-edge X-ray Absorption Spectra. *Chem. Rev.* **120**, 4056–4110 (2020).

21. Okubo, M. & Yamada, A. Molecular Orbital Principles of Oxygen-Redox Battery Electrodes. *ACS Appl. Mater. Interfaces* **9**, 36463–36472 (2017).

22. Dau, H., Liebisch, P. & Haumann, M. X-ray absorption spectroscopy to analyze nuclear geometry and electronic structure of biological metal centers potential and questions examined with special focus on the tetra-nuclear manganese complex of oxygenic photosynthesis. *Anal. Bioanal. Chem.* **376**, 562–583 (2003).

23. Ament, L. J. P., Van Veenendaal, M., Devereaux, T. P., Hill, J. P. & Van Den Brink, J. *Resonant inelastic x-ray scattering studies of elementary excitations*. *Reviews of Modern Physics* vol. 83 (2011).

24. Zhou, K. J. *et al.* I21: an advanced high-resolution resonant inelastic X-ray scattering beamline at Diamond Light Source. *J. Synchrotron Radiat.* **29**, 563–580 (2022).

25. Maitra, U. *et al.* Oxygen redox chemistry without excess alkali-metal ions in $Na_{2/3}[Mg_{0.28}Mn_{0.72}]O_2$. *Nat. Chem.* **10**, 288–295 (2018).

26. Luo, K. *et al.* Charge-compensation in 3d-transition-metal-oxide intercalation cathodes through the generation of localized electron holes on oxygen. *Nat. Chem.* **8**, 684–691 (2016).

27. House, R. A. *et al.* Superstructure control of first-cycle voltage hysteresis in oxygen-redox cathodes. *Nature* **577**, 502–508 (2020).

28. Massiot, D. *et al.* Modelling one- and two-dimensional solid-state NMR spectra. *Magn. Reson. Chem.* **40**, 70–76 (2002).

29. Andrew, E. R. Magic Angle Spinning in Solid State n . m . r . Spectroscopy. *Philos. Trans. R. Soc. London. Ser. A, Math. Phys. Sci.* **299**, 505–520 (1981).

30. Pecher, O., Carretero-Gonzalez, J., Griffith, K. J. & Grey, C. P. Materials' methods: NMR in battery research. *Chem. Mater.* **29**, 213–242 (2017).

31. Suryanarayana, C. & Grant Norton, M. *Xray Diffraction: A Practical Approach*. *Plenum Press* (Plenum Press, 1998). doi:10.1017/CBO9781107415324.004.

32. Bragg, W. H. & Bragg, W. L. The reflection of X-rays by crystals. *Proc. R. Soc. London. Ser. A, Contain. Pap. a Math. Phys. Character* **88**, 428–438 (1913).

33. Karl Cockcroft, J. *et al. Powder Diffraction : Theory and Practice*. (Royal Society of Chemistry, 2008).

34. Kisi, E. H. & Howard, C. J. *Applications of Neutron and Powder Diffraction*. *Oxford Scholarship* (2008). doi:10.1093/acprof.

35. Rietveld, H. M. A profile refinement method for nuclear and magnetic structures. *J. Appl. Crystallogr.* **2**, 65–71 (1969).

36. Toby, B. H. & Von Dreele, R. B. GSAS-II: The genesis of a modern open-source all purpose crystallography software package. *J. Appl. Crystallogr.* **46**, 544–549 (2013).

37. Toby, B. H. R factors in Rietveld analysis: How good is good enough? . *Powder Diffr.* **21**, 67–70 (2006).

38. Pennycook, S. J. & Nellist., P. D. Scanning Transmission Electron Microscopy: imaging and analysis. *Springer* **17**, 1022 (2011).

39. Nellist, P. D. *et al.* Direct sub-angstrom imaging of a crystal lattice. *Science (80-.).* **305**, 1741 (2004).

40. Egerton, R. F. Electron Energy Loss Spectroscopy in the Electron Microscope (Plenum Press, 1986). *MRS Bull.* **12**, 56 (1987).

Chapter 3
Investigating Voltage Fade in Li-rich Layered Oxides

Table of Contents

3.1 Introduction 71
3.2 Experimental 73
3.3 Results and Discussion 76
3.3.1 Structural Characterisation 76
3.3.2 Electrochemical Characterisation 80
3.3.3 Low Temperature Annealing of $Li_{1.2}Ni_{0.13}Co_{0.13}Mn_{0.54}O_2$ 84
3.3.4 The Origin of Voltage Fade in Li-rich Cathode Materials 88
3.4 Conclusion 101
3.5 References 103

3.1 Introduction

As stated in the introduction to this thesis, Li-rich cathodes supported by the participation of both TM redox and O-redox can deliver higher capacities than stoichiometric cathodes.[1–5] The presence of a high-voltage plateau (indicative of a two-phase reaction) on charge makes this class of materials very attractive for commercial purposes, as it allows for a significant amount of capacity (~200 mAh g^{-1}) to be delivered above 4.5 V vs Li^+/Li. However, the plateau is not reversible on discharge, instead showing an S-like discharge profile with a large hysteresis.

The loss of the high voltage plateau after the first charge is a characteristic electrochemical signature of layered Li-rich cathodes. As the material is de-lithiated, Li in the TM layer is extracted to leave behind a vacancy. Oxidation of the oxide sublattice is

followed by the in-plane migration of TM cations which leads to the formation of molecular O_2 trapped in vacancy clusters. This irreversible structural re-arrangement means the high-voltage plateau is lost on discharge and, instead, follows an S-shaped discharge curve. This has been shown to occur across a wide range of O-redox compounds, including $Li_{1.2}Ni_{0.13}Co_{0.13}Mn_{0.54}O_2$ (LNCMO).[6–8]

The first part of this chapter contains a study investigating the link between superstructure and the high-voltage plateau in the first cycle load curve. Structural analysis of LNCMO shows that the high voltage plateau is reliant on the presence of a superstructure, reflecting similar claims made by House et al.[8] For this study, a sol-gel synthesised LNCMO was chosen due to the ease of the synthesis procedure.

Voltage fade, where the average discharge voltage of the cell gradually diminishes over cycling, is another issue which is not well understood in Li-rich layered oxides. This continuous loss of energy density over cycling represents a big disadvantage for commercialisation of these materials. While previous studies have focused on the evolving nature of the TM redox couples involved in charge compensation of Li-rich cathode materials,[9] the influence of the O^{2-}/O_2 redox couple on the discharge voltage remains unclear.

In the second part of this chapter, the changing nature of the O^{2-}/O_2 redox process during cycling is investigated in order to establish its role in voltage fade. A thorough study of the 2nd and 100th cycles of LNCMO was undertaken with high resolution RIXS and ^{17}O NMR being used to probe the O^{2-}/O_2 redox couple. Due to the commercial relevancy of this project, co-precipitation synthesised LNCMO was used, to simulate a material prepared for commercial purposes. This study unveils a continuous loss of O-redox activity over cycling which is linked to a continuous loss of O_2 from the bulk of the material.

3.2 Experimental

Sol-gel synthesis: $Li_{1.2}Ni_{0.13}Co_{0.13}Mn_{0.54}O_2$ was synthesised using a Resorcinol Formaldehyde sol-gel synthesis.[10] A metal solution was prepared by dissolving stoichiometric amounts of $LiCH_3COO{\cdot}2H_2O$ (99.0%, Sigma), $Ni(CH_3COO)_2{\cdot}4H_2O$ (99.0%, Sigma), $Co(CH_3COO)_2{\cdot}4H_2O$ (99.0%, Sigma) and $Mn(CH_3COO)_2{\cdot}4H_2O$ (99.0%, Fluka) in 50 mL of distilled water. A gel solution was prepared by dissolving resorcinol (99.0%, Fluka) in formaldehyde (Fluka 36.5% in water, methanol-stabilized) in a molar ratio of (1:1.5). Li_2CO_3 (99.0%, Fluka) was then added to this solution in a 5 mol % excess of Li. The molar ratio between metals and the gel was (1:6). The metal and gel solutions were then added together and stirred in an oil bath at 80 ^oC to form a solid gel. The mixture was dried at 90 °C for 8 hrs then heated to 475 ^oC for 15 hrs with slow heating to remove the organic matter. This mixture was left to cool, re-ground, then calcined as a loose power at 900 °C for 15 hr under air to obtain the final material.

Co-precipitation synthesis: A $Ni_{0.163}Mn_{0.675}Co_{0.163}CO_3$ precursor were prepared by co-precipitation route. $NiNO_3{\cdot}6H_2O$ (⩾98%, Sigma), $MnNO_3{\cdot}4H_2O$ (⩾99%, Sigma) and $CoNO_3{\cdot}6H_2O$ (⩾99%, Sigma) were dissolved in deionized H_2O with a molar ratio of 0.13:0.54:0.13 to prepare a 1.5M solution. In addition, a 1.5 M solution of Na_2CO_3 (≥99.5%, ACS reagent, Sigma) was prepared. The solutions were added dropwise into a beaker under continuous stirring at a temperature of 40 ^0C and pH = 7.8. After addition of the TM solution, the beaker was left covered overnight under stirring. The resulting carbonate mix was washed with deionized H_2O, filtered, and dried at 120 °C overnight. The dried carbonate precursor was then mixed with Li_2CO_3 (≥99%, ACS reagent, Sigma) using a mole ratio of (1:1.5) and calcined at 900 °C for 15 hrs under O_2 flow to obtain the desired compound. ^{17}O-labelled samples were prepared the same way except the final calcination step was performed under a sealed O_2 atmosphere (CortecNet >70 atom% ^{17}O) by Dr. Robert House.

Cathode annealing procedure: Cycled cathodes were first washed after disassembly from cells. Each cathode was then placed in a split tube and heated under an Argon atmosphere for 1hr at the desired temperature (150 ^{o}C to 310 ^{o}C). The split tube was then transferred to a glove box to recover the sample.

Electrochemical characterization: Electrodes were prepared by combining the active material (80wt%), Super P carbon (10wt%) and polytetrafluoroethylene (PTFE) binder (10wt%) using a mortar and pestle. The mixture was then rolled to a thickness of about 100μm to form self-supporting films. Electrodes were assembled into coin cells using Whatman glass fibre separators and 1M $LiPF_6$ in ethylene carbonate / dimethyl carbonate 50:50 (battery grade, Sigma) electrolyte, with a Li metal counter electrode. Galvanostatic cycle testing was carried out using Maccor Series 4000. The cells and electrodes were prepared and assembled/disassembled in the glove box under an inert atmosphere.

OEMS: Carried out by flowing Ar carrier gas through an ECC-std electrochemical cell (EL-CELL) with gas inlet and outlet ports and into a BT Prima mass spectrometer (Thermo Fischer). The cathode material was cycled vs a Li metal counter electrode and an electrolyte of 1 M LiPF6 in propylene carbonate (Merck).

SEM / EDX: SEM imaging and EDX analysis was performed on a Carl Zeiss Merlin high resolution field emission gun SEM instrument by Jennifer Holter and Dr. Dominic Spencer-Jolly.

TGA: TGA measurements were performed on a Netzsch Jupiter STA 449 F3 thermogravimetric analysis instrument, installed in-house.

ICP-OES: Analysis on the sol-gel synthesised material was done in-house. The pristine cathode material was dissolved in aqua regia ($HCl:HNO_3$ / 25:75 (v/v%)), before diluting the solution for measurement. A calibration curve was created using standard solutions. Elemental analysis was carried out using a Perkin-Elmer Optima 7300DV ICP-

OES. Due to an issue with the ICP-OES instrument at the time, the co-precipitation synthesised sample was sealed in a vial and sent to the Yusuf Hamied Department of Chemistry at the University of Cambridge for analysis.

PXRD: Diffraction data for the sol-gel synthesised samples were collected at the I11 beamline at the Diamond Light Source using monochromated X-ray radiation of wavelength $\lambda = 0.82660$ Å. Diffraction data for the co-precipitation synthesised samples were collected on a Rigaku 9 kW SmartLab Cu-source diffractometer equipped with a Hypix 2D detector. GSAS-II was used to conduct Rietveld refinements against the collected data.[11,12] X-ray diffraction data of cycled electrodes was performed using a 600 W Rigaku MiniFlex x-ray diffractometer, fitted with an un-monochromated Cu K_α radiation source using parallel beam geometry, contained in a N_2-filled glovebox. A Ni filter was used to remove K_β radiation.

ADF - STEM: ADF-STEM micrographs were measured by Dr. Alex Robertson using an aberration-corrected JEOL ARM 200F microscope operated at 200 kV. A convergence semi-angle of 22 mrad was used, with a collection semi-angle of 69.6–164.8 mrad (ADF). Sets of fast-acquisition multiframe images were taken and corrected for drift and scan distortions using SmartAlign43. To avoid the exposure to air, sample transfer to the STEM microscope was carried out with a vacuum transfer suitcase.

RIXS: High resolution RIXS data were collected using the I21 beamline at Diamond Light Source. To produce the data sets for the quantitative analysis, scans at 531 eV were recorded at fifteen different sample locations and averaged together, with little inhomogeneity in the signal observed.

Solid-state ^{17}O and ^{6}Li MAS NMR: All ^{6}Li and ^{17}O MAS ($\upsilon_R = 37037$ Hz) solid state NMR data were collected and processed by Dr. Gregory Rees. The MAS NMR was completed at 9.45 T ($\upsilon_0{}^{6}$Li = 58.92 MHz, $\upsilon_0{}^{17}$O = 54.25 MHz) using a Bruker Avance III HD spectrometer and a 1.9 mm double air bearing MAS probe. All ^{6}Li and ^{17}O spectra are

referenced to 1 M $^{6}LiCl_{(aq)}$ and $H_2{}^{17}O$, respectively, at 0 ppm. All spectra were recorded using a Hahnecho ($^{\pi}/_{2}$-τ-π-τ) sequence, where τ is $1/\upsilon_R$ and $^{\pi}/_{2}$ is 250 kHz, the resultant FID is processed as a half echo. The ^{6}Li spectra were achieved with a recycle delay of 300 ms. The ^{17}O NMR spectra were completed with relaxation times of 2 ms (fast relaxation) and 100 ms (slow relaxation).

^{129}Xe Static NMR: All ^{129}Xe NMR data were collected and processed by Dr. Gregory Rees. A J-Young NMR tube containing the LNCMO cathode, transferred in argon, was evacuated and filled with natural abundance xenon gas (BOC, UK) at 1 atm of pressure. The ^{129}Xe nuclear magnetic resonance (NMR, 298.1 K, 1 atm) spectrum were completed at 9.45 T (υ_0 = 110.69 MHz) using a 5 mm solution-state NMR probe at a controlled temperature of 298.1 K. A 25 kHz pulse was utilized for all experiments with a recycle delay of 0.5 seconds. All shifts are referenced to natural abundance Xe (gas, 1 atmosphere and 298.1 K) at 0 ppm.

3.3 Results and Discussion

3.3.1 Structural Characterisation

LNCMO was synthesised by sol-gel and co-precipitation methods. The crystal structure of the $R\bar{3}m$ space group is depicted in Figure 3.3. The material is *O*3-type, showing an alternating *abc abc* oxygen stacking sequence, with alternating transition metal (TM) and alkali metal (AM) layers, with additional Li^+ in the TM layer. Both the co-precipitation material (Figure 3.2, Table A3.1) and the sol-gel material (Figure 3.3, Table A3.2) were analysed using powder x-ray diffraction (PXRD). When carrying out the refinement, the total Li and Ni fractions were constrained to equal 1.2 and 0.13 respectively, while the fraction of atoms on the alkali metal layer sites (3*b*) were constrained to 1. X-rays cannot distinguish which TM ion(s) sit in the Li layer, so Ni was used as a proxy. U_{iso} values were constrained to be equivalent for each atomic site. Due to the charge repulsions between Mn^{4+}

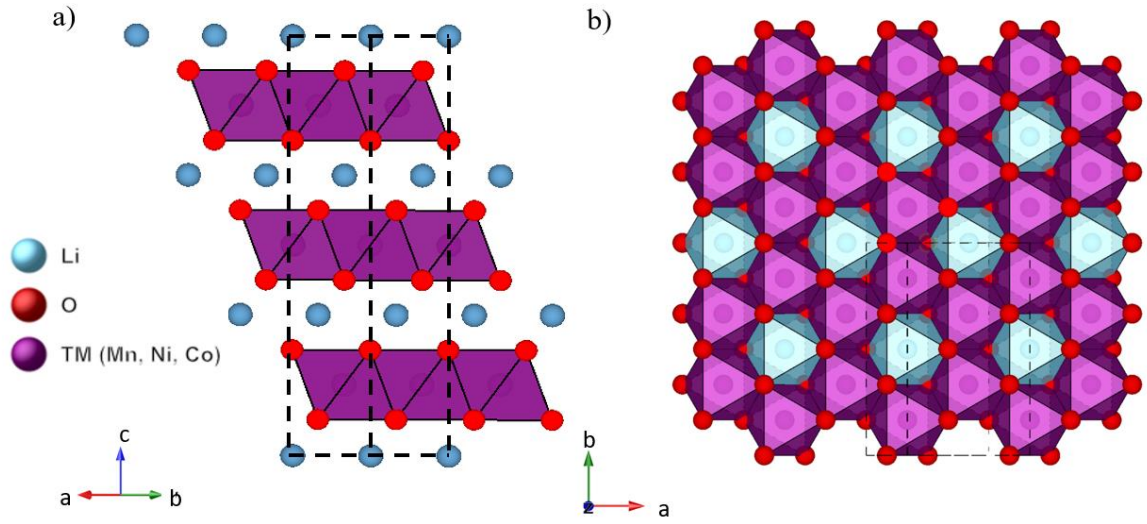

Figure 3.1: The structure of $Li_{1.2}Ni_{0.13}Co_{0.13}Mn_{0.54}O_2$. a) *O*3-type structure with an oxygen stacking sequence of *abc abc* and alternating octahedral TM and AM layers. b) Representation of the honeycomb ordering which occurs between TM and Li-ions in the TM layer.

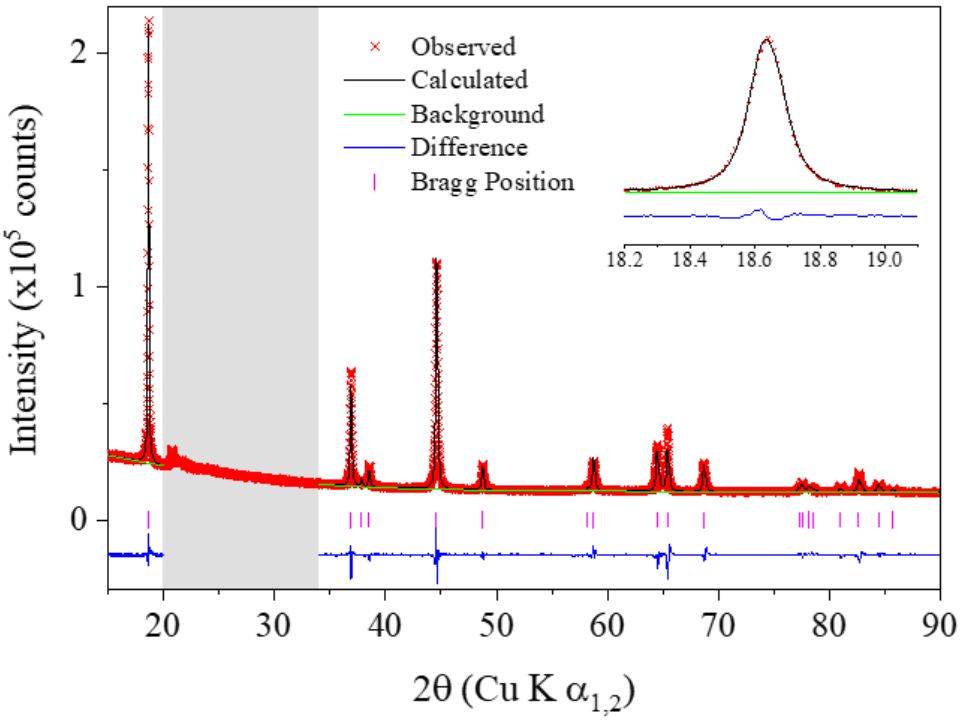

Figure 3.2: Rietveld refinement of co-precipitation synthesised LNCMO. The diffraction data were collected using an un-monochromated Cu *Kα* X-ray source. Inset shows the fitting of the 003 reflection. The greyed-out area shows the region of the superstructure peaks which have not been included in the refinement.

and Li^+, LNCMO displays a honeycomb arrangement of the TM and Li ions within the TM layer, giving rise to a set of superstructure peaks. These peaks are not well defined due to the presence of stacking faults within the structure, causing asymmetric peak shapes in the diffraction pattern. Such peak shapes cannot be refined when using the GSAS-II software.

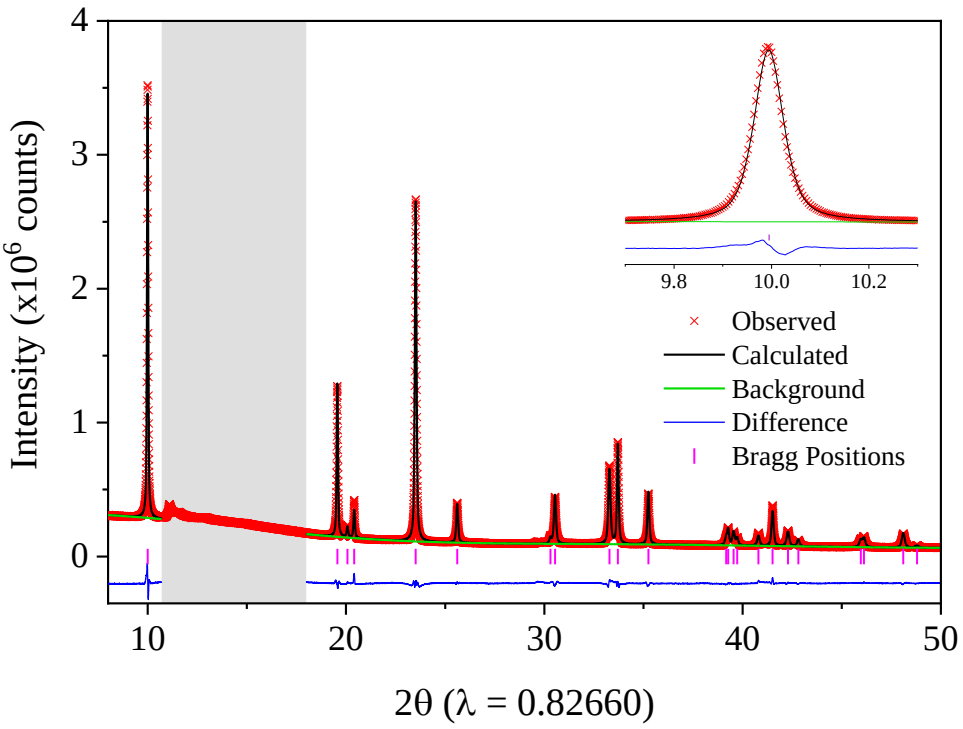

Figure 3.3: Rietveld refinement of sol-gel synthesised LNCMO. The diffraction data were collected at I11 beamline at the Diamond Light Source using monochromated X-ray radiation of wavelength λ = 0.82660 Å. Inset shows the fitting of the 003 reflection. The greyed-out area shows the region of the superstructure peaks which have not been included in the refinement.

Therefore, the superstructure peaks were left out of the refinement and the structure was fitted to the $R\bar{3}m$ space group (Figure 3.1). The superstructure peaks can be seen in the greyed-out areas of the plots. From the refinement parameters, both synthesis routes yield materials with similar unit cell sizes: the *a* lattice parameters are very close, while the co-precipitation material shows a slightly larger *c* lattice parameter, which could be due to the Li deficiency of the sample. Both materials also show similar amounts of anti-site disorder in the material (<1%). The R_{exp} value for the sol-gel material is much smaller as the sample was measured using synchrotron radiation.

Scanning Electron Microscopy (SEM) images were collected to further study the structure and morphology of the two synthesis methods of LNCMO. Energy Dispersive X-ray analysis (EDX) was also used to study the elemental homogeneity of the two synthesis methods. The images for both synthesis procedures are shown in Figure 3.4.

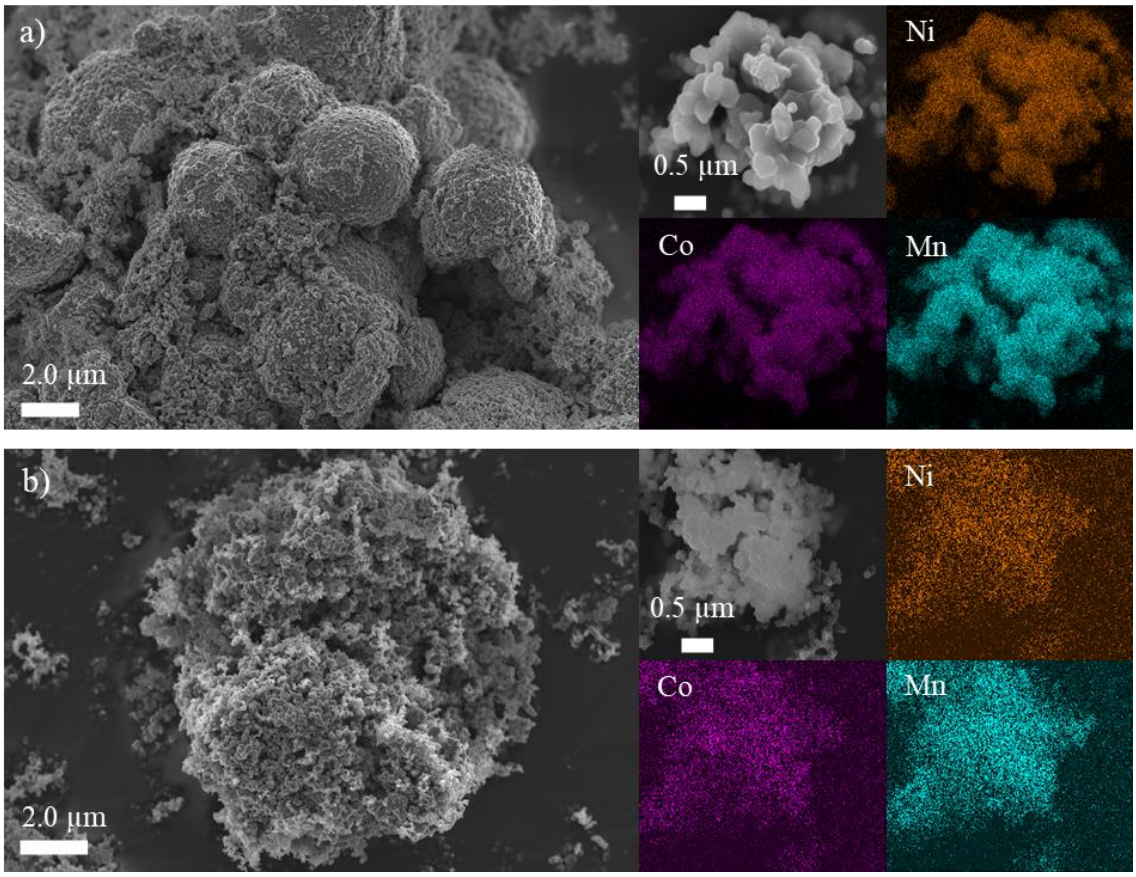

Figure 3.4: SEM images and EDX analysis of pristine LNCMO, a) synthesised by co-precipitation method. Spherical secondary particles are seen, with a diameter of 3-4 µm. Primary particles are around 500nm in size, with a homogenous elemental distribution seen throughout. b) synthesised by sol-gel method. No secondary particle structure is seen. Primary particles are seen to be less than 500nm in diameter. A homogenous elemental distribution is seen throughout.

The co-precipitation synthesis yields spherical secondary particles of 3-4 µm in diameter, with a primary particle size of 0.5 µm. The spherical morphology is produced during the co-precipitation step of the precursors.[13] Elemental distribution is seen to be homogenous throughout. The sol-gel synthesis yields a much smaller particle size, with primary particles being less than 500 nm in diameter. The particles are seen to agglomerate in large masses ~5 µm in size, with a rough, irregular morphology. Again, the elemental distribution from EDX analysis is homogenous throughout.

Elemental analysis of the samples was carried out by Inductively Coupled Plasma Optical Emission Spectroscopy (ICP-OES). The ICP measurements for the sol-gel synthesised material were done in-house, while the measurements for the co-precipitation

Synthesis route	Element	Li	Mn	Co	Ni
Co-precipitation	Concentration (ppm)	0.751	2.799	0.762	0.736
	Normalized Composition	1.133	0.533	0.135	0.132
Sol Gel	Concentration (ppm)	0.48 (4)	1.81 (2)	0.47 (1)	0.45 (2)
	Normalized Composition	1.147 ± 0.039	0.543 ± 0.009	0.127 ± 0.002	0.130 ± 0.007

Table 3.1: Elemental composition of LNCMO synthesised by co-precipitation and sol-gel methods as measured by ICP-OES. The elemental concentration can be seen for each synthesis method, as well as the normalized composition.

material were done by an external company (errors for the measurement were not provided). The results are shown in Table 3.1. The final measurements show that each synthesis method yields samples which are slightly Li deficient (~5%). This is due to Li evaporation during the synthesis. However, the TM ratios are aligned with the synthesised composition.

3.3.2 Electrochemical Characterisation

The electrochemical behaviour of LNCMO was studied using galvanostatic cycling in a half cell set up vs a Li metal anode. A voltage window of 2.0 V to 4.8 V was used, with a rate of 100 mA g^{-1}. No formation cycles were used. Figure 3.5 shows the electrochemical analysis of the co-precipitation synthesised sample. The first cycle shows a sloping region from 3.5 V to 4.5 V where charge compensation has been attributed to TM redox,[9] accounting for 0.39 mol of Li de-intercalation. Following the TM redox, the load curve shows a flat plateau between 4.5 V and 4.6 V, accounting for ~0.6 mol of Li de-intercalation. Charge compensation in this region is from O-redox.[7] On discharge, the plateau is no longer seen, with a large voltage hysteresis of ~600 mV being observed instead along an S-shaped load curve, completing a first cycle coulombic efficiency of 88%. On subsequent charge-discharge cycles, the S-shaped load curve remains. By the 60th cycle, there is a significant

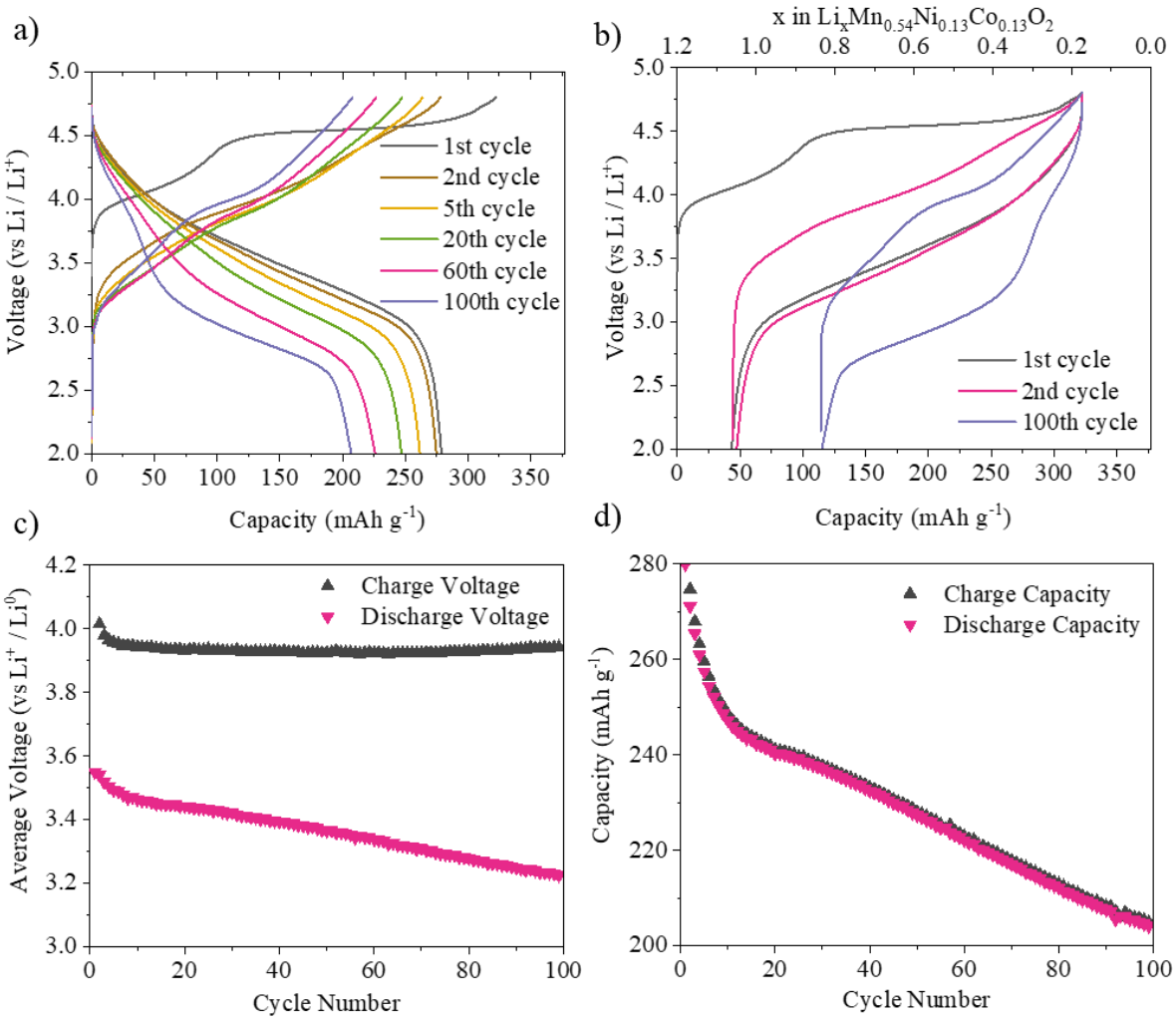

Figure 3.5: Electrochemical analysis of co-precipitation synthesised LNCMO. a) Load curve of the 1st, 2nd, 5th, 20th, 60th and 100th cycle. The cell was cycled between 2.0 V and 4.8 V with a current density of 100 mA g^{-1}. b) Cyclical load curve of the 1st, 2nd and 100th cycle, highlighting the hysteresis observed over cycling. c) Average charge and discharge voltage over 100 cycles. d) Average charge and discharge capacity observed over 100 cycles.

loss (~0.25 V) of voltage on discharge. This is more visible on the 100th cycle where a clear 'voltage-step' can be seen on the discharge: the electrochemical signature of the voltage fade phenomenon. The average voltage and capacity of cycling are also shown. This further highlights the loss of discharge voltage and capacity fade of the material which, altogether produces a lower energy density.

In Figure 3.6 the load curve of the sol-gel synthesised sample is shown. The first cycle load curve is identical to the co-precipitation sample, with a long oxygen redox plateau observed on the first cycle as well as the loss of the plateau and large hysteresis seen on the

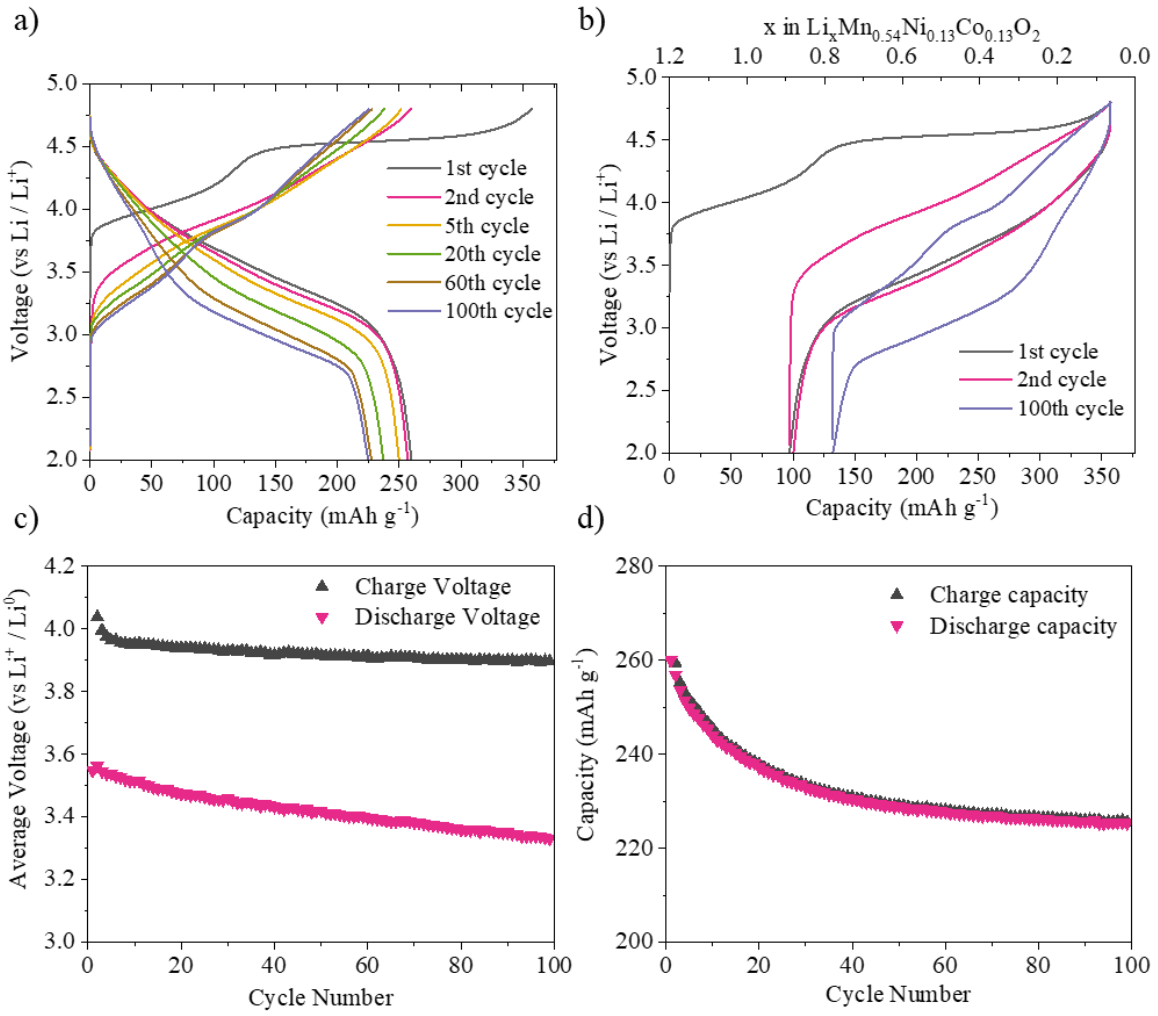

Figure 3.6: Electrochemical analysis of sol-gel synthesised LNCMO. a) Load curve of the 1st, 2nd, 5th, 20th, 60th and 100th cycle. The cell was cycled between 2.0 V and 4.8 V with a current density of 100 mA g^{-1}. b) Cyclical load curve of the 1st, 2nd and 100th cycle, highlighting the hysteresis observed over cycling. c) Average charge and discharge voltage over 100 cycles. d) Average charge and discharge capacity observed over 100 cycles.

first discharge. The first cycle coulombic efficiency of the sol-gel synthesise sample is much lower at ~74%. Subsequent cycles also show a loss in voltage during discharge and capacity loss as well. While the average voltage drops at a similar rate to the co-precipitation material, the sol-gel material shows better capacity retention after 100 cycles (220 mAh g^{-1} compared to 200 mAh g^{-1} after 100 cycles). To try and understand this difference in cycling behaviour, OEMS was used to track gas loss from the cathode over the first charge.

For the co-precipitation synthesised material, the cathode was charged at a rate of 20 mA g^{-1} within a voltage window of 2.0 V to 4.8 V vs Li^+/Li. The rate of gas flow passing

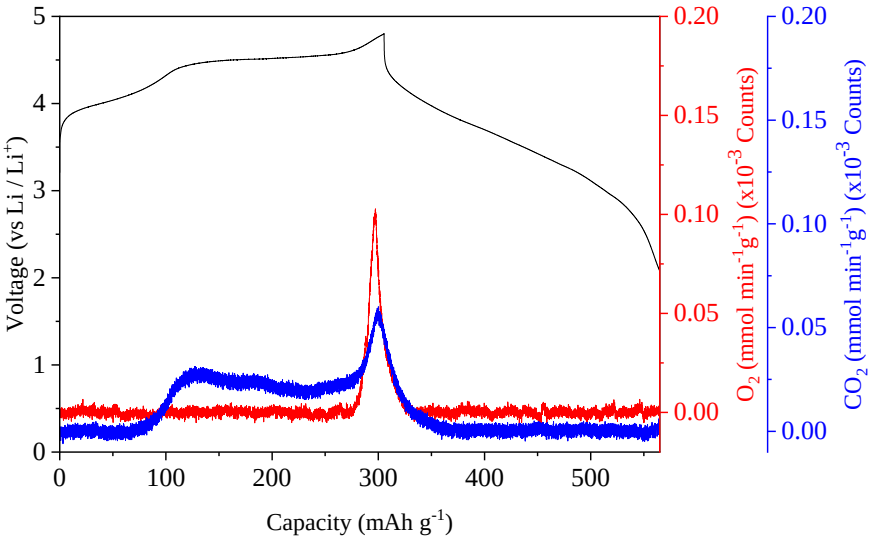

Figure 3.7: OEMS analysis of co-precipitation synthesised LNCMO. O_2 (m/z = 32) and CO_2 (m/z = 44) were monitored during the experiment. The data was collected by Dr. Robert House.

through the cell was kept constant at 1.0 ml min^{-1} for the duration of the experiment (Figure 3.7). Following the load curve on charge, CO_2 evolution begins just before the start of the plateau on charge, with the evolution continuing for the during of the high-voltage plateau. This preliminary gas loss is linked due to electrolyte degradation on charge.[14,15] As the load curve reaches 4.6 V, CO_2 evolution is shown to increase again, coinciding with O_2 evolution from the cathode.[14,15] In the co-precipitation synthesised sample, 0.006 mol of O_2 gas per mol of cathode material was produced during the first charge, with 0.014 mol of CO_2 being produced per mol of cathode material. The data for OEMS experiment of the sol-gel synthesised material is shown in Figure 3.8. In this experiment, the cathode was charged at a rate of 50 mA g^{-1} within a voltage window of 2.0 V to 4.8 V vs Li^+/Li. The rate of gas flow passing through the cell was kept constant at 1.0 ml min^{-1} for the duration of the experiment. The gas evolution follows a comparative trend to the co-precipitation sample. However, a larger amount of O_2 gas is evolved in the first cycle, with a total of 0.031 mol of O_2 gas per mol of cathode material produced during the first charge, and 0.019 mol of CO_2 being produced per mol of cathode material.

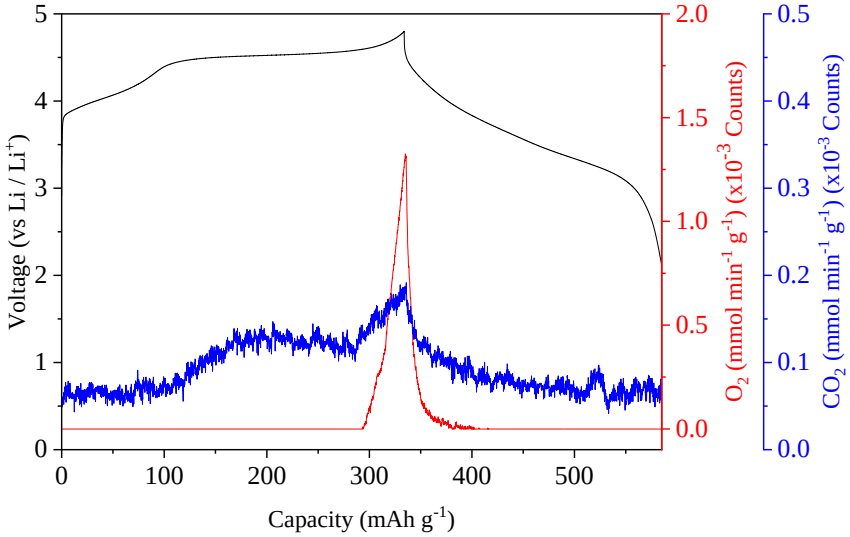

Figure 3.8: OEMS analysis of the sol-gel synthesised LNCMO. O_2 (m/z = 32) and CO_2 (m/z = 44) were monitored during the experiment.

The difference in O_2 evolution from LNCMO synthesised by different methods explains the differences in coulombic efficiency seen on the first cycle between the samples. The small particle size of the sol-gel synthesised sample leads to a larger surface area and increase O_2 loss on the first cycle compared to co-prep. This in turn leads to increased gas evolution on the first cycle, contributing to a smaller first cycle coulombic efficiency.

3.3.3 Low Temperature Annealing of $Li_{1.2}Ni_{0.13}Co_{0.13}Mn_{0.54}O_2$

The loss of the plateau and large hysteresis seen on discharge in this material is caused by the formation of gaseous O_2 through the material on charge, leading to severe structural re-arrangements.[7] Recent work by A. Singer et al reported a facile post-cycling treatment process to re-order a cycled material and re-gain the high voltage plateau over the subsequent charge.[16,17] The simple procedure requires heating the cycled cathode at low temperatures (~300 ^oC) under an argon atmosphere, leading to the material superstructure being re-formed. The study reported that the formation of dislocations within the layered LNCMO material were the cause of the voltage fade seen in these materials. In this work, the heat treatment was studied to investigate the link between the high voltage plateau and the materials superstructure.

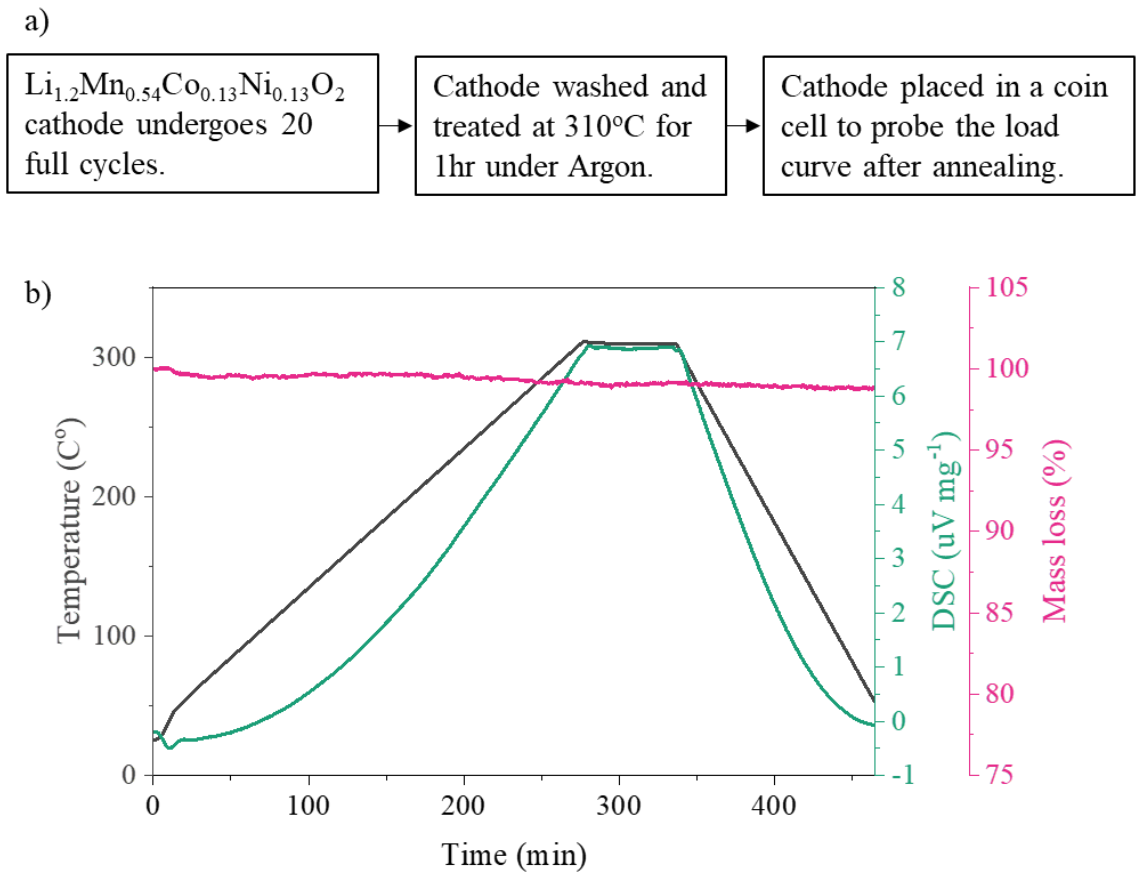

Figure 3.9: Post-cycling heat treatment of LNCMO cathodes. a) A description of the methodology used to heat treat the cathodes. b) TGA analysis of a cycled LNCMO cathode, showing no mass loss when heated to 310 °C.

Heat treatment of cycled $Li_{1.2}Ni_{0.13}Co_{0.13}Mn_{0.54}O_2$

The facile heat treatment on cycled LNCMO cathodes was repeated to find the optimum temperature for the 're-setting' of the honeycomb ordering. The procedure used for the heat treatment is described in Figure 3.9. A screening process was carried out to identify the ideal conditions. Coin cells were cycled 20 times at a rate of 50 mA g^{-1} within a voltage window of 2.0 V to 4.8 V. After cycling, the cells were disassembled, and the electrodes washed. The temperature for the annealing process was then probed, starting at 150 °C and increasing in 20 °C steps until 310 °C. An upper limit of 310 °C was set, as the melting point of the PTFE binder is 326 °C.[18] After annealing, PXRD was used to investigate the return of the material superstructure as well as each electrode being put in a cell to probe the return of the high voltage plateau. These results will be discussed in the

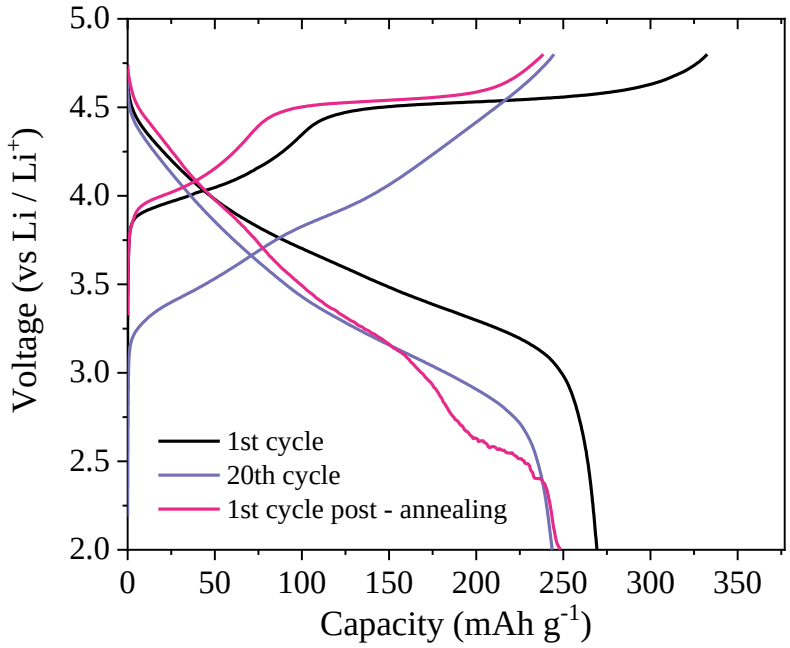

Figure 3.10: Load curve of the 1st cycle, 20th cycle, and 1st cycle after annealing of sol-gel synthesised LNCMO. The cell was cycled between 2.0 V and 4.8 V with a current density of 50mA g^{-1}.

following sections. The optimum temperature for this procedure was identified as 310°C and this temperature was used for the remainder of the study. Thermogravimetric Analysis (TGA) was carried out on the cathode to confirm that heating the sample to this temperature would not induce decomposition of the cathode film (Figure 3.9). The material was heated to 310 °C over a period of 4 hrs, then held at temperature for 1 hr, before being left to cool naturally. No discernible mass loss was observed during the experiment, confirming the stability of the cathode at those temperatures.

Electrochemical Analysis of Heat Treated $Li_{1.2}Ni_{0.13}Co_{0.13}Mn_{0.54}O_2$

The cycling behaviour of the annealed cathode was investigated to confirm the reappearance of the plateau (Figure 3.10). Using the annealing method described above, cycled cathodes were treated then placed into coin cells and cycled at 50 mA g^{-1} within a voltage window of 2.0 V and 4.8 V. After annealing, the re-appearance of a long flat plateau at 4.5 V is seen on charge, while the discharge shows an S-shaped load curve. The capacity of the cathode has decreased, as the annealing process does not increase the Li content.

Structural Analysis of Heat Treated $Li_{1.2}Ni_{0.13}Co_{0.13}Mn_{0.54}O_2$ and Discussion

To further understand the impact of the annealing on the cathode material, Nuclear Magnetic Resonance (NMR) and PXRD were used to study the pristine material structure, and the material before and after annealing. The results of this are shown in Figure 3.11. ^{6}Li NMR was used to track the changes in the Li environments over the cycling and annealing process. In the pristine material, three distinct Li environments are observed, with clear peaks being observed in the NMR spectrum. Two AM environments are observed due to the ordering of the TM cations which occurs in the TM layer.[14] A third environment corresponding to Li in the TM layer is observed. This peak is shifted to higher ppm from the paramagnetism of the surrounding Mn cations. A full deconvolution of the NMR spectrum for pristine LNCMO in the appendices (Figure A3.1). Comparing the NMR spectra for the pristine and the 20th cycle, the sharp peaks observed in the pristine material are replaced by a single broad peak, indicative of indistinguishable Li environments and an increase of disorder in the material. This is accompanied by a loss of the superstructure in the PXRD. When comparing the 20th cycle to the annealed material, the two distinct Li environments are observed once more, indicating that Li order has been re-established within the material. This is also seen in the PXRD, where the superstructure peaks observed ~21° - 22° 2θ are shown to re-appear after annealing.

In the original study by A Singer et al.,[16] the appearance of structural defects over cycling was observed using Bragg coherent diffractive imaging. The appearance of dislocations in the layer ordering during cycling suggested a link between defects and the voltage fade observed over cycling in LNCMO. Using the heating treatment described above, the authors show that the average voltage on discharge can be increased after annealing, claiming that this is due to a removal of the dislocations. However, this does not explain why the plateau is returned in the electrochemical load curve after annealing. The

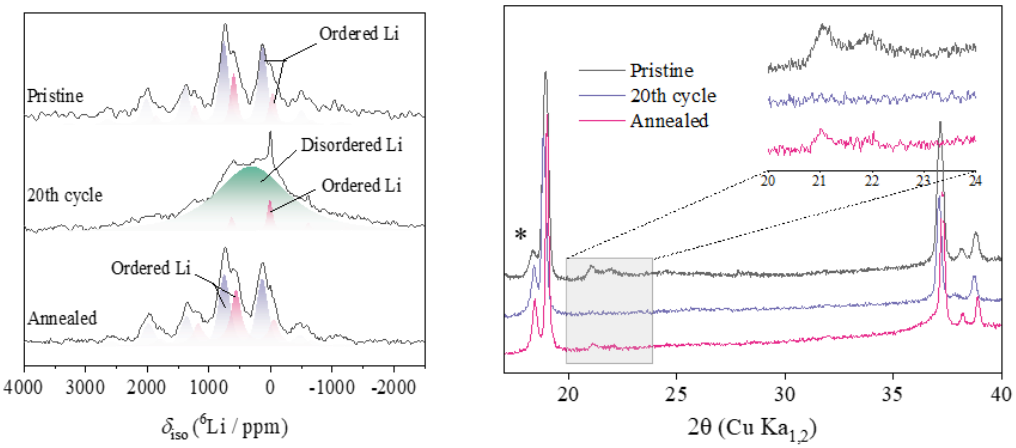

Figure 3.11: ^{6}Li NMR and PXRD analysis on pristine, 20th cycle and annealed cathode films. The NMR results clearly track the disordering and re-ordering of the Li environments in LNCMO after the annealing process. The PXRD results also highlight the reformation of the honeycomb superstructure. * denotes PTFE peak from electrode binder.

link between high voltage O-redox and the superstructure of cathode materials was made by R. House et al. when studying model Na-ion cathode materials.[8] The results presented here agree well with this model which shows the importance of TM superstructure in influencing O-redox behaviour. This further illustrates that this model can also be attributed to Li-rich cathode materials.

3.3.4 The Origin of Voltage Fade in Li-rich Cathode Materials

Despite the potential for increasing the energy density of cathodes that Li-rich layered oxides demonstrate, voltage fade remains a crucial issue to be solved. Previous investigations on voltage fade have revealed large structural changes which occur over cycling, as well as a change in the TM redox couples involved in the charge compensation. However, the shift in oxygen activity over cycling is not well understood and has not been studied directly. The study presented here provides direct insight into the evolution in activity of the O^{2-}/O_2 redox couple over cycling in LNCMO.

Ruling out Kinetic Effects on Voltage Fade in $Li_{1.2}Ni_{0.13}Co_{0.13}Mn_{0.54}O_2$

The samples prepared for the study on voltage fade were all cycled at a rate of 100 mA g^{-1} which corresponds to a C rate of C/3. This rate was used to be able to prepare samples

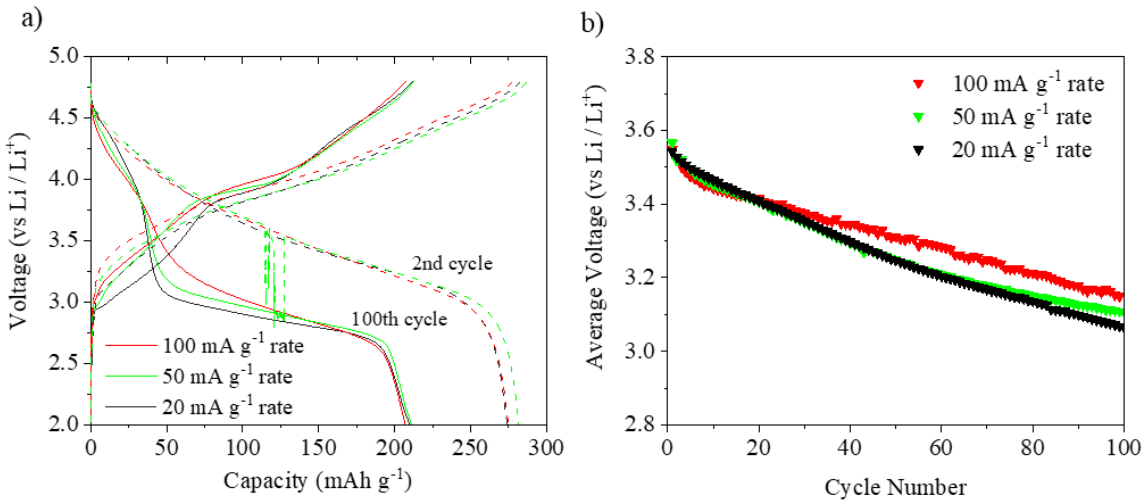

Figure 3.12: Comparison of galvanostatic cycling data for LNMCO cycled at different rates. a) Load curves of the 2nd (dashed) and 100th cycles (solid) of LNMCO cycled at 20 mA g^{-1}, 50 mA g^{-1} and 100 mA g^{-1}. b) Average voltage over cycling for LNCMO cycled at 20 mA g^{-1}, 50 mA g^{-1} and 100 mA g^{-1}.

within a reasonable timeframe (100 cycles at 100 mA g^{-1} for LNCMO takes approximately 3 weeks to complete). However, this high rate of cycling could be considered to influence the degree of voltage fade and capacity fade observed in the material over cycling. To show that the rate of cycling had no bearing on the magnitude of voltage fade observed, LNCMO was cycled at three different rates: 20 mA g^{-1}, 50 mA g^{-1}, and 100 mA g^{-1} (Figure 3.12). When comparing the load curves in Figure 3.12 a, no difference in capacity fade between the three rates of cycling was observed. In addition, all three rates of cycling display a prominent voltage step after 100 cycles. When comparing the average voltage vs cycle number in Figure 3.12 b, all three rates of cycling show a similar rate of voltage fade. To conclude, the data presented here shows that the rate of cycling in LNCMO has no effect on the amount of voltage fade seen after 100 cycles.

Studying the Evolution of the O^{2-}/O_2 Redox Couple

Previous studies on LNCMO using high resolution Resonant Inelastic X-ray Spectroscopy (RIXS) and ^{17}O NMR have shown that molecular O_2 is formed during O^{2-} oxidation in Li-rich cathodes.[7] Quantitative high resolution RIXS at the O K-edge was used

to follow changes in the amount of molecular O_2 formed on cycling. In the high resolution RIXS spectra, two main features can be associated with molecular O_2: an energy loss feature at ~8 eV, and a series of vibrational progression peaks propagating from the elastic RIXS peak at 0 eV. The area under the vibrational progression peaks (from 0.125 eV to 2.2 eV) was integrated to track the relative amount of O_2. This feature was chosen as the peak intensity arises solely from molecular O_2, with no contribution from other oxygen species. This method is described in more detail in the methods chapter.

For this study, eight charge points on the 2nd and 100th cycle load curves for LNCMO were used to track changes over cycling. These were: quarter charge (QC), half charge (HC), three-quarter charge (3QC), full charge (FC), quarter discharge (QD), half discharge (HD), three quarter discharge (3QD) and full discharge (FD) (Figure 3.13 a, d). At each charge point, RIXS scans were taken at multiple sample locations to minimise any effect of sample inhomogeneity. A plot of all the scans taken for the 2nd and 100th full charge samples are shown in the appendices to illustrate this point (Figure A3.2). These scans were then averaged and plotted for both the 2nd and 100th cycles (Figure 3.13 b, d). In both sets of scans, the appearance and disappearance of the vibrational progression peaks arising from O_2 over the full cycle are observed. The integrated signal intensity under the O_2 vibrational progression peaks was then plotted as a function of charge and discharge (Figure 3.13 c, f). Significant differences in oxygen activity over cycling are observed. During the 2nd cycle charging process, signal intensity from O_2 is seen to increase continuously from 2.0V to 4.8V. This behaviour is mirrored in the discharge, with a smooth decrease in intensity of the O_2 signal (Figure 3.13 c). This behaviour is quite different in the 100th cycle, which shows a continuous increase in O_2 on charge. However, on discharge, the reduction of O_2 to O^{2-} occurs between half discharge and full discharge points on the load curve (Figure 3.13 f). The half discharge point is at ~3 V, suggesting that the O^{2-}/O_2 redox couple is mainly active

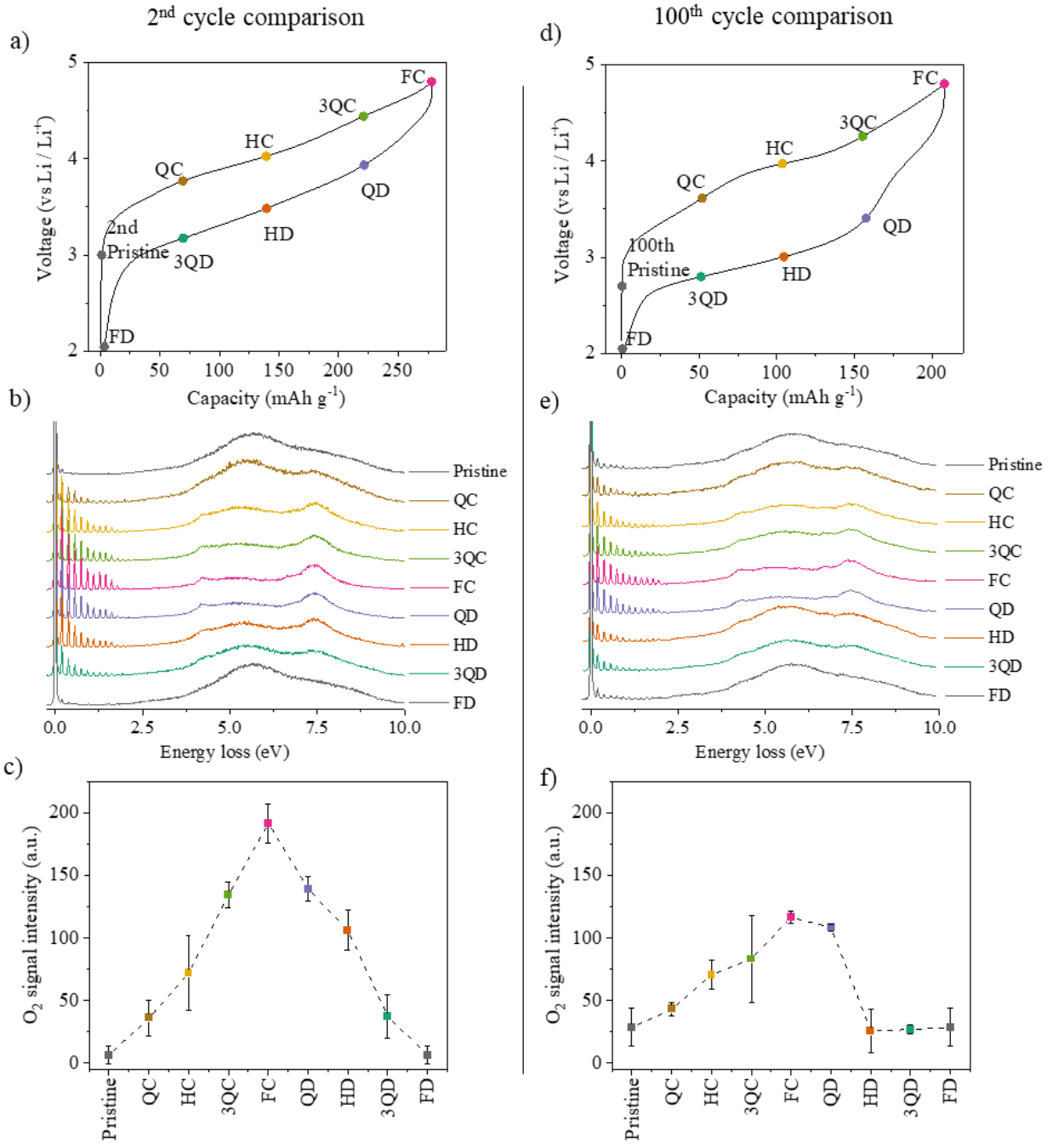

Figure 3.13: Evolution in bulk O-redox activity over cycling. Load curves for the (a) 2nd and (d) 100th cycles for LNCMO, with the states of charge studied. RIXS spectra at 531.5 eV collected over the (b) 2nd and (e) 100th cycles. Variation in intensity of the molecular O_2 signal in the RIXS spectra over the (c) 2nd and (f) 100th cycles (see Methods).

above 3 V on discharge. This leaves the remainder of the discharge capacity to the reduction of the $Ni^{2+/4+}$, $Co^{2+/4+}$ and $Mn^{3+/4+}$ redox couples, as has been observed in previous studies.[9,19] While these data provide a comparison of the 2nd and 100th cycles, they do not give any information about the general trends of O_2 activity over cycling. To investigate this further,

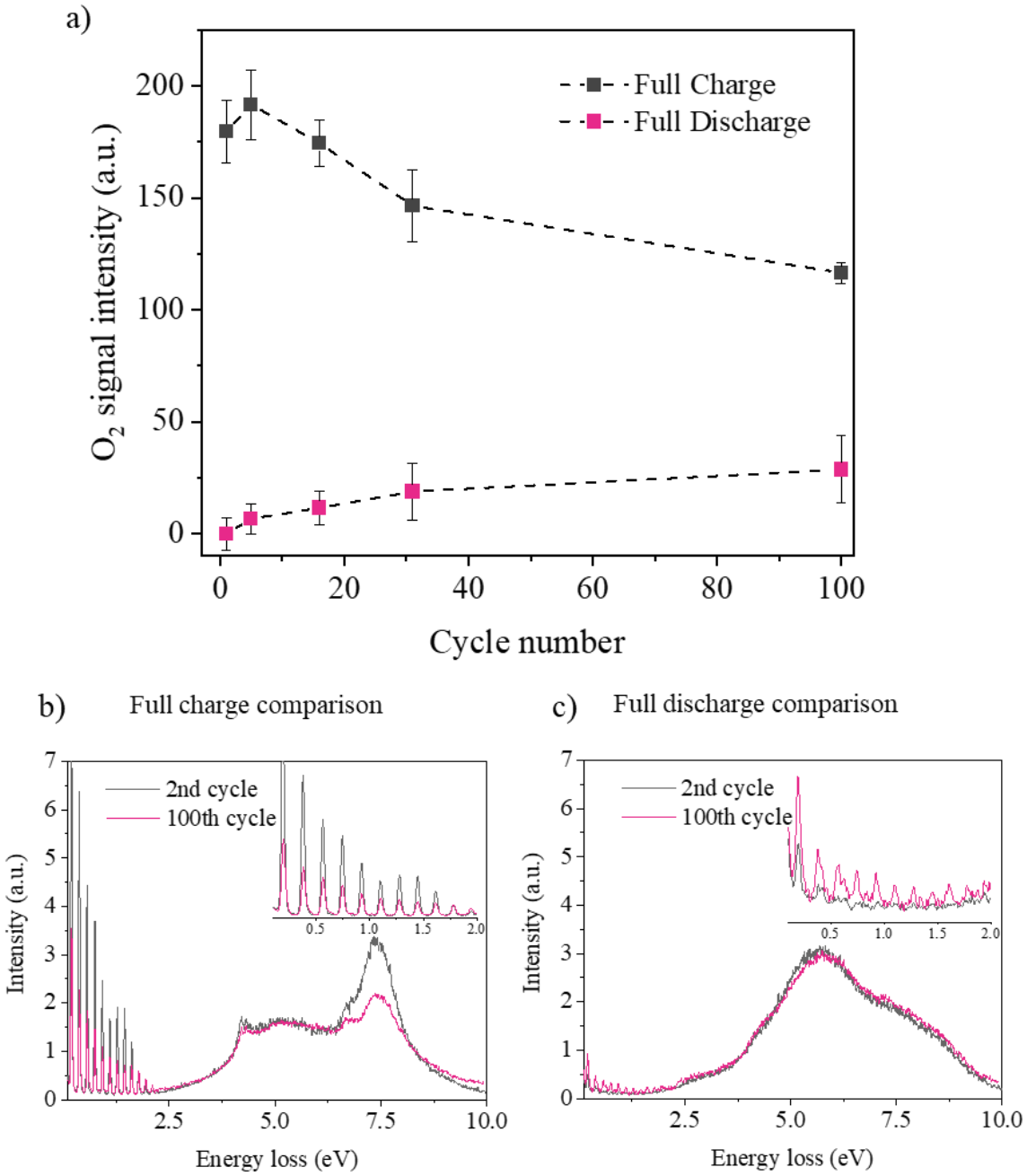

Figure 3.14: Evolution in intensity of the molecular O_2 signal. a) direct comparison of the O_2 signal intensity over cycling in the charged and discharged states. The amount of O_2 formed in the charged materials decreases with cycling and there is increasing evidence of O_2 that is not reduced on discharge. b) The raw RIXS data for the 2nd and 100th cycle full charge. c) The raw RIXS data for the 2nd and 100th cycle full discharge.

the intensity of the O_2 signal was tracked as a function of cycle number at full charge and full discharge (Figure 3.14). The data in Figure 3.14 a) shows the progressive decrease of the total amount of trapped O_2 in the charged cathodes over cycling, corresponding to a 44% loss from the 2nd full charge to the 100th full charge. In addition to this, the amount of O_2

which has not been reduced at the end of discharge appears to increase from the 2nd to the 100th cycle. This trend can also be observed in the comparison of the raw RIXS spectra in Figure 3.14 b) and c).

The build-up of O_2 at the end of discharge suggests an increase in the amount of electrochemically inactive trapped O_2. By taking the difference of the O_2 signal intensities at the end of charge and discharge across the 2nd and 100th cycles, the amount of lost O_2 capacity can be determined. The amount of O-redox capacity decreases from 0.48 e^- per formula unit on the 2nd cycle, to 0.22 e^- per formula unit on the 100th cycle. The contribution of the O^{2-}/O_2 redox couple to the overall charge compensation diminishes from 55% on the 2nd cycle to 34% on the 100th cycle, demonstrating the increasing proportion of TM redox in the overall charge compensation.[9] This loss of O-redox capacity results from two effects: the formation of electrochemically inactive O_2 that is still trapped but cannot be reduced on each cycle, and from the overall loss of O_2 from the particles. This is also reflected in the 44% loss of O_2 between the 2nd and 100th full charge points (Figure 3.14 a). The remaining active O-redox capacity on the 100th cycle (0.22 e^- per formula unit) aligns with the charge passed between FC and HD load curve points, meaning the charge passed above 3 V. In summary, the loss of O-redox activity, through a combination of O_2 release from particles and electrochemically inactive O_2, accounts for the reduced contribution of charge above 3 V on the 100th cycle, leading to voltage fade and much of the capacity loss on cycling.

Void Formation in $Li_{1.2}Ni_{0.13}Co_{0.13}Mn_{0.54}O_2$

To examine the source of the fading O_2 activity with cycling, STEM imaging was carried out to probe changes in the particle microstructure. The images shown in Figure 3.15 demonstrate the substantial changes which occur over cycling within individual grains of LNCMO, consistent with previous reports.[19,20] A comparison of the images for the pristine, 2nd discharge and the 100th discharge clearly show the formation of very significant voiding

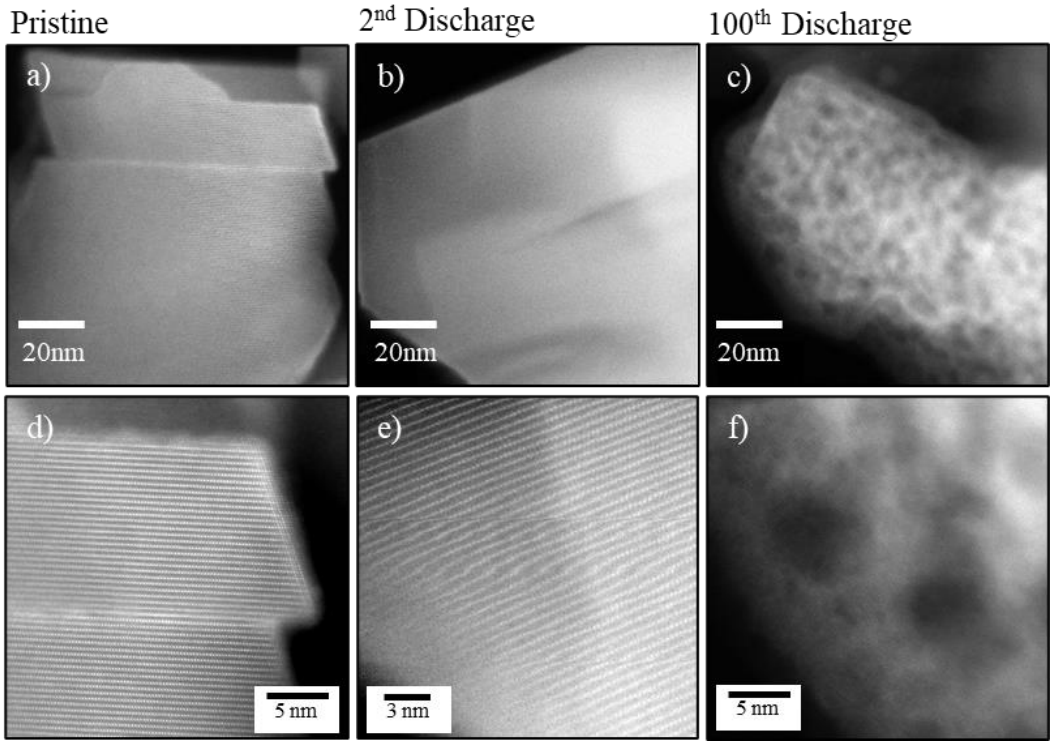

Figure 3.15: Formation of voids within Li-rich particles over cycling, imaged by ADF-STEM. The images show single grains of the pristine (a, d), 2nd discharge (b, e) and 100th discharge (c, f) material showing the formation of voids about 6 nm in diameter over extended cycling. Some larger agglomerations seen in c) are seen to be 10-14nm in size.

with a high density of voids, as seen by the darker areas in the STEM images. The voids are on average ~6 nm in size and are distributed throughout the particle, with some larger pores coming to 10-14nm, similar to previously reported pore sizes in Li-rich layered oxides (Table A3.3).[20] It is also worth noting may of the pores are closely packed, suggesting these could be interconnected into large agglomerations. A more detailed analysis of the pore size distribution is presented in the appendices (Table A3.3 and Figure A3.3).

To investigate the nature of the voids and the extent to which they are occluded or open, ^{129}Xe NMR was used. Xenon-129 (I = 1/2) is an inert gas with a large polarizable electron cloud, giving Xe a significant chemical shift range.[21] Constraining ^{129}Xe within a void brings it into contact with the surface of the void causing a distortion to the electron cloud and a chemical shift to be observed.[22] This shift has a well-known relationship with void size that has been experimentally determined (Figure A3.4).[23] The experiment was

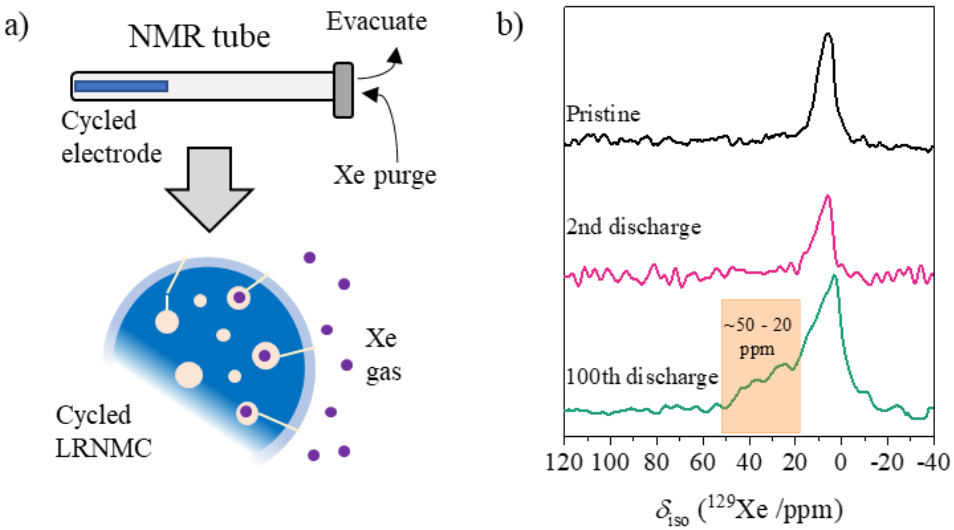

Figure 3.16: Investigation of pore formation using ^{129}Xe NMR. a) ^{129}Xe NMR experiments. Samples were extracted from cells and infiltrated with Xe gas to probe the open porosity. b) ^{129}Xe NMR of the pristine, 2nd discharge and 100th discharge materials. The orange region highlighted indicates the presence of open voids of 17nm diameter and greater after 100 cycles.

conducted as follows: LNCMO was placed under vacuum to evacuate the sample, then flushed with xenon gas (Figure 3.16). The Xe spectra for samples of the pristine, 2nd and 100th discharge material all show resonances centred at ~10 ppm. This is consistent with the paramagnetic broadening of bulk xenon gas, due to interactions with the surface of the cathode material. The signal could also arise from large (>40 nm) open pores at the surface, although no such pores are evident in the STEM. After 100 cycles, an increase in spectral density between 20 and 50 ppm is observed in the ^{129}Xe NMR spectra. This signal is not present in the pristine or 2nd cycled material, meaning new open voids with a minimum size of 17 nm have formed over cycling, comparable to previous reports on Li-rich materials.[20]

^{6}Li and ^{17}O NMR Studies on Cycled $Li_{1.2}Ni_{0.13}Co_{0.13}Mn_{0.54}O_2$

While the ^{129}Xe NMR data presents evidence of non-occluded pores forming over cycling, the extent to which these pores participate in the charge compensation process remains unknown. To investigate changes to Li deintercalation over cycling, ^{6}Li and ^{17}O solid state Magic Angle Spinning NMR (MAS-NMR) was used. The ^{6}Li solid state MAS NMR of the pristine material (Figure 3.17 a) shows two regions of resonances. The first is

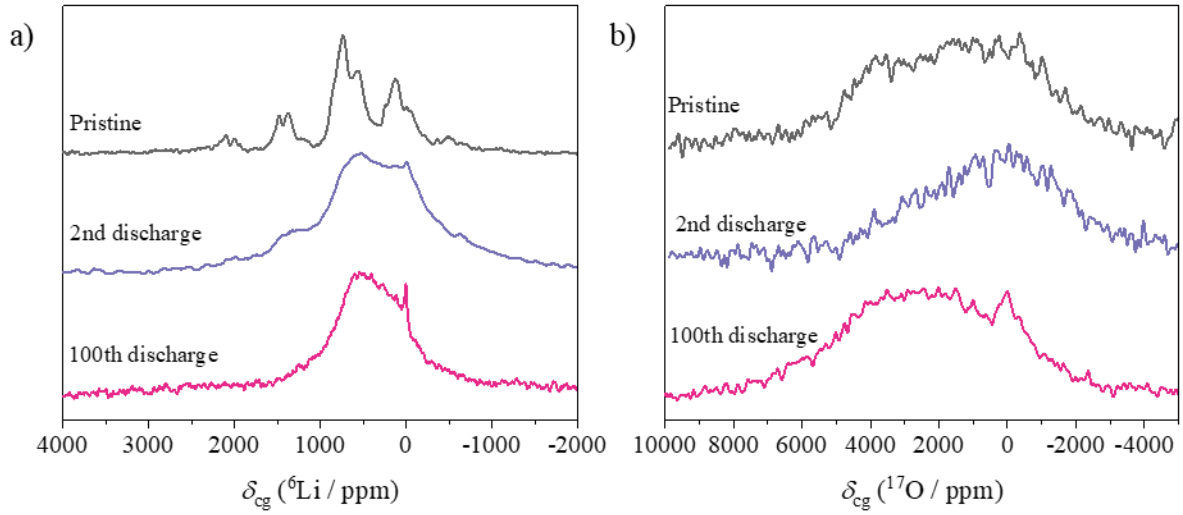

Figure 3.17: ^{6}Li (a) and ^{17}O NMR (b) isolating slow and fast relaxing environments. The sharp peaks at 0 ppm in the ^{6}Li and slow relaxing ^{17}O NMR spectra indicate the formation of large diamagnetic Li-rich regions on extended cycling.

a resonance at ~1500 ppm which arises from Li in the TM layer (Li_{TM}) and is consistent with well-defined honeycomb ordering. The second resonance is from Li in the AM layers (Li_{AM}) which sits between 400 and 900 ppm.[7,24] After the 2nd cycle, signal broadening and a substantial shift in the centre of gravity of the resonance (from ~700 to ~350 ppm) is observed. This is consistent with local disordering of the honeycomb superstructure and a clustering of Li into more diamagnetic regions. This reduces the number of transition metal neighbours for the Li-ions, and these changes have been discussed previously.[7] After the 100th cycle, a notable sharp resonance at ~5 ppm is observed which is consistent with Li in an extended diamagnetic environment (i.e. Li_2O-like regions), rather than Li in an Li_2CO_3 environment.[25]

^{17}O MAS NMR spectra were also collected for the Pristine, 2nd cycle and 100th cycle samples (Figure 3.17 b). The pristine material shows a broad amorphous line shape with very limited resolution. This can be attributed to a range of oxide-ion environments, which are broadened due to paramagnetic interactions. At the end of discharge on the 100th cycle, the spectral density of the resonance has shifted to a slightly higher frequency. This suggests that TM-rich regions are forming, i.e., where the oxide ions are coordinated by several TM

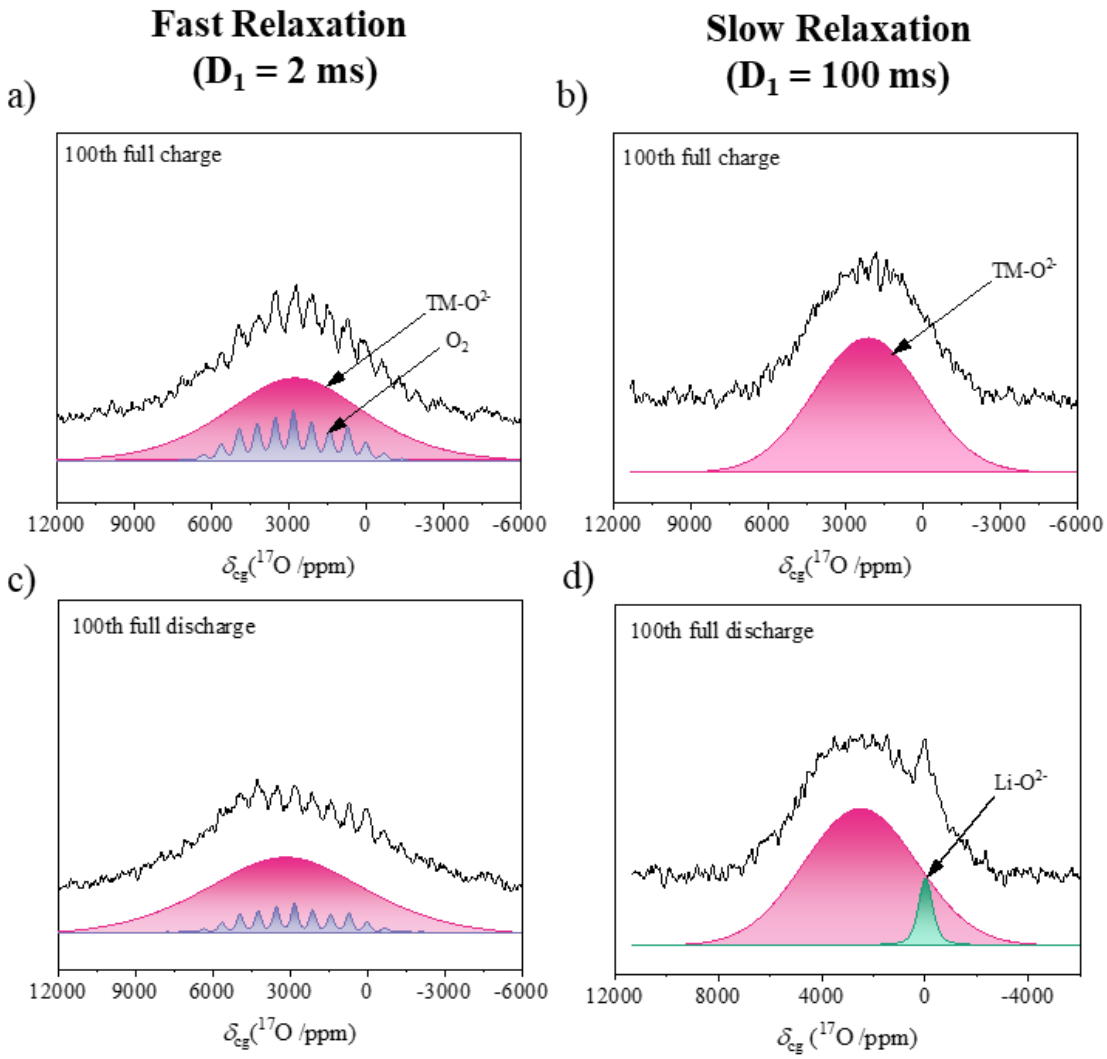

Figure 3.18: Partial reduction of O_2 trapped in voids to form Li-coordinated O^{2-} on the 100th discharge. ^{17}O NMR spectra isolating fast (a, c) and slow relaxing (b, d) ^{17}O environments. The sharp peaks in a) are assigned to trapped molecular O_2 which decrease in intensity on discharge. There is still evidence of some residual molecular O_2 in the discharged sample (c), δcg ($^{17}O_2$) = 2770 ppm. b) The slow relaxation ^{17}O is dominated by oxide environments coordinated to paramagnetic transition metal ions (TM-O^{2-}), δcg = 2100-2300 ppm. After discharge (d), a new ^{17}O environment is formed corresponding to oxide surrounded by Li (i.e. Li-O^{2-}) created by the reduction of O_2 in the voids and reinsertion of Li^+ into the voids coordinated by the O^{2-}, centred at δcg = 0 ppm.

ions (O-TM_3, O-TM_4 …). A clear peak at ~0 ppm can also be seen which is consistent with the 100th cycle ^6Li spectrum. This can be attributed to the formation of Li-rich regions in the cathode (O-Li_5, O-Li_6) rather than other diamagnetic Li species (e.g. LiF). Together, the ^{17}O and ^6Li MAS NMR results indicates that the material segregates over extended cycling into regions of highly paramagnetic TM-rich and diamagnetic Li-rich clusters.

To investigate oxygen activity over the 100th cycle, ^{17}O NMR spectra were collected on the 100th full charge and full discharge. For these spectra, fast relaxing (2 ms) and slow relaxing (100 ms) measurements were collected to selectively enhance the oxygens which experience substantial paramagnetic relaxation enhancement. The reason for using two different relaxation procedures is that O_2 molecules, possessing two unpaired electrons, are expected to have a much stronger paramagnetic relaxation enhancement than oxides. The fast relaxing spectra (Figure 3.18 a, c) show a well-defined chemical environment centred at δ_{cg} = 2770 ppm with a manifold of spinning sidebands, consistent with previous measurements of trapped molecular O_2.[7,26] Decreasing intensity of the O_2 resonance can be seen from the 100th charge to the 100th discharge as the O_2 is reduced to O^{2-}, however, there is evidence of some residual O_2 present in the 100th discharged sample. Results from the ^{17}O MAS NMR are in accord with RIXS measurements shown previously (Figure 3.14) and indicate that O_2 is only partially reduced over the 100th cycle. In addition to this, the slow relaxing spectra, (Figure 3.18 b, d), reveal that the ^{17}O diamagnetic peak resulting from O^{2-} surrounded predominantly by Li, is no longer present in the 100th full charge sample. This evidence supports the conclusion that the occluded voids seen in ADF-STEM are filled with O_2 and that, on discharge this oxygen is partially reincorporated into the lattice as O^{2-}. This is accompanied by the reinsertion of Li^+ ions into the void space coordinated by the O^{2-}, Li-rich regions as has been described previously.[7]

Discussion on the Effect of Trapped O_2 Over Cycling

As was previously described in the introduction to this thesis, recent work using high resolution RIXS and ^{17}O NMR has shown that over the first cycle of LNCMO O^{2-} is oxidised to O_2 with the loss of honeycomb TM ordering and formation of small vacancy clusters[7]. These clusters are evenly distributed throughout the particle as evidenced by small-angle X-

ray scattering,[27] with O_2 molecules trapped within. By the end of the 1st cycle, the trapped O_2 is completely reduced back to O^{2-}, accounting for the reversible O-redox capacity.

The measurements carried out over extended cycling show that the O-redox mechanism is not static and continues to evolve albeit more gradually. On cycling, there is increasing accumulation of O_2 at the end of discharge (Figure 3.14) indicating that not all O_2 formed on charge is reduced on the subsequent discharge. This demonstrates a decrease in activity of the O^{2-}/O_2 redox couple. The amount of O_2 trapped at the top of charge also decreases with cycling, signalling a loss of O_2 from the particles. The loss of activity of the O^{2-}/O_2 redox couple, coupled with the loss of O_2 from the particles leads to a loss of 0.26 e^- per formula unit in O redox capacity, corresponding to a reduction in the percentage of the capacity due to O–redox from 55 % on the 2nd cycle to 34 % on the 100th cycle. As the O^{2-}/O_2 couple occurs above 3 V, the loss of O-redox capacity at the expense of increased TM capacity leads to the overall voltage loss on cycling. This ties the capacity loss and voltage fade seen over extended cycling to the in the O-redox activity at the higher voltages.

As well as significant changes to the charge compensation mechanisms, LNCMO exhibits pronounced changes in the cathode particle microstructure. The issue of voiding in Li-rich materials has been well covered by existing literature. It has been studied using STEM, ptychography and small angle scattering[19,20,27]. Voids also cause a reduction in average particle density, which has been recently observed.[19] The STEM images presented above (Figure 3.15) provide additional evidence for this, showing voids develop that are about 2-6 nm in diameter within individual particles after 100 cycles. Previous studies have proposed that void formation begins on the 1st charge, corresponding to a few vacant cation sites with a size of approximately 1 nm in diameter, implying the voids grow on cycling.

The ^{129}Xe NMR data show that the cathode particles develop an increased number of voids open to the particle surfaces on cycling, with a diameter >17nm. There is also a wider

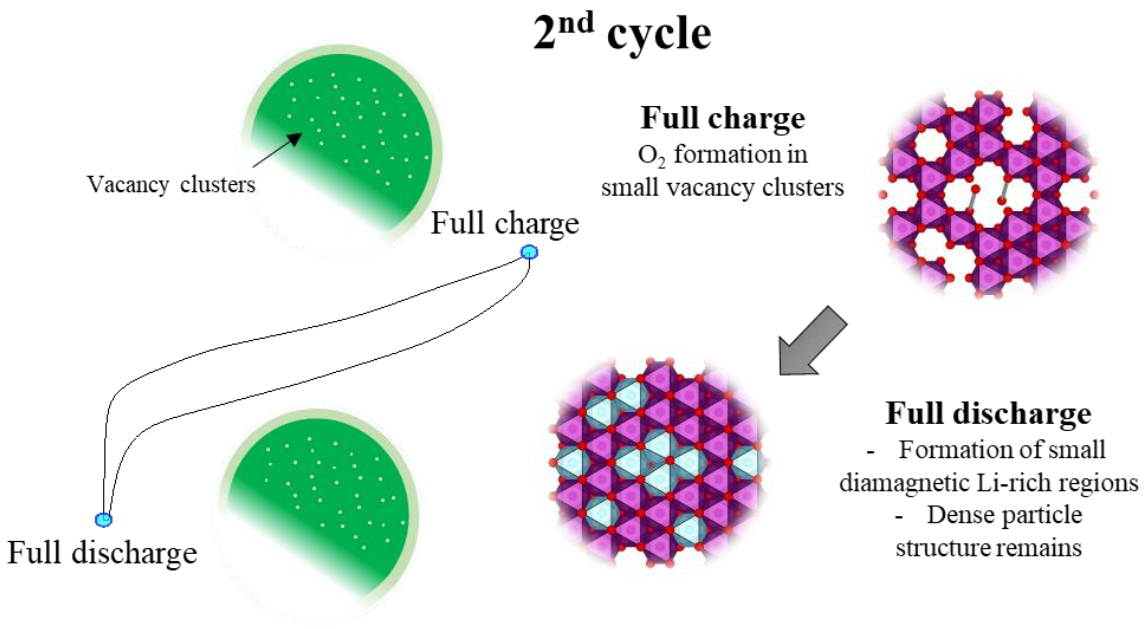

Figure 3.19: Depiction of the voltage fade mechanism over the 2nd cycle. Reversible O-redox involves the formation of molecular O_2 trapped in small vacancy clusters throughout the particle. O_2 molecules are fully reduced to O^{2-} on discharge forming small diamagnetic Li-rich regions. These small vacancy clusters form from the re-arrangement of the TM layer in LNCMO.

body of evidence showing that Li-rich NMC materials suffer from particle cracking which had commonly been associated with increased lattice strain.[28,29] Together, this suggests that the increased density of relatively large voids filled with O_2 upon cycling may result in weakening and hence fracturing of the particles, releasing O_2 and explaining its loss on extended cycling (Figure 3.19 and Figure 3.20). As the voids grow, reduction of trapped O_2 is expected to be more difficult than in the much smaller voids present on the 1st and 2nd cycles, due to the poor electronic conductivity of increasingly large Li_2O regions. This result is in agreement with the RIXS observations at the end of the 100th discharge, showing increasing amounts of unreduced O_2 over cycling, and with the ^{17}O NMR which also shows evidence of residual O_2 at the end of the 100th discharge. Additionally, investigation of the oxide environments using ^{17}O NMR on the 100th cycle reveals that, as the trapped O_2 is reduced to O^{2-}, diamagnetic ^{17}O environments form that were not present in the charged sample, indicative of O^{2-} in ionic, Li-rich environments. This evidence further strengthens the conclusion that the occluded voids formed on cycling are filled with O_2 and that on

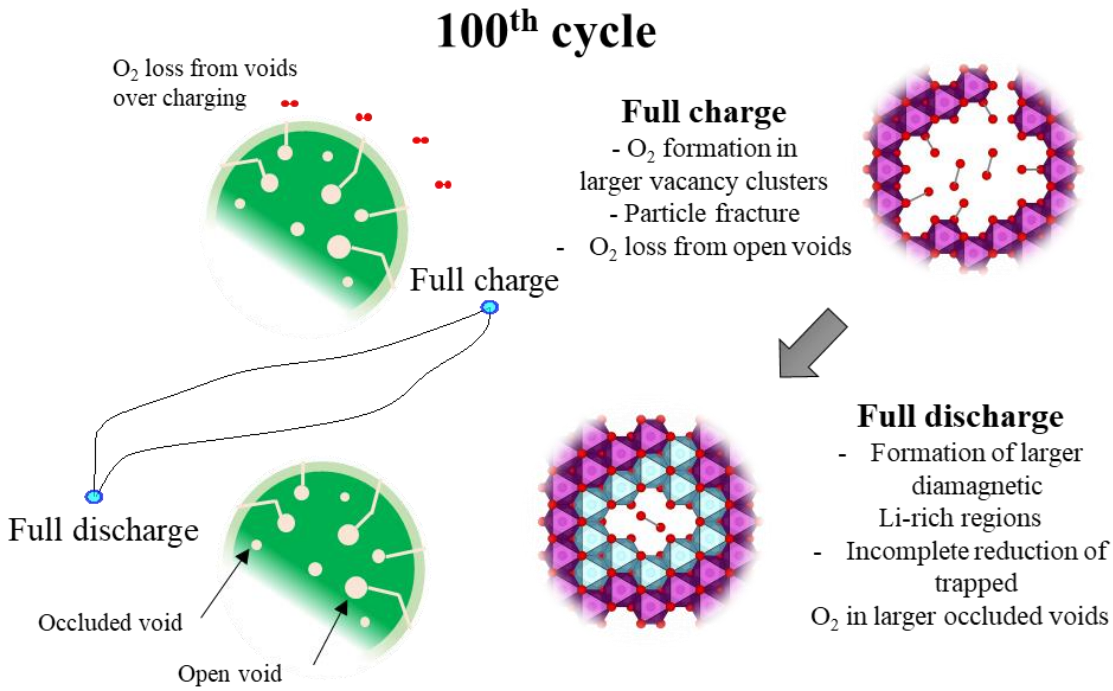

Figure 3.20: Depiction of the voltage fade mechanism over the 100th cycle: Further transition metal migration leads to agglomeration and coarsening of clusters into larger voids driven by the formation of more O_2. The large voids and their prevalence in the particles leads to a weakening of the particle structure, cracking and O_2 release. It is also more difficult to reduce O_2 in larger voids.

discharge some of the trapped O_2 is reduced to O^{2-}, which is reincorporated into the lattice along with the re-inserted Li^+.

These results clearly define the root cause of voltage fade in LNCMO, indicating that contribution to the capacity from O-redox must be preserved to avoid voltage fade. There is some promise already from implementing surface treatment strategies to prevent O_2 loss. In recent work by Li et al, a gradient Li-rich material was made with a stoichiometric surface composition and Li-rich bulk using a molten salt treatment.[30] This strategy protects the surface from O_2 loss and strengthens the particle against cracking, thus improving the average discharge voltage by 0.4 V after 200 cycles compared to an untreated sample.

3.4 Conclusion

Sol-gel synthesised LNCMO was prepared to study the link between the TM superstructure in layered Li-rich NMC and the high voltage O-redox plateau seen during

charging. The loss of the TM superstructure after just one cycle leads to a large voltage hysteresis on discharge, a process which can be reversed with a simple heat treatment process. Using TGA, ^{6}Li NMR and PXRD, the re-ordering of the TM layer by annealing was characterised and shown to be linked to the return of a high voltage plateau. This is a new model for O-redox materials which was demonstrated in Na-ion compounds and has now been extended to Li-rich materials.

Co-precipitation synthesised LNCMO was used to evaluate changes to the O_2/O^{2-} redox couple on extended cycling. High resolution RIXS and ^{17}O NMR were used to track O-redox activity over cycling, while STEM and ^{129}Xe NMR were deployed to investigate the structural rearrangements known to occur in these materials over extended cycling, with small vacancies clusters eventually forming large voids in LNCMO. Within these voids, O_2 molecules are trapped, inhibiting O_2 reduction, resulting in fewer O_2 molecules being reduced on discharge. The large voids and their high concentration eventually crack the weakened particles releasing some O_2. The O-redox process, which proceeds by the formation and reduction of trapped O_2 molecules, becomes less prevalent on cycling LNCMO. Together the O_2 loss and reduced O^{2-}/O_2 activity decreases the contribution of O-redox to the overall capacity, leading to capacity fade and an increasing dependence on the lower voltage TM redox couples, $Mn^{3+/4+}$ and $Co^{2+/3+}$. The gradual decrease of O^{2-}/O_2 participation in the charge compensation reaction over cycling provides a clear explanation for the voltage fade phenomenon. This draws together the observations of structural reorganisation, void formation, void opening, and transition metal reduction into a single mechanism. This work further outlines the importance of strategies which either work to reinforce the surface of Li-rich particles to prevent the cracking and escape of O_2 or suppress the formation of O_2 in the bulk.

3.5 References

1. Lu, Z., Beaulieu, L. Y., Donaberger, R. A., Thomas, C. L. & Dahn, J. R. Synthesis, Structure, and Electrochemical Behavior of Li[Ni[sub x]Li[sub 1/3−2x/3]Mn[sub 2/3−x/3]]O[sub 2]. *J. Electrochem. Soc.* **149**, A778 (2002).
2. Lu, Z., MacNeil, D. D. & Dahn, J. R. Layered $Li[Ni_xCo_{1-2x}Mn_x]O_2$ cathode materials for lithium-ion batteries. *Electrochem. Solid-State Lett.* **4**, 4–8 (2001).
3. Thackeray, M. M. *et al.* Li_2MnO_3 stabilized $LiMO_2$ (M = Mn, Ni, Co) electrodes for lithium-ion batteries. *J. Mater. Chem.* **17**, 3112–3125 (2007).
4. Johnson, C. S. *et al.* The significance of the Li_2MnO_3 component in 'composite' $xLi_2MnO_3 \cdot (1-x)LiMn_{0.5}Ni_{0.5}O_2$ electrodes. *Electrochem. commun.* **6**, 1085–1091 (2004).
5. Lu, Z. & Dahn, J. R. Understanding the Anomalous Capacity of $Li/Li[Ni_xLi_{(1/3-2x/3)}Mn_{(2/3-x/3)}]O_2$ Cells Using In Situ X-Ray Diffraction and Electrochemical Studies. *J. Electrochem. Soc.* **149**, A815 (2002).
6. House, R. A. *et al.* Covalency does not suppress O_2 formation in 4d and 5d Li-rich O-redox cathodes. *Nat. Commun.* **12**, 1–7 (2021).
7. House, R. A. *et al.* First-cycle voltage hysteresis in Li-rich 3d cathodes associated with molecular O_2 trapped in the bulk. *Nat. Energy* **5**, 777–785 (2020).
8. House, R. A. *et al.* Superstructure control of first-cycle voltage hysteresis in oxygen-redox cathodes. *Nature* **577**, 502–508 (2020).
9. Hu, E. *et al.* Evolution of redox couples in Li- and Mn-rich cathode materials and mitigation of voltage fade by reducing oxygen release. *Nat. Energy* **3**, 690–698 (2018).
10. Luo, K. *et al.* One-Pot Synthesis of Lithium-Rich Cathode Material with Hierarchical Morphology. *Nano Lett.* **16**, 7503–7508 (2016).
11. Rietveld, H. M. A profile refinement method for nuclear and magnetic structures. *J. Appl. Crystallogr.* **2**, 65–71 (1969).
12. Toby, B. H. & Von Dreele, R. B. GSAS-II: The genesis of a modern open-source all purpose crystallography software package. *J. Appl. Crystallogr.* **46**, 544–549 (2013).
13. Pimenta, V. *et al.* Synthesis of Li-Rich NMC: A Comprehensive Study. *Chem. Mater.* **29**, 9923–9936 (2017).
14. Luo, K. *et al.* Charge-compensation in 3d-transition-metal-oxide intercalation cathodes through the generation of localized electron holes on oxygen. *Nat. Chem.* **8**, 684–691 (2016).
15. House, R. A. *et al.* What Triggers Oxygen Loss in Oxygen Redox Cathode Materials? *Chem. Mater.* **31**, 3293–3300 (2019).
16. Singer, A. *et al.* Nucleation of dislocations and their dynamics in layered oxide cathode materials during battery charging. *Nat. Energy* **3**, 641–647 (2018).
17. Qiu, B. *et al.* Metastability and Reversibility of Anionic Redox-Based Cathode for High-Energy Rechargeable Batteries. *Cell Reports Phys. Sci.* **1**, 100028 (2020).
18. Christakopoulos, F., Troisi, E. & Tervoort, T. A. Melting kinetics of nascent poly(tetrafluoroethylene) powder. *Polymers (Basel).* **12**, 1–18 (2020).

19. Csernica, P. M. *et al.* Persistent and partially mobile oxygen vacancies in Li-rich layered oxides. *Nat. Energy* **6**, 642–652 (2021).

20. Yan, P. *et al.* Injection of oxygen vacancies in the bulk lattice of layered cathodes. *Nat. Nanotechnol.* **14**, 602–608 (2019).

21. Fraissard, J. & Ito, T. ^{129}Xe NMR study of adsorbed xenon: A new method for studying zeolites and metal-zeolites. *Zeolites* **8**, 350–361 (1988).

22. *Hyperpolarized Xenon-129 Magnetic Resonance*. (The Royal Society of Chemistry, 2015). doi:10.1039/9781782628378.

23. Terskikh, V. V. *et al.* A general correlation for the ^{129}Xe NMR chemical shift-pore size relationship in porous silica-based materials. *Langmuir* **18**, 5653–5656 (2002).

24. Dogan, F. *et al.* Solid State NMR Studies of Li_2MnO_3 and Li-Rich Cathode Materials: Proton Insertion, Local Structure, and Voltage Fade . *J. Electrochem. Soc.* **162**, A235–A243 (2015).

25. Wan, C. *et al.* Multinuclear NMR Study of the Solid Electrolyte Interface Formed in Lithium Metal Batteries. *ACS Appl. Mater. Interfaces* **9**, 14741–14748 (2017).

26. Gerothanassis, I. P., Momenteau, M. & Loock, B. Hydrogen-Bond Stabilization of Dioxygen, Conformation Excitation, and Autoxidation Mechanism in Hemoprotein Models as Revealed by 170 NMR Spectroscopy. *J. Am. Chem. Soc.* **111**, 7006–7012 (1989).

27. Grenier, A. *et al.* Nanostructure Transformation as a Signature of Oxygen Redox in Li-Rich 3d and 4d Cathodes. *J. Am. Chem. Soc.* **143**, 5763–5770 (2021).

28. Sharifi-Asl, S. *et al.* Revealing Grain-Boundary-Induced Degradation Mechanisms in Li-Rich Cathode Materials. *Nano Lett.* **20**, 1208–1217 (2020).

29. Liu, T. *et al.* Origin of structural degradation in Li-rich layered oxide cathode. *Nature* **606**, 305–312 (2022).

30. Zhu, Z. *et al.* Gradient Li-rich oxide cathode particles immunized against oxygen release by a molten salt treatment. *Nat. Energy* **4**, 1049–1058 (2019).

Chapter 4
In-Operando Analysis of $Na_{0.6}Mn_{0.8}Li_{0.2}O_2$

Table of Contents

4.1 Introduction 105

4.2 Experimental 107

4.3 Results 109

4.3.1 Characterisation of $Na_{0.6}Mn_{0.8}Li_{0.2}O_2$ 109

4.3.2 *In-Operando* Studies of the Mn K-edge in $Na_{0.6}Mn_{0.8}Li_{0.2}O_2$ 111

4.3.3 Investigation on the stability of oxygen holes in $Na_{0.6}Mn_{0.8}Li_{0.2}O_2$ 114

4.3.4 Electrochemical cell development for *In-Operando* analysis of the O K-edge in $Na_{0.6}Mn_{0.8}Li_{0.2}O_2$ 116

4.4 Conclusion 121

4.5 References 122

4.1 Introduction

A better understanding of the operating mechanisms within battery materials is essential to increasing the performance of Li-ion and Na-ion batteries. While post-mortem examination of battery samples ex-situ still provide valuable information, they are limited by only providing information about a material at a particular point in time after the cell has been disassembled. In contrast, *in-operando* measurements (where a material is analysed in an operational or functional state) provide insight into the temporal evolution of a material.[1] Such measurements, although difficult to carry out, provide a more accurate picture of the material behaviour during operation by allowing intermediate or meta-stable states to be visualized and studied. Additionally, such measurements provide a temporal evolution of

the system in operation, providing an additional level of detail. In the context of O-redox materials, *in-operando* measurements could provide valuable insight to the nature of oxidised oxygen in fully charged O-redox cathode materials. Several mechanisms have been proposed to explain the cause of the anomalous capacity observed in O-redox materials, including peroxo-like distortions to the oxide sub-lattice,[2] molecular O_2 formation,[3] electron hole formation on oxygen,[4,5] and Mn^{4+} over-oxidation.[6] Of particular interest are a small group of O-redox materials which display O-redox activity at a comparatively high voltage on discharge: *P*2 and *P*3 $Na_{0.6}Mn_{0.8}Li_{0.2}O$,[4,7] $Na_{0.6}Mn_{0.6}Ti_{0.2}Li_{0.2}O_2$,[8] and $Na_2Mn_3O_7$.[9–11] The electrochemical properties of all these materials are of particular interest due to the high voltage plateau present on the first discharge, in contrast to the large hysteresis observed in the vast majority of Li-ion and Na-ion O-redox compounds.[3,12]

In this chapter, the Mn K-edge of *P*2-type $Na_{0.6}Mn_{0.8}Li_{0.2}O_2$ (NMLO) will be investigated via *in-operando* measurements. The nominal oxidation state of Mn in pristine NMLO is Mn^{4+}: therefore, removal of Na^+ must be accompanied by oxidation of Mn or the oxygen sub-lattice. Analysis of the Mn K-edge will uncover the possibility of Mn^{4+} oxidation in O-redox compounds. Subsequently, the development of a Soft X-ray Absorption Spectroscopy (SXAS) *in-operando* cell will be presented, allowing O K-edge measurements to be performed on a working O-redox cathode material. The successful development of this cell will provide insight into the nature of oxidised oxygen in a reversible, high-voltage O-redox compound. In addition, this cell could be used for *in-operando* RIXS measurements, a technique which is yet to be applied to O-redox materials.

4.2 Experimental

Solid state synthesis: NMLO was prepared by solid state reaction between Na_2CO_3 (≥99%, Aldrich), Li_2CO_3 (≥99%, Aldrich) and MnO_2 (≥99%, Aldrich). First, precursors were ball-milled at 350 rpm for 1 hr in ethanol, then pressed into pellets and calcined at 800 ^oC for 12 hrs under flowing O_2. A heating rate of 5 $^oC\ min^{-1}$ was used, while a cooling rate of 2 $^oC\ min^{-1}$ was used. The material was then transferred to an Ar glovebox.

$Na_2Mn_3O_7$ was prepared by solid state reaction between $NaNO_3$ (≥99%, Aldrich), and $MnCO_3$ (≥99%, Alfa Aesar). First, precursors were ball-milled at 350 rpm for 1 hr in ethanol, then pressed into pellets and calcined at 600 ^oC for 12 hrs under flowing O_2. A heating and cooling rate of 5 $^oC\ min^{-1}$ was used. The material was then transferred to an Ar glovebox.

Electrochemical cycling: Electrodes were prepared by combining the active material (80wt%) and Super P carbon (10wt%) in a mortar and pestle before adding polytetrafluoroethylene binder (10wt%). The electrode film was then rolled to a thickness of about 100μm. Electrodes were assembled into coin cells using glass fibre separators and 1 M $NaPF_6$ in propylene carbonate (PC) or acetonitrile (ACN) electrolyte, with a Na metal counter electrode. Galvanostatic cycle testing was carried out using Maccor Series 4000. The cells and electrodes were prepared and assembled/disassembled in the glove box under an inert atmosphere. Cycling was performed between 2.0V and 4.5V vs Na^+/Na^0 at a rate of 10mA/g for all cells.

Electrolyte preparation: Solutions of 1 molar $NaPF_6$ in propylene carbonate (99.7%, anhydrous, Sigma) and 1 molar $NaPF_6$ in acetonitrile (electronic grade, 99.999%, anhydrous, Sigma) were made as follows. The electrolyte solvents were used as bought from Sigma. $NaPF_6$ (from Kishida, 99.9%) was dried for 24 hrs under vacuum at 70 ^oC, then weighed out in the correct molar ratio into a clean dry vial. The electrolyte solvent was then added to the salt and stirred for 1 hr to allow complete dissolution.

PXRD: Diffraction data were collected on a Rigaku 9 kW SmartLab Cu-source diffractometer equipped with a Hypix 2D detector. GSAS-II was used to conduct Rietveld refinements against the collected data.[13,14]

HERFD-XAS: *In-operando* Mn K-edge High Energy Resolution Fluorescence detected X-ray Absorption Spectroscopy (HERFD-XAS) was collected at beamline I20-scanning at the Diamond Light Source (3 GeV, 300 mA) using K_a radiation, with the beam attenuated to prevent beam damage issues. A Si(111) double crystal monochromator was used for energy selection of the incident beam. Data was collected at room temperature. Mn K-edge XAS spectra were collected in fluorescence mode using a four-element Vortex Si-drift detector. *In-operando* cells were prepared in glove boxes under Argon atmosphere and placed at 45 degrees to the beam to be measured under fluorescence conditions. Sample standards were vacuum sealed in pouches.

SXAS: These data were collected at the I21 beamline at Diamond Light Source. The data shown was collected in Total Fluorescence Yield mode.

RIXS: High resolution RIXS data were collected using the I21 beamline at Diamond Light Source. The data shown is an average of 15 scans measured at 531 eV recorded at different sample locations and averaged together.

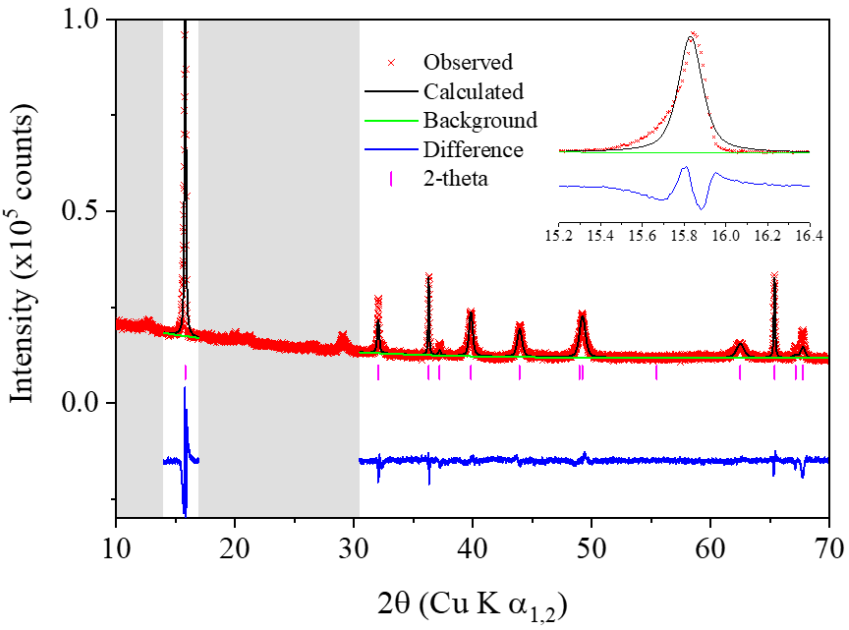

Figure 4.1: Rietveld refinement of NMLO. The superstructure region (10° – 14° 2θ and 17° – 31° 2θ) was greyed out and excluded from the refinement. Diffraction data was collected in house on a 9kW Rigaku diffractometer.

4.3 Results

4.3.1 Characterisation of NMLO

NMLO was prepared as outlined in the experimental section. At high temperatures, honeycomb ordering is favoured in the transition metal layer. In order to produce the particular ribbon ordering observed with this composition, slow cooling the material from 800 °C at a rate of 2 °C min^{-1} is necessary.[4]

The crystal structure of NMLO was then characterised using PXRD. The collected PXRD pattern can be well fitted to the *P*63/*mmc* space group (Figure 4.1, Table A4.1). This space group is one of the simplest to describe *P*2 layered compounds and cannot be used to refine the superstructure peaks which arise due to the in-plane ordering of the Li and Mn cations (Figure 4.2). The superstructure peaks observed can be described by the *C*2/*c*, *P*21/*c* and *Cmcm* space groups, depending on the inter-layer arrangement of the ordering scheme.[4] The Rietveld refinement reveals lattice parameters of a = 2.85018 (1) Å and c = 11.13656 (2) Å, in agreement with previous studies on this material.

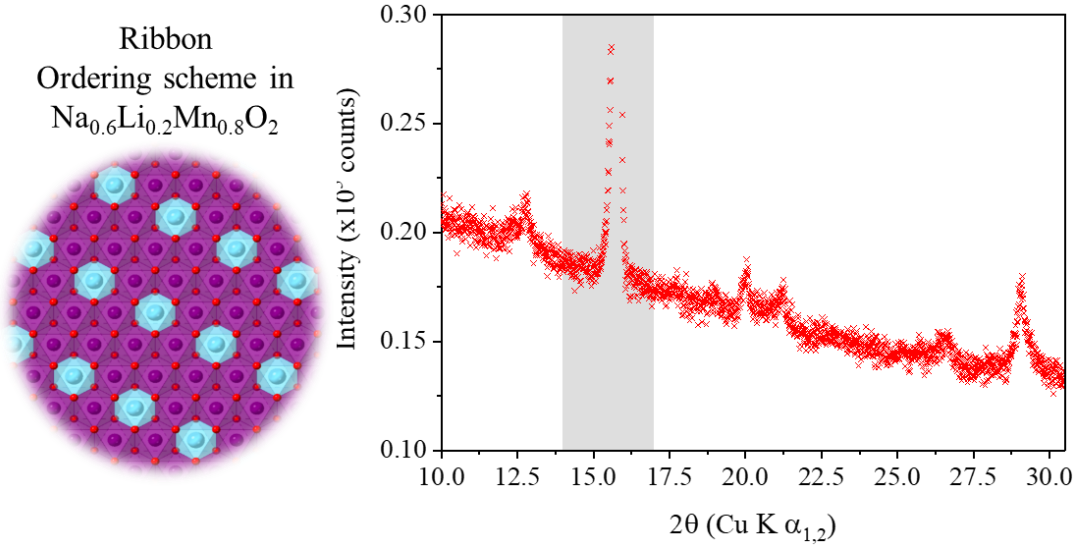

Figure 4.2: Depiction of the ribbon ordering scheme present in the TM layer of NMLO, alongside an enhanced view the superstructure region of the XRD pattern of NMLO, showing the outline of the superstructure peaks which arise from the ribbon ordering. Mn atoms are shown in purple, O in red and Li in light blue.

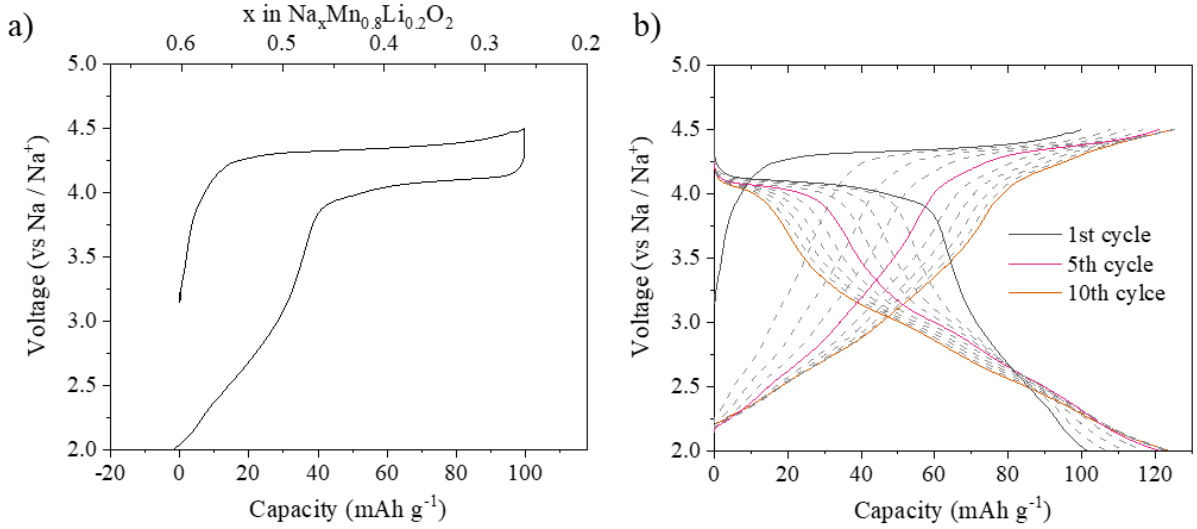

Figure 4.3: Electrochemical cycling of NMLO at a rate of 10 mA g^{-1}. a) First cycle load curve for NMLO, showing reversible, high-voltage O-redox activity. b) Evolution of the load curve for NMLO over cycling, showing a continuous loss of the high-voltage plateau on charge and discharge.

The electrochemical properties of NMLO were studied by cycling against a Na metal anode, (Figure 4.3). Over the first cycle, a long flat plateau is observed at 4.2 V giving a capacity of 100 mAh g^{-1}. On discharge, a high voltage discharge plateau is also observed, with a capacity of 65 mAh g^{-1} being delivered above 4 V. The load curve then drops in voltage, demonstrating that the plateau is not completely reversible. Over subsequent cycles,

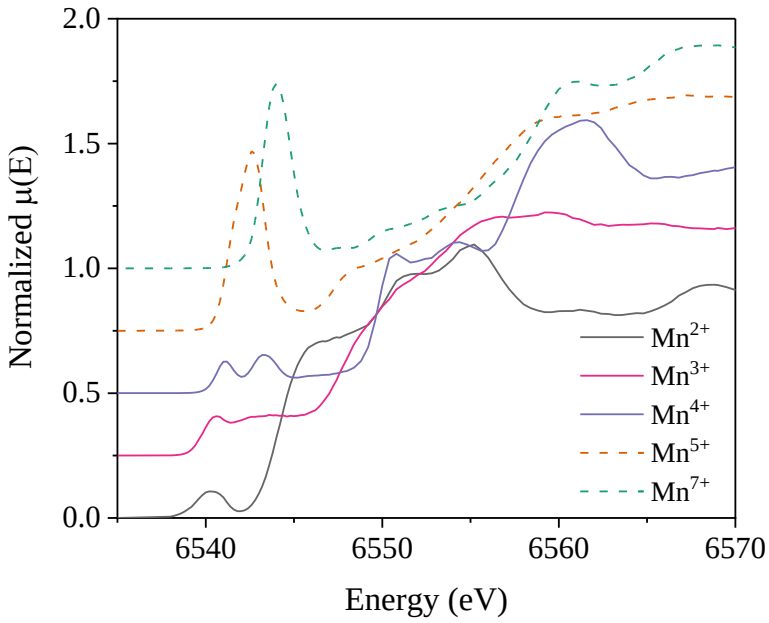

Figure 4.4: Plot of all Mn K-edge HERFD-XAS absorption spectra for measured the Mn standards. The octahedrally coordinated Mn samples are shown with solid lines, while the tetrahedrally coordinated Mn samples are shown with dashed lines. The compounds which were measured to collect these standards were as follows: MnO for Mn^{2+}, Mn_2O_3 for Mn^{3+}, Li_2MnO_3 for Mn^{4+}, Na_3MnO_4 for Mn^{5+} and $KMnO_4$ for Mn^{7+}.

the high voltage plateau remains present on both charge and discharge; however, it continuously shortens in length over cycling, with a larger share of capacity being delivered at lower voltages (Figure 4.3 b). This suggests that the charge compensation mechanism within the material is continuously evolving over cycling.

4.3.2 *In-Operando* Studies of the Mn K-edge in NMLO

In order to investigate previous claims of Mn^{4+} oxidation in O-redox compounds,[6] *in-operando* XAS was used to study the Mn K-edge over the first charge in NMLO. First, a wide selection of Mn standards were measured by XAS, providing insight into the XANES profiles of different oxidation states of Mn. The standards measured were MnO for Mn^{2+}, Mn_2O_3 for Mn^{3+}, Li_2MnO_3 for Mn^{4+}, Na_3MnO_4 for Mn^{5+} and $KMnO_4$ for Mn^{7+}. The results of these measurements can be seen in Figure 4.4. Comparing the profiles for the octahedrally coordinated Mn^{2+}, Mn^{3+} and Mn^{4+}, the main edge of the XANES and the white line energy

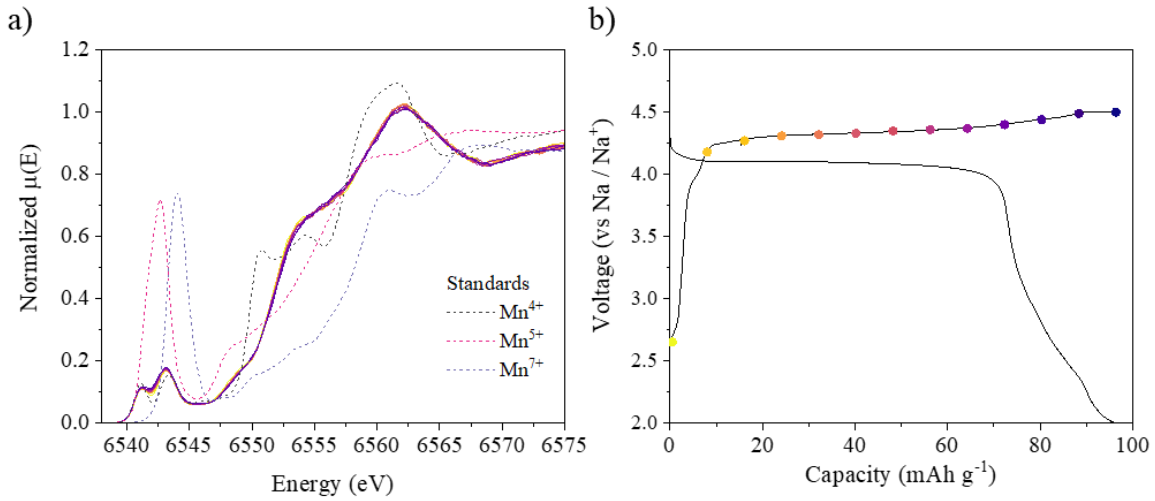

Figure 4.5: a) In-operando Mn K-edge XAS spectra for NMLO, compared to Mn^{4+}, Mn^{5+} and Mn^{7+} references. b) Electrochemical load curve obtained for NMLO during the operando measurement. In total 11 points were measured across the charge, with a final voltage hold at 4.5V to ensure the measurement of the Mn K-edge at the top of charge.

shifts to higher energies in line with the increasing oxidation state. Moving on to Mn^{5+} and Mn^{7+}, dramatic differences are observed in the pre-edge regions, as well as a further shift in the main XANES edge to higher energies. The large pre-edge peaks observed at 6542 eV and 6544 eV for the Mn^{5+} and Mn^{7+} samples respectively arise due to the different coordination environment of Mn in these oxidation states. While Mn^{4+} is octahedrally coordinated, Mn^{5+} and Mn^{7+} are both tetrahedrally coordinated within their complexes, losing the octahedral centrosymmetric coordination environment. As a result, symmetry selection rules (i.e. the LaPorte selection rule, where $\Delta l = \pm 1$)[15] are relaxed in Mn^{5+} and Mn^{7+} compounds, allowing previously forbidden transitions to occur. In TM complexes where the TM cation is tetrahedrally coordinated, the intense pre-edge features have been attributed to transitions from the 1s orbital to 3d-4p hybridized orbitals.[15,16] To capitalise on the enhanced Mn pre-edge feature of tetrahedrally coordinated Mn, the Mn K-edge was subsequently monitored during the first charge cycle in NMLO. The *in-operando* cell used is described in the methods chapter of this thesis.

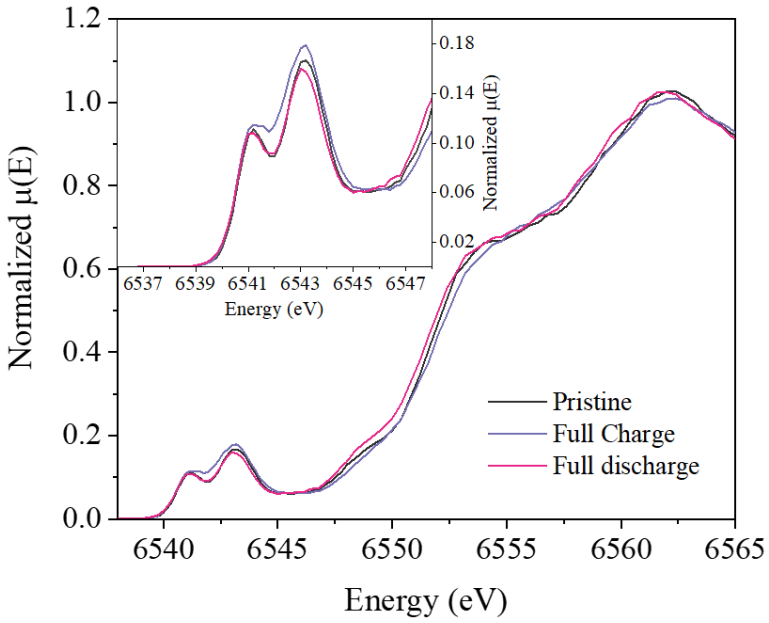

Figure 4.6: A comparison of the pristine, full charge and full discharge points collected during in-operando Mn K-edge XAS measurements on NMLO. The inset provides a closer look at the changes to the pre-edge region.

The data collected over the first charge cycle are presented in Figure 4.5. This shows the progression of the Mn K-edge over the first charge in $Na_{0.6}Li_{0.2}Mn_{0.8}O_2$, in comparison to the Mn^{4+}, Mn^{5+} and Mn^{7+} standards. The main edge does not shift to higher energies during the first charge, while the position of the white line energy remains constant. This indicates that no further oxidation of Mn is taking place. Figure 4.6 shows a comparison between the pristine, full charge and full discharge charge points of NMLO in order to clearly highlight the differences between the measurement points. The inset highlights the changes to the pre-edge feature in the XANES, showing a slight increase in intensity at the top of charge, which is lost on discharge. However, this increase in intensity is minimal compared to that of Mn^{5+} or Mn^{7+}, ruling out the possible formation of tetrahedrally coordinated Mn during the first charge. To rule out the effects of beam damage, the beam was moved to measure a different spot at the top of charge (Figure A4.1). The Mn K-edge spectra taken at the new spot almost perfectly overlays the initial measurment taken at the

top of charge, indicating that beam damage had no influence on the *in-operando* measurements carried out.

The *in-operando* data presented in this section shows that neither Mn^{5+}, nor Mn^{7+}, are present in signifncant amounts during the charge of NMLO. This excludes Mn^{4+} oxidation as a possible charge compensation mechanism in NMLO and confirms by inference that O-redox is the primary charge compensation mechanism.

4.3.3 Investigation on the stability of oxygen holes in $Na_{0.6}Mn_{0.8}Li_{0.2}O_2$

As outlined in the introduction to this thesis, there is a growing body of evidence supporting the formation of molecular O_2 in O-redox cathode materials during charge.[3,17–19] The mechanism for this process begins by charging the material and removing alkali metal cations from the layered structure. As the oxidation of the oxygen sub-lattice occurs, the structural rearrangement of the TM layer in layered O-redox cathodes leads to the formation of molecular O_2 trapped within vacancy clusters in the bulk of the material. On discharge, a large hysteresis is observed as the O_2 molecule is reduced back to O^{2-}, leading to the reversible cycling of the O^{2-}/O_2 redox couple on subsequent cycles at a reduced voltage. In contrast, reversible, high-voltage O-redox activity is possible though the O^{2-}/O^{-} redox couple. This mechanism is based on the formation of electron holes on the oxide sub-lattice, and has been observed in a handful of O-redox cathodes, including *P*2-type NMLO.[4,9,11]

The formation of electron holes on the oxide sub-lattice of NMLO is evidenced by an increase in intensity before the pre-edge in the O K-edge X-ray XAS at the top of charge. To probe the relative stability of these electron holes, O K-edge XAS was conducted on two samples of NMLO: One aged sample which was charged to 4.5 V and left to rest for 1 month before analysis, and a charged sample which was prepared 1 day before analysis. The results from this study are presented in Figure 4.7. The pre-edge feature in the O K-edge XAS is

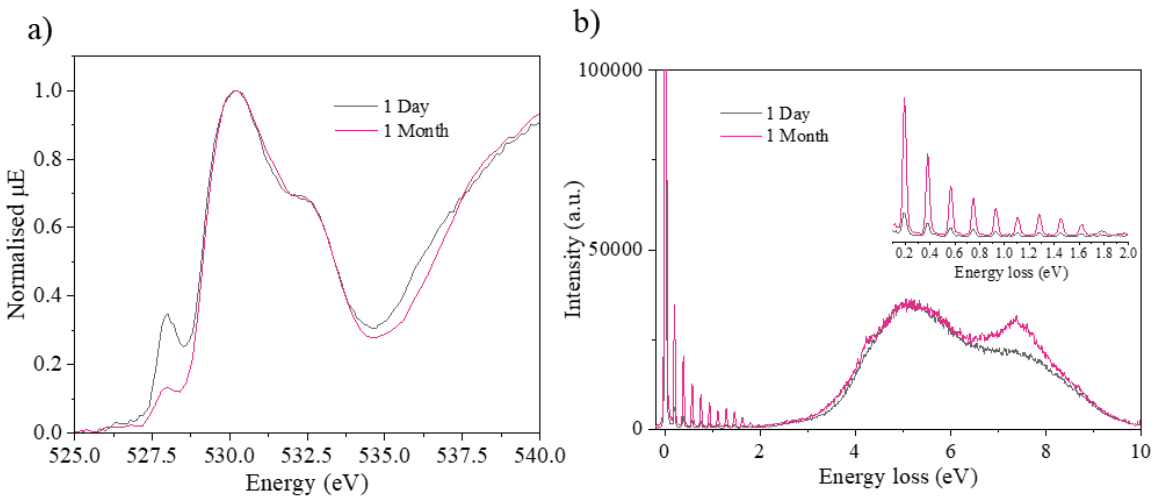

Figure 4.7: a) O K-edge SXAS spectra of NMLO at the top of charge. Each sample was aged for a different period of time, one for 1 month and one for 1 day. b) O K-edge RIXS data collected at an excitation energy of 531 eV on the same samples.

much stronger in the 1-day old sample, indicating that a higher concentration of electron holes are present in the newly charged sample. In addition, high resolution Resonant Inelastic X-ray Scattering (RIXS) was used to probe the presence of molecular O_2 in the same charged NMLO samples. The signal arising from molecular O_2 in the 1-day old sample is much weaker than the 1-month-old sample, indicating a larger amount of molecular O_2 in the bulk of the aged sample (Figure 4.7b).

These results highlight the relative instability of the electron holes in charged NMLO, by showing the eventual decay of the electron holes to form molecular O_2 which remains trapped in the material. This instability illustrates the need for *in-operando* measurements to be used in the study of O-redox cathode materials, enabling the measurement of meta-stable oxygen states over cycling.

4.3.4 Electrochemical cell development for *In-Operando* analysis of the O K-edge in $Na_{0.6}Mn_{0.8}Li_{0.2}O_2$

Although *in-operando* studies of AM-ion cathode materials have previously been carried out, they were limited to monitoring the O K-edge XAS signal during operation.[20] Methods and protocols should also be established for the *in-operando* measurement of the O K-edge RIXS of AM-ion cathode materials. The successful development of an electrochemical cell suitable for *in-operando* O K-edge monitoring is required in order to carry out these measurements.

Conducting *in-operando* studies on the O K-edge of AM-ion cathode materials faces two main challenges. The energy of the O K-edge lies in the soft X-ray energy range (≤3000 eV), meaning measurements must be conducted under ultra-high vacuum conditions. In addition to this, conventional Li-ion and Na-ion battery electrolytes all use carbonate-based solvents which contain oxygen atoms embedded within the molecule (C=O functional group). This makes it impossible to accurately study the O K-edge of cathode materials. These two challenges can both be solved independently: By using a purpose-built SXAS *operando* cell, capable of operating under ultra-high vacuum conditions, and by using a battery chemistry capable of operating without conventional electrolyte formulations.

Operando SXAS cell Design

The cell developed for this study was designed by Dominic Forstermann, with the cell components being produced by Protolabs from CAD drawings. The cathode side of the cell (cell top) is a circular base made of Al, with a small hole drilled through the centre. A square in-lay cut into the cell top accommodates the Si_3N_4 window. Finally, a circular Al-foil with a hole cut in the centre was used as a current collector (Figure 4.8). The anode side of the cell (cell base) is made of stainless steel and features a circular in-lay to accommodate the

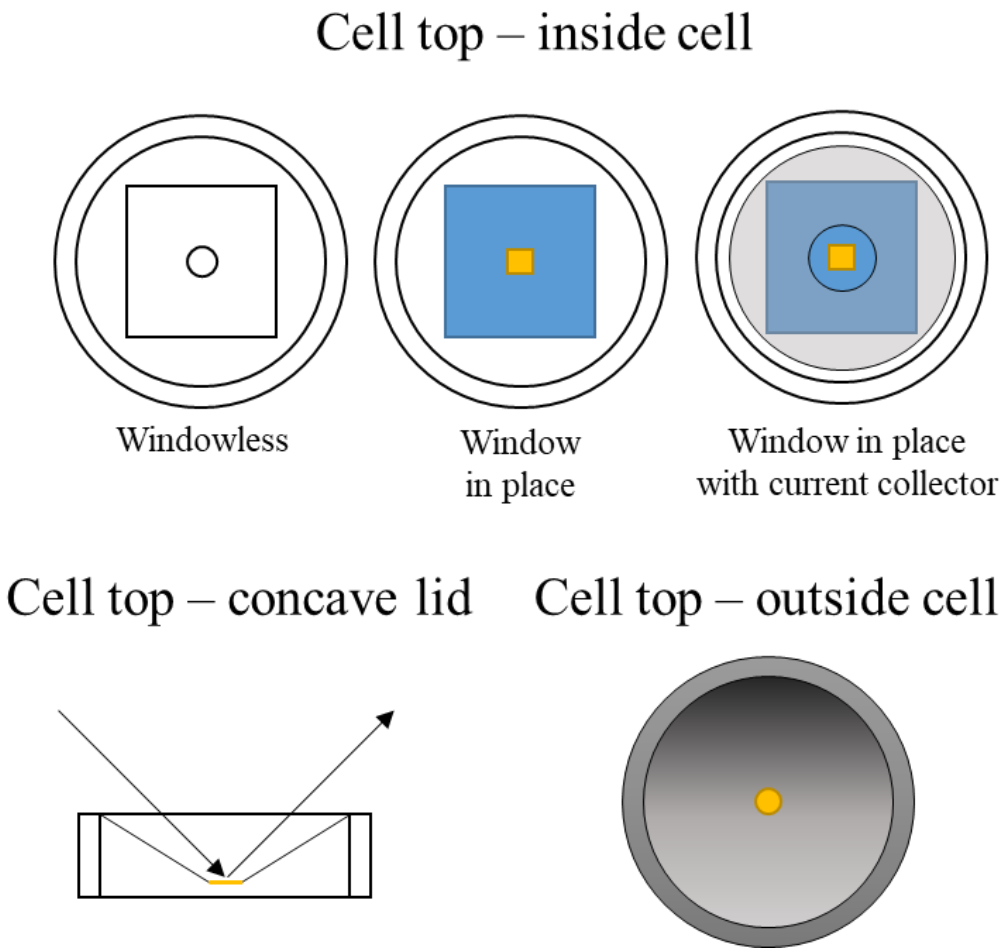

Figure 4.8: A representation of the cathode side, or cell top, of the *in-operando* SXAS cell. This schematic shows how the Si_3N_4 window and current collectors fit into the cell. The outer cell view highlights the concave shape of the cell top, to allow for fluorescence measurements.

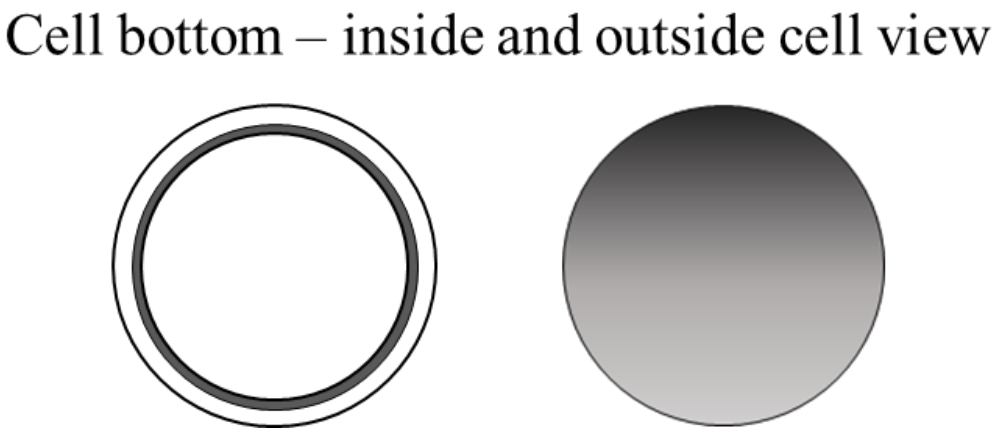

Figure 4.9: A representation of the anode side, or cell bottom, of the *in-operando* SXAS cell. This schematic shows the groove where the O-ring lies to seal the cell in black.

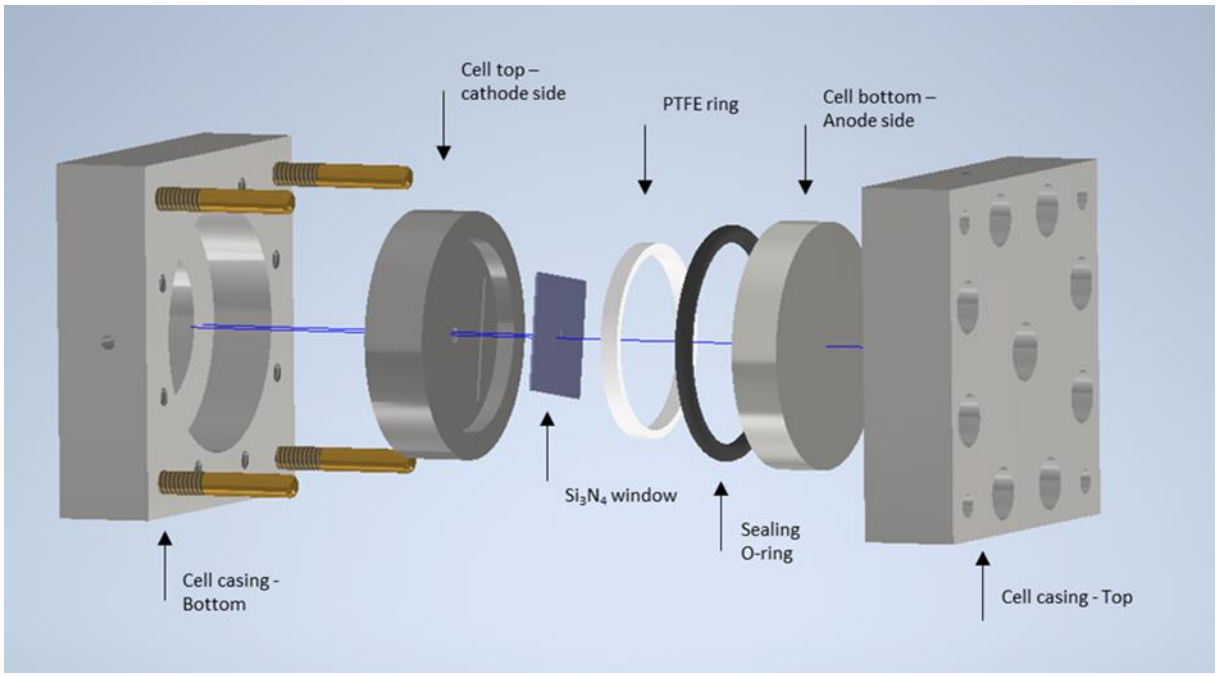

Figure 4.10: An exploded view of the in-operando SXAS cell, revealing the full contents of the cell. The guiding pins are shown in gold, attached to the bottom cell casing.

rubber O-ring which seals the cell (Figure 4.9). Within the cell, a PTFE gasket is used to prevent shortages. The whole cell is enclosed within a peak casing of dimensions 30 mm x 30 mm x 20 mm. M2 screws were used to screw the cell casing shut. An exploded view of the cell is seen in Figure 4.10. In order to control the stack pressure within the cell, three 14 mm glass fibre separators were used when the cell was assembled. In addition, 0.3 mm thick washers were placed on each of the four guiding pins, to ensure the cell could not be closed too tight.

Several different thicknesses of Si_3N_4 windows were tested. While a thicker window would prove to be more resistant to the internal pressure of the cell, a thinner window would allow for less attenuation of the X-ray beam during the measurement. A window thickness of 150 nm proved optimal after preliminary testing. The operation of the cell under vacuum was tested by placing the cell within the ante chamber of a glovebox and connected to wires which ran into the antechamber. These tests proved successful, allowing for NMLO to be cycled over one full cycle without bursting the Si_3N_4 window.

Development of an oxygen-free electrolyte system

To obtain a clear signal of the O K-edge of cathode materials *in-operando*, electrolyte formulations not containing oxygen must be used. One of the more commonly used oxygen-free solvents for electrolyte formulations is acetonitrile, which has a chemical formula of CH_3CN.[21] Common electrolyte salts such as $LiPF_6$ or $NaPF_6$ can be readily dissolved in acetonitrile,[22] and it has also previously been used for *in-operando* studies of disordered rock salt cathode materials.[20] As such, 1 M $NaPF_6$ in acetonitrile was prepared as an oxygen-free electrolyte system to be used for *in-operando* studies. However, the disadvantage of using acetonitrile-based electrolytes is their incompatibility with Li or Na metal anodes, which react readily to form LiCN or NaCN. Therefore, alternative anode chemistries must be investigated.

As discussed in section 1.2.3, the voltage profile of a two-electrode cell is a combination of the voltage profiles of the anode and the cathode. In a conventional, half-cell set up using a Na metal anode, the Na/Na^+ reaction occurs at a constant voltage of ~0.3V vs Li/Li^+, providing a flat voltage plateau against which to cycle the desired cathode material. However, flat voltage profiles are not always present in electrode materials. Referring again to section 1.2.3, homogenous changes in composition will illicit a sloping voltage profile (i.e. single-phase behaviour), while inhomogeneous changes in composition will exhibit a flat voltage profile (i.e. two-phase behaviour). Thus, as an alternative to Na metal anodes, a Na-ion anode material displaying two-phase behaviour on discharge should be used. An example of such a material is $Na_2Mn_3O_7$.[9] While this material exhibits reversible, high-voltage O-redox behaviour on charge, on discharge it produces a flat voltage plateau at 2.05 V vs Na/Na^+, corresponding to the reduction of Mn^{4+} in response to further Na intercalation. A further 2 mols of Na can be intercalated into the material on discharge, producing a plateau capacity of ~120 mAh g^{-1} (Figure A4.2) at 2.05 V. On charge, (i.e. de-

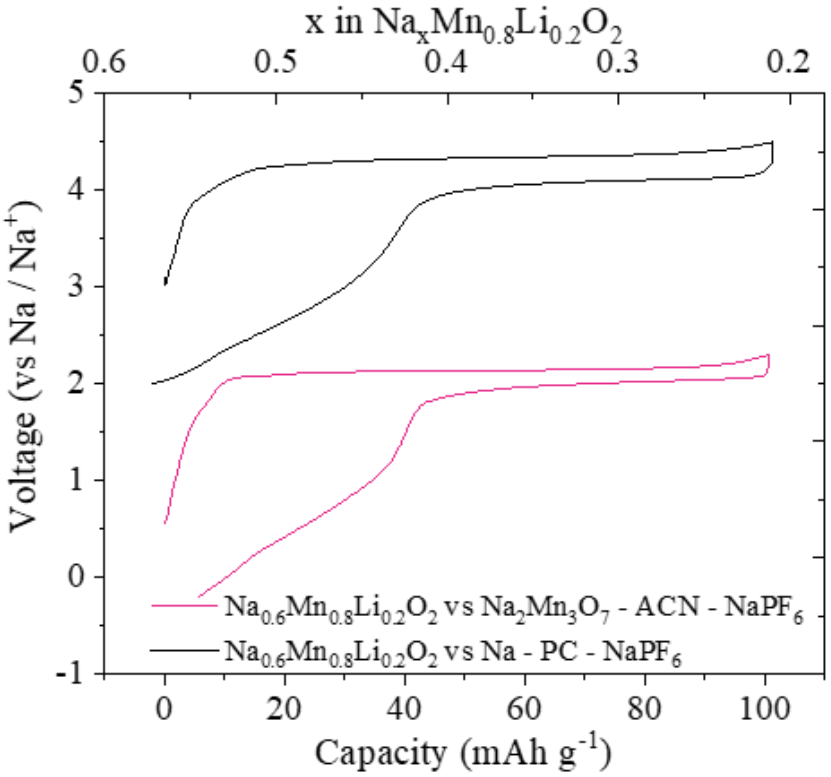

Figure 4.11: A comparison of the electrochemical cycling in the operando SXAS cell under external vacuum, between a conventional battery system and the oxygen free electrolyte system when cycling with NMLO. A cycling rate of 10 mA g^{-1} was used for both systems.

intercalation of Na^+ from the anode) this plateau remains present at a slightly higher voltage of 2.2 V due to a small amount of hysteresis in the material. To prepare the $Na_2Mn_3O_7$ anodes for cycling, the anode material was built into a coin cell and discharged for a period of 20 mins at a rate of 10 mA g^{-1}. This was done to ensure that the state of charge of the material lies on the flat voltage plateau, which will allow the cathode to be cycled against a relatively stable voltage profile.

Probing In-Operando Cell Performance with NMLO

The electrochemical cycling performance of the *operando* SXAS cell described in the chapter was tested using NMLO as the cathode material. At first, the *in-operando* cell was assembled with a NMLO cathode being cycled vs a Na metal anode. An electrolyte

formulation of 1 M $NaPF_6$ in PC was used. This system is identical to that used to test the material in coin cells. A second cell was assembled with a NMLO cathode being cycled vs a pre-cycled $Na_2Mn_3O_7$ anode and a 1 M $NaPF_6$ in ACN electrolyte formulation. This system represents the oxygen free electrolyte system developed for O K-edge *in-operando* studies. Both cells were assembled in an Ar filled glovebox with a 150 nm Si_3N_4 window in place, then cycled in a glovebox ante chamber under vacuum to simulate the conditions present on a SXAS beam line. The results of the cycling are shown in Figure 4.11.

The load curve for the oxygen free electrolyte system is shifted to lower voltages by ~2.1 V due to the operational voltage of the anode in that system. Both systems show excellent cycling, with each set-up reaching a charge capacity beyond 100 mAh g^{-1}. On discharge the characteristic high-voltage plateau of NMLO is observed. It is interesting to note that the oxygen free electrolyte system shows a slightly smaller hysteresis on discharge. This could be due to the difference in electrolyte systems being used between the systems.

This result demonstrates the ability of the SXAS *operando* cell to operate successfully with an oxygen free electrolyte system under vacuum conditions without bursting the Si_3N_4 membrane. The electrochemical cell presented and discussed above will allow for successful *in-operando* studies of the O K-edge in NMLO and other O-redox cathode materials.

It is worth noting that this particular project intended to present data probing the formation of electron holes in NMLO over the first charge as monitored by *in-operando* O K-edge XAS and RIXS. However, due to the significant impact of COVID-19 on this study, these measurements were unable to be completed. A more detailed overview of the impact of COVID-19 on this chapter is outlined at the beginning of this thesis.

4.4 Conclusion

In conclusion, *in-operando* measurements of the Mn K-edge in NMLO reveal that the oxidation of Mn^{4+} to Mn^{5+} or Mn^{7+} does not occur in this O-redox material, refuting previous

claims of Mn^{4+} oxidation in O-redox compounds. This finding confirms that electron hole formation on the oxide sub-lattice to be the main charge compensation mechanism. However, these electron holes were shown to be unstable over time using *ex-situ* O K-edge XAS and RIXS data. This lack of stability reinforces the need to develop new O-redox compounds with good stability over cycling. It also re-iterates the importance of developing *in-operando* XAS and RIXS techniques to enable a more complete study of O-redox compounds. To make such measurements possible, an electrochemical cell was successfully developed to be used for *in-operando* XAS and RIXS measurements on O-redox cathodes. This process involved the optimisation of an in-house cell design, as well as the development of an oxygen free electrolyte system.

4.5 References

1. Gourdin, G. & Doan-Nguyen, V. In situ, operando characterization of materials for electrochemical devices. *Cell Reports Phys. Sci.* **2**, 100660 (2021).
2. McCalla, E. *et al.* Visualization of O-O peroxo-like dimers in high-capacity layered oxides for Li-ion batteries. *Science (80-.).* **350**, 1516–1521 (2015).
3. House, R. A. *et al.* First-cycle voltage hysteresis in Li-rich 3d cathodes associated with molecular O2 trapped in the bulk. *Nat. Energy* **5**, 777–785 (2020).
4. House, R. A. *et al.* Superstructure control of first-cycle voltage hysteresis in oxygen-redox cathodes. *Nature* **577**, 502–508 (2020).
5. Luo, K. *et al.* Charge-compensation in 3d-transition-metal-oxide intercalation cathodes through the generation of localized electron holes on oxygen. *Nat. Chem.* **8**, 684–691 (2016).
6. Radin, M. D., Vinckeviciute, J., Seshadri, R. & Ven, A. Van Der. Mn oxidation as the origin of the anomalous capacity of Mn - containing Li - excess cathode materials. *Nat. Energy* 19–21 (2019) doi:10.1038/s41560-019-0439-6.
7. Du, K. *et al.* Exploring reversible oxidation of oxygen in a manganese oxide. *Energy Environ. Sci.* **9**, 2575–2577 (2016).
8. Eum, D. *et al.* Coupling structural evolution and oxygen-redox electrochemistry in layered transition metal oxides. *Nat. Mater.* (2022) doi:10.1038/s41563-022-01209-1.
9. Mortemard de Boisse, B. *et al.* Highly Reversible Oxygen-Redox Chemistry at 4.1 V in $Na_{4/7-x}[[_]_{1/7}Mn_{6/7}]O_2$ ([_]: Mn Vacancy). *Adv. Energy Mater.* **2**, 1800409 (2018).

10. Song, B. *et al.* Understanding the Low-Voltage Hysteresis of Anionic Redox in $Na_2Mn_3O_7$. *Chem. Mater.* 1–10 (2019) doi:10.1021/acs.chemmater.9b00772.

11. Tsuchimoto, A. *et al.* Nonpolarizing oxygen-redox capacity without O-O dimerization in $Na_2Mn_3O_7$. *Nat. Commun.* 1–7 doi:10.1038/s41467-020-20643-w.

12. Wang, Q. *et al.* Unlocking anionic redox activity in *O*3-type sodium 3d layered oxides via Li substitution. *Nat. Mater.* **20**, (2021).

13. Rietveld, H. M. A profile refinement method for nuclear and magnetic structures. *J. Appl. Crystallogr.* **2**, 65–71 (1969).

14. Toby, B. H. & Von Dreele, R. B. GSAS-II: The genesis of a modern open-source all purpose crystallography software package. *J. Appl. Crystallogr.* **46**, 544–549 (2013).

15. Yamamoto∗, T. Assignment of pre-edge peaks in K-edge x-ray absorption spectra of 3d transition metal compounds: electric dipole or quadrupole? *X-Ray Spectrom.* **37**, 572–584 (2008).

16. NIGAM, H.L. and Srivastava, U. G. X-Ray Absorption Edge Spectrometry (XAES) as applied to coordination chemistry. **9**, 275–310 (1973).

17. House, R. A. *et al.* Environmental Science Detection of trapped molecular O_2 in a charged Li-rich cathode by Neutron PDF. 376–383 (2022) doi:10.1039/d1ee02237g.

18. Grenier, A. *et al.* Nanostructure Transformation as a Signature of Oxygen Redox in Li-Rich 3d and 4d Cathodes. *J. Am. Chem. Soc.* **143**, 5763–5770 (2021).

19. House, R. A. *et al.* Covalency does not suppress O_2 formation in 4d and 5d Li-rich O-redox cathodes. *Nat. Commun.* **12**, 1–7 (2021).

20. Yamamoto, K. *et al.* Charge Compensation Mechanism of Lithium-Excess Metal Oxides with Different Covalent and Ionic Characters Revealed by Operando Soft and Hard X-ray Absorption Spectroscopy. *Chem. Mater.* **32**, 139–147 (2020).

21. Yamada, Y. *et al.* Unusual stability of acetonitrile-based superconcentrated electrolytes for fast-charging lithium-ion batteries. *J. Am. Chem. Soc.* **136**, 5039–5046 (2014).

22. Amara, S. *et al.* Comparative Study of Alkali-Cation-Based (Li^+, Na^+, K^+) Electrolytes in Acetonitrile and Alkylcarbonates. *ChemPhysChem* **20**, 581–594 (2019).

Chapter 5

Pillaring as a Strategy to Prevent Bulk Formation of Molecular O_2

Table of Contents

5.1 Introduction 125

5.2 Experimental 128

5.3 Results 130

5.3.1 Synthesis and Characterisation of $NaMn_{0.72}Mg_{0.28}O_2$ 130

5.3.2 Investigation of Ca^{2+} Insertion into $Na_{0.67}Mn_{0.72}Mg_{0.28}O_2$ 131

5.3.3 Confirming the Presence of Ca^{2+} in $Na_{0.47}Ca_{0.1}Mn_{0.72}Mg_{0.28}O_2$ 135

5.3.4 Evaluating Ca^{2+} Insertion Limits in $Na_{0.67-2x}Ca_xMn_{0.72}Mg_{0.28}O_2$ 137

5.3.5 Electrochemical Analysis of $Na_{0.47}Ca_{0.1}Mn_{0.72}Mg_{0.28}O_2$ 140

5.3.6 Discussion 142

5.4 Conclusion 144

5.5 References 145

5.1 Introduction

O-redox activity has been demonstrated to occur in a number of different material systems: Li-rich layered oxides comprising of 3d, 4d and 5d TM,[1–3] disordered rock salt materials,[4,5] and Na-ion layered oxides.[6,7] However, the vast majority of these examples demonstrate O-redox activity which leads to the formation of molecular O_2 in the bulk. Moreover, the small number of example materials which do demonstrate reversible, high voltage O-redox are model Na-ion cathode materials, not suited for commercial applications.[8,9] In order to expand the applicability of O-redox cathode materials, efforts must be directed towards improving the reversibility of O-redox activity over cycling. The

ideal O-redox cathode would show a long, high voltage plateau on charge which could be reversibly cycled on discharge. This can be achieved by inhibiting the formation of molecular O_2 during the charging process, thus facilitating the reversible formation of electron holes on oxygen (O^{2-}/O^{-}) during extended cycling.

$Na_{0.67}Mn_{0.72}Mg_{0.28}O_2$ (NMMO) is an O-redox active cathode material exhibiting a long, high-voltage plateau which has been attributed to O-redox.[10] However, the material shows a large hysteresis on discharge, due to the formation of molecular O_2 during charging. Further investigations by E. Boivin et al. showed that the formation of molecular O_2 is facilitated by the reversible out of plane migration of Mg from the TM layer in NMMO.[11] This migration is caused by the phase transition from *P*2 to *O*2 type stacking which occurs in NMMO during charging, allowing Mg^{2+} to migrate from the TM layer into tetrahedral sites which leaves behind a vacancy for intra-layer migration to occur.

In this chapter, the possibility of promoting the reversible cycling of the O^{2-}/O^{-} redox couple in NMMO is explored using a pillaring strategy (Figure 5.1). The pillaring of layered structures using large cations such as K^{+} has already been studied as a method to alleviate detrimental structural transitions that Na-ion cathodes undergo during desodiation.[12,13] Pillaring also represents a promising strategy to improve the cyclability of O-redox materials by preventing phase transitions in Na-ion cathodes which occur during charging. This will inhibit the inter-layer migration of cations, which leads to the formation of trapped O_2 during cycling, thus facilitating the reversible cycling of the O^{2-}/O^{-} redox couple.

For the implementation of this strategy, NMMO was chosen due to its facile synthesis and large O-redox capacity.[10] In addition, Ca^{2+} was chosen as the pillaring cation as it has a similar ionic radii to Na^{+}.[14] The ion-exchange process presented in this chapter is a solvent-free, room temperature ion-exchange method involving the simple mechanical mixing of

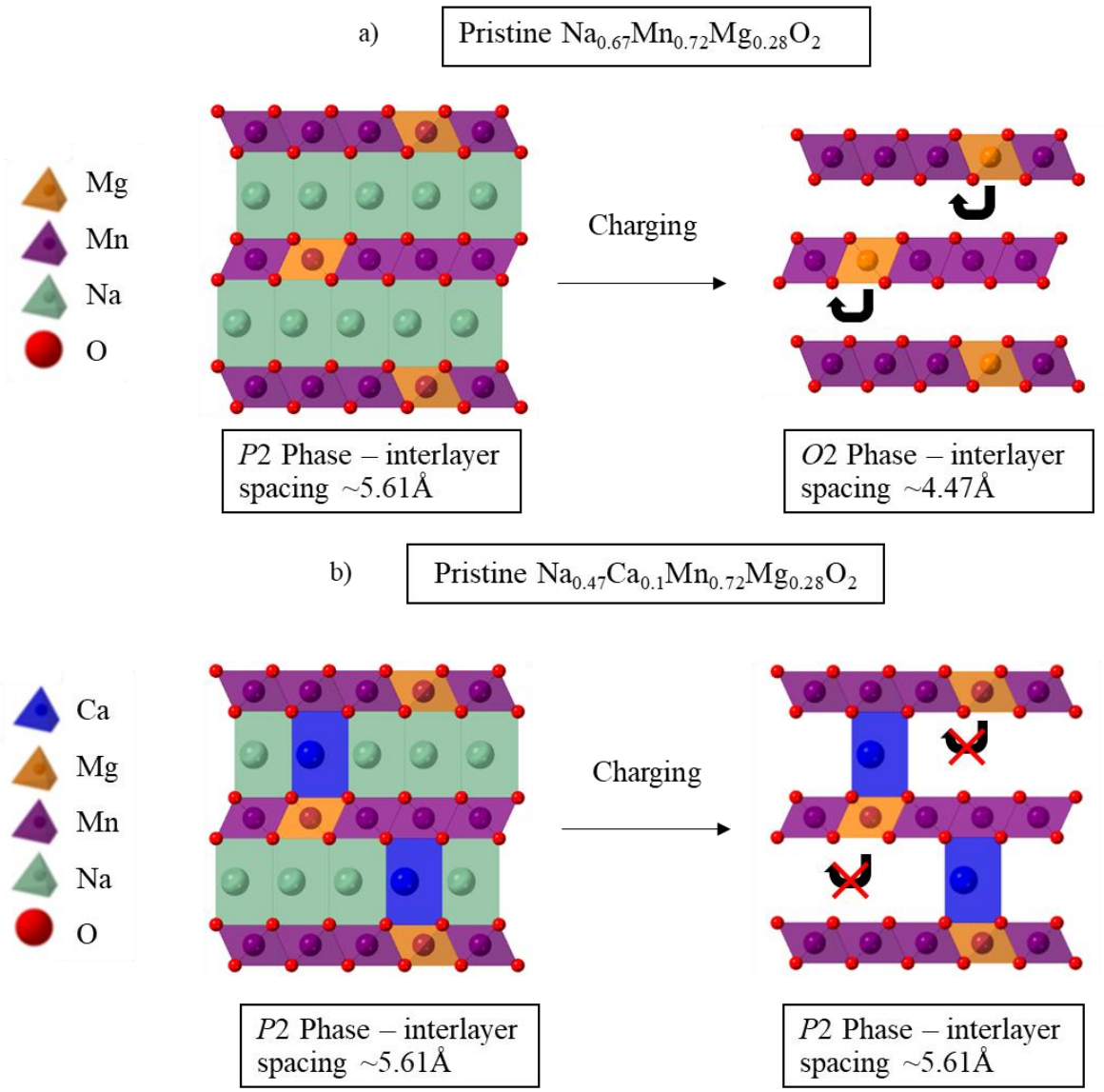

Figure 5.1: Demonstrating the effect of pillaring on NMMO. a) Pristine, *P*2-type $Na_{0.67}Mn_{0.72}Mg_{0.28}O_2$ material, which undergoes a phase transformation from *P*2 to *O*2 during charge, facilitating the migration of cations out of plane. b) Ca^{2+} doped NMMO. It is hoped that by doping large Ca^{2+} ions into the AM layer, phase changes to *O*2 will be prevented, inhibiting the out-of-plane migration of cations.

CaI_2 with NMMO under ambient conditions. The reaction proceeds in the solid-state via the formation of crystalline hydrates of CaI_2 which form spontaneously when exposed to air. The ion-exchanged materials are characterised using a combination of PXRD, ICP-OES, SEM/EDX and EELS, demonstrating the successful incorporation of Ca^{2+} into the layered cathode up to a limit of about 0.1 Ca. In addition, the electrochemical behaviour of the ion-exchanged material is discussed.

5.2 Experimental

Solid state synthesis: $Na_{0.67}Mn_{0.72}Mg_{0.28}O_2$ was synthesized via a solid-state reaction using stoichiometric amounts of Na_2CO_3 (≥99.0%, Aldrich), MgO (≥99.99%, Aldrich) and Mn_2O_3 (≥99.9%, Aldrich). A planetary ball-mill was used to mix the precursors for 2 h at a rotation speed of 350 rpm. The precursors were then pelletized and heated at 800 °C for 10 hrs under flowing O_2 then cooled to room temperature at 5°C min^{-1}.

Electrochemical characterisation: Both cells and electrodes were prepared and assembled/disassembled in a glove box under an inert atmosphere. Electrodes were prepared by combining the active material (80wt%) and Super P carbon (10wt%) in a mortar and pestle before adding polytetrafluoroethylene binder (10wt%). The electrode film was then rolled to a thickness of ~ 100 μm. Electrodes were assembled into coin cells using glass fibre separators and 1M $NaPF_6$ in propylene carbonate (PC) electrolyte, with a Na metal counter electrode. Galvanostatic cycling was carried out using a Maccor Series 4000. Cycling was performed between 2.0 V and 4.5 V vs Na^+/Na at a rate of 10 mA g^{-1} for all cells.

Ion exchange procedure: To form the Ca-ion exchanged product of $Na_{0.67}Mn_{0.72}Mg_{0.28}O_2$, appropriate molar amounts of CaI_2 (≥98.0%, Aldrich) and pristine $Na_{0.67}Mn_{0.72}Mg_{0.28}O_2$ were weighed out in a glovebox and mixed by hand using a mortar and pestle. The targeted ion-exchanged products were represented by $Na_{0.67-2x}Ca_xMn_{0.72}Mg_{0.28}O_2$ (x = 0.05, 0.1, 0.15). The mixture was then left in air for 6hrs. The powders were washed with acetone three times, to remove the NaI by-product, dried and moved into a glovebox under inert argon atmosphere.

PXRD: In-situ PXRD measurements, diffraction data were collected on a Rigaku 9 kW SmartLab Cu-source diffractometer. All other diffraction data were collected on a Rigaku MiniFlex 650 W Cu-source diffractometer.

SEM: SEM imaging and EDX analysis was performed on a Carl Zeiss Merlin high resolution field emission gun SEM instrument by Shengda Pu.

ICP-OES: Pristine and Ca-exchanged $Na_{0.67}Mn_{0.72}Mg_{0.28}O_2$ samples were dissolved in aqua regia ($HCl:HNO_3$ / 25:75 by weight), before diluting the solution by a factor of 200 for measurement to feed into the ICP. Standard solutions of Na, Ca, Mg and Mn were used to create calibration curves for analysis. Elemental analysis was carried out by ICP-OES using a Perkin-Elmer Optima 7300DV ICP-OES.

EELS: EELS data were collected on an aberration corrected JEOL ARM 200F operated at 200 kV and equipped with a Gatan GIF Quantum 965 ER. The convergence semi angle used was 22 mrad, and the collection semi angle was 69.6–164.8 mrad (ADF). EELS peak area plots were obtained by performing a power-law background subtraction fitted to a 20-30eV window before the edges of interest and integrating under the Ca L peaks and Mn L peaks. This data was collected and formatted by Dr. Alex Robertson.

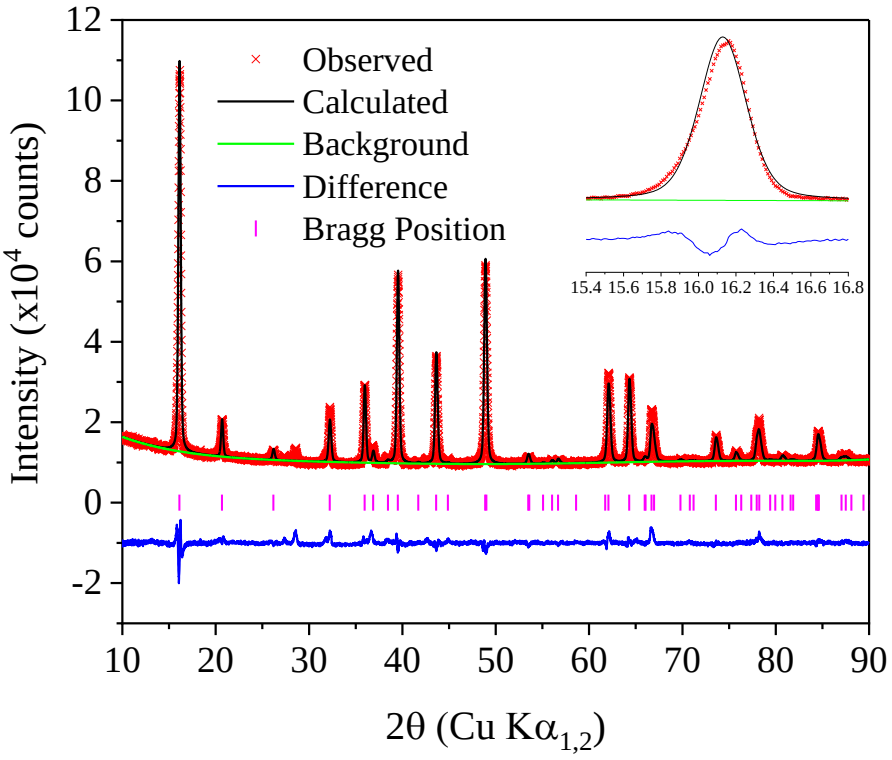

Figure 5.2: PXRD refinement for pristine NMMO. PXRD was collected on a Rigaku 650 W diffractometer contained inside a N_2 filled glovebox.

5.3 Results

5.3.1 Synthesis and Characterisation of $NaMn_{0.72}Mg_{0.28}O_2$

NMMO was successfully synthesised by solid state reaction, with the resulting PXRD data and Rietveld refinement confirming the structure is *P*2-type (Figure 5.2 and Table A5.1). The material contains an *ab ba* stacking of the oxide sub-lattice and was refined to the *P*63/*mcm* space group. Honeycomb ordering of the Mn and Mg ions in the TM layer was evidenced by a peak in the diffraction pattern at ~22° 2θ. During the refinement, the total fractions at each Mn/Mg site (2*b* and 4*d*) were constrained to be equal 1.0 at each site. U_{iso} values were not refined and set to 0.01 $Å^2$ at each crystallographic site.

Electrochemical testing of the material shows the characteristic high-voltage plateau attributed to O-Redox in this material, which leads to a large hysteresis on discharge (Figure 5.3). This hysteresis has been previously attributed to the reversible out of plane migration

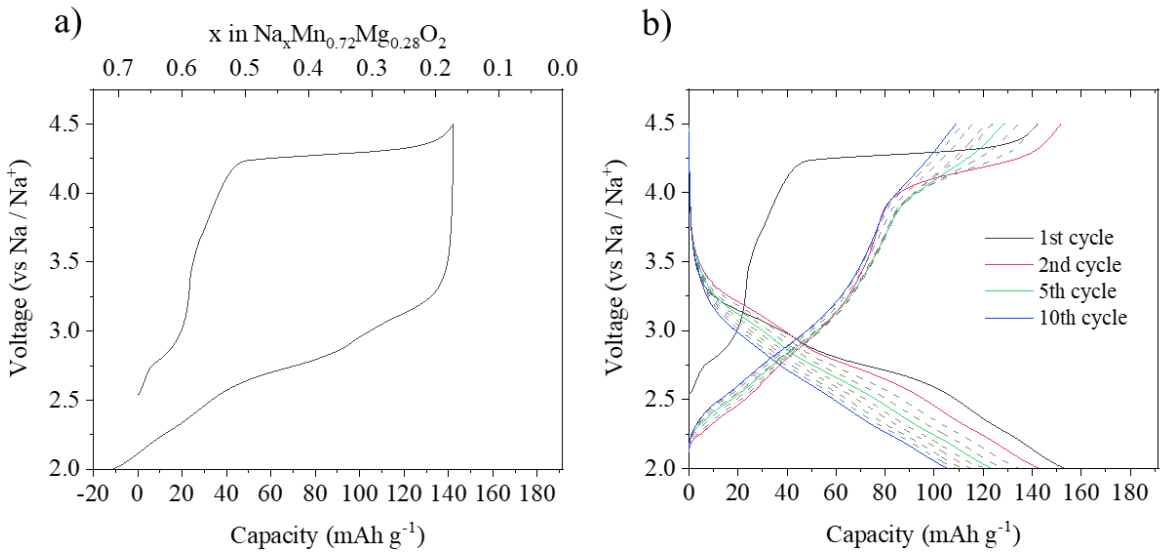

Figure 5.3: a) First cycle load curve for NMMO. b) Galvanostatic cycling for the first 10 cycles of NMMO The material was cycled at a rate of 10 mA g^{-1} between a voltage window of 2.0 V and 4.5V.

of the Mg^{2+} cation from the TM layer into tetrahedral sites of the *O*2 type stacked material at the top of charge.[11] The material was cycled at a rate of 10 mA g^{-1} between a voltage window of 2.0 V and 4.5 V vs Na^+/Na. Beyond the first cycle, a shortened high-voltage plateau was present on charge. The plateau length continues to diminish over the first 10 cycles of the material.

5.3.2 Investigation of Ca^{2+} Insertion into $Na_{0.67}Mn_{0.72}Mg_{0.28}O_2$

Ion-exchange procedures can be carried out using a variety of methods, including *chimie douce*, where a material is dispersed in a concentrated metal halide solution (LiBr, $CaBr_2$, etc…),[15–17] or molten salt exchange methods.[18] However, these methods must be used for the full ion-exchange of a material. Initially, Ca insertion was going to be carried out using a thermally driven exchange reaction between a Ca salt and the pristine Na-ion cathode. A similar method had been previously used to make $Ca_{0.5}CoO_2$ from $NaCoO_2$.[19]

Surprisingly, it was found the ion-exchange of $2Na^+$ with Ca^{2+} proceeded spontaneously in air between the mixed solids, without the need for elevated temperatures. The method behind this solid-state, room temperature partial ion-exchange of NMMO is

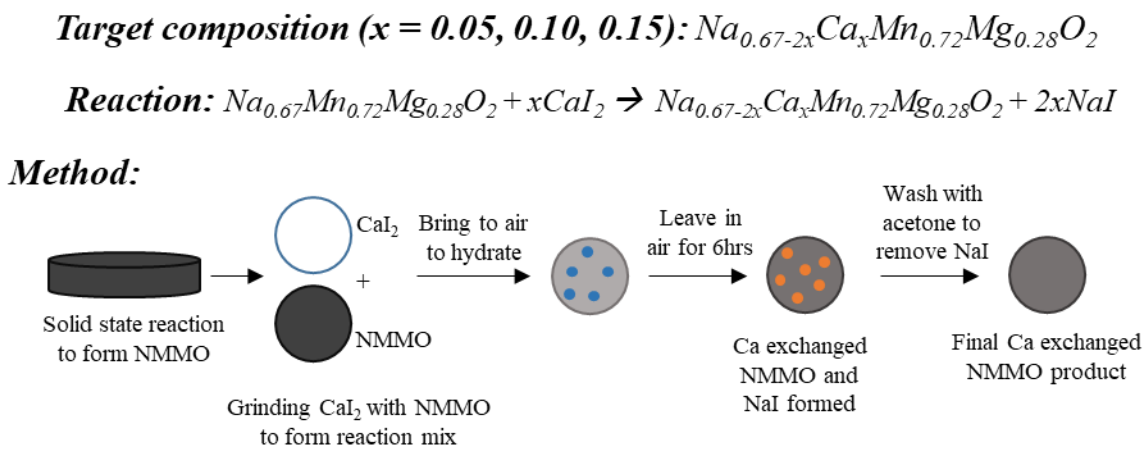

Figure 5.4: Description of the Ca^{2+} insertion synthesis process. All these steps are carried out in air. The final product can be transported into a glovebox for further characterisation.

described in Figure 5.4. CaI_2 and pristine NMMO were ground together in a glovebox in the desired stoichiometric amount to make $Na_{0.67-2x}Ca_xMn_{0.72}Mg_{0.28}O_2$ (x = 0.05, 0.1, 0.15). The mixture was then bought out to react in air for 6 hrs, before washing with acetone and then drying under vacuum. To follow the ion-exchange process in air over time, CaI_2 and NMMO mixed in a mole ratio of 0.1:1 were ground together in a glovebox, then removed to air and measured *in situ* with PXRD (Figure 5.5). CaI_2 is highly hygroscopic and initially forms two hydrated phases with moisture in the air within minutes of exposure (denoted by the orange and green arrows, right hand panel). After just 7 mins there is evidence for the formation of NaI as a product of the ion-exchange reaction, as diffraction peaks at $2\theta = 23^o$, 27° and 47° degrees (denoted by red-arrows, right hand panel) begin to appear. After 14 minutes the peak intensities of the NaI begin to decay as the salt hydrates leading to a loss of crystallinity. The exchange process is also evidenced by the continual shift in the 002 peak during the reaction (Figure 5.5, left-hand panel) showing a continuous increase in the *c* lattice parameter. While Na^+ is being removed for Ca^{2+}, the overall removal of 0.1 mol of cations from the AM layer would decrease the cationic screening between the oxide sub-lattice. This increases inter-TM layer repulsions leading to an increase in inter layer spacing.

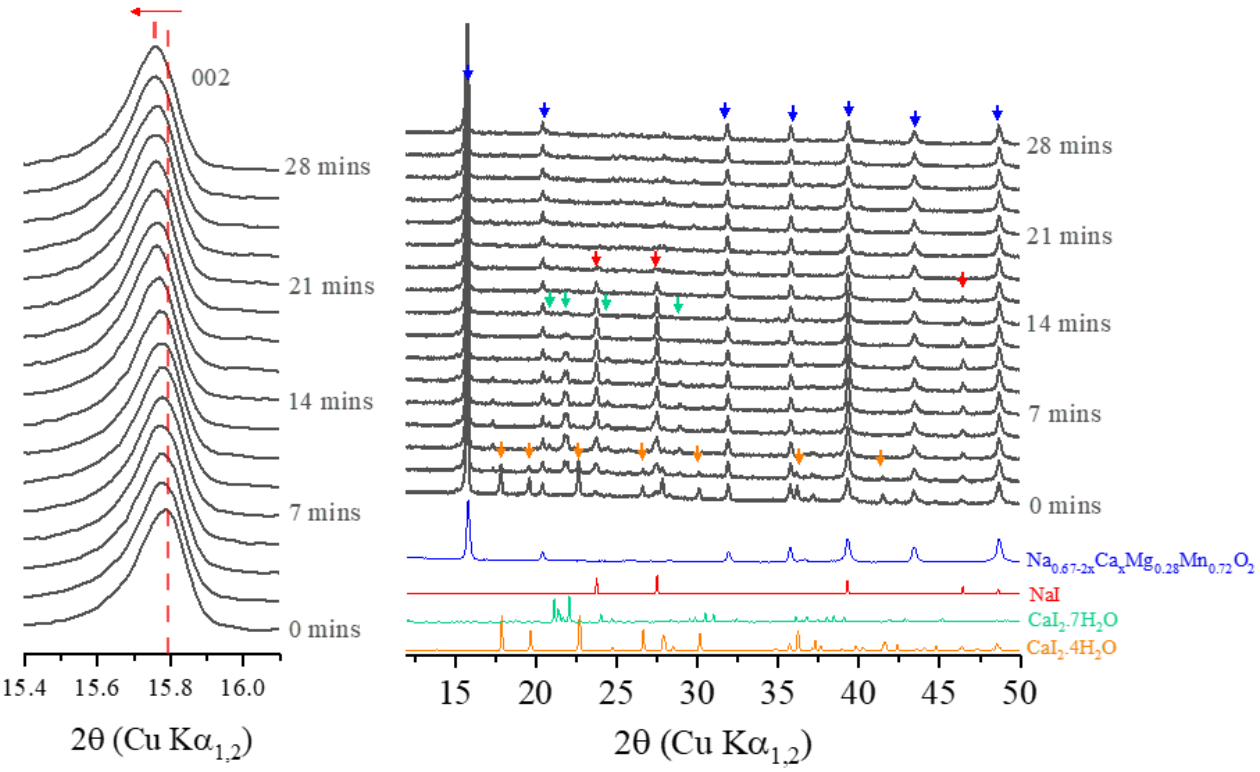

Figure 5.5: In-situ measurement of the reaction mixture of NMMO and CaI_2 being left in an air atmosphere. The spectra clearly show the formation of NaI in significant quantities after just 14 mins. Beyond this point, the iodide salts are no longer crystalline through hydration.

From the in-situ experiment it appears that iodide hydration may play a role in the ion exchange process. To investigate the impact of H_2O exposure on the reaction, mixtures of NMMO and CaI_2 were left for several hours in the absence and in the presence of ambient moisture to investigate possible reaction mechanisms. Mixtures of NMMO and CaI_2 were left to react in a N_2 atmosphere and in air. In the first example when reacting under N_2 in the absence of H_2O, no evidence of reaction between the calcium precursor and the pristine material was found (Figure 5.6 a). CaI_2 is clearly evidenced in the PXRD, even after being left to react for 6 hrs. In the second example NMMO and CaI_2 were mixed together in a N_2 filled glovebox then bought out to react in air. The mixture was then bought

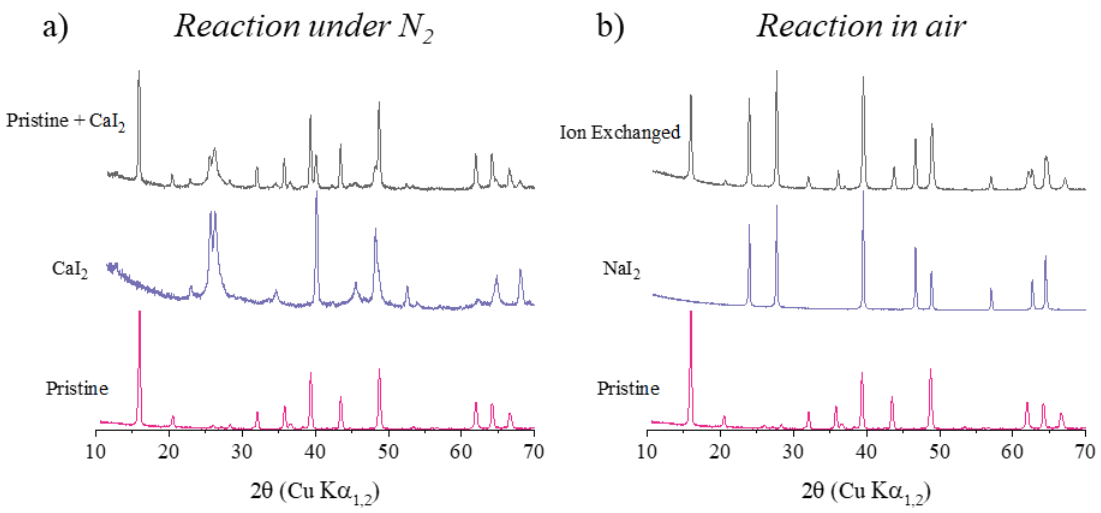

Figure 5.6: Comparing the insertion of Ca into NMMO to form CaNMMO under different conditions. a) XRD spectra of pristine NMMO, CaI_2 and the reaction mixture of NMMO and CaI_2 after being left in a N_2 atmosphere for 6hrs. b) XRD spectra of pristine NMMO, NaI and the ion exchanged product after being left in an air atmosphere for 6 hrs.

back into a N_2 filled glovebox to measure the sample by PXRD. In the dry conditions of the glovebox the hydrated salts recrystallise showing the formation of NaI to be present in the ion exchanged mixture after reacting in air (Figure 5.6 b) suggesting that a direct exchange of Ca for Na has occurred. It should also be noted that no CaI_2 is seen in the ion exchanged product after reacting in air. To remove the NaI waste product, the sample was washed four times in acetone then dried under vacuum overnight before being placed in a glovebox for storage. The effect of acetone on the cycling of the material was negligible, as shown in Figure A5.1.

Overall, this data shows that the hydration of CaI_2 is necessary to promote the room temperature ion-exchange of Ca^{2+} for Na^{+} in $Na_{0.67}Mn_{0.72}Mg_{0.28}O_2$. The proposed mechanism for ion exchange is as follows: CaI_2 (a hygroscopic salt) is hydrated from moisture in the air, and when placed in contact with $Na_{0.67}Mn_{0.72}Mg_{0.28}O_2$, exchange between Ca and Na readily occurs within the hydrated phase, leaving NaI as a by-product.

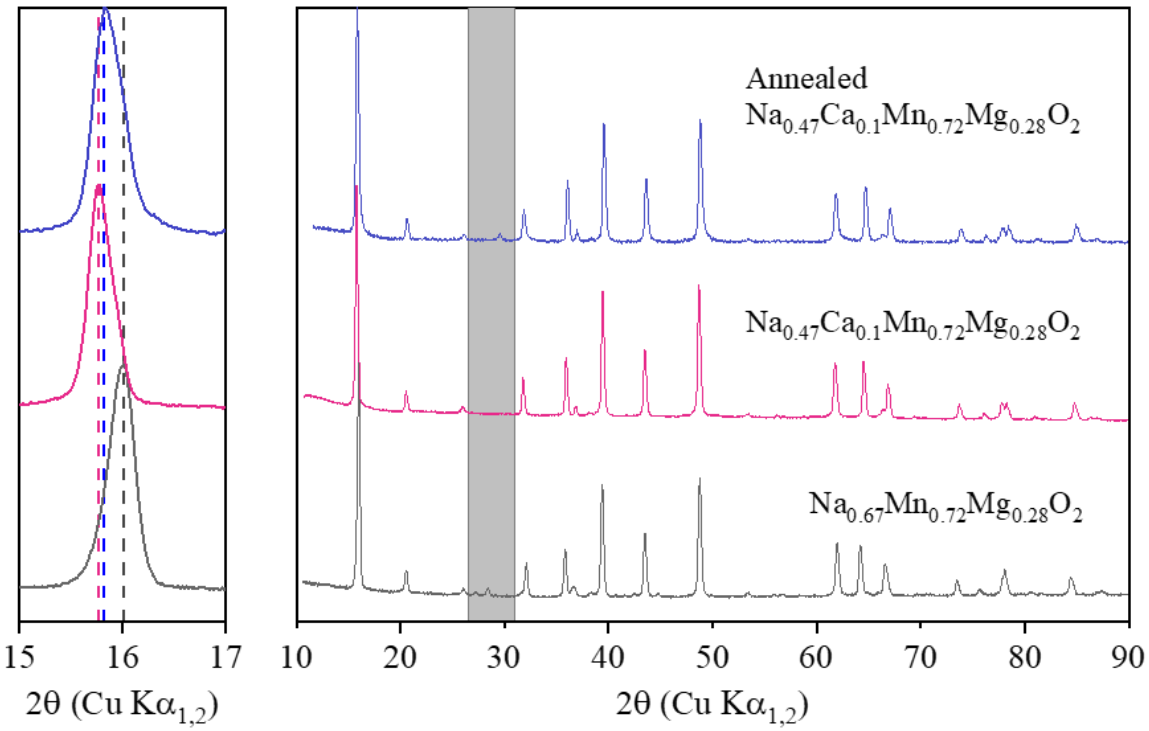

Figure 5.7: XRD comparison of NMMO, CaNMMO and annealed CaNMMO. The left-hand panel shows the shift of the 002 peak in more detail, while the shaded region in the right-hand panel highlights the peaks which arise from ordering in the AM layer.

5.3.3 Confirming the Presence of Ca^{2+} in $Na_{0.47}Ca_{0.1}Mn_{0.72}Mg_{0.28}O_2$

Following the successful reaction between CaI_2 and NMMO, further characterisation of the ion-exchanged product of $Na_{0.47}Ca_{0.1}Mn_{0.72}Mg_{0.28}O_2$ (CaNMMO) was performed to verify the presence of Ca^{2+} after ion-exchange. First, PXRD was performed to analyse the material structure (Figure 5.7). It is clear the structure remains *P*2-type after Ca insertion, implying that Ca occupies trigonal prismatic sites in the Na layer. A shift can be seen in the 002 peak after Ca insertion indicating an increase in the *c* lattice parameter from 11.191461 (4) Å to 11.275804 (4) Å (Table 5.2) in line with successful Ca^{2+} exchange. Furthermore, there is evidence of a change in Na-ion ordering. In the pristine material, two peaks at ~27° 2θ arise due to Na-ion ordering in the AM layer.[20] After the initial room temperature ion exchange, these peaks disappear revealing a change to the Na-ion ordering by the introduction of Ca^{2+}.

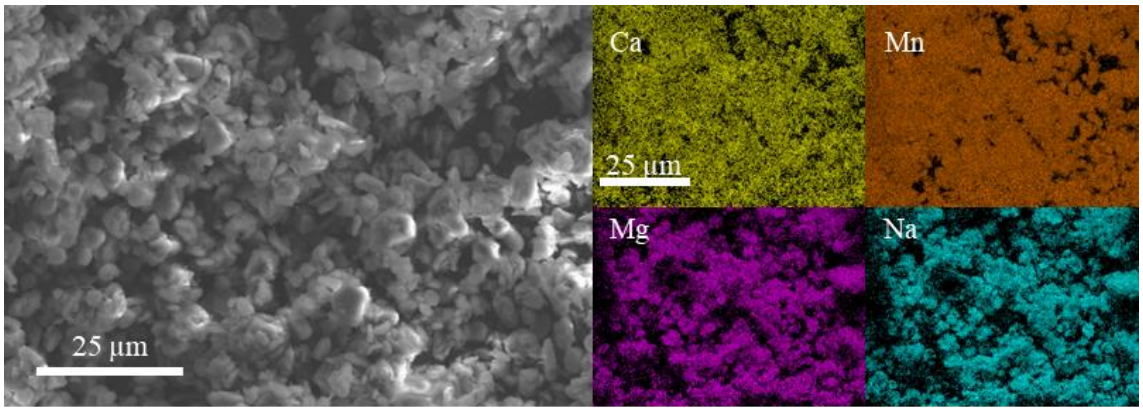

Figure 5.8: SEM and EDX analysis of CaNMMO. The SEM image reveals small, plate like particles about 1-2 µm in size. A homogenous distribution of all elements can be seen in the EDX analysis.

Ordering within the AM layer appears to be re-introduced after annealing at 350°C for 48hrs, with a new peak appearing in this region (Figure 5.7). After annealing the *c* lattice parameter changes slightly, from 11.275804 (4) Å to 11.283602 (1) Å, possibly due to the re-ordering of the AM ions within the layer. All further characterisation was done on non-annealed samples.

Next, SEM and EDX analysis of CaNMMO exchanged at room temperature were performed to investigate the elemental distribution within the material. A low magnification image was taken to ensure that a large number of particles were probed. The SEM image reveals a plate like morphology to the particles, with a size of 1–2 µm. The EDX reveals a homogenous distribution of Ca (yellow) and Mn (orange), showing that the ion-exchange has occurred across the whole sample. To probe Ca distribution deeper into the bulk, EELS line scans were conducted on single particles of CaNMMO. For these experiments, the EELS spectra for the Ca and Mn L-edges were continuously monitored across the particle. Integrating the area under the peaks for each element provides an elemental distribution across the line scan. By comparing the peak areas from the EELS spectra of Mn and Ca across the line scan, the relative concentrations of these elements across the particles can be obtained. This data, presented in Figure 5.9, reveals that the Mn and Ca concentrations

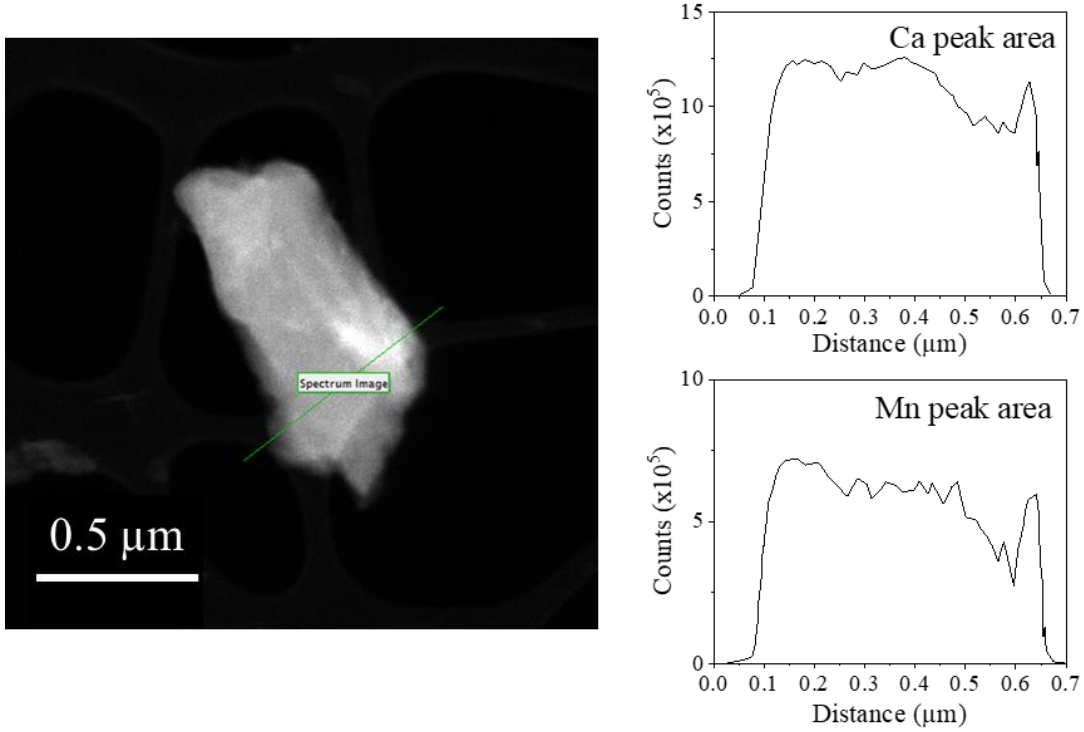

Figure 5.9: STEM image of a CaNMMO particle being analysed by EELS. The EELS line scan can be seen in green in the left-hand image. Mn and Ca peak areas from the EELS line scan are shown on the right. The similar shapes in the traces indicate that Ca has been introduced to the bulk of the structure.

across the particle follow a very similar trend, suggesting that Ca has indeed been introduced to the bulk of the particle via room temperature ion exchange. Another example of an EELS line scan is presented in Figure A5.2. Taken together, PXRD, EDX and EELS analysis confirm homogeneous incorporation of Ca within the Na layers throughout the bulk of the particles.

5.3.4 Evaluating Ca^{2+} Insertion Limits in $Na_{0.67-2x}Ca_xMn_{0.72}Mg_{0.28}O_2$

To investigate the extent to which Ca could be exchanged into NMMO, the exchange of Ca^{2+} was attempted in different molar amounts (x = 0.05, 0.1, 0.15) to form $Na_{0.67-2x}Ca_xMn_{0.72}Mg_{0.28}O_2$. The products of these syntheses were characterised by ICP (Table 5.1) and PXRD (Table 5.2). For the x = 0.05 , 0.1 and 0.15 exchanges, the ICP results confirm

Target composition	Element	Na	Mn	Mg	Ca
$Na_{0.67}Mn_{0.72}Mg_{0.28}O_2$	Concentration (ppm)	0.89 (4)	2.52 (5)	0.35 (2)	-
	Normalized Composition	0.64 ± 0.03	0.76 ± 0.03	0.24 ± 0.02	0
$Na_{0.57}Ca_{0.05}Mn_{0.72}Mg_{0.28}O_2$	Concentration (ppm)	0.64 (4)	2.16 (6)	0.32 (1)	0.08 (1)
	Normalized Composition	0.53 ± 0.04	0.75 ± 0.04	0.25 ± 0.01	0.04 ± 0.002
$Na_{0.47}Ca_{0.10}Mn_{0.72}Mg_{0.28}O_2$	Concentration (ppm)	0.62 (5)	2.39 (2)	0.32 (3)	0.17 (1)
	Normalized Composition	0.48 ± 0.04	0.77 ± 0.01	0.23 ± 0.02	0.07 ± 0.005
$Na_{0.37}Ca_{0.15}Mn_{0.72}Mg_{0.28}O_2$	Concentration (ppm)	0.54 (5)	2.10 (3)	0.29 (2)	0.12 (1)
	Normalized Composition	0.47 ± 0.05	0.77 ± 0.05	0.23 ± 0.02	0.07 ± 0.006

Table 5.1: ICP-OES results from the various Ca-inserted compounds.

the successful exchange of Na^+ for Ca^{2+}. Ca^{2+} concentrations were found to be close to the targeted compositions for the 0.05 and 0.1 insertion runs (0.04 ± 0.002 and 0.07 ± 0.005 respectfully), however for the 0.15 insertion run only a molar amount of 0.07 ± 0.006 Ca^{2+} could be inserted. These results suggest that Ca can be successfully exchanged up to a limit of approximately 0.07, beyond which the excess Ca remains as CaI_2 and is washed away in the acetone. The synthesis products were also analysed by PXRD. LeBail fittings were carried out to extract the lattice parameter information for each sample, which are seen to change significantly for each sample, with a contraction in the *a* lattice parameter and an expansion of the *c* lattice parameter being observed with increasing Ca insertion (Table 5.2). As mentioned above, the removal of Na-ions from the AM layer removes a proportion of

Target composition	Measured composition	*a*	*c*
$Na_{0.67}Mn_{0.72}Mg_{0.28}O_2$	$Na_{0.64}Mn_{0.76}Mg_{0.24}O_2$	5.040256 (9) Å	11.191461 (4) Å
$Na_{0.57}Ca_{0.05}Mn_{0.72}Mg_{0.28}O_2$	$Na_{0.53}Ca_{0.04}Mn_{0.75}Mg_{0.25}O_2$	5.007496 (9) Å	11.237613 (4) Å
$Na_{0.47}Ca_{0.10}Mn_{0.72}Mg_{0.28}O_2$	$Na_{0.48}Ca_{0.07}Mn_{0.77}Mg_{0.23}O_2$	5.005222 (6) Å	11.275804 (4) Å
$Na_{0.47}Ca_{0.10}Mn_{0.72}Mg_{0.28}O_2$ Annealed	$Na_{0.48}Ca_{0.07}Mn_{0.77}Mg_{0.23}O_2$ Annealed	4.998234 (2) Å	11.283602 (1) Å
$Na_{0.37}Ca_{0.15}Mn_{0.72}Mg_{0.28}O_2$	$Na_{0.47}Ca_{0.07}Mn_{0.77}Mg_{0.23}O_2$	5.002044 (7) Å	11.273604 (8) Å

Table 5.2: Le Bail fit results from the various Ca-inserted compounds.

the shielding these cations provide between the oxide layers. As this shielding is decreased, the electrostatic repulsion between the layers will increase, thus expanding the *c* axis parameter. As such, the *c* axis is seen to expand from 11.191461 (4) Å to 11.237613 (4) Å between the pristine NMMO sample and the 0.05 insertion sample. This expands further in the 0.01 insertion sample to 11.275804 (4) Å. However, comparing the 0.01 and 0.15 insertion samples shows that both samples exhibit similar lattice parameters (Table 5.2), in line with the previous ICP-OES result. The contraction in the *a* lattice parameter could be linked to the *c* axis expansion, as the TM layers will be compressed on both sides from the repulsed oxide sub-lattice, causing a lattice contraction within the TM layer, leading to a decrease in the *a* lattice parameter. Following on from the characterisation of the Ca-inserted samples, the electrochemical behaviour of CaNMMO was investigated.

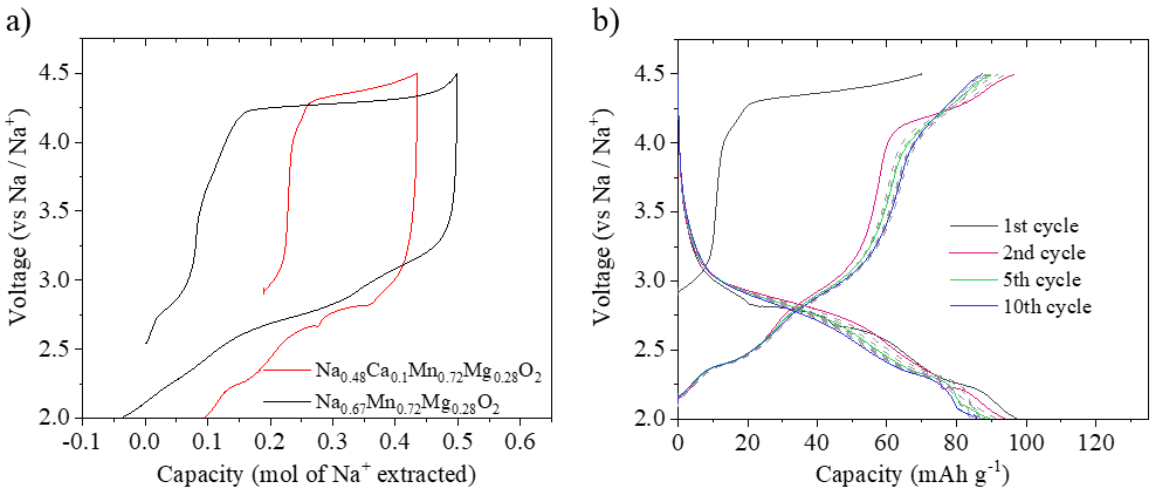

Figure 5.10: Structural and electrochemical characterisation of CaNMMO. a) Load curve comparison of CaNMMO and NMMO plotted vs mol of Na de-intercalated. Both materials were cycled at 10 mA g^{-1}. b) Galvanostatic cycling for the first 10 cycles of CaNMMO at a rate of 10 mA g^{-1} between a voltage window of 2.0 V and 4.5 V.

5.3.5 Electrochemical Analysis of $Na_{0.47}Ca_{0.1}Mn_{0.72}Mg_{0.28}O_2$

The effect of Ca-ion exchange on the electrochemical behaviour of NMMO was investigated by assembling Na half cells with CaNMMO as the cathode active material. Figure 5.10 shows the first cycle of NMMO compared to the first cycle of CaNMMO. Both cells were cycled galvanostatically at a rate of 10 mA g^{-1} within a voltage widow of 2.0 V and 4.5 V. NMMO is plotted as starting at 0.0 mol of Na, while CaNMMO is plotted as starting from 0.19 mol of Na due to its lower Na content after exchange (Table 5.1). The ion-exchanged material exhibits the same high voltage plateau that is seen in NMMO during the first charge, with the plateau length being noticeably shorter due to the removal of ~0.19 mol of Na during the ion exchange process. On charge the ion exchanged material reaches 0.45 mol of Na de-intercalation (adjusted for the loss of Na during exchange) in comparison to pristine NMMO which reaches 0.5 mol of Na de-intercalation. However, on the first discharge, a large hysteresis is observed in the ion-exchange material. Over the first 10

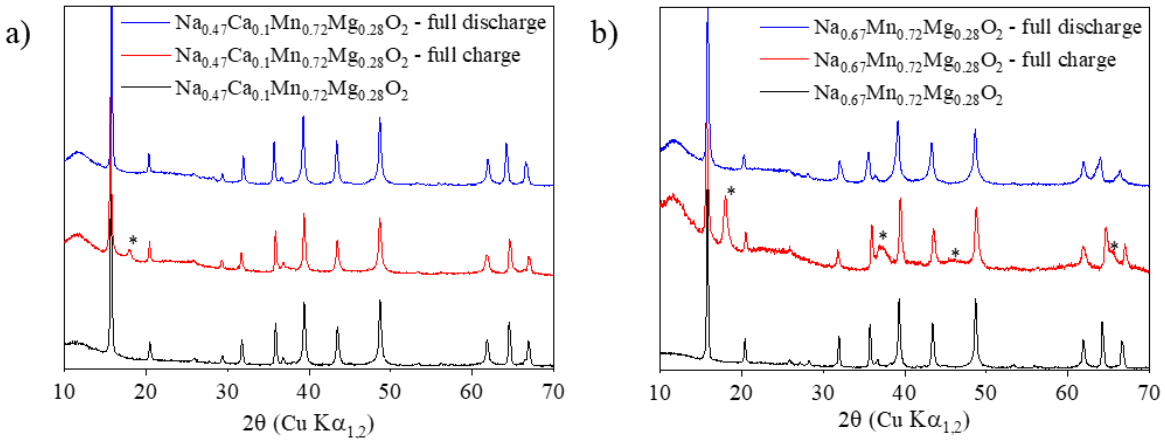

Figure 5.11: PXRD comparison of a) CaNMMO and b) NMMO in the pristine, charged, and discharged states. The * denote the peaks arising from the *O*2 phase of the material.

cycles this does not improve as the hysteresis continues to be observed and the high-voltage plateau observed on the first cycle is gradually lost. No significant improvement to the hysteresis observed on charge was observed.

To further investigate why the ion-exchanged material continues to show hysteresis, PXRD was used during the first cycle to investigate the structural evolution over cycling in both $Na_{0.47}Ca_{0.1}Mn_{0.72}Mg_{0.28}O_2$ and NMMO (Figure 5.11). In NMMO, a clear phase transition from *P*2 to *O*2 is observed by the appearance of a peak at ~ 18° 2θ in the fully charged sample, in line with previous measurements on this material.[10] On discharge, the material returns to *P*2. In CaNMMO, a small peak appears at ~ 18° 2θ in the fully charged sample, suggesting that a smaller amount of the material is undergoing phase transitions from *P*2 to *O*2 type. However, CaNMMO also undergoes a much smaller amount of de-intercalation of Na^+ from the material, meaning a smaller amount of phase transition would be expected. On discharge, the material also reverts back to a *P*2 structure. Disappointingly, this data suggests that the insertion of Ca^{2+} into NMMO has not prevented the *P*2 to *O*2 phase transition from occurring in NMMO, thus leading to the formation of molecular O_2 in the bulk of the cathode.

5.3.6 Discussion

Typically, ion exchange is performed using *Chemie Douce* methods to synthesise thermodynamically metastable compounds that cannot be prepared by conventional reaction between solids at high temperature.[16,21–23] Such methods usually involve exposing the material to be modified to a salt containing the ion to be introduced, with the salt being either in the molten state or as the solute of a solution.[19] However, the method described in this chapter presents a new route to preparing ion-exchanged materials for layered AM cathode materials, with potential applications elsewhere in battery research. One of the biggest challenges facing Na-ion cathodes is the prevalence of phase transitions at high voltage, associated with poor cycling stability. Several strategies to prevent phase transitions in Na-ion cathode have been explored, including doping of the TM layer,[24–26] and the introduction of large cations within the AM layer.[12,27] The ion exchange method presented in this chapter represents a simple, scalable, and low-cost strategy for introducing pillar ions into Na-ion cathodes, as exemplified by the preparation of CaNMMO. These observations open the door to the possibility of facile solid-state ion exchange with other battery cathodes and alkali ion substitutions and should be the subject of future work.

With regards to the effect of pillaring on O-redox activity, it is clear that the introduction of Ca^{2+} ions into NMMO did not prevent the large hysteresis on discharge. While pillaring the material with Ca^{2+} does seem to suppress the phase transition at high voltages, the phase transition from *P*2 to *O*2 type stacking continues to occur, which ultimately leads to the out-of-plane migration of Mg^{2+}. This in turn causes the formation of molecular O_2 on charge, leading to a large hysteresis being observed on discharge.

It is worth considering the effect that pillaring could have the material from an O-redox perspective. If the phase transition from *P*2 to *O*2 type could be successfully mitigated in NMMO, there would be no octahedral site for the Mg^{2+} to migrate into at the top of charge,

leaving the TM layer intact and fully dense (i.e. without vacancies). Would this situation still promote O-redox activity? To answer this question, the "orphaned orbital" model which was introduced in the introduction to this thesis should be considered.[28] This theory appears to hold true in a wide range O-redox materials, which can be divided into three tiers.

The first tier contains Na-ion and Li-ion cathode materials with Li^+ ions in the TM layer in a honeycomb arrangement which exhibit capacity beyond the TM limit. Example compositions include $Li_{1.2}Mn_{0.54}Ni_{0.13}Co_{0.13}O_2$ or $NaLi_{1/3}Mn_{2/3}O_2$.[2,29] On charge, Li^+ in the TM layer migrates to the AM layer, producing Li_{AM}^+-O-$[_]_{TM}^+$ or Na_{AM}^+-O-$[_]_{TM}^+$ arrangements.[29,30] These highly ionic arrangements activate the oxide sub-lattice to become O-redox active. However, the electron holes formed on charge are unstable, eventually leading to the disproportionation reaction $2O^-$ -> O_2 + O^o due to the honeycomb superstructure in these materials.[9,31]

The second tier of materials encompasses Na-ion cathode materials showing reversible, high-voltage O-redox activity. These compositions are $Na_{0.6}Mn_{0.8}Li_{0.2}O_2$ with Na_{AM}^+-O-Li_{TM} arrangements, and $Na_2Mn_3O_7$ with Na_{AM}^+-O-$[_]_{TM}$ arrangements (where $[_]_{TM}$ represents TM layer vacancies).[8,9,32] On charge, both materials exhibit ionic Na_{AM}^+-O-$[_]_{TM}$ arrangements which activate O-redox. However, thanks to the non-honeycomb type ordering of the vacancies in these materials, the electron holes formed are stable to disproportionation, allowing the electron holes to be cycled reversibly.

The final tier of materials consists of O-redox materials which do not contain Li^+ or [_] in the TM layer, including $Na_{0.67}Mn_{0.72}Mg_{0.28}O_2$ and $Li_2Ir_{0.5}Sn_{0.5}O_3$.[3,11] These materials show Na_{AM}^+-O-Mg_{TM}^{2+} and Li_{AM}^+-O-Sn_{TM}^{4+} arrangements in the pristine state. However, on charge, both Mg^{2+} and Sn^{4+} have been found to migrate from the TM layer, forming Na_{AM}^+-O-$[_]_{TM}^+$ and Li_{AM}^+-O-$[_]_{TM}$ arrangements which activate O-redox.

In each tier of materials, the activation of O-redox was determined by two key factors: the ability to extract capacity from the material beyond the TM redox limit, and the presence of AM^+-O-[_]$_{TM}$ type arrangements at the top of charge, generated through the migration of cations from the TM layer. These requirements beg the question: Could a AM^+-O-Mg_{TM}^{2+} type arrangement present at the top of charge generate O-redox activity? Or could this only be generated by AM^+-O-[_]$_{TM}$ type arrangements? While this discussion is far from the original objective of this chapter, it raises important questions which should be addressed in future works on O-redox cathodes.

5.4 Conclusion

To conclude, the successful ion-exchange of $Na_{0.67}Mn_{0.72}Mg_{0.28}O_2$ with Ca^{2+} was presented in this chapter, using a novel solid-state, room temperature procedure. The ion-exchange mechanism was shown to rely on the formation of hydrated phases of CaI_2, which facilitates the exchange of Ca^{2+} and Na into the bulk of $Na_{0.67}Mn_{0.72}Mg_{0.28}O_2$ to form $Na_{0.47}Ca_{0.1}Mn_{0.72}Mg_{0.28}O_2$. ICP and PXRD results demonstrate that this method can be used to dope a range of Ca amounts into the layered structure, up to a limit of 0.07 Ca^{2+}. Additional structural characterisation utilising both EELS and SEM/EDX analysis confirm that this method can successfully dope Ca-ions into the bulk of the structure. This method has the potential to be used to prepare doped Na-ion cathodes with larger cations to prevent phase transformations across a range of compositions.

However, the electrochemistry of the ion-exchange sample continued to show a large hysteresis on discharge. Ex-situ PXRD measurements reveal that the *P*2 to *O*2 phase transition continues to occur in the ion-exchanged composition, suggesting that the O-redox activity in the material continues to for molecular O_2.

5.5 References

1. House, R. A. *et al.* Covalency does not suppress O_2 formation in 4d and 5d Li-rich O-redox cathodes. *Nat. Commun.* **12**, 1–7 (2021).
2. Luo, K. *et al.* Charge-compensation in 3d-transition-metal-oxide intercalation cathodes through the generation of localized electron holes on oxygen. *Nat. Chem.* **8**, 684–691 (2016).
3. Csernica, P. M. *et al.* Metal–oxygen decoordination stabilizes anion redox in Li-rich oxides. *Nat. Mater.* **18**, (2019).
4. Sharpe, R. *et al.* Redox Chemistry and the Role of Trapped Molecular O_2 in Li-Rich Disordered Rocksalt Oxyfluoride Cathodes. *J. Am. Chem. Soc.* **142**, 21799–21809 (2020).
5. Yamamoto, K. *et al.* Charge Compensation Mechanism of Lithium-Excess Metal Oxides with Different Covalent and Ionic Characters Revealed by Operando Soft and Hard X-ray Absorption Spectroscopy. *Chem. Mater.* **32**, 139–147 (2020).
6. Zheng, W. *et al.* Stabilizing the oxygen lattice and reversible oxygen redox in Na-deficient cathode oxides. *J. Power Sources* **439**, 227086 (2019).
7. Eum, D. *et al.* Coupling structural evolution and oxygen-redox electrochemistry in layered transition metal oxides. *Nat. Mater.* (2022) doi:10.1038/s41563-022-01209-1.
8. Mortemard de Boisse, B. *et al.* Highly Reversible Oxygen-Redox Chemistry at 4.1 V in $Na_{4/7-x}[[_]_{1/7}Mn_{6/7}]O_2$ ([_]: Mn Vacancy). *Adv. Energy Mater.* **2**, 1800409 (2018).
9. House, R. A. *et al.* Superstructure control of first-cycle voltage hysteresis in oxygen-redox cathodes. *Nature* **577**, 502–508 (2020).
10. Maitra, U. *et al.* Oxygen redox chemistry without excess alkali-metal ions in $Na_{2/3}[Mg_{0.28}Mn_{0.72}]O_2$. *Nat. Chem.* **10**, 288–295 (2018).
11. Boivin, E. *et al.* Bulk O_2 formation and Mg displacement explain O-redox in $Na_{0.67}Mn_{0.72}Mg_{0.28}O_2$. *Joule* **5**, 1267–1280 (2021).
12. Wang, Y. *et al.* Pillar-beam structures prevent layered cathode materials from destructive phase transitions. *Nat. Commun.* **12**, 1–11 (2021).
13. Wang, Q. C. *et al.* Tuning *P*2-Structured Cathode Material by Na-Site Mg Substitution for Na-Ion Batteries. *J. Am. Chem. Soc.* **141**, 840–848 (2019).
14. Shannon, R. D. Revised effective ionic radii and systematic studies of interatomic distances in halides and chalcogenides. *Acta Crystallogr. Sect. A* **32**, 751–767 (1976).
15. Eum, D. *et al.* Voltage decay and redox asymmetry mitigation by reversible cation migration in lithium-rich layered oxide electrodes. *Nat. Mater.* **19**, 419–427 (2020).
16. ARMSTRONG, A. R. & BRUCE, P. G. Synthesis of Layered $LiMnO_2$ as an Electrode for Rechargeable Lithium Batteries. *Nature* **381**, 499–500 (1996).
17. Paulsen, J. M. & Dahn, J. R. Studies of the layered manganese bronzes, $Na_{2/3}[Mn_{1-2x}M_x]O_2$ with M = Co, Ni, Li, and Li $[Mn_{1-2x}M_x]O_2$ prepared by ion-exchange. **126**, 3–24 (1999).

18. Yabuuchi, N. *et al.* New *O*2/*P*2-type Li-excess layered manganese oxides as promising multi-functional electrode materials for rechargeable Li/Na batteries. *Adv. Energy Mater.* **4**, (2014).

19. Cushing, B. L. & Wiley, J. B. Topotactic Routes to Layered Calcium Cobalt Oxides. *J. Solid State Chem.* **141**, 385–391 (1998).

20. Somerville, J. W., Adam Sobkowiak, N. T.-R., Billaud, J., Juan G. Lozano, R. A. H. & Leighanne C. Gallington, Tore Ericsson, Lennart Haggstrom, Matthew R. Roberts, U. M. and P. G. B. Nature of the '"Z"'-phase in layered Na-ion battery cathodes. *Energy Environ. Sci.* **12**, 2223 (2019).

21. Ollivier, P. J., Mallouk, T. E., O, T. N. & Srta, K. A " Chimie Douce " Sythesis of Perovskite-Type SrTa 2 O 6 and and useful route to metastable solid-state compounds. *Chem. Mater.* 2585–2587 (1998).

22. Livage, J. Synthesis of polyoxovanadates via '"chimie douce"'. *Coord. Chem. Rev.* **178**, 999–1018 (1998).

23. Gopalakrishnan, J. Chimie Douce Approaches to the Synthesis of Metastable Oxide Materials. *Chem. Mater.* **7**, 1265–1275 (1995).

24. Tapia-Ruiz, N. *et al.* High voltage structural evolution and enhanced Na-ion diffusion in *P*2-$Na_{2/3}Ni_{1/3-x}Mg_xMn_{2/3}O_2$ ($0 \leq x \leq 0.2$) cathodes from diffraction, electrochemical and ab initio studies. *Energy Environ. Sci.* **11**, 1470–1479 (2018).

25. Singh, G. *et al.* High Voltage Mg-Doped $Na_{0.67}Ni_{0.3-x}Mg_xMn_{0.7}O_2$ (x = 0.05, 0.1) Na-Ion Cathodes with Enhanced Stability and Rate Capability. *Chem. Mater.* **28**, 5087–5094 (2016).

26. Wang, Q. *et al.* Reaching the Energy Density Limit of Layered *O*3-$NaNi_{0.5}Mn_{0.5}O_2$ Electrodes via Dual Cu and Ti Substitution. *Adv. Energy Mater.* **9**, 1–11 (2019).

27. Han, S. C. *et al.* Ca-doped Na_xCoO_2 for improved cyclability in sodium ion batteries. *J. Power Sources* **277**, 9–16 (2015).

28. Seo, D. H. *et al.* The structural and chemical origin of the oxygen redox activity in layered and cation-disordered Li-excess cathode materials. *Nat. Chem.* **8**, 692–697 (2016).

29. Wang, Q. *et al.* Unlocking anionic redox activity in *O*3-type sodium 3d layered oxides via Li substitution. *Nat. Mater.* **20**, (2021).

30. Li, X. *et al.* Lithiation and delithiation dynamics of different Li Sites in Li-Rich battery cathodes studied by operando nuclear magnetic resonance. *Chem. Mater.* **29**, 8282–8291 (2017).

31. House, R. A. *et al.* First-cycle voltage hysteresis in Li-rich 3d cathodes associated with molecular O2 trapped in the bulk. *Nat. Energy* **5**, 777–785 (2020).

32. Tsuchimoto, A. *et al.* Nonpolarizing oxygen-redox capacity without O-O dimerization in $Na_2Mn_3O_7$. *Nat. Commun.* 1–7 doi:10.1038/s41467-020-20643-w.

Chapter 6
$Na_{0.66}Li_{0.1}Ni_{0.3}Mn_{0.6}O_2$ as a Reversible High Voltage O-redox Cathode

Table of Contents

6.1 Introduction 147
6.2 Experimental 149
6.3 Results 151
6.3.1 Structural Characterisation 151
6.3.2 Electrochemical Characterisation 154
6.3.3 Surface and Structural Stability Characterisation over Cycling 157
6.3.4 Spectroscopic Characterisation 161
6.3.5 Discussion 165
6.4 Conclusion 168
6.5 References 169

6.1 Introduction

Chapter 5 of this thesis presented the possibility of avoiding the formation of molecular O_2 in the bulk of cathode materials by pillaring the layered structure with a larger cation. In this chapter, the possibility of stabilising the O^{2-}/O^{-} redox couple will be studied by introducing a novel ordering scheme to the TM layer. Honeycomb ordering, so often seen in O-redox cathode materials, readily undergoes TM migration at high states of charge which leads to the formation of molecular O_2 in the bulk (section 1.4.3).[1–3] Creating a TM ordering scheme where

Li^+ or other dopants are spaced further apart (such as those seen in $Na_{0.6}Mn_{0.8}Li_{0.2}O_2$ or $Na_2Mn_3O_7$)[2,4] could inhibit the TM re-arrangement on charge, thereby stabilising the O^{2-}/O^- redox couple (section 1.5.3).[5]

There are several design principles which were considered when devising the material composition to be targeted in this chapter:

- First, the metal ratio within the TM layer should be far off the tie-line for honeycomb type ordering, i.e. in the ratio of 2:1. For example, there are materials close to the 2:1 ratio between elements in the TM layer (e.g. $Na_{0.66}Mn_{0.72}Mg_{0.28}O_2$ or $Na_{0.75}Mn_{0.75}Li_{0.25}O_2$) that still contain honeycomb ordering.[2,6,7]
- Second, the choice of dopant in the TM layer to enable O-redox is important. For the material studied in this chapter, Li^+ was the dopant of choice. Due to its single charge, it enables compositions with high TM oxidation states to be targeted. This allows for a significant proportion of O-redox capacity to be activated, and for higher TM oxidation states, increasing the average cathode voltage.
- Third, a Na-ion cathode material should be synthesised. Na-ion compositions can be synthesised at various degrees of Na content enabling a larger variety of compositions to be targeted.

By following these design principles, a novel O-redox active cathode material $Na_{0.66}Li_{0.1}Ni_{0.3}Mn_{0.6}O_2$ (NLNMO) was synthesised. This chapter will outline the structural, electrochemical, and spectroscopic characterisation of NLNMO. A study of the charge compensation mechanism reveals NLNMO to be a material relying on reversible, high voltage TM and O-redox; the first such material to be presented. The activity of the O^{2-}/O^- was found to be active over multiple cycles. In addition, the performance of NLNMO will be compared to other high performing Na-ion cathodes.

6.2 Experimental

Solid State Synthesis: $Na_{0.66}Li_{0.1}Ni_{0.3}Mn_{0.6}O_2$ was synthesised via the solid-state method. Stoichiometric amounts of $NaNO_3$ (>99%, Sigma), $LiNO_3$ (>99%, Sigma), $NiCO_3$ (98%, Alfa) and $MnCO_3$ (99.9%, Alfa) were mixed in a planetary ball-mill for 2 hrs. The precursors were then pressed into pellets and heated to 800 ^oC for 8 hrs under flowing O_2. A heating rate of 3 ^oC min^{-1} was used, and the furnace was left to cool naturally after the synthesis.

Electrochemical characterisation: Electrode preparations and cell (dis)assembly was performed in a glove box under an inert argon atmosphere (H_2O < 0.1ppm and O_2 < 0.1 ppm). Electrodes were prepared by combining the active material (80wt%) and Super P carbon (10wt%) in a mortar and pestle before adding PTFE binder (10wt%). The electrode film was then rolled to a thickness of ~ 100 μm. Electrodes were assembled into coin cells using glass fibre separators and 1M $NaClO_4$ in PC with 5% FEC (99.9%, DodoChem), and a Na metal counter electrode. Galvanostatic cycling was carried out using a Maccor Series 4000. Cycling was performed between 2.0 V and 4.5 V vs Na^+/Na at a rate of 20 mA g^{-1} for all cells for all samples unless stated otherwise. Typical mass loadings were 15 mg cm^{-2}

GITT: Galvanostatic Intermittent Titration Technique (GITT) protocols were performed using a Biologic VMP3 potentiostat. Cells were assembled in a glovebox then cycled at 20 mA g^{-1} between 2.0 V and 4.5 V for as many cycles as needed. Once any preparatory cycles were finished, cells were placed on the Biologic and charged for 30 mins at 20 mA g^{-1} before being rested for 6 hrs. Cut off voltages of 2.0 V and 4.5 V were used.

PXRD: Diffraction data were collected on a Rigaku 9 kW SmartLab Cu-source diffractometer equipped with a Hypix 2D detector. Operando PXRD data were collected using an electrochemical cell provided by Rigaku with a beryllium window.

SEM: SEM imaging and EDX analysis were performed on a Carl Zeiss Merlin high resolution field emission gun SEM instrument. This data was collected by Dr. Jun Chen.

OEMS: OEMS experiments were carried out by flowing Ar carrier gas (99.9% purity, BOC) through an ECC-std electrochemical cell (EL-CELL) with gas inlet and outlet ports and into a BT Prima mass spectrometer (Thermo Fischer). The cathode material was cycled vs a Na metal counter electrode and an electrolyte of 1M NaPF6 in PC.

NMR: All ^{7}Li and ^{23}Na magic angle spinning (MAS, υR = 37037 Hz) solid state NMR measurements were completed at 9.45 T (υ07Li = 155.53 MHz, υ023Na = 105.86 MHz) using a Bruker Avance III HD spectrometer and a 1.9mm double air bearing MAS probe. All ^{7}Li and ^{23}Na spectra are referenced to 1M LiCl(aq) and 1M NaCl(aq) in D_2O, respectively, at 0 ppm. All spectra were recorded using a Hahnecho (π/2-τ-π-τ) sequence. Where τ is 1/υR and π/2 is 250 kHz, the resultant FID is processed as a half echo. The ^{7}Li spectra were achieved with a recycle delay of 300 ms. The ^{23}Na NMR spectra were collected with relaxation times of 500 ms. The isotropic resonance was determined by varying the spinning speed between 30-39kHz to isolate the spinning sidebands. Data collection and analysis was done by Dr. Gregory Rees.

ICP-OES: The pristine cathode material was dissolved in aqua regia ($HCl:HNO_3$ / 25:75 (v/v%)) before diluting the solution for measurement. A calibration curve was created using standard solutions of Li, Ni, Mn and Na. Elemental analysis was carried out using a Perkin-Elmer Optima 7300DV ICP-OES.

RIXS: High resolution RIXS data were collected using the I21 beamline at Diamond Light Source. To produce the data sets for the quantitative analysis, scans at 531 eV were recorded at fifteen different sample locations and averaged together, with little inhomogeneity in the signal observed.

SXAS: O K-edge and TM L-edge data were collected in fluorescence mode using the I21 beamline at Diamond Light Source. Data were averaged across 3 scans.

XANES: Ex-situ TM K-edge data were collected at the B18 beamline at Diamond Light Source. These data were collected in transmission mode.

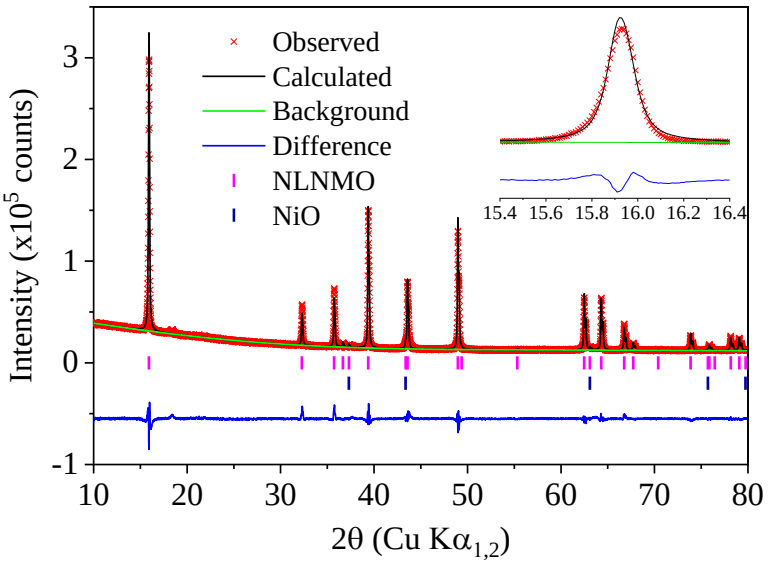

Figure 6.1: Rietveld refinement of NLNMO. The diffraction data were collected using an un-monochromated Cu *Kα* X-ray source. Inset shows the fitting of the 002 reflection. An impurity phase of NiO remained in the sample, with a phase fraction of 1.3%.

6.3 Results

6.3.1 Structural Characterisation

NLNMO was successfully synthesised by solid state reaction as described in the Experimental. Rietveld refinement of the resulting PXRD data confirms the structure is *P*2-type (Figure 6.1 and Table A6.1) containing an *ab ba* stacking of the oxide sub-lattice. The material was refined to the *P*63/*mmc* space group. A small amount of NiO impurity remains in the sample (1.3% from Rietveld Refinement). During the refinement the fraction of the Li, Ni and Mn sites (2*a*) were constrained to be equal to their stoichiometric fractions. U_{iso} values were refined and set to be equivalent across elements within the 2*a* site as well as being equivalent for the 2*b* and 2*d* sites. The Na content between the 2*b* and 2*d* sites was constrained to equal 0.66. A small peak is present in the PXRD pattern at ~ 18.3° 2θ which is not described by the *P*63/*mmc* space group. The position of this peak was compared to the 110 peak in the *P*63/*mcm* space group which arises from honeycomb ordering in the TM layer (Figure A6.1). However, the peak observed in NLNMO does not align with this reflection. This suggests that

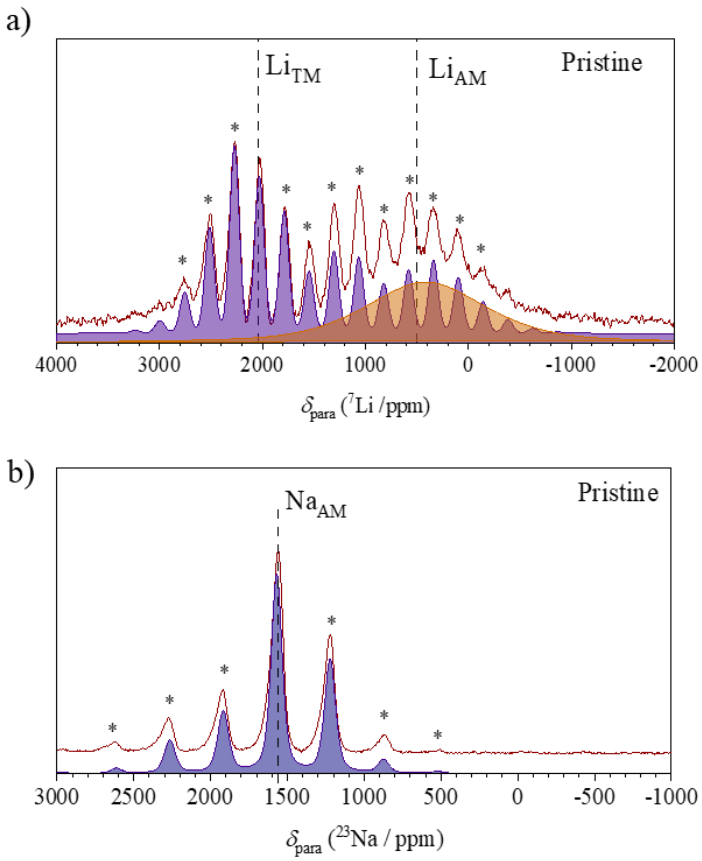

Figure 6.2: ^{7}Li (a) and ^{23}Na (b) NMR of pristine NLNMO. The ^{7}Li NMR spectra shows two Li environments, one shifted to 2040 ppm (Li_{TM}) and the other shifted to 500 ppm (Li_{AM}). The spinning side bands of the Li_{TM} and Na_{AM} resonances are denoted by *.

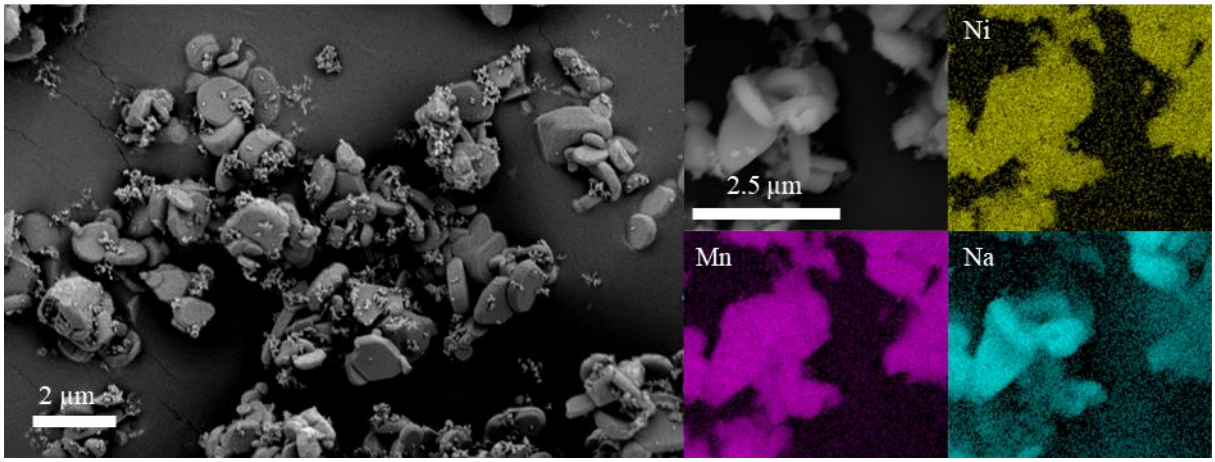

Figure 6.3: SEM images and EDX analysis of pristine NLNMO. Plate like particles can be seen in the SEM, being 1 – 2 µm in diameter and ~0.2 - 0.5 µm thick. A homogenous elemental distribution is seen throughout the particles.

if this peak arises due to TM ordering, it will not be due to honeycomb ordering. Other in-plane ordering schemes could arise from Ni/Mn ordering in the TM layer, which would require further investigation using Neutron diffraction.

Element	Li	Mn	Ni	Na
Targeted Composition	0.1	0.6	0.3	0.66
Concentration (ppm)	0.20 (7)	9.87 (2)	5.48 (1)	4.43 (1)
Normalized Composition	0.096 ± 0.005	0.607 ± 0.012	0.298 ± 0.013	0.633 ± 0.019

Table 6.1: Elemental composition of as synthesised NLNMO as measured by ICP-OES.

In order to investigate the structure further ^{7}Li and ^{23}Na NMR were conducted on the pristine sample (Figure 6.2). The ^{7}Li NMR reveals two distinct Li environments. The first (labelled Li_{TM}) is an ordered environment with the chemical shift centred at 2040 ppm corresponding to Li present in the TM layer. This environment is shifted to higher ppm due to the paramagnetism of the surrounding Mn cations in the TM layer, agreeing with previously measured ^{7}Li NMR in Mn based $NaTMO_2$.[8] The second environment, labelled Li_{AM}, is a smaller broad peak centred at 500 ppm indicative of indistinct Li environments which are most likely attributed to Li ions in octahedral sites in *O*-type stacking faults within the Na-layer. This classification follows previous research on Li doped $NaTMO_2$.[8] The ^{23}Na NMR shows one environment centred at 1570 ppm despite there being two crystallographic sites for Na. This is due to the rapid exchange of Na-ions between the sites which occur on a similar timescale to the NMR measurements.[9]

The morphology of NLNMO was investigated using SEM imaging. These measurements reveal a plate like morphology with a particle size of 1-2 μm and plate thickness of ~500 nm, consistent with other Na-ion cathodes prepared by solid state synthesis. EDX analysis reveals a homogenous distribution of Na, Mn and Ni within the particles. The material composition was also confirmed using ICP-OES analysis (Table 6.1). The calculations for the Ni content via ICP-OES accounted for the NiO impurity observed by PXRD.

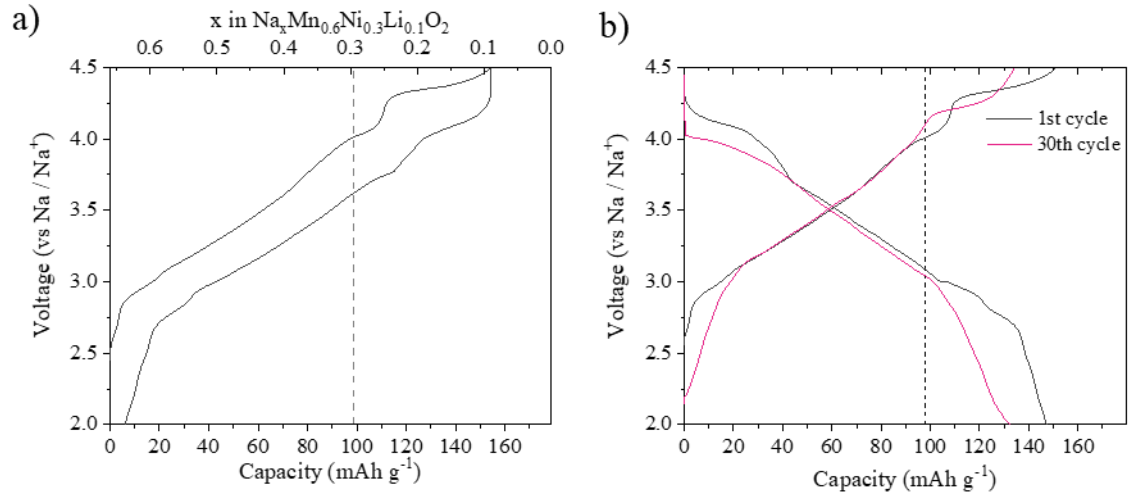

Figure 6.4: Electrochemical analysis of NLNMO. a) Load curve of the 1st cycle for NLNMO, cycled between 2.0 V and 4.5 V at a rate of 20 mA g^{-1}. b) Load curve comparison of the 1st and 30th cycles for NLNMO. In both charge cycles, the high voltage plateau ~ 4.25V is present. The dotted line in each figure represents the TM redox capacity.

6.3.2 Electrochemical Characterisation

The 1st cycle electrochemical load curve of NLNMO is shown in Figure 6.4a. On charge, the material shows a long sloping region up to 4 V beyond which a high voltage plateau accounting for ~ 40 mAh g^{-1} of capacity is observed. On discharge, a significant proportion of plateau capacity is returned above 4 V before turning to a steady sloping region down to 2 V. A hysteresis of ~250 mV is observed when charging to 4.5 V. The 1st cycle charge capacity is 151 mAh g^{-1}, corresponding to 0.56 mol of Na de-intercalation, with a third of the charge capacity extracted beyond the limit of the Ni^{3+}/Ni^{4+} redox couple. Further analysis will be carried out to uncover the charge compensation mechanism later in the chapter (section 6.3.4). The 1st cycle coulombic efficiency is 97.4%, displaying minimal 1st cycle capacity loss.

The extended cycling performance of $Na_{0.66}Li_{0.1}Ni_{0.3}Mn_{0.6}O_2$ is plotted in Figure 6.4b. The high voltage plateau observed in the 1st cycle is still present after 30 cycles, with the discharge load curve continuing to begin above 4 V. Some degree of capacity loss is observed, with a smoother load curve profile observed after 30 cycles.

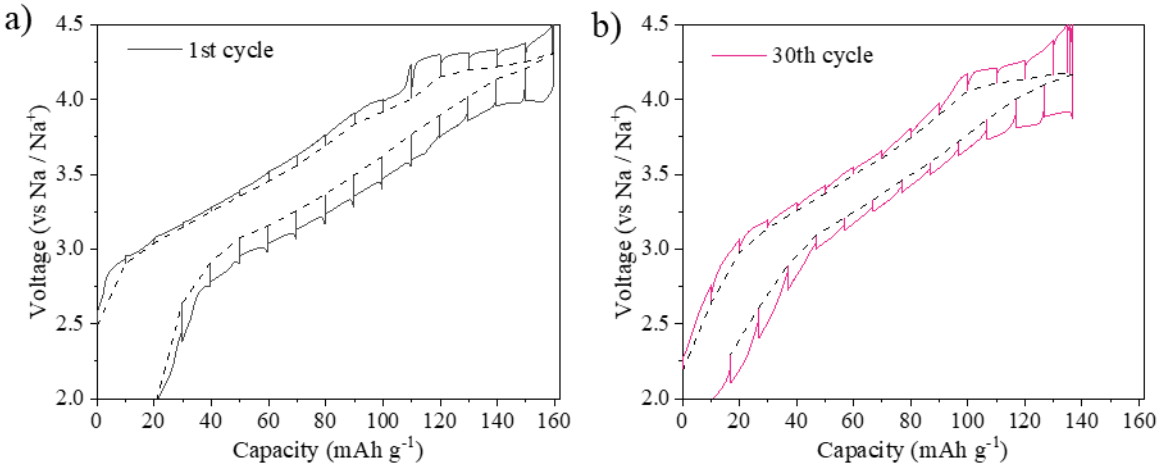

Figure 6.5: GITT analysis of NLNMO over the 1st and 30th cycles. For each measurement run, the cell was charged at a rate of 20 mA g^{-1} for 30 minutes, then set to rest for 6 hrs. The dotted line connects the minimum voltage of each cell rest.

To further investigate the load curve evolution over cycling, GITT was performed over the 1st and 30th cycles to examine any changes in overpotential (Figure 6.5). During the 1st cycle GITT, minimal overpotential is observed over the initial sloping region. At ~ 4.1V there is a voltage step leading to the high voltage plateau where an increase in overpotential is observed (approximately 100 mV). While a slightly larger overpotential is observed right at the beginning of discharge, a constant overpotential of ~ 150mV is present along the load curve down to 2V. The GITT of the 30th cycle is very similar to that of the 1st cycle, although less overpotential is present along the discharge slope. These results show that the cycling of NLNMO remains stable over multiple cycles.

Further analysis of the electrochemical performance of NLNMO was performed. Figure 6.6 a presents the capacity loss over cycling. After 50 cycles, the discharge capacity drops to 125.2 mAh g^{-1}, corresponding to a capacity retention of 85%. High coulombic efficiency is also observed over cycling. The average charge and discharge voltages are shown in Figure 6.6 b. The average 1st cycle discharge voltage was found to be 3.37 V. NLNMO shows minimal

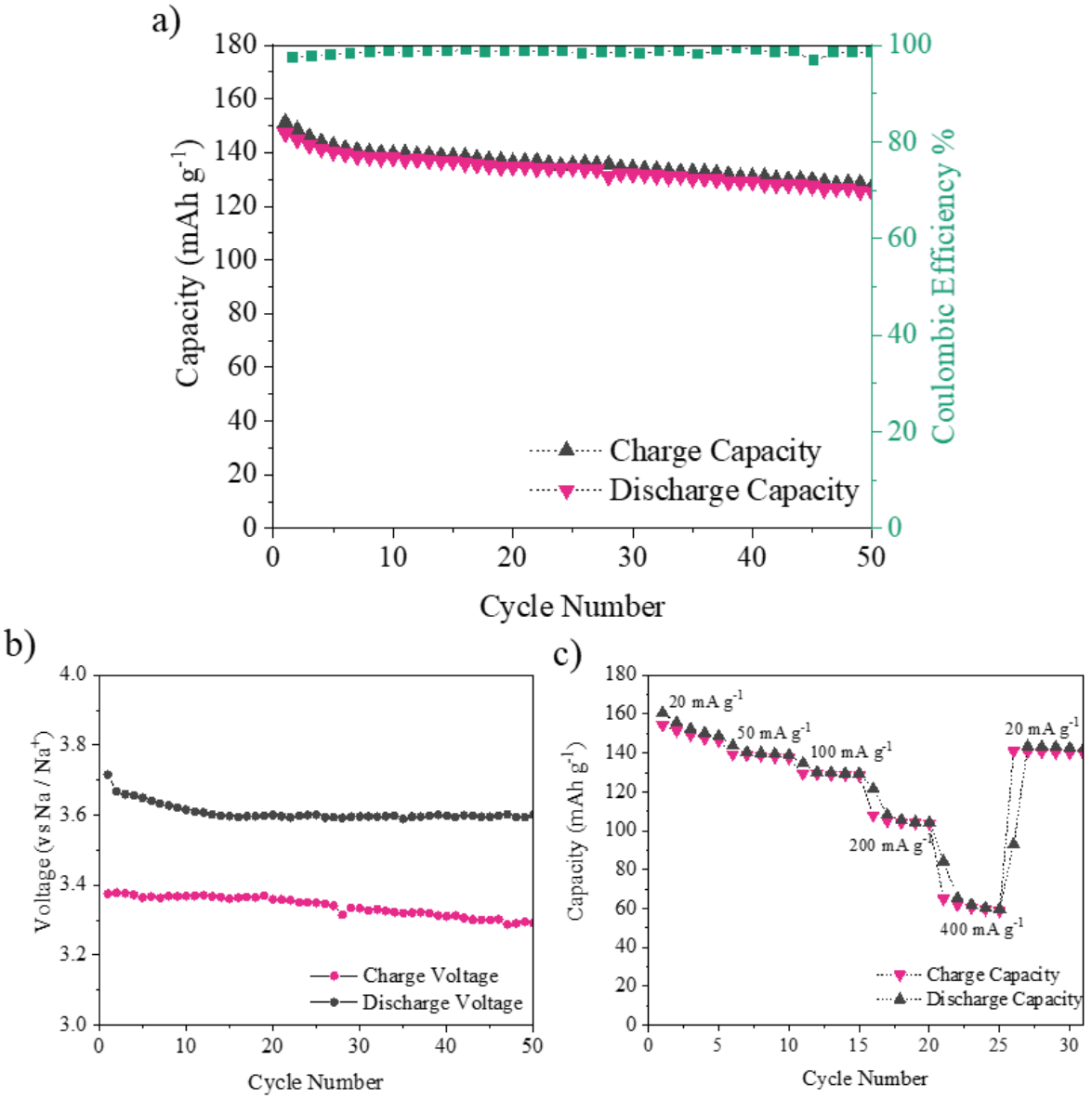

Figure 6.6: a) Capacity loss and coulombic efficiency of cycling in NLNMO over the first 50 cycles. b) Average charge and discharge voltages for NLNMO over the first 50 cycles. c) Rate capabilities for NLNMO. The cell was charged at a rate of 20 mA g^{-1}, then 50 mA g^{-1}, then 100 mA g^{-1}, then 200 mA g^{-1}, then 400 mA g^{-1}, before going back to 20 mA g^{-1}. At each rate, 5 cycles were carried out.

voltage fade over cycling with a slight decrease of 0.07V after 50 cycles. Finally, the rate capabilities of NLNMO are presented in c. The material was charged for 5 cycles at each rate, starting at 20 mA g^{-1}, 50 mA g^{-1}, 100 mA g^{-1}, 200 mA g^{-1}, and 400 mA g^{-1}, before reverting to cycling at 20 mA g^{-1}. The results show NLNMO is capable of delivering >100 mAh g^{-1} capacity at a rate of 200 mA g^{-1} (corresponding to a C rate of 1.33).

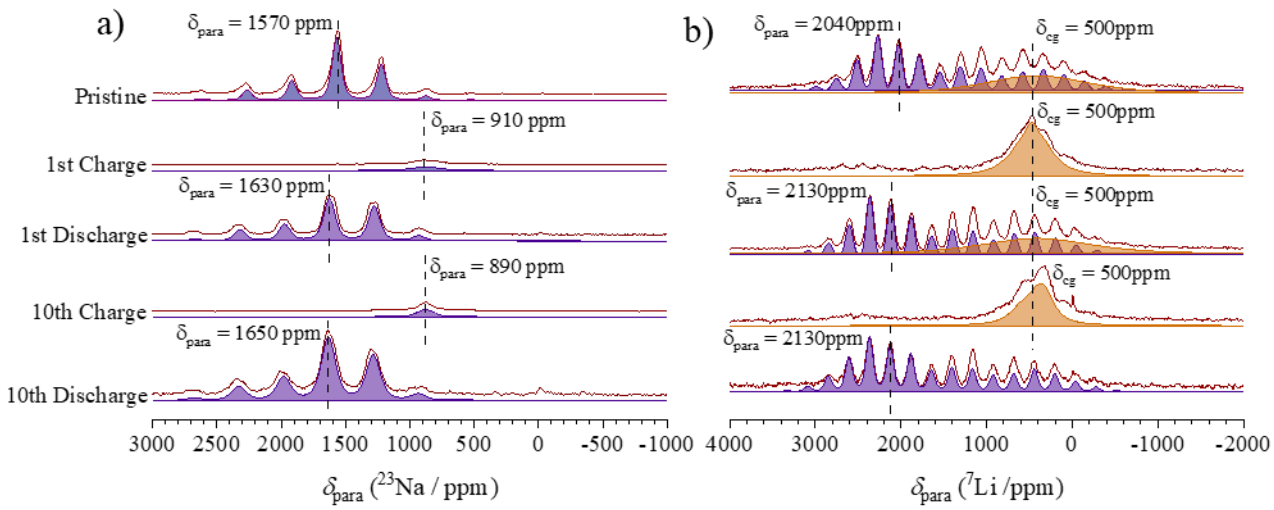

Figure 6.7: Ex-situ a) ^{23}Na and b) ^{7}Li NMR of multi-cycled NLNMO. Pristine, 1st charge, 1st discharge, 10th charge and 10th discharged samples were prepared by cycling at 20 mA g^{-1} between 2 V and 4.5 V using coin cells, then disassembled for ex-situ measurements.

6.3.3 Surface and Structural Stability Characterisation over Cycling

In order to investigate the structural stability, phase changes over cycling, and O-loss, NMR, *in operando* XRD and OEMS were performed. First, ^{7}Li and ^{23}Na NMR analysis was carried out on cycled NLNMO to track the changes to the local environmental around Li and Na (Figure 6.7). The ^{23}Na NMR signal reveals a shift from 1570 ppm in the pristine sample to 910 ppm in the charged sample in line with the oxidation of Ni^{3+} to Ni^{4+} which is diamagnetic.[9] The ^{23}Na signal becomes paramagnetically shifted again on discharge to 1630 ppm as Ni^{4+} is reduced. Over the 10th charge / discharge cycle, the ^{23}Na signal shows a similar range of shifts from 890 ppm on charge to 1650 ppm on discharge. Similar behaviour is observed in the ^{7}Li signal. At the top of the 1st charge, the ^{7}Li signal reveals a broad peak at 500 ppm which is consistent with Li in the Na layer in octahedral sites. This result confirms that Li migrates from the TM layer to the AM layer on charge. On the 1st discharge, the ^{7}Li spectra remains similar to the pristine sample with two distinct Li environments: the first shifted to 2130 ppm attributed to Li_{TM} and the second shifted to 500 ppm corresponding to Li_{AM}. The Li_{TM} signal on the 1st discharge is sharp with multiple spinning sidebands as in the pristine sample. The results from

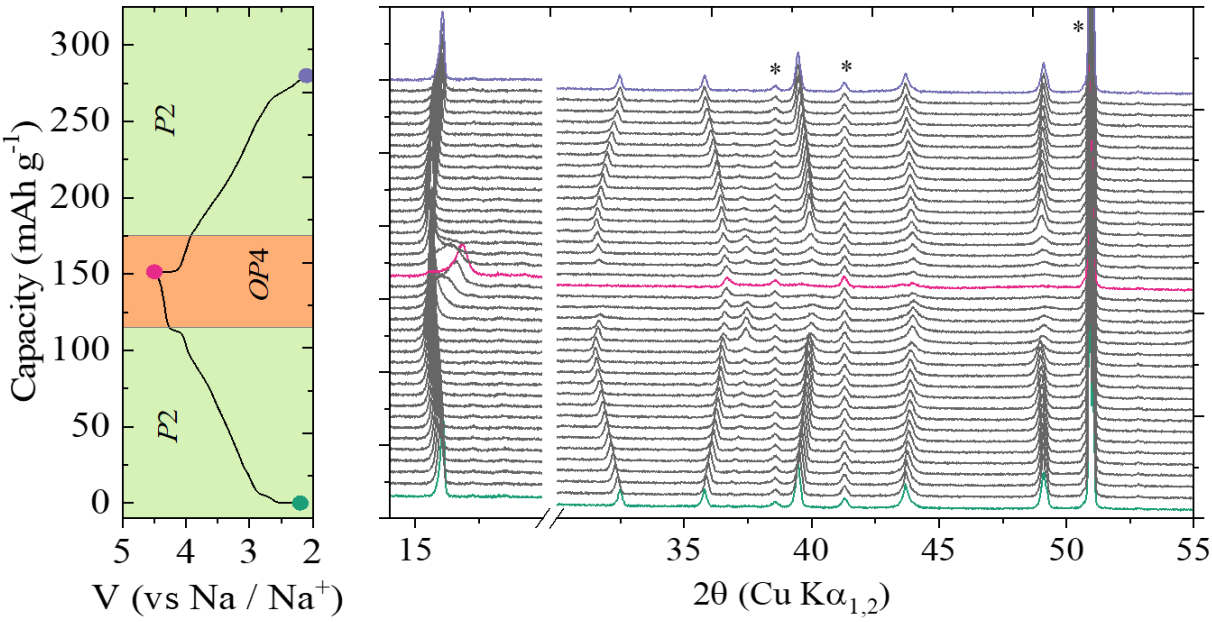

Figure 6.8: *In-operando* PXRD of NLNMO over the 1st cycle. The pristine material was mixed with carbon black and loaded into the operando cell and charged at a rate of 10 mA g^{-1} between 2.0V and 4.5V. The cycling of the cell is shown on the left-hand panel. The right-hand panel shows the evolution of the PXRD pattern over cycling. The patterns in green, red and blue correspond to the pristine, 1st charge and 1st discharge points respectively. The * denotes peaks from the beryllium window of the operando cell.

the 10th charge show Li migrating to the AM layer, with the shift being consistent at 500 ppm. On discharge, the Li returns once again to the TM layer with a shift at 2130 ppm. However, only one Li environment is observed, with the Li_{AM} signal being lost. This could be due to loss of Li over cycling from the electrode to the electrolyte. The small increases in the chemical shifts for Na and Li in the discharged state could be due to small changes to the bulk magnetic susceptibility from a slight Mn reduction. Overall, these NMR results show that Li reversibly migrates from the TM layer to the AM layer over cycling. Although the exact arrangement of Li in the TM remains unknown, the invariant sharp peak shape of the Li in the TM layer over cycling indicates there are no significant changes to the environment.

Next, operando PXRD was used to investigate phase changes over the 1st cycle (Figure 6.8). On charge, the material shows a continuous shift of the 002 peak towards lower 2θ values which corresponds to an increase in the inter-layer spacing. At the beginning of the high voltage

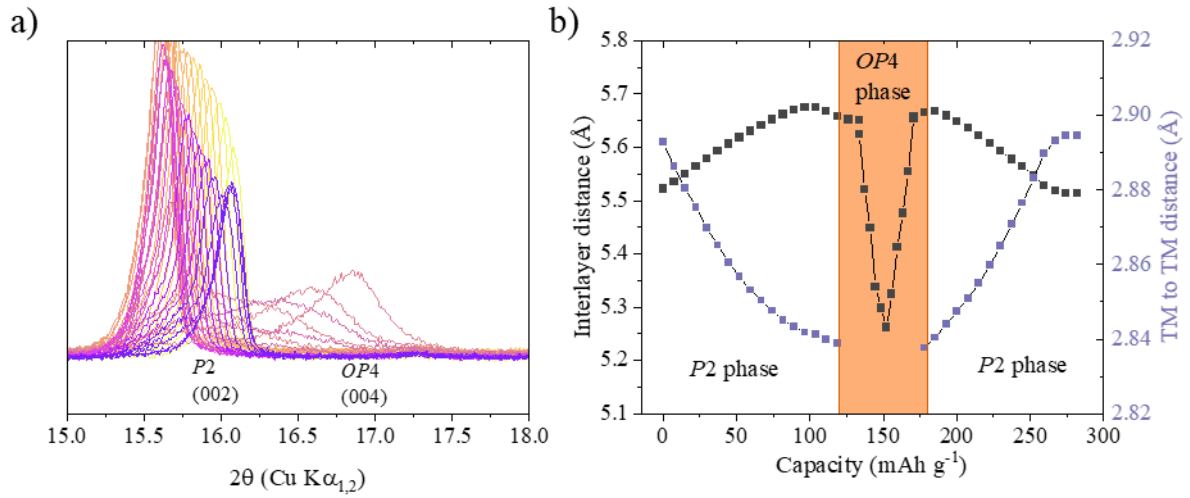

Figure 6.9: a) Following the peak shape change of the 002 peak in the *P*2 structure over cycling. On charge this peak moves to ~16.5° 2θ due to the phase change from *P*2 to *OP*4. This change is reversible over cycling. b) Lattice parameters extracted from refinement of the Operando PXRD measurements.

plateau a phase change is observed from *P*2 to *OP*4 type stacking. This change is reversible, with the material reverting back to *P*2 stacking on discharge. As the material begins to change from *P*2 to *OP*4 type stacking, a peak at 37.5° 2θ (attributed to the 111 reflection of the *P*2 phase) increases intensity. The intensity of this peak is sensitive to the fraction of Na present in the 2*d* crystallographic sites indicating a Na site preference, i.e. Na ordering (Figure A6.2). This particular shift occurs at a Na content of 0.3 Na according to the electrochemical profile of the *in operando* run. An enlarged plot of the 002 peak and the cell parameter changes from the PXRD measurements are shown in Figure 6.9. The continuous shift of the 002 peak is shown in Figure 6.9a. This shows that the phase change from *P*2 to *OP*4 type stacking occurs homogenously throughout the material. At the top of charge only one peak can be seen attributed to the *OP*4 phase, rather than two peaks corresponding to the *P*2 and *OP*4 phases. Figure 6.9b presents the changes in lattice parameters over the cycle. Lattice parameters were extracted by doing a sequential LeBail refinement of all the PXRD patterns. When extracting the lattice parameters for the *OP*4 phase, the 2θ value corresponding maximum height of the 002 peak was used to determine the change in *c* lattice parameter. The *a* lattice parameter was not extracted for the *OP*4 phase as the signal intensity for other diffraction peaks was too low.

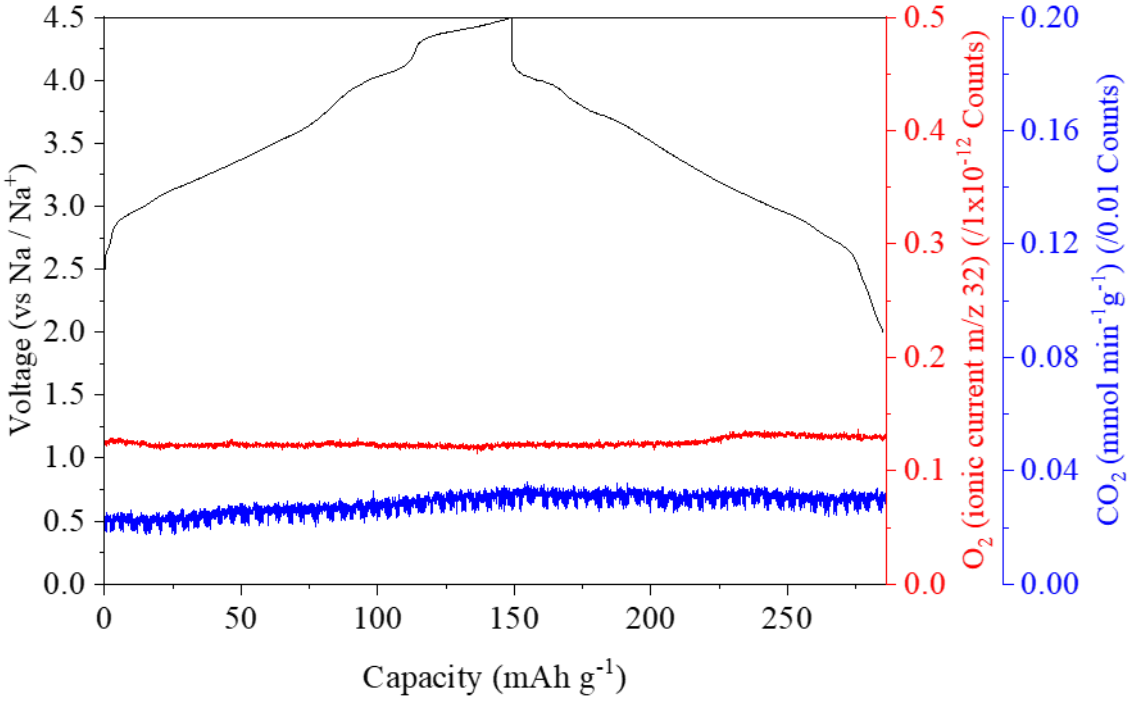

Figure 6.10: OEMS analysis of NLNMO. For this measurement, O_2 (m/z = 32) and CO_2 (m/z = 44) were monitored throughout the experiment. The material was cycled at a rate of 20 mA g^{-1} between 2.0 and 4.5 V

This analysis reveals a continuous increase in inter-layer spacing (which is derived from the *c* lattice parameter) from 5.52 Å to 5.67 Å along the 1st charge. The inter-layer spacing then contracts with the formation of the *OP*4 phase, dropping to a low of 5.26 Å. Through discharge, the inter-layer spacing increases once more as the *OP*4 phase returns to *P*2, and the inter-layer spacing then gradually decreases through discharge.

The sloping voltage profile of the cathode can be well described by the single-phase mechanism shown by the *in operando* PXRD. However, although the evolution from *P*2 to *OP*4 occurs through a single-phase mechanism, NLNMO exhibits a two-phase electrochemical response with the presence of a high-voltage plateau at the end of charge. This type of behaviour has previously been reported in another Na-ion cathode, $Na_{2/3}Ni_{1/6}Mn_{1/2}Fe_{1/3}O_2$.[10] The authors showed, using *in operando* PXRD and ADF-STEM, that the *OP*4 phase was in fact an intermediate between the two end member phases, *P*2 and *O*2. On charge, Na^+ removal leads to *O*-type stacking faults within the *P*2 structure, increasing in proportion until an ordered

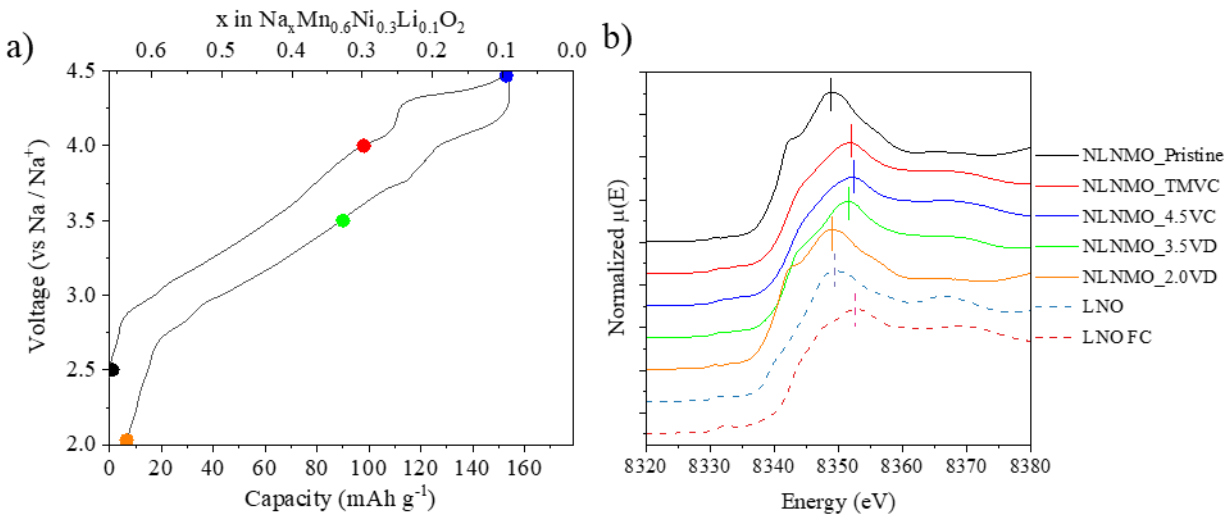

Figure 6.11: a) Load curve of NLNMO showing the points of charge which were studied using ex-situ Ni and Mn K-edge XANES, and O K-edge RIXS and SXAS. b) Ni K-edge XANES over the 1st cycle. The straight line at the peak of each XANES spectra denotes the position of the white-line energy, used to define the oxidation state of Ni. Two reference spectra, shown with dotted lines, were also measured using pristine (Ni^{3+}) and charged (Ni^{4+}) $LiNiO_2$.

*OP*4 phase forms, which leads to an *O*2 structure on further charging. Changes in the *a* lattice parameter are also presented. The reversible contraction in *a* over charge is consistent with the oxidation of Ni from 3+ to 4+. Ex-situ PXRD measurements were also taken over cycling, showing that NLNMO undergoes no major structural changes, remaining in the *P*2 phase after 30 cycles (Figure A6.3).

Finally, in order to examine the surface stability of NLNMO, OEMS was performed on the material to investigate CO_2 and O_2 evolution from the surface (Figure 6.10). No detectable gas loss was observed from the material when charged to 4.5V.

6.3.4 Spectroscopic Characterisation

In order to investigate the charge compensation mechanism in NLNMO, ex-situ XAS measurements of the O, Ni and Mn K-edges were taken on charged cathodes. Five charge points were chosen: Pristine, TMVC (denoting the end of TM redox), 4.5VC, 3.5VD and 2.0VD (Figure 6.11). Due to variations in the shape of the Ni K-edge across charging, the white line energy was used to determine the oxidation state of Ni. The pristine Ni K-edge exhibits a white line energy of 8349.01 eV, in good agreement with the Ni^{3+} reference (8349.65 eV). On

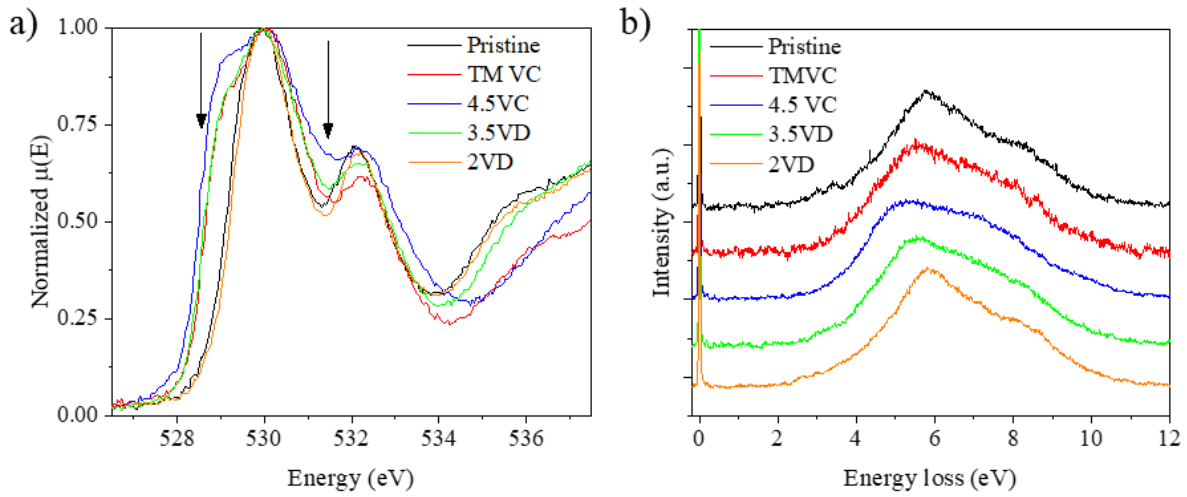

Figure 6.12: Ex-situ measurements of the O K-edge of NLNMO over the 1st cycle by SXAS (a) and RIXS (b). The RIXS measurements were conducted at an excitation energy of 531 eV.

charge the white line energy reaches 8351.92 eV at TMVC and 8352.25 eV at 4.5VC, in good agreement with the measured Ni^{4+} reference (8352.57 eV). On discharge, the Ni is gradually reduced back to 3+, with the white line energy of the 2.0VD sample being the same as for the pristine material. The Mn K-edge XANES was also measured, showing no change on charge or discharge, confirming that Mn remains 4+ and does not participate in the charge compensation for NLNMO (Figure A6.4).

The small shift in the Ni K-edge between the TMVC and 4.5VC charge points shows that the $Ni^{3+/4+}$ redox couple still contributes to charge compensation beyond 4.0 V. By assuming that all the capacity extracted between the pristine and TMVC charge points can be attributed to the $Ni^{3+/4+}$ redox couple, the amount of capacity extracted beyond the $Ni^{3+/4+}$ redox couple can be determined. Only 11 mAh g^{-1} of the capacity beyond the 4.0VC charge point can be attributed to the $Ni^{3+/4+}$ redox couple, leaving a further 45 mAh g^{-1} of capacity beyond the limits of TM oxidation.

Since there is negligible O-loss observed, this charge must be compensated for by oxidation of oxide ions in the bulk. To investigate the possibility of O-redox in NLNMO, the O K-edge was probed using SXAS and RIXS (Figure 6.12). The O K-edge shows an increase

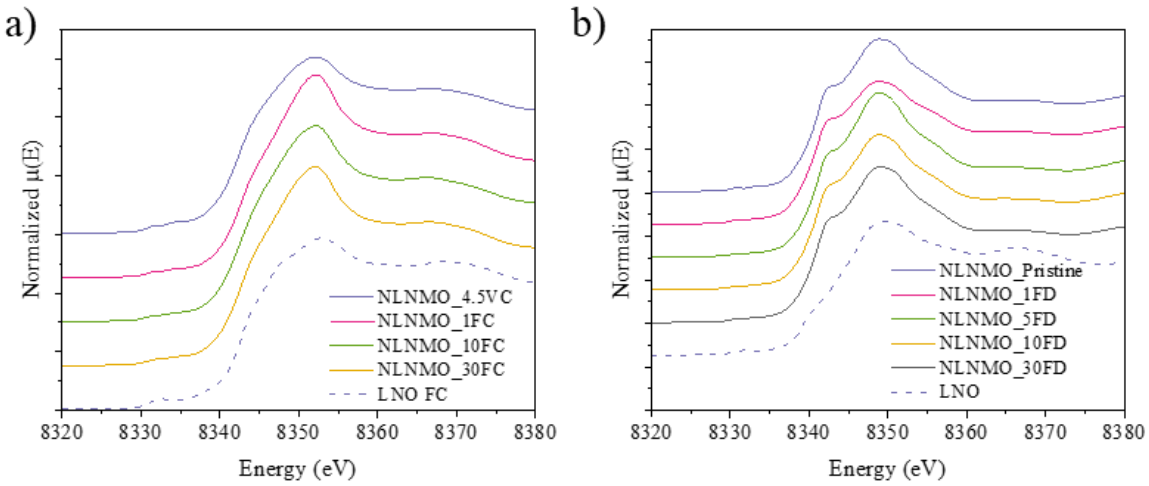

Figure 6.13: Ex-situ measurements of the Ni K-edge XANES in NLNMO over cycling. The dotted spectra refer to the measurement of Ni reference samples, charge $LiNiO_2$ (a) and pristine $LiNiO_2$ (b).

in the pre-edge intensity of the SXAS measurements between the pristine and 4.0VC charge points. This is due to TM oxidation as seen in the Ni K-edge.[1] The pre-edge features presented arise from the hybridisation of the O and TM. On charge the TM are oxidised, forming hole states in the hybridised O2p-Ni3d t_{2g} orbitals causing an increase in intensity in the pre-edge. Between the TMVC and 4.5VC charge points, a further increase in the pre-edge intensity is observed, which cannot be attributed to Ni oxidation and must therefore signify the formation of electron hole states on the oxide sub-lattice. The feature arising from the formation of electron holes in NLNMO (528 – 529 eV) is consistent with previous measurements of electron holes in Na-ion O-redox cathodes.[2] On discharge the increase in pre-edge intensity is reduced, with the 2.0VD spectra looking identical to that of the pristine material. High resolution RIXS was used to further probe the nature of the oxidised O in this material and investigate the possible presence of trapped molecular O_2 (Figure 6.12b). On charge there are some subtle changes to the main energy loss feature centred at ~ 6eV in agreement with small changes in the O K-edge SXAS at that excitation energy. Interestingly, no evidence of O_2 formation is observed over the 1st charge. These results confirm the presence of a reversible O^{2-}/O^{-} redox couple in NLNMO and absence of the hysteretic O^{2-}/O_2 O-redox mechanism.

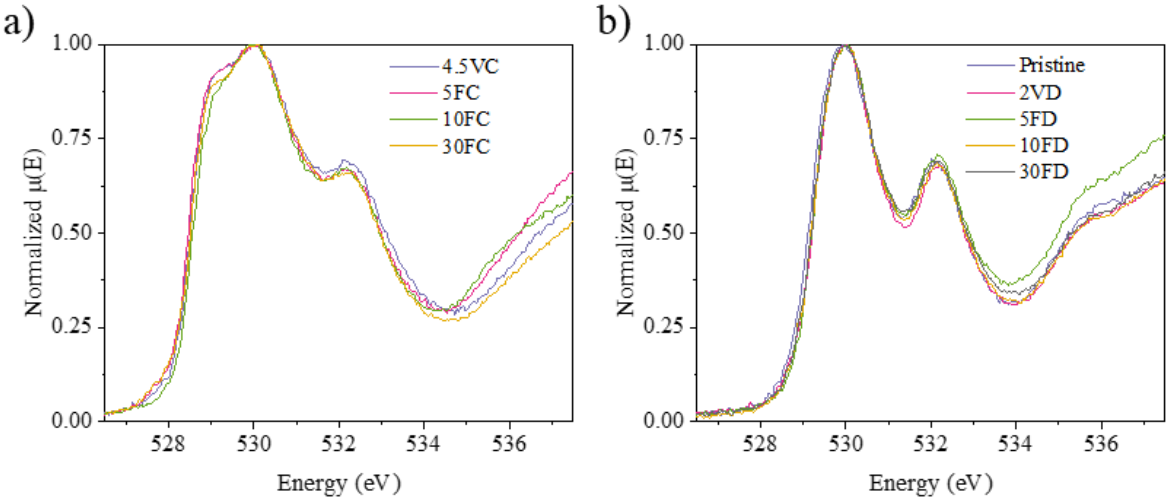

Figure 6.14: Ex-situ measurements of the O K-edge of NLNMO by SXAS.

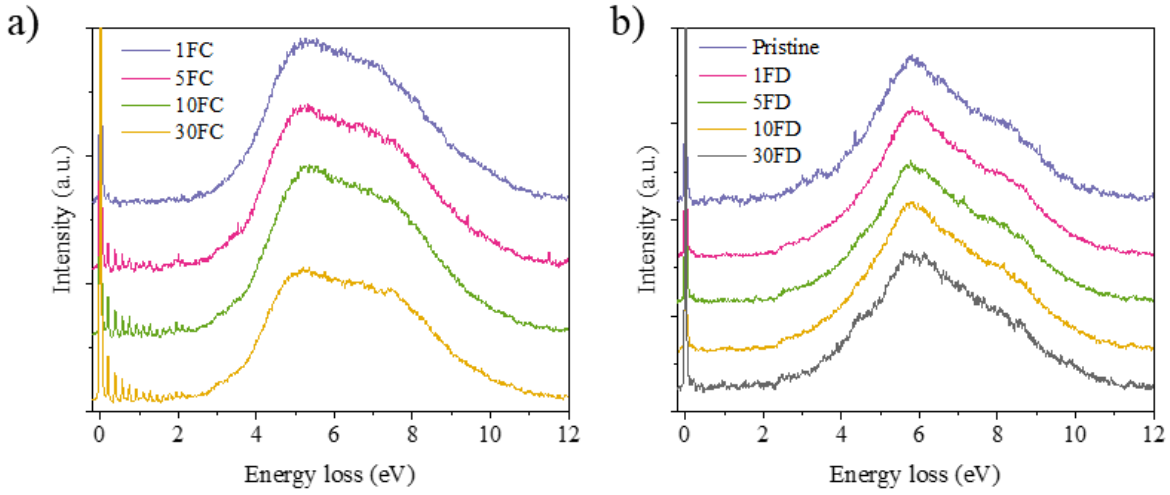

Figure 6.15: Ex-situ RIXS measurements of NLNMO over cycling. The RIXS spectra were collected at an excitation energy of 531eV.

The evolution of the charge compensation mechanism over cycling was investigated through ex-situ measurements of cycled samples of NLNMO. Ni K-edge XANES data show that the $Ni^{3+/4+}$ redox couple remains active after 30 cycles, with no over reduction of Ni observed (Figure A6.4). In addition, no reduction of Mn is observed after 30 cycles (Figure A6.3). The O K-edge SXAS shows that the pre-edge feature attributed to electron hole formation on the oxide sub-lattice is still present after 30 cycles, although this intensity of this feature has slightly decreased. No changes are observed in the discharged state (Figure 6.14). To address the decrease in the pre-edge intensity, O K-edge RIXS was performed on the cycled

samples to probe for the potential formation of O_2 (Figure 6.15). While no signal of molecular O_2 was observed in the 1st charge sample, there is a consistent increase in signal arising from molecular O_2 in NLNMO in the fully charged state. This is consistent with the decrease in signal from the O^{2-}/O^{-} redox couple. On discharge this signal is lost, with no trapped O_2 observed at 2.0V after 30 cycles.

6.3.5 Discussion

Although the compositional space of NLNMO has previously been investigated, there have been no reports of anomalous capacity during cycling. Compositions such as $Na_{0.8}Li_{0.12}Ni_{0.22}Mn_{0.6}O_2$, $Na_{0.83}Li_{0.07}Ni_{0.31}Mn_{0.62}O_2$ and $Na_{1.0}Li_{0.2}Ni_{0.25}Mn_{0.75}O_2$ have all been previously reported to cycle reversibly using the $Ni^{2+/4+}$ or $Ni^{3+/4+}$ redox couples.[8,11,12] The novelty of NLNMO lies in the charge compensation mechanism which shows both reversible TM redox and reversible high-voltage O-redox activity over multiple cycles. The SXAS and RIXS results presented above confirm the O-redox activity present in NLNMO.

Despite the reversible activity of the O^{2-}/O^{-} redox couple over multiple cycles, NLNMO still exhibits molecular O_2 formation over extended cycling. It is worth noting, however, that the signal arising from molecular O_2 in charged NLNMO is eight times lower than previously reported on O-redox materials. This includes compositions which reversibly cycle the O^{2-}/O_2 redox couple,[1,3,13,14] and those which activate the O^{2-}/O^{-} redox couple.[2] In addition, these cathodes all exhibit substantial amounts of molecular O_2 formation on the 1st charge, while NLNMO is able to delay this for 30 cycles, representing a significant step forward in the stability of O-redox active materials.

It is worth recalling the reasons for pursuing high-voltage O-redox activity. O-redox represents one of the best opportunities to extend the energy density of cathode materials, by increasing the capacity of certain compositions, and by providing a redox couple operating at

Composition	Average discharge voltage vs Na^+/Na^0	Potential Window	Cycling rate / mA g^{-1}	Discharge capacity / mAh g^{-1}	Discharge capacity / Wh kg^{-1}	Capacity retention after (X) cycles	Notes
$Na_{0.66}Li_{0.1}Ni_{0.3}Mn_{0.6}O_2$	3.37 V	2.0 – 4.5	20	147.1	495.7	85% (50 cycles)	This work
$Na_{0.66}Ni_{0.33}Mn_{0.67}O_2$	3.55 V	2.0 – 4.5	12	120	426.0	46% (50 cycles)	Ref[15]
$Na_{0.66}Ni_{0.23}Mg_{0.1}Mn_{0.67}O_2$	3.30 V	2.0 – 4.5	12	128.2	423.1	95.4% (50 cycles)	Ref[15]
$Na_{0.67}Mn_{0.72}Mg_{0.28}O_2$	2.6 V	1.5 – 4.5	10	220	572.0	68% (30 cycles)	Ref[7]
$Na_{0.8}Li_{0.12}Ni_{0.22}Mn_{0.66}O_2$	3.4 V	2.0 – 4.4	12	118	401.2	91% (50 cycles)	Ref[8]
$NaNi_{0.4}Cu_{0.1}Mn_{0.4}Ti_{0.1}O_2$	3.3 V	2.4 – 4.5	24	172.9	570.6	75.2% (100 cycles)	Ref[16]
$Na_3V_2(PO_4)_2F_3$	3.85 V	3.1 – 4.4	15	120	462.0	97% (25 cycles)	Ref[17]
$Na_3V_2(PO_4)_3$	3.35 V	2.7 – 3.7	10	110	368.5	91% (80 cycles)	Ref[18]

Table 6.2: A comparison of performance metrics of NLNMO vs other high-performance Na-ion cathode materials. It should be noted that this list is non-exhaustive.

a higher voltage than conventional TM redox. To that end, the electrochemical performance of NLNMO was compared to other high-performance Na-ion cathode materials in order to benchmark its performance (Table 6.2). It should be noted that only metrics collected on discharge were compared in the table as this represents the useable energy to be extracted from the battery when in use. These metrics cover the average discharge voltage, the potential

window over which the cathodes were cycled, the cycling rate at which the cathodes were tested, the discharge capacity and capacity retention. The average voltage of NLNMO at 3.37 V is comparable to other high-voltage TM redox materials such as $Na_{0.66}Ni_{0.23}Mg_{0.1}Mn_{0.67}O_2$ (3.30 V), $Na_{0.8}Li_{0.12}Ni_{0.22}Mn_{0.66}O_2$ (3.40 V), and $Na_3V_2(PO_4)_3$ (3.35 V). The 1st cycle discharge capacity for NLNMO is among the highest reported, reaching 495.7 Wh kg^{-1}. From the comparison of the data in the table, it is clear that NLNMO exhibits promising performance metrics allowing it to be considered as a prospective Na-ion cathode.

Looking forward, the successful synthesis and characterisation of NLNMO demonstrate the effective implementation of the design principles introduced in this chapter. This opens new avenues for further research into high energy density O-redox active cathodes. Further compositions should be targeted which increase the amount of available O-redox capacity. A promising strategy could be to increase the average oxidation state of the TM present in the material, thus decreasing the charge compensation capabilities of TM redox and increasing those of O-redox. This could be achieved by increasing the amount of Li in the TM layers. Alternatively, redox inactive dopants, such as Al^{3+}, could be incorporated into potential compositions to replace redox active components, such as Ni^{3+}.

Another interesting avenue for further research could be the incorporation of the $Fe^{3+/4+}$ redox couple with reversible high-voltage O-redox. Fe is a cheap, earth abundant element with a redox couple that operates at a high voltage making it a great candidate for a constituent in Na-ion batteries. However, Fe containing compounds typically show poor cyclability and large capacity loss due to Fe migration on charge.[19–21] Recent investigations comparing two Fe based Na-ion cathodes, $Na_{0.67}Fe_{0.5}Mn_{0.5}O_2$ and $Na_{0.67}Fe_{0.25}Mn_{0.6}Mg_{0.15}O_2$, provide a better understanding of the $Fe^{3+/4+}$ redox couple.[22] In $Na_{0.67}Fe_{0.5}Mn_{0.5}O_2$, Fe^{3+} oxidation reaches only $Fe^{3.3+}$ before a *P*2 to *O*2 type transition is triggered. This allows the remaining Fe^{3+} to migrate into the AM layer, leaving behind vacancies which trigger O-redox activity on further charge.

The migration of Fe is only partially reversible, leading to a gradual loss of $Fe^{3+/4+}$ activity. In contrast, the removal of Na from $Na_{0.67}Fe_{0.25}Mn_{0.6}Mg_{0.15}O_2$ allows the oxidation of Fe^{3+} to Fe^{4+} before the phase transition to *O*-type stacking occurs thus preventing Fe^{3+} migration. In addition, the presence of Mg^{2+} also triggers O-redox, increasing the useable capacity from the cathode. This finding increases the potential compositional space of materials to be investigated to include materials containing Fe.

6.4 Conclusion

In conclusion, NLNMO was presented as a novel Na-ion cathode. The material composition was confirmed by ICP-OES and EDX analysis, with further structural characterisation done using SEM imaging. ^{7}Li NMR revealed the existence of two Li environments which were attributed to Li in the TM layer and Li in *O*-type stacking faults of the AM layer. Over extended cycling, the environment of the Li_{TM} was found to remain unchanged, demonstrating the stability of the TM layer structure in NLNMO. Operando analysis of the material over the 1st cycle revealed a reversible phase transition from *P*2 to *OP*4 on charge, while OEMS showed no evidence of gas evolution over the 1st cycle. Spectroscopic characterisation of the material uncovered the charge compensation mechanism which consisted of a combination of $Ni^{3+/4+}$ redox and O^{2-}/O^- redox. No molecular O_2 formation was observed on the 1st cycle. The O^{2-}/O^- redox couple was found to be active over multiple cycles, a significant leap forward in comparison to other O-redox cathodes. From a performance perspective, NLNMO exhibits a 1st cycle discharge capacity of 495.7 Wh g^{-1}, with a high average discharge voltage of 3.37 V with only 0.07 V voltage fade over the first 50 cycles. Further work should also be undertaken to better understand the TM superstructure present in NLNMO, using Neutron diffraction and high-resolution STEM imaging.

6.5 References

1. House, R. A. *et al.* First-cycle voltage hysteresis in Li-rich 3d cathodes associated with molecular O2 trapped in the bulk. *Nat. Energy* **5**, 777–785 (2020).
2. House, R. A. *et al.* Superstructure control of first-cycle voltage hysteresis in oxygen-redox cathodes. *Nature* **577**, 502–508 (2020).
3. House, R. A. *et al.* Covalency does not suppress O*2* formation in 4d and 5d Li-rich O-redox cathodes. *Nat. Commun.* **12**, 1–7 (2021).
4. Mortemard de Boisse, B. *et al.* Highly Reversible Oxygen-Redox Chemistry at 4.1 V in $Na_{4/7-x}[[_]_{1/7}Mn_{6/7}]O_2$ ([_]: Mn Vacancy). *Adv. Energy Mater.* **2**, 1800409 (2018).
5. House, R. A. *et al.* The role of O_2 in O-redox cathodes for Li-ion batteries. *Nat. Energy* **6**, 781–789 (2021).
6. Maitra, U. *et al.* Oxygen redox chemistry without excess alkali-metal ions in $Na_{2/3}[Mg_{0.28}Mn_{0.72}]O_2$. *Nat. Chem.* **10**, 288–295 (2018).
7. Yabuuchi, N., Hara, R., Kubota, K., Paulsen, J. & Komaba, S. A new electrode material for rechargeable sodium batteries: *P*2-type $Na_{2/3}[Mg_{0.28}Mn_{0.72}]O_2$ with anomalously high reversible capacity. *J. Mater. Chem. A* **3**, 16851–16855 (2014).
8. Xu, X. *et al.* Identifying the Critical Role of Li Substitution in *P*2-$Na_x(Li_yNi_xMn_{1-y-z})O_2$ (0 less than x, y, z less than 1) Intercalation Cathode Materials for High Energy Na-ion Batteries. *Chem. Mater.* **26**, 1260–1269 (2014).
9. Gotoh, K. ^{23}Na Solid-State NMR Analyses for Na-Ion Batteries and Materials. *Batter. Supercaps* **4**, 1267–1278 (2021).
10. Somerville, J. W., Adam Sobkowiak, N. T.-R., Billaud, J., Juan G. Lozano, R. A. H. & Leighanne C. Gallington, Tore Ericsson, Lennart Haggstrom, Matthew R. Roberts, U. M. and P. G. B. Nature of the ‘“Z”’-phase in layered Na-ion battery cathodes. *Energy Environ. Sci.* **12**, 2223 (2019).
11. Kim, D. *et al.* Enabling sodium batteries using lithium-substituted sodium layered transition metal oxide cathodes. *Adv. Energy Mater.* **1**, 333–336 (2011).
12. Xie, Y. *et al.* Role of Lithium Doping in *P*2-$Na_{0.67}Ni_{0.33}Mn_{0.67}O$ for Sodium-Ion Batteries. *Chem. Mater.* **33**, 4445–4455 (2021).
13. Sharpe, R. *et al.* Redox Chemistry and the Role of Trapped Molecular O_2 in Li-Rich Disordered Rocksalt Oxyfluoride Cathodes. *J. Am. Chem. Soc.* **142**, 21799–21809 (2020).
14. Boivin, E. *et al.* Bulk O_2 formation and Mg displacement explain O-redox in $Na_{0.67}Mn_{0.72}Mg_{0.28}O_2$. *Joule* **5**, 1267–1280 (2021).
15. Singh, G. *et al.* High Voltage Mg-Doped $Na_{0.67}Ni_{0.3-x}Mg_xMn_{0.7}O_2$ (x = 0.05, 0.1) Na-Ion Cathodes with Enhanced Stability and Rate Capability. *Chem. Mater.* **28**, 5087–5094 (2016).
16. Wang, Q. *et al.* Reaching the Energy Density Limit of Layered *O*3-$NaNi_{0.5}Mn_{0.5}O_2$ Electrodes via Dual Cu and Ti Substitution. *Adv. Energy Mater.* **9**, 1–11 (2019).
17. Yan, G. *et al.* Higher energy and safer sodium ion batteries via an electrochemically made disordered $Na_3V_2(PO_4)_2F_3$ material. *Nat. Commun.* **2**, (2019).

18. Jian, Z. *et al.* Superior Electrochemical Performance and Storage Mechanism of $Na_3V_2(PO_4)_3$ Cathode for Room-Temperature Sodium-Ion Batteries. doi:10.1002/aenm.201200558.

19. Yabuuchi, N. *et al. P*2-type $Na_x[Fe_{1/2}Mn_{1/2}]O_2$ made from earth-abundant elements for rechargeable NaÂ batteries. *Nat. Mater.* **11**, 512–517 (2012).

20. Thorne, J. S., Dunlap, R. A. & Obrovac, M. N. Investigation of *P*2-$Na_{2/3}Mn_{1/3}Fe_{1/3}Co_{1/3}O_2$ for Na-Ion Battery Positive Electrodes. *J. Electrochem. Soc.* **161**, A2232–A2236 (2014).

21. Talaie, E., Duffort, V., Smith, H. L., Fultz, B. & Nazar, L. F. Structure of the high voltage phase of layered *P*2-$Na_{2/3-z}[Mn_{1/2}Fe_{1/2}]O_2$ and the positive effect of Ni substitution on its stability. *Energy Environ. Sci.* **8**, 2512–2523 (2015).

22. Boivin, E., House, R. A., Marie, J. J. & Bruce, P. G. Controlling Iron Versus Oxygen Redox in the Layered Cathode $Na_{0.67}Fe_{0.5}Mn_{0.5}O_2$: Mitigating Voltage and Capacity Fade by Mg Substitution. *Adv. Energy Mater.* **12**, (2022).

Chapter 7
Conclusion

Table of Contents

7.1 Conclusion..... 171
7.2 Future Work..... 173
7.2.1 Investigating Surface Coatings to Prevent O_2 Loss..... 174
7.2.2 *In Operando* O K-edge XAS and RIXS of O-redox Cathodes 174
7.2.3 Exploring Room Temperature Ion-Exchange 174
7.2.4 Investigating O-redox Activity in Fully Dense Layered Oxides..... 175
7.2.5 Further Research into Non-Honeycomb Ordered Cathodes..... 175

7.1 Conclusion

O-redox continues to show the potential to increase the energy density of Li-ion and Na-ion cathodes. Invoking the oxidation chemistry of the oxide sub-lattice in transition metal oxides allows greater capacities to be extracted from the cathode at a higher voltage than conventional TM redox. This leads to the formation of electron holes on oxygen during charge, producing the O^{2-}/O^{-} redox couple which can be reversibly cycled at high voltages. However, recent research has uncovered that the O^{2-}/O^{-} redox couple remains unstable during charging, causing the vast majority of O-redox materials to form molecular O_2 instead, leading to the reversible cycling of the low voltage O^{2-}/O_2 redox couple. The work presented in this thesis is linked by the intent to produce an O-redox cathode material capable of cycling the O^{2-}/O^{-} redox couple reversibly over many cycles.

In Chapter 3, two synthetic methods were used to produce $Li_{1.2}Ni_{0.13}Co_{0.13}Mn_{0.54}O_2$. Using a sol-gel synthesised material, a link between the honeycomb ordering of the TM layer and the high voltage O-redox plateau (previously demonstrated in Na-ion materials) was established in a Li-rich compound. $Li_{1.2}Ni_{0.13}Co_{0.13}Mn_{0.54}O_2$ synthesised by Co-precipitation methods was used to investigate the long-term effect of cycling the O^{2-}/O_2 redox couple. Directly probing and quantifying the O-redox process over cycling uncovered a loss in activity of the O^{2-}/O_2 redox couple after 100 cycles. Over extended cycling, the small vacancy clusters formed during the first cycle eventually combine to produce large pores throughout the bulk of the material. This weakens the structure of the material, causing particle cracking which releases the trapped O_2. This process occurs continually over cycling, causing the gradual decreases in contribution of the O^{2-}/O_2 redox couple to charge compensation, which is replaced by lower voltage TM redox couples of $Mn^{3+/4+}$ and $Co^{2+/3+}$. This theory provides a clear explanation for the voltage fade phenomenon, bringing together observations of structural reorganisation, void formation, void opening, and TM reduction into a single model.

In Chapter 4, a model Na-ion O-redox cathode, $Na_{0.6}Mn_{0.8}Li_{0.2}O_2$, was chosen to investigate fundamental questions about the O-redox process. *In-operando* measurements of the Mn K-edge refuted claims of Mn^{4+} oxidation as the source of anomalous capacity observed in this material, establishing $Na_{0.6}Mn_{0.8}Li_{0.2}O_2$ as a pure O-redox cathode. Next, the stability of the electron holes formed during charge in this material was discussed, reinforcing the need to use *in-operando* techniques to study O-redox compounds. Finally, the development of a SXAS cell to be used for future *in-operando* measurements was discussed, presenting the exciting prospect of carrying out *in-operando* XAS and RIXS measurements on the O K-edge of O-redox cathodes.

In Chapter 5, the pillaring of $Na_{0.67}Mn_{0.72}Mg_{0.28}O_2$ with a large Ca^{2+} cations was explored as a potential strategy to facilitate the reversible cycling of the O^{2-}/O^{-} redox couple. Ca^{2+} was introduced to the AM layer of $Na_{0.67}Mn_{0.72}Mg_{0.28}O_2$ through a novel room temperature ion-exchange method. The mechanism for the ion-exchange was found to rely on the hydration of CaI_2 when exposed to air, which lead to the spontaneous exchange of Ca^{2+} for Na. Further characterisation of the material showed the successful introduction of Ca^{2+} into the bulk of the structure, up to a limit of 0.07 ± 0.006 Ca. However, hysteresis continued to be observed in the ion-exchanged material during cycling, suggesting that the O^{2-}/O_2 redox couple remained active within the material.

In Chapter 6 a novel cathode material, $Na_{0.6}Li_{0.1}Ni_{0.3}Mn_{0.6}O_2$, was presented. This particular cathode material was derived using a set of design principles to enable the synthesis of a cathode material with a TM layer stable against structural re-arrangement. Although the definitive nature of the TM layer ordering was not defined, spectroscopic characterisation of $Na_{0.6}Li_{0.1}Ni_{0.3}Mn_{0.6}O_2$ confirmed the activation of the O^{2-}/O^{-} redox couple with no molecular O_2 formation observed on the 1st cycle. Over multiple cycles, charge compensation in $Na_{0.6}Li_{0.1}Ni_{0.3}Mn_{0.6}O_2$ functioned using a combination of $Ni^{3+/4+}$ TM redox and reversible, high-voltage O^{2-}/O^{-} O-redox. This represents a significant step-forward in the development of future cathode materials. In addition, the capabilities of $Na_{0.6}Li_{0.1}Ni_{0.3}Mn_{0.6}O_2$ was benchmarked against other high-performing Na-ion cathode materials, exhibiting promising performance.

7.2 Future Work

Whilst the work presented in this thesis has provided new insight into the behaviour of O-redox materials, it has also uncovered a number of promising avenues for future research. These will be introduced below.

7.2.1 Investigating Surface Coatings to Prevent O_2 Loss

The instability of the cathode / electrolyte interface is a well-studied problem in the context of both stoichiometric Li-ion cathodes and Li-rich cathode materials. For O-redox compounds, the surface loss of O_2 is an extension of the irreversible disproportionation of O^- to O_2 in the bulk. Whilst the use of surface coatings would mean accepting the reversible cycling of the low voltage O^{2-}/O_2 redox couple in the bulk, preventing the loss of O_2 at the surface has been shown to reduce the degree of voltage fade over extended cycling. Established strategies include the use of surface treatments or coatings to protect the surface from degradation mechanisms. Although this is already an active area of research, the potential to deliver real step change in the energy density of Li-ion cathode materials gives incentive to study these strategies further. The reward for solving this problem would be a Li-ion cathode material capable of delivering a discharge capacity in excess of 250 mAh g^{-1} at an average voltage of ~3.6 V vs Li/Li^+.

7.2.2 *In Operando* O K-edge XAS and RIXS of O-redox Cathodes

Because of difficulties accessing resources during Covid-19, the *in operando* SXAS cell developed in Chapter 4 was not able to be used under measurement conditions. The development and optimisation of the cell is an important step towards performing *in operando* measurements of the O K-edge of O-redox materials. Such measurements will allow the meta-stable electron hole states formed on charge to be probed directly through O K-edge XAS measurements. In addition, conducting *in operando* RIXS measurements at the O K-edge of an O-redox material for the 1st time would be a sizeable achievement.

7.2.3 Exploring Room Temperature Ion-Exchange

Na-ion materials undergo tend to undergo a number of phase transitions during cycling, which are detrimental to the cycling performance of the material. Strategies to

prevent such phase transitions involve doping the TM or AM layers in Na-ion compounds. The room temperature ion-exchange method which was characterised in this thesis presents a novel route towards cationic doping of Na-ion materials. This method should be explored further to better understand the limits of the ion-exchange process. The ability for ion exchange using different Ca salts or different elements such as K^+ should be evaluated. In addition, the effect of the introduction of pillaring cations using this method on the long-term cycling performance of Na-ion cathodes must be evaluated.

7.2.4 Investigating O-redox Activity in Fully Dense Layered Oxides

An interesting point of discussion in this thesis presents the possibility of activating the O^{2-}/O^- redox couple within a fully dense TM layer. Extensive research into O-redox materials has shown that the presence of AM_{AM}^+-O-$[_]_{TM}$ type arrangements at the top of charge, created through the migration of cations from the TM layer, are prerequisites for O-redox activity. However, it remains unclear if a AM_{AM}^+-O-TM_{TM}^{X+} type arrangement present at the top of charge would promote electron hole formation on O. To answer this question, O-redox activity should be explored in a compound with a fully dense TM layer. Such a study would be extremely important to understand the limits of O-redox.

7.2.5 Further Research into Non-Honeycomb Ordered Cathodes

Finally, further work must be carried out to explore the compositional space surrounding non-honeycomb ordered cathode materials. Compositions could be derived from $Na_{0.6}Li_{0.1}Ni_{0.3}Mn_{0.6}O_2$ to enhance the O-redox capacity of the material, by increasing the Li content of the TM layer or by introducing redox inactive dopants. Furthermore, recent advances in the understanding of Fe redox in Na-ion compounds allows for compositions exhibiting a combination of $Fe^{3+/4+}$ TM redox and O-redox to be studied, paving the way for low-cost, high-energy density cathode materials.

Appendices

Table of Contents

Appendices for Chapter 3 ..... **177**
Investigating Voltage Fade in Li-rich Layered Oxides 177
Appendices for Chapter 4 ..... **181**
In-Operando Analysis of $Na_{0.6}Mn_{0.8}Li_{0.2}O_2$ 181
Appendices for Chapter 5 ..... **183**
Pillaring as a Strategy to Prevent Bulk Formation of Molecular O_2 183
Appendices for Chapter 6 ..... **185**
$Na_{0.66}Li_{0.1}Ni_{0.3}Mn_{0.6}O_2$ as a Reversible High Voltage O-redox Cathode 185

Appendices for Chapter 3

Investigating Voltage Fade in Li-rich Layered Oxides

S.G. $R\bar{3}m$, a: 2.85057 (7) Å, c: 14.23842 (9) Å, R_w: 7.66%, R_{exp} : 3.62%					
Atom	*x*	*y*	*z*	*SOF*	*Uiso (Å²)*
Li (3b)	0	0	0	0.999	0.03673 (8)
Ni (3b)	0	0	0	0.001	0.03673 (6)
Li (3a)	0	0	0.5	0.201	0.01184 (8)
Ni (3a)	0	0	0.5	0.129	0.01184 (6)
Co (3a)	0	0	0.5	0.130	0.01184 (6)
Mn (3a)	0	0	0.5	0.540	0.01184 (6)
O (6c)	0	0	0.23896 (9)	1.000	0.02577 (5)

Table A3.1: Table of XRD Rietveld refinement parameters for co-precipitation synthesised LNCMO.

S.G. $R\bar{3}m$, a: 2.85046 (1) Å, c: 14.22732 (5) Å, R_w: 2.64%, R_{exp} : 0.87%					
Atom	*x*	*y*	*z*	*SOF*	*Uiso (Å²)*
Li (3b)	0	0	0	0.991	0.00666 (2)
Ni (3b)	0	0	0	0.009	0.00666 (2)
Li (3a)	0	0	0.5	0.209	0.00271 (5)
Ni (3a)	0	0	0.5	0.121	0.00271 (5)
Co (3a)	0	0	0.5	0.130	0.00271 (5)
Mn (3a)	0	0	0.5	0.540	0.00271 (5)
O (6c)	0	0	0.24111 (3)	1.000	0.00826 (1)

Table A3.2: Table of XRD Rietveld refinement parameters for co-precipitation synthesised LNCMO.

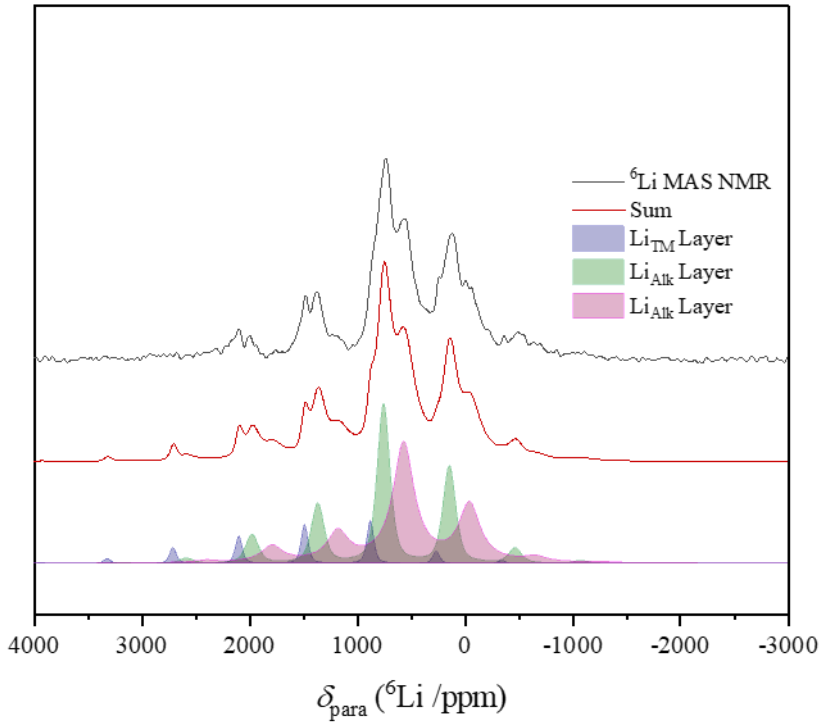

Figure A3.1: NMR deconvolution of ^{6}Li NMR spectrum of pristine LNCMO. Three Li environments can be observed, with two being centred at lower ppm arising from Li in the alkali metal layer, and a higher shift Li environment arising from Li in the TM layer.

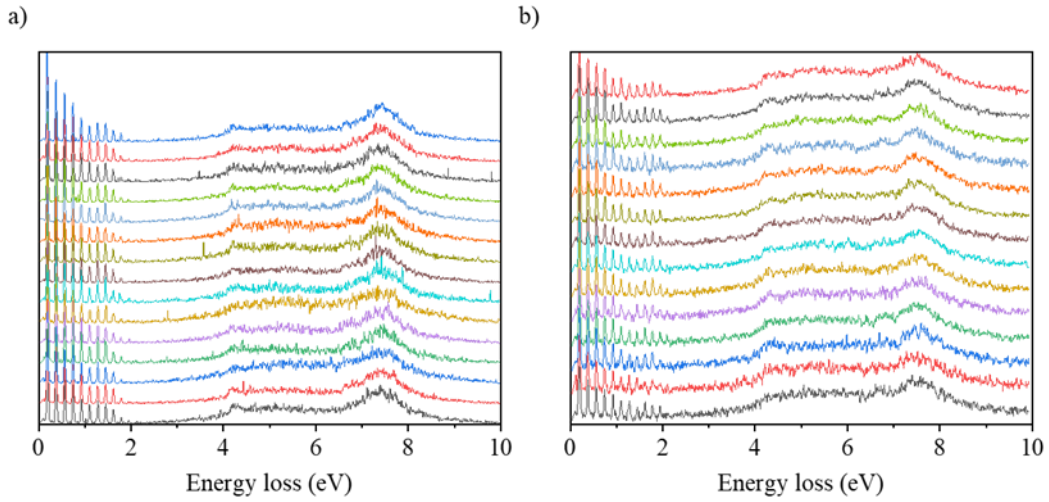

Figure A3.2: Plots of the individual high resolution RIXS scans taken at different sample locations for the a) 2nd cycle full charge and b) 100th cycle full charge.

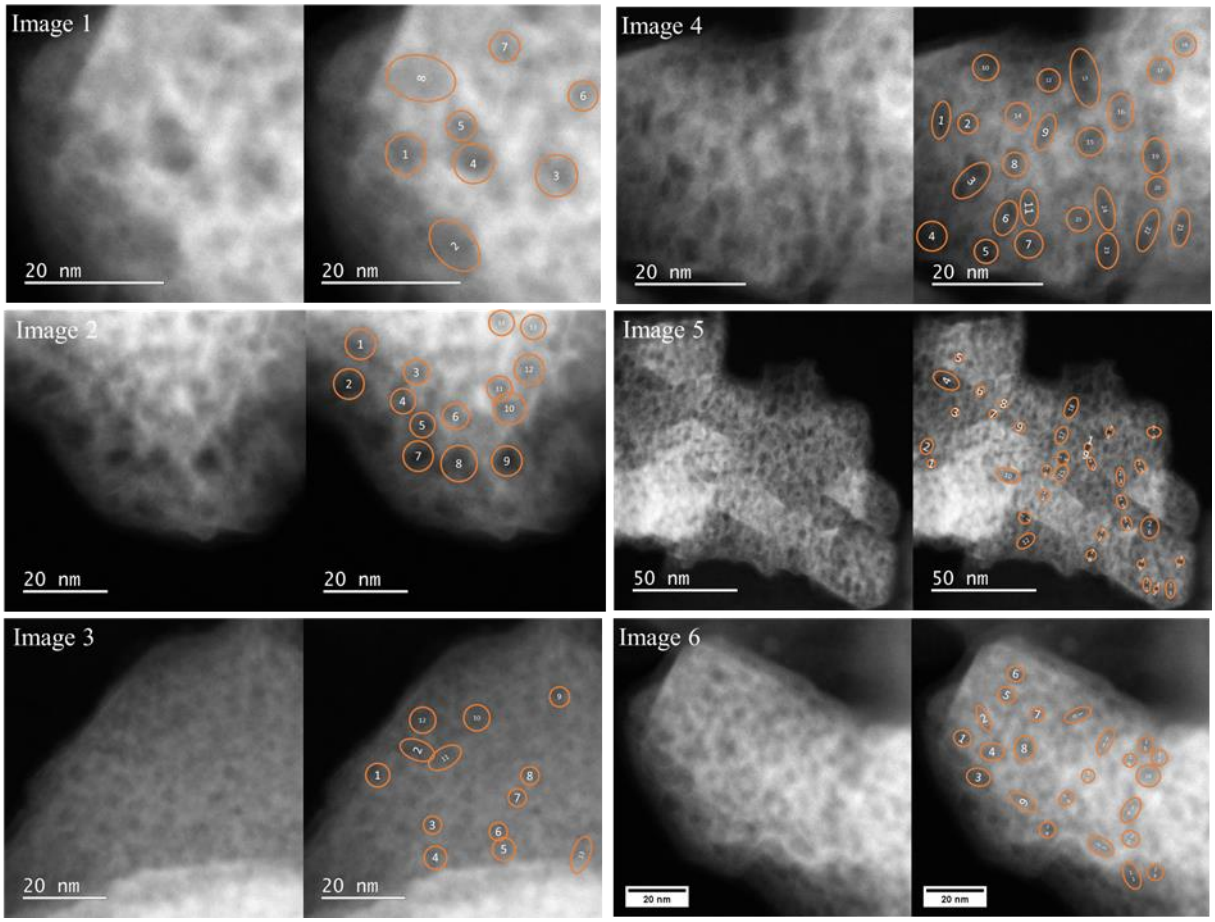

Figure A3.3: Selection of ADF-STEM images taken on 100th cycle LNCMO in the discharged state. All images show a large proportion of voids.

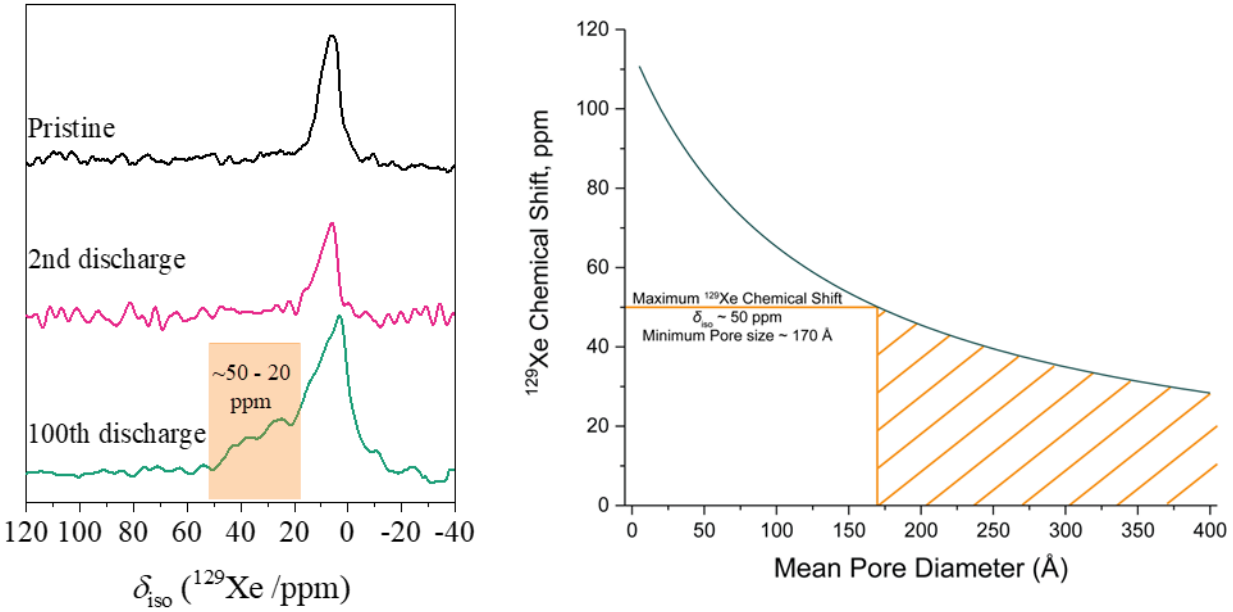

Figure A3.4: ^{129}Xe NMR data alongside a plot of void size vs chemical shift[29]. The minimum void size in the samples is around ~17 nm, as taken from a maximum chemical shift of 50 ppm.

Image Number	One	Two	Three	Four	Five	Six
Average / nm	6.1	6.7	5.9	5.8	6.5	7.4
Max / nm	9.9	8.6	9.0	10.7	13.3	10.5
Min / nm	4.2	6.0	4.3	3.6	3.8	4.5
Mean / nm	5.8	6.7	5.7	5.6	5.9	7.0

Table A3.3: Distribution of pore sizes collected from six different ADF-STEM images.

Appendices for Chapter 4

In-Operando Analysis of $Na_{0.6}Mn_{0.8}Li_{0.2}O_2$

S.G. *P*63/*mmc*, *a*: 2.85018 (1) Å, *c*: 11.13656 (2) Å, R_w: 4.98%, R_{exp} : 2.46%					
Atom	*x*	*y*	*z*	*SOF*	*Uiso (Å²)*
Li (2a)	0	0	0	0.2	0.00931 (2)
Mn (2a)	0	0	0	0.8	0.00931 (2)
O (4f)	0.6667	0.3333	-0.0841 (2)	1.0	0.02575 (7)
Na (2b)	0	0	0.25	0.184 (1)	0.002 (4)
Na (2d)	0.6667	0.3333	0.25	0.416 (1)	0.002 (4)

Table A4.1: Table of XRD Rietveld refinement parameters for NMLO.

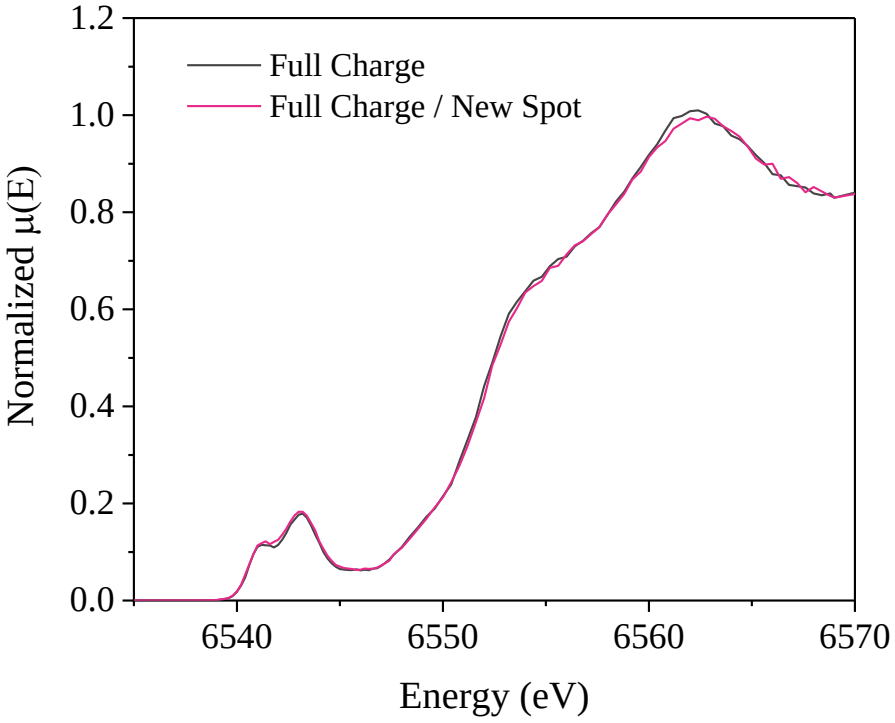

Figure A4.1: A comparison between two Mn K-edge XAS spectra taken at different spots on a full charge sample of NMLO, to highlight the effects of beam damage. No significant changes are observed, confirming that the beam damage was avoided.

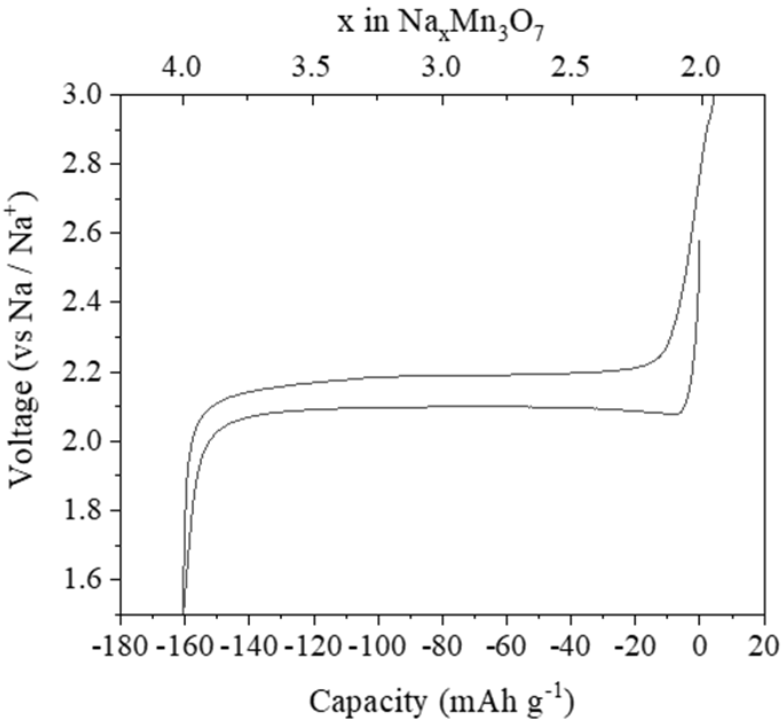

Figure A4.2: Electrochemical load curve of $Na_2Mn_3O_7$ when cycled between 1.5 V and 3.0 V at a rate of 10 mA g^{-1}.

Appendices for Chapter 5

Pillaring as a Strategy to Prevent Bulk Formation of Molecular O_2

S.G. *P63/mcm*, *a*: 5.033182 (9) Å, *c*: 11.209465 (5) Å, R_w: 4.75%, R_{exp} : 2.84%				
Atom	*x*	*y*	*z*	*SOF*
Mg (2b)	0	0	0	0.606 (1)
Mn (2b)	0	0	0	0.394 (3)
Mg (4d)	1/3	2/3	0	0.008 (1)
Mn (4d)	1/3	2/3	0	0.992 (4)
O (12k)	0.35817 (6)	0.35817 (6)	0.09614 (6)	1
Na1 (6g)	0.28826 (4)	0	0.25	0.435 (1)
Na2 (4c)	1/3	2/3	0.25	0.365 (1)

Table A5.1: Refinement results for pristine NMMO.

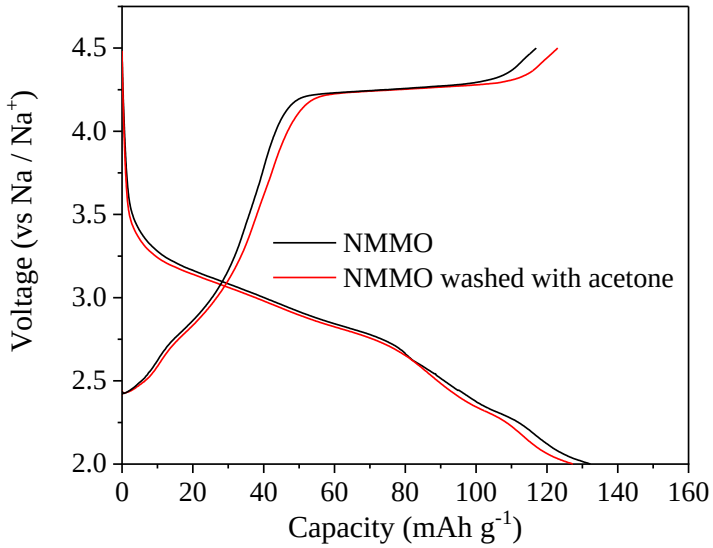

Figure A5.1: A Load curve comparison of cycling pristine NMMO and NMMO which has been washed in acetone.

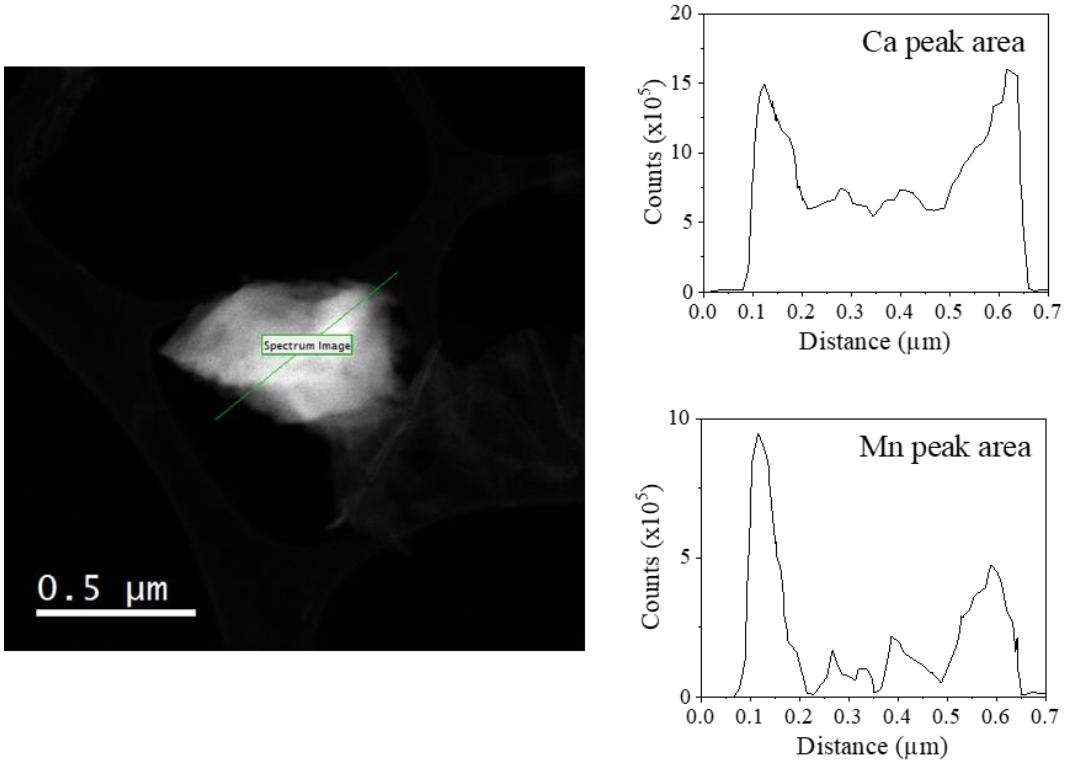

Figure A5.2: A STEM image of a CaNMMO particle being analysed by EELS. The EELS line scan can be seen in green. On the right hand side, Mn and Ca peak areas from the EELS line scan of $Na_{0.47}Ca_{0.1}Mn_{0.72}Mg_{0.28}O_2$. In this particular image, the dip in intensity seen in both line scans is a result of the particle thickness, as thicker regions will attenuate the EELS signal. Despite this, the Ca and Mn signals can be seen to follow the same trends across the first and last 100 nm of the particle, showing that Ca has indeed been introduced to the bulk of the structure.

Appendices for Chapter 6

$Na_{0.66}Li_{0.1}Ni_{0.3}Mn_{0.6}O_2$ as a Reversible High Voltage O-redox Cathode

Phase 1: S.G. *P*63/*mmc*, *a*: 2.89024 (4) Å, *c*: 11.04344 (3) Å, R_w: 4.18%, R_{exp} : 2.87% - Wt. Fraction 98.7%					
Atom	*x*	*y*	*z*	*SOF*	*Uiso (Å²)*
Li (2a)	0	0	0	0.1	0.00612 (2)
Ni (2a)	0	0	0	0.3	0.00612 (2)
Mn (2a)	0	0	0	0.6	0.00612 (2)
O (4f)	0.6667	0.3333	-0.0955 (2)	1.0	0.02470 (3)
Na (2b)	0	0	0.25	0.184 (1)	0.01154 (1)
Na (2d)	0.6667	0.3333	0.25	0.416 (1)	0.01154 (1)
Phase 2: S.G. *Fm*$\bar{3}$*m*, *a*: 4.158204 (1) Å, R_w: 4.18%, R_{exp} : 2.87% - Wt. Fraction 1.3%					
Atom	*x*	*y*	*z*	*SOF*	*Uiso (Å²)*
Ni (4a)	0	0	0	1.0	0.00524 (4)
O (4b)	0.5	0.5	0.5	1.0	0.00773 (6)

Table A6.1: Rietveld refinement parameters of NLNMO. The parameters of the major phase (NLNMO) are shown in the top table, while the impurity phase of NiO is presented in the lower table.

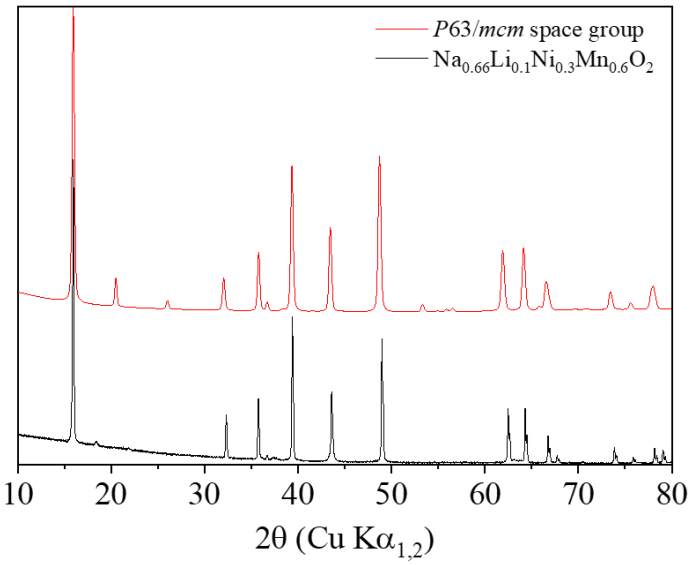

Figure A6.1: A comparison of the PXRD spectra of NLNMO and that of the *P*63/*mcm* space group, showing that the superstructure peaks present in the *P*63/*mcm* space group do not align with any of the peaks in NLNMO.

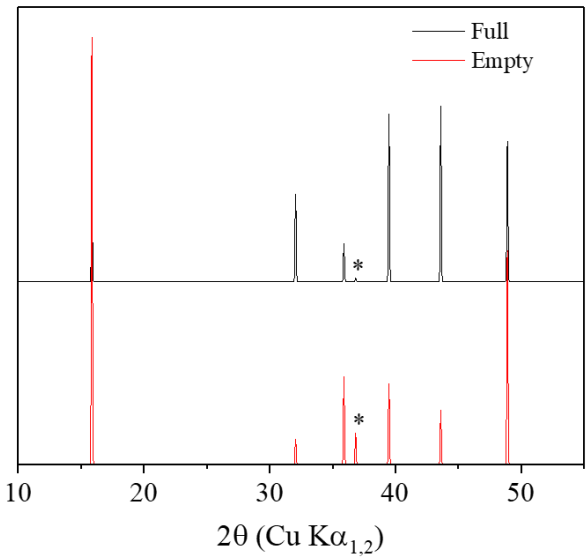

Figure A6.2: A comparison of the PXRD spectra of the *P*63/*mmc* space group with the Na 2*d* site full (black) and the Na 2*d* site empty (red).

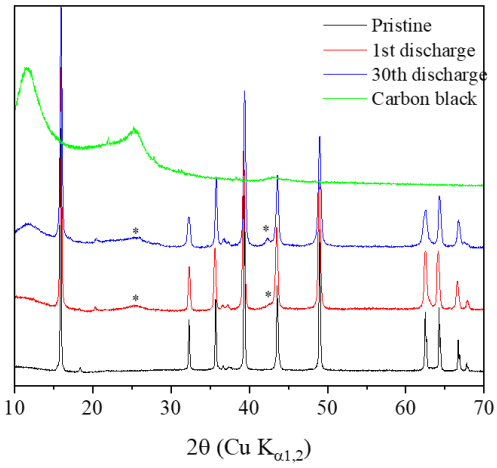

Figure A6.3: Ex-situ PXRD measurements of NLNMO comparing the pristine, 1st cycle and 30th cycle. A pattern of carbon black is shown due to the presence of some peaks from the carbon powder.

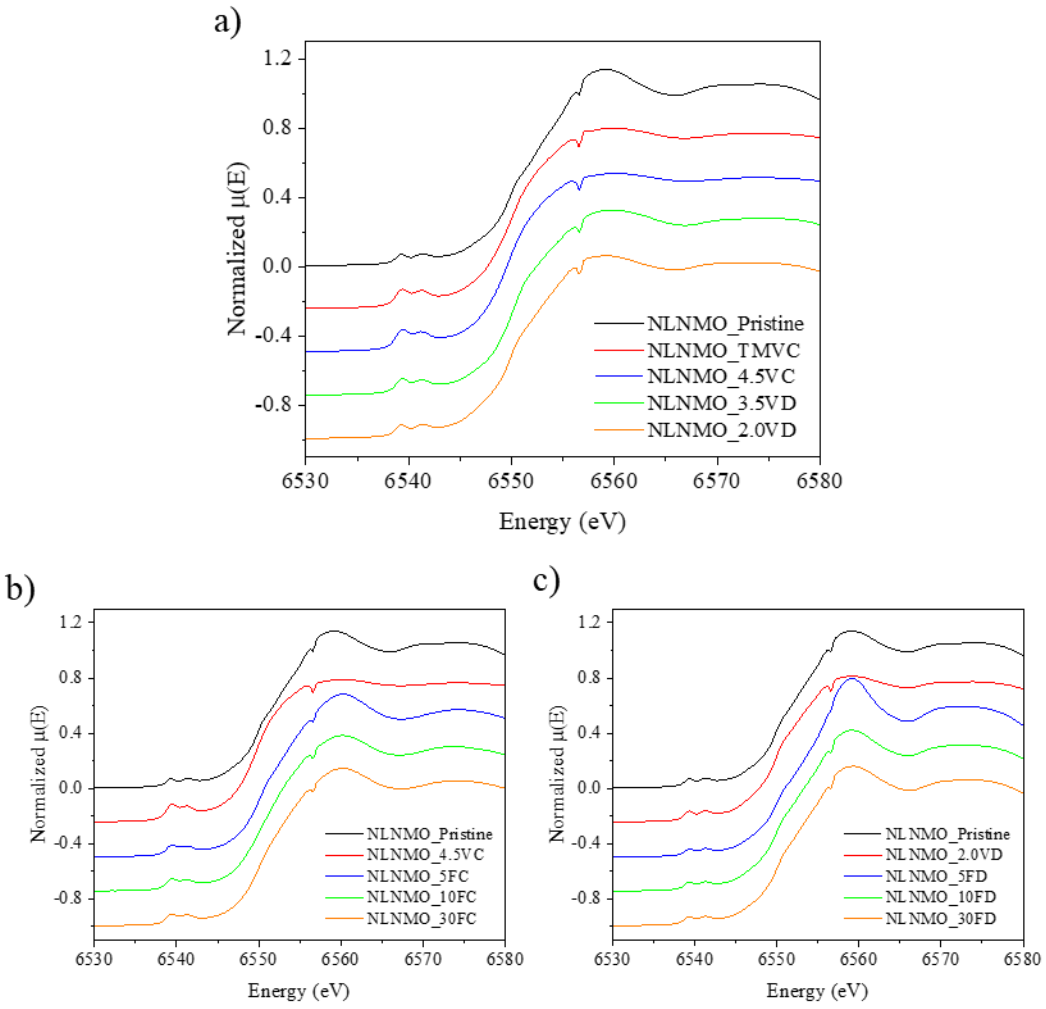

Figure A6.4: Comparison of ex-situ measurements of the Mn K-edge XANES in NLNMO over cycling. The graph in a) shows measurements taken over the 1st cycle, while panels b) and c) present the measurements over multiple cycles. Note that the small dip seen in all the spectra at ~ 6555 eV is caused by the grating used to get a monochromatic beam of radiation.

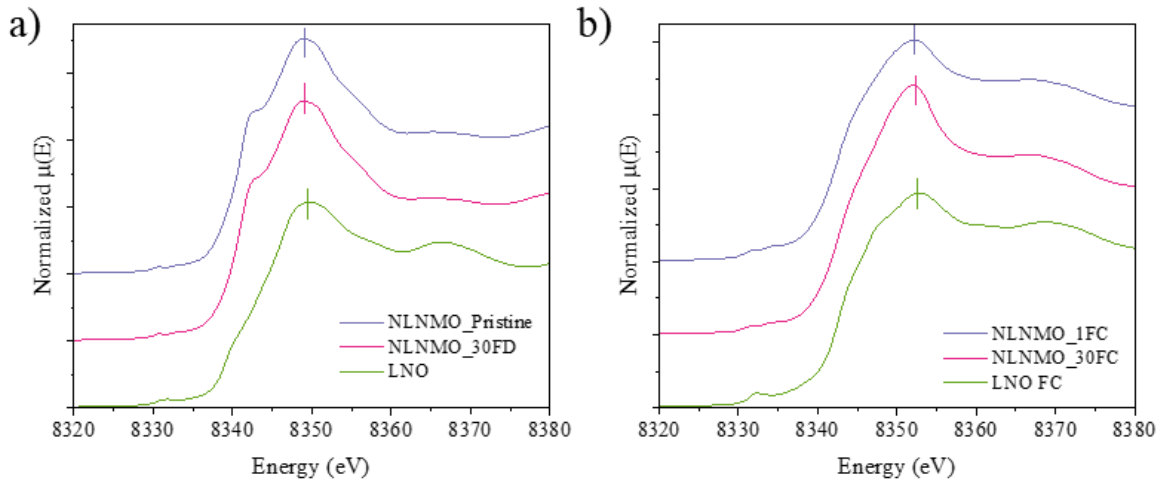

Figure A6.5: Comparison of ex-situ measurements of the Ni K-edge XANES in NLNMO over cycling. The straight lines are used to denote the position of the white line energy. The charged and discharged samples of NLNMO are identical (comparing the pristine and 1st cycle charged samples to their 30th cycle equivalents), confirming the stability and reversibility of the $Ni^{3+/4+}$ redox couple.

Being smart does not make you immune from stupidity.